

Photonic and Electronic Co-integration for Millimetre-Wave Hybrid Photonic-Wireless Links

Citation for published version (APA):

Konstantinou, D. (2022). *Photonic and Electronic Co-integration for Millimetre-Wave Hybrid Photonic-Wireless Links*. [Phd Thesis 1 (Research TU/e / Graduation TU/e), Electrical Engineering]. Eindhoven University of Technology.

Document status and date:

Published: 28/01/2022

Document Version:

Publisher's PDF, also known as Version of Record (includes final page, issue and volume numbers)

Please check the document version of this publication:

- A submitted manuscript is the version of the article upon submission and before peer-review. There can be important differences between the submitted version and the official published version of record. People interested in the research are advised to contact the author for the final version of the publication, or visit the DOI to the publisher's website.
- The final author version and the galley proof are versions of the publication after peer review.
- The final published version features the final layout of the paper including the volume, issue and page numbers.

[Link to publication](#)

General rights

Copyright and moral rights for the publications made accessible in the public portal are retained by the authors and/or other copyright owners and it is a condition of accessing publications that users recognise and abide by the legal requirements associated with these rights.

- Users may download and print one copy of any publication from the public portal for the purpose of private study or research.
- You may not further distribute the material or use it for any profit-making activity or commercial gain
- You may freely distribute the URL identifying the publication in the public portal.

If the publication is distributed under the terms of Article 25fa of the Dutch Copyright Act, indicated by the "Taverne" license above, please follow below link for the End User Agreement:

www.tue.nl/taverne

Take down policy

If you believe that this document breaches copyright please contact us at:

openaccess@tue.nl

providing details and we will investigate your claim.

Photonic and Electronic Co-integration for Millimetre-Wave Hybrid Photonic-Wireless Links

PROEFSCHRIFT

ter verkrijging van de graad van doctor aan de
Technische Universiteit Eindhoven, op gezag van
de rector magnificus prof.dr.ir. F.P.T. Baaijens,
voor een commissie aangewezen door het College
voor Promoties, in het openbaar te verdedigen
op vrijdag 28 januari 2022 om 11:00 uur

door

Dimitrios Konstantinou

geboren te Athene, Griekenland

Dit proefschrift is goedgekeurd door de promotoren en de samenstelling van de promotiecommissie is als volgt:

voorzitter:	prof.dr.ir. M. J. Bentum
promotor:	prof.dr.ir. I. Tafur Monroy
co-promotor:	dr. S. Rommel
co-promotor:	dr. U. Johannsen
leden:	prof.dr.ir. A. B. Smolders
	prof.dr. G. Ducournau (Université de Lille)
	prof.dr. L. Dittman (Danmarks Tekniske Universitet)
	dr. F. van Dijk (III-V Lab)

Het onderzoek of ontwerp dat in dit proefschrift wordt beschreven is uitgevoerd in overeenstemming met de TU/e Gedragscodes Wetenschapsbeoefening.

A catalogue record is available from the Eindhoven University of Technology Library.

ISBN: 978-90-386-5431-7

NUR: 959

Title: Photonic and Electronic Co-integration for Millimetre-Wave Hybrid Photonic-Wireless Links

Author: Dimitrios Konstantinou

Eindhoven University of Technology, 2022

Keywords: Millimetre wave wireless communications, optical heterodyning, optoelectronic conversion, co-integration and systems on-chip

Copyright © 2022 by Dimitrios Konstantinou

All rights reserved. No part of this publication may be reproduced, stored in a retrieval system, or transmitted in any form or any means without prior written consent of the author.

Typeset using L^AT_EX, printed in the Netherlands.

“To see the world, things dangerous to come to, to see behind walls,
draw closer, to find each other, and to feel.
That is the purpose of life.”

THE SECRET LIFE OF WALTER MITTY
in the memory of my father,
to my dear family and friends

Summary

In the dawn of 5G, the future radio access networks will provide 1000 times more wireless capacity supporting high-speed connections with guaranteed quality of service (QoS) and exceptionally low latency (<1 ms). It is expected by the key performance indicators (KPIs) that the capacity of 5G communications will offer data rates varying between 0.25 to 1 Gbit/s with a peak of 10 Gbit/s to a large number of users concentrated in hot-spot areas such as malls, universities and football stadiums. These system requirements can be dynamically achieved by employing hybrid optical-wireless fronthaul links operating in the lightly licensed millimetre wave (mm-wave) bands (30 - 300 GHz), allowing transmission of large bandwidth signals. The convergence between optics and electronics will take place on integrated devices within the future base stations. Such units will entail broadband photodiodes where optical signals are converted to mm-waves and transmitted in the wireless domain by RF electronic circuits. The assembly of a low-cost and low-energy consumption optoelectronic transmitter that can be replicated through photonic and electronic co-integration will eventually fulfil the massive deployment of numerous mm-wave base stations within urban areas accommodating the impending wireless demands predicted to reach 280 exabytes (EB) per month in 2022.

This work experimentally investigates the significant aspects of analogue radio-over-fibre (ARoF) fronthaul links that exhibit high capacity, showcasing future wireless communications' dynamic potential. Furthermore, a thorough analysis focuses on the co-integration of various components (photonic and electronic) on-chip performing the optoelectronic conversion, amplification and wireless transmission of mm-wave signals. While a variety of topics are discussed, the contributions can be divided into two main tracks. First, the centralised ARoF systems based on optical heterodyning are studied while photonic modulated signals are multiplexed based either on wavelength or space within the optical distribution networks. The realised experimental demonstrations follow the 5G KPIs where OFDM waveforms based on new-radio numerology are synthesised. Moreover, various essential elements towards the practical implementation of high-speed networks are also analysed, such as the real-time transmission/reception and analogue beamforming.

Second, in relation to the combination of different integrated circuits on a single device, the features of high-speed uni-travelling carrier photodiodes (UTC-PDs) are presented involving the evaluation of their physical properties through experimental characterisation and extensive equivalent circuit modelling, including the study of de-embedding techniques. Furthermore, the advances of electronic integration on indium phosphide (InP) are investigated to realise a high-gain, low-noise transimpedance amplifier (TIA) matching the characteristics of the UTC-PDs. Finally, different approaches and technologies are reviewed, leading to the design of an end-fire broadband antenna enabling the radiation into the free space of the boosted mm-waves. The examined integrated components are merged to a system on-chip providing a multi-Gbit/s mm-wave transmitter for high-capacity wireless communications.

The presented discussions and results in the published articles and the dissertation contribute to optimising the interface between optics and RF electronics by synthesising a compact, high-bandwidth, low-noise millimetre wave module accommodating the requirements of future high capacity 5G wireless communications. This work is part of the ‘5G System Technological Enhancements Provided by Fiber Wireless Deployments (5G STEP FWD)’ project, funded by the Horizon 2020 research and innovation program of the European Union.

Contents

Summary	vii
1 Introduction	1
1.1 Motivation	2
1.1.1 Millimetre wave wireless communications	3
1.1.2 Device miniaturization through III-V photonic/electronic integration	4
1.1.3 State-of-the-art in mm-wave photonic-wireless links	5
1.2 Research objectives and overview	6
1.2.1 Overview of the thesis	7
2 System-level Hybrid Photonic Wireless Links	9
2.1 Fundamental ARoF system definitions	10
2.1.1 Beyond D-RAN towards 5G C-RAN employing ARoF	11
2.1.2 Modulation formats: From OOK to 5G-NR OFDM	12
2.1.3 The electro-optic conversion	15
2.1.4 Optical heterodyning for mm-wave generation	17
2.1.5 ARoF signal generation schemes	18
2.1.6 Optical fibre propagation	19
2.1.7 Optoelectronic conversion and mm-wave generation	22
2.1.8 Wireless channel propagation	24
2.1.9 End-user detection	26
2.2 Signal multiplexing in ARoF architectures	27
2.2.1 Analogue fronthaul radio access network scenario based on UDWDM PON and SDM	28
2.2.2 Enabling phased array antenna systems for mobile communications	33
2.3 Experimental validation of ARoF schemes	36
2.3.1 Broadband fibre-wireless access to rural areas	36
2.3.2 Coherent ARoF mm-wave generation transmitting carrier aggregated 5G OFDM signals	39

2.3.3	High capacity real-time hybrid optical wireless 5G fronthaul with dynamic beam steering	43
2.4	Summary	46
3	High-speed photodiodes for mm-wave generation	49
3.1	Properties of photodetecting devices	50
3.1.1	Fundamental definitions	50
3.1.2	Photodetecting structures	52
3.1.3	Modelling a UTC-PD with lumped circuit elements	54
3.2	UTC-PD measurement processes	55
3.2.1	Experimental Measurements of UTC-PDs	56
3.2.2	Reflection coefficient measurements with a VNA	59
3.2.3	Full Equivalent Circuit Analysis	61
3.3	De-embedding Techniques	63
3.3.1	The open-short de-embedding	64
3.3.2	A correction to the open-short method	67
3.3.3	The S-parameter based de-embedding method	68
3.3.4	Evaluating the asymmetry assumption for the TML	69
3.3.5	S-parameter comparison between de-embedding methods	71
3.4	Summary	75
4	Broadband RF Components	77
4.1	A mm-wave transimpedance amplifier	78
4.1.1	HBT transistor principles	79
4.1.2	The transimpedance amplifier	83
4.1.3	Fabrication of an emitter follower TIA	87
4.2	A photonics-enabled V-band Vivaldi antenna	91
4.2.1	The antenna structure	92
4.2.2	Antenna measurement results	97
4.3	Active component interconnection	99
4.3.1	RF choke design	99
4.4	Summary	102
5	A broadband, highly integrated, hybrid photonic-wireless mm-wave transmitter module	105
5.1	The functional design of the mm-wave Tx	106
5.2	Co-integration of all integrated devices	107
5.2.1	Seamless chip interconnection techniques	108
5.2.2	Base design and housing the integrated circuits	110
5.2.3	Assembly simulation results	114
5.3	Device characterisation processes	116
5.3.1	Small-signal parametric response measurements	116
5.3.2	Transmission of 5G NR OFDM signals in V-band	117
5.4	Summary	118

6	Conclusions and future outlook	119
6.1	Summary and conclusions	119
6.2	Recommendations and Future Outlook	122
6.2.1	Analysis and improvement processes	122
6.2.2	Enhancing the functions of the integrated system	124
6.2.3	The road to 5G and beyond	127
	Bibliography	129
	List of Acronyms	163
	List of Publications	169
	Acknowledgements	173
	Curriculum Vitae	177

CHAPTER 1

Introduction

Since the implementation of the semaphore line by Claude Chappe in 1792 and the invention of the telegraph in 1837 by Samuel Morse, telecommunications, i.e., the transport of information over long distances, have become the cornerstone of our everyday lives [1]. During the '90s, the commercialisation of components supporting wireless communications enabled the transfer of a multitude of network connections from the underground copper cables over the air. Today, a great number of devices such as our laptops and mobile phones allow us to be connected to the rest of the world. More and more, novel applications require their perpetual connection with the wireless networks while many of these gadgets constantly remain online, exchanging information through the internet of things (IoT) [2]. IoT is the key towards the next industrial revolution, i.e., shift to industry 4.0, where machines and systems will revolutionise production chain [3]. Therefore, the future generations of wireless interactions will be characterised by demanding and stringent key performance indicators (KPIs). Furthermore, they will require broadband connections with ultra-short response times and high quality of service (QoS) while supporting the environment with low CO₂ emissions [4].

As a result, the ever-growing number of wireless devices increase the internet protocol (IP) influx, and it is expected that this trend will perpetuate in the future. The global IP traffic grows each year exponentially with a compound annual growth rate (CAGR) of 34.7%. As it is predicted in Fig.1.1a), by the year 2022, the traffic demands will reach 275 exabytes (EB) per month, where 70% of media will be provided by mobile and wireless fidelity (WiFi) terminals [5]. Furthermore, 26 billion systems will be connected to the communication networks, including smartphones and tablets, while half of this amount represents the devices' interconnections through machine-to-machine (M2M) routing [6]. For example, M2M type of signals will be applied to the automotive industry for vehicle to vehicle (V2V) and vehicle to everything (V2X) communications. Therefore, it is evident that the

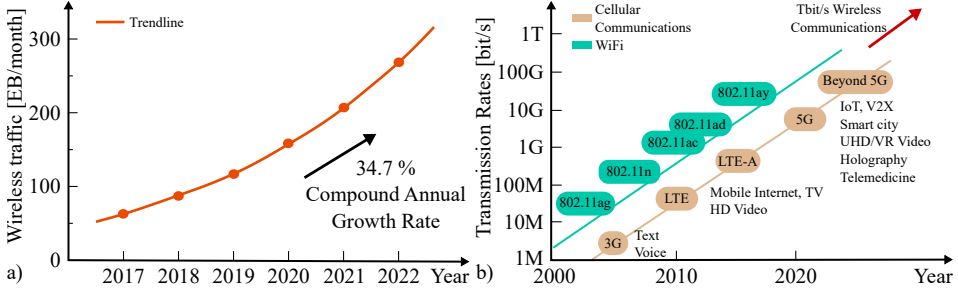


Figure 1.1: The growing trend of the wireless IP traffic growth estimations: a) IP wireless traffic required by mobile and WiFi terminals based on [5]; b) the evolution trend of wireless communication technologies (mobile and WiFi) including transmission rates.

increasing demands for IP traffic will extend the following years even further and novel methods in indoor and outdoor wireless systems need to be examined and implemented.

1.1 Motivation

Following the ascending IP specifications trend, higher data rates are required to support the increasingly large volume of wireless data traffic demands. The capacity C in [bit/s] providing the data rate with which an information signal can be transmitted over an additive white Gaussian noise channel operating over a bandwidth (BW [Hz]) can be calculated based on Shannon's formula in Eq. 1.1 [7].

$$C[\text{bit/s}] = BW \times \log_2 \left(1 + \frac{S}{N} \right) \quad (1.1)$$

where S/N is the signal-to-noise ratio (SNR) showing the relation between the average received signal power (S) and the average noise power (N) over the same frequency channel. Thus, based on this equation, the capacity can be increased either by boosting the signal power (logarithmic increase) or by broadening the channel bandwidth (linear increase) [8]. Towards sizeable data rates, the second option is preferred because of the linear growth in C and also due to the power limitations of communication devices restricting the first option [9], [10].

Therefore, the higher the carrier frequency, the broader the portion of spectrum (i.e., high BW) allowing multi-Gbit/s data rates (i.e., high C). This is verified in Fig. 1.1b) illustrating the evolution of transmission rates in the wireless domain both for WiFi and mobile communications [11], [12]. The supported data volume has increased by 100 fold the last decade due to the emerging new technologies in the millimetre wave (mm-wave) and sub-terahertz (sub-THz) frequencies. WiFi signals will be shifted from carriers at 2.4 or 5 GHz (e.g., 802.11ac) to 60 GHz (802.11ay) supporting data rates in the range of 20 to 40 Gbit/s [13]. Furthermore,

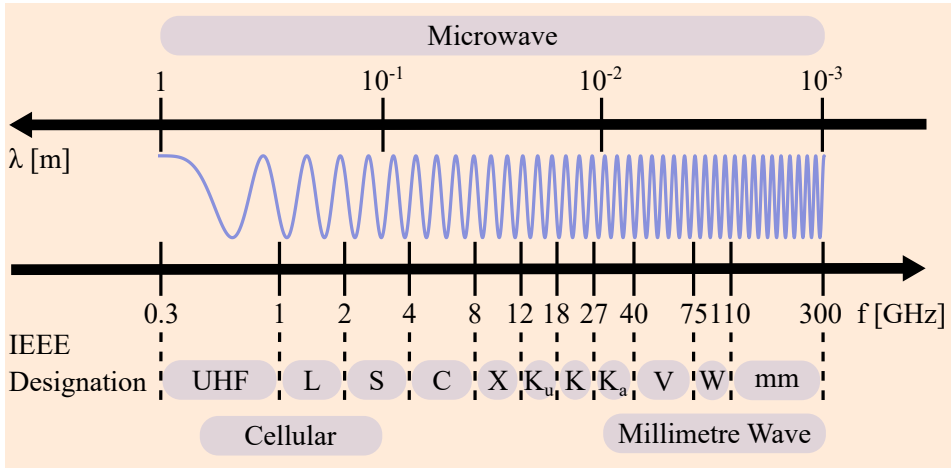


Figure 1.2: Millimetre wave mobile broadband: including the 30 to 300 GHz spectrum.

the fifth generation (5G) of mobile communications already defined frequency allocations beyond 24.25 GHz and user throughput higher than 10 Gbit/s [14]. Therefore, it is expected in the following years that Tbit/s wireless communications will be enabled [15].

1.1.1 Millimetre wave wireless communications

Figure 1.2 illustrates the frequency spectrum between 300 MHz to 300 GHz. A signal centred at a carrier located within the range of 30-300 GHz (i.e., 1-10 mm) is defined as mm-wave. As suggested by the institute of electrical and electronics engineering (IEEE), this part of the spectrum is divided into sub-bands, namely, Ka, V, W and mm [16]. The future wireless communication systems will operate in the lightly licensed or unlicensed mm-wave bands (e.g., a segment of V-band: 57-71 GHz) [17]. The beneficial aspect of operating in an unlicensed band resides on the non-existing channel segmentation allowing carrier aggregation of the whole bandwidth for point-to-point (P2P) links. Thus, broadband signals can be transmitted in outdoor P2P connections bridging buildings or rural areas with obstacles where fibre deployment is impossible [18]. Moreover, various potential applications in these bands are based on establishing indoor wireless links such as providing multi-Gbit/s access in kiosk downloading, rack-to-rack communications in data centres and high-speed WiFi to the home.

Despite the promising potential of moving from the sub-6 GHz communications to mm-wave frequencies, several issues need to be addressed. More specifically, the increasing free space path losses (FSPL) are an essential impediment considered while calculating a communications system's power budget. An additional

effect that is highly observed in the unlicensed part of the V-band is the absorption resonances of oxygen and water vapour molecules in the atmosphere that may significantly limit the range of wireless connections [19]. On the other hand, shorter wavelengths reduce the antenna sizes and their configuration into arrays with high gain. Moreover, implementing novel methods such as beamforming and multiple-input multiple-output (MIMO) techniques maximise the effective antenna gain [20]. These methods support the generated beams' control compensating for the increased losses posed by high-frequency operation.

This work focuses on studying the generation and detection of mm-wave signals based on the hybrid photonic-wireless connections, also known as radio-over-fibre (RoF) links. These systems use the advantageous properties of optical fibres and their ability to transport information over several kilometres with minimal cable losses, enabling the communication networks' centralisation. There are different ways of transferring the generated signals on a mm-wave carrier through optoelectronic conversion in high-speed photodiodes (PDs) [21], [22]. In the Chapters to follow, optical heterodyning is applied, where two photonic signals spaced by the desired frequency beat within the PDs so as to transfer the optical modulation in the electrical domain [23]. Finally, various mm-wave detection mechanisms will be discussed, including the interconnection of broadband envelope detectors (EDs) or downconversion to an intermediate frequency through electronic mixers, providing seamless processing of the received signals [24].

1.1.2 Device miniaturization through III-V photonic/electronic integration

In order to achieve the mm-wave generation based on optical heterodyning, photonic and electronic components need to be optimally interfaced, forming hybrid transceivers. At the same time, they are required to be as small (in size) and lightweight as possible with enhanced autonomy (e.g., battery operated) to be implemented far and wide, supporting the plethora of mm-wave applications. The device miniaturisation can be realised through the developments and breakthroughs applied in the field of circuit integration. The majority of active photonic integrated circuits (PICs) are grown on III-V based semiconductor materials due to their direct bandgap allowing the fabrication of devices with high efficiencies such as laser sources, amplifiers and photodetectors [25], [26]. More specifically, PICs based on indium phosphide (InP) technology are widely used in optical telecommunication wavelengths (e.g., 1310 or 1550 nm) due to its high absorption efficiency. InP is characterised by high electron velocities supporting the synthesis of broadband and increased output power photodiodes. On the other hand, electronic integrated circuits (ICs) are dominated by complementary metal-oxide-semiconductor (CMOS) technologies on silicon wafers. However, to date, InP-based IC amplifiers have been reported to exhibit the highest gain in mm-wave frequencies, making them an optimal choice to compensate for the excessive

path losses [27], [28]. Therefore, hybrid interconnection of InP photonic and electronic integrated circuits interfaced by low-cost laminate antenna technologies will lead to the minimisation of mm-wave front-ends towards the dawn of the future ultra-wideband communications [29].

1.1.3 State-of-the-art in mm-wave photonic-wireless links

Table 1.1: Summary of state-of-the-art and experimental demonstrations of mm-wave hybrid photonic-wireless links including several systems on-chip. Acronyms: QPSK: quadrature phase-shift keying, QAM: quadrature amplitude modulation, PAM: pulse-amplitude modulation, PIN-PD: PIN photodiode, UTC-PD: uni-travelling carrier photodiode, HBT: heterojunction bipolar transistor, HEMT: high electron mobility transistor, B2B: back to back, TSA: tapered slot antenna, ED: envelope detector, and ADC: analogue to digital converter.

Date	Data rate [Gbit/s]	Distance [m]	Frequency band	Modulation format	Technology Tx/Rx	Ref.
10/'15	100	100	W	QPSK	PD/mixer	[30]
11/'15	20	1700	W	QPSK	PD/mixer	[31]
04/'16	100	0.75	mm	QPSK	PD/mixer	[32]
10/'16	11	1	W	16QAM	UTC-PD, HEMT/ADC	[33]
11/'16	192	1	Ka	64QAM	PD/ADC	[34]
12/'16	70	5	V	32QAM	PD/mixer	[35]
03/'17	60	50	W	16QAM	PD/mixer	[36]
09/'17	54	2500	W	8QAM	PD/mixer	[37]
10/'17	144	2.5	V	16QAM	PD/mixer	[38]
03/'18	15	10	Ka	32QAM	PD/mixer	[39]
05/'18	52	3	V	16QAM	PD/mixer	[40]
09/'18	1056	3.1	mm	64QAM	PD/mixer	[41]
08/'19	20	5	Ka	QPSK	PD/ADC	[42]
10/'19	80	1	W	16QAM	PD/mixer	[43]
10/'19	3	0.5	V	NRZ	UTC-PD, TSA/ED	[44]
03/'20	60	3	mm	8PAM	PD/mixer	[45]
03/'20	100	1	mm	64QAM	UTC-PD, mHEMT/mixer	[46]
03/'20	12	1	Ka	QPSK	PD/mixer	[47]
05/'20	87.37	3	V	16QAM	PD/mixer	[48]
09/'20	612.65	2.8	mm	64QAM	UTC-PD/mixer	[49]
11/'20	101	1	W	QPSK	PD/mixer	[50]
11/'20	160	0.5	mm	32QAM	PIN-PD/mixer	[51]
05/'21	10	2	W	1024QAM	PD/ADC	[52]
06/'21	4.8	0.8	Ka	64QAM	PD/mixer	[53]
07/'21	20	B2B	V	32QAM	UTC-PD, HBT/ADC	[54]

Table 1.1 summarises different mm-wave wireless link demonstrations in the literature, including several figures of merit such as capacity, wireless distance, and modulation formats. Furthermore, several systems on-chip are presented using uni-travelling carrier photodiodes (UTC-PDs) and transistor technologies that achieve the highest data rates. The presented state-of-the-art table is a source of inspiration for this dissertation. A thorough analysis of hybrid photonic wireless links, integrated UTC-PDs, mm-wave amplifiers and wireless transmission with planar antennas will be investigated in the following Chapters.

1.2 Research objectives and overview

The PhD project described in this dissertation was carried out within the ‘5G System Technological Enhancements Provided by Fiber Wireless Deployments (5G STEP FWD)’ project, funded by the Horizon 2020 research and innovation program of the European Union [55]. The scope of 5G STEP FWD is to pave the path towards the evolution of the current passive optical networks to support the increasing data rate demands in the dawn of 5G. It includes research tracks such as the study of the network physical layer where 5G signals are converted from the optical to the millimetre wave domain towards the increased amount of wireless end-users. Furthermore, it elaborates on higher communication layers such as network centralisation by implementing dynamic resource allocation through software defined networking and network function virtualisation. The author’s project falls within the photonic wireless analysis of 5G STEP FWD. The primary purpose of this work is to introduce, design, and optimise a converged mm-wave/passive optical network configuration in a dense urban area by identifying the physical layer requirements of the fibre-based and wireless network to support 5G users.

Research Question: How can we bridge photonics and RF electronics towards the generation and wireless transmission of mm-waves ?

The dissertation attempts to answer this question by covering the theoretical analyses, simulations, and experimental works conducted by the author in the field of hybrid photonic-wireless communications. Various techniques of employing such systems in Ka-band are discussed. Furthermore, a thorough investigation towards the realisation of an integrated low-cost mm-wave module able to generate, amplify and transmit over the air 5G based broadband signals in V-band is presented. The work was mainly carried out at the Eindhoven University of Technology (TU/e), the Netherlands. It also includes a six-month external stay at the III-V Lab facilities in Palaiseau, France and an eight-month internship at Ferdinand Braun Institute (FBH) in Berlin, Germany.

1.2.1 Overview of the thesis

The contributions of the author are detailed throughout the following Chapters and the outline of the thesis is given as follows:

- **Chapter 2** includes the theoretical definitions describing the main aspects of 5G hybrid optical-wireless links. It also analyses a 5G based network scenario that can support the high capacity requirements of both the fixed optical connections and 5G analogue fronthaul. Experimental demonstrations of three analogue radio-over-fibre (ARoF) links transmitting various modulation formats provide a solid comparison between the different ARoF signal generation schemes while wireless signal transmission methods such as analogue beamforming are also investigated.
- **Chapter 3** takes the first step towards the miniaturisation of the previously presented bulky devices in the remote unit by initially discussing the physical aspects and properties of integrated uni-travelling carrier photodiodes. In addition, a detailed overview of the calculation of the full-equivalent circuit of these components allows further analysis of their characteristics as well as uncovers if there was an on-wafer process issue on the diode chips during fabrication. Finally, de-embedding techniques based on reflection coefficients removing the parasitic effects of the electrical transmission lines are presented, enabling the accurate analysis of their active region.
- **Chapter 4** demonstrates RF components responsible for amplification, interconnection and wireless transmission of the mm-waves generated by the UTC photodiodes in V-band. Therefore, as a first step, the Chapter elaborates on the various aspects of high-speed transistors synthesising a TIA widely used in optoelectronic interfaces. Important properties such as amplifier gain and noise are discussed while an emitter-follower TIA is fabricated and measured, providing satisfactory characteristics. Furthermore, a broadband Vivaldi antenna is designed on PCB exhibiting end-fire radiation and high gain such that it can be matched with the TIA circuit. Finally, a three-port RF choke synthesised to operate at 60 GHz allows the biasing of the UTC-PDs without causing RF power fading of the signals towards the input of the TIA.
- **Chapter 5** includes the processes towards the interconnection of all presented designs and assembly to form the mm-wave transmitter. A biasing network on PCB can support the four integrated chips and the decoupling capacitors that are necessary for avoiding DC oscillations at the input to the active components. Furthermore, component interconnection through various techniques such as wirebonding and application of conducting adhesives are assessed. Two experimental setups are suggested for measuring the characteristics of the device.

- **Chapter 6** provides a summary of this work and the conclusions. Furthermore, suggestions for future investigation are also discussed, while an overview of possible schemes for enhancing the mm-wave transmitter capabilities, such as beamforming solutions towards beyond-5G communications, are presented.

5G Hybrid photonic-wireless links

Optical fibre communication systems are able to transport broadband signals over hundreds of kilometres with ultra-low loss compared to traditional copper-based cables [56], [57]. This technology is also implemented on mobile links supporting the transfer of locally generated digital signals over fibre towards the wireless remote units (RUs) [58]–[60]. However, due to the emergence of 5G centralised networks, the RUs cannot sustain the increased requirements for high-speed digital to analogue conversion. Thus, analogue transport of already high data rate modulated signals becomes a promising solution eliminating the digital processing within the RUs. As a result, hybrid photonic-wireless links that are also known as analogue radio-over-fibre (ARoF) systems combine the valuable aspects of optical fibres and radio, establishing the backbone of the future communication networks [61].

Based on ITU-T FG-IMT-2020 [62], 5G should provide 1000 times more wireless capacity enabling internet connection to over 7 trillion wireless devices among billions of people with exceptionally low latency (< 1 ms). Especially concerning the capacity in small cells, it is expected that the data rate requirements will range between 100 to 1000 Mbit/s with a peak of 10 Gbit/s. Figure 2.1 illustrates an overview of several potential applications where radio over fibre (RoF) links can be integrated with the already deployed fibre access core networks. RoF can support broadband wireless access in mobile communications, indoor wireless distribution, bridging buildings or provide interconnection to regions where fibre deployment is not possible. Furthermore, these networks will control applications in agriculture and vehicular communications with ultra-fast connectivity.

This Chapter initially presents the fundamental definitions synthesising various types of analogue RoF links while providing a solid background on understanding their principle of operation. Then, a 5G-based network scenario is discussed, pinpointing the main approaches towards the evolution of the existing network infras-

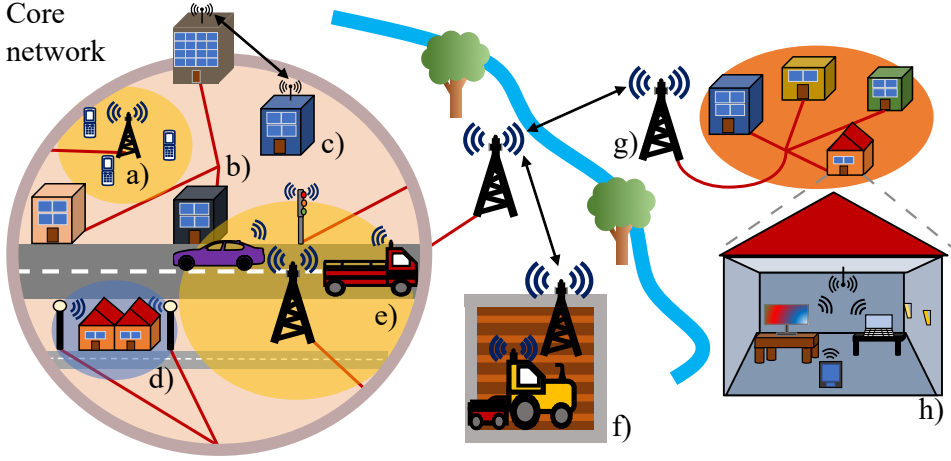


Figure 2.1: The urban environment of a future city where all the infrastructure is 5G enabled and interconnected through a fibre ring responsible for the management of all public functions, including communications and traffic. Scenarios for the use of mm-wave RoF links include: a) mobile front-/backhaul; b) fibre to the home (FTTH); c) broadband wireless access to buildings without fibre provision; d) wireless connection to the home through the city infrastructure (signals from lamp posts, traffic lights); e) vehicular communications; f) connection to agriculture; g) bridging physical obstacles; h) indoor high-speed wireless distribution.

structure in order to support the advanced future communications. The promising potential and different aspects of the presented scenario are verified by three experimental demonstrations testing the theoretically examined RoF signal generation methods while carrying 5G modulation formats. Furthermore, wireless transmission techniques, including analogue beamforming, are also tested. The network scenario, as well as the experimental processes and results covered in this Chapter, are discussed in [J1] and [C1]–[C3], respectively.

2.1 Fundamental ARoF system definitions

The main purpose of this section is to provide a solid theoretical background on the main building blocks comprising a hybrid photonic-wireless link. Figure 2.2 briefly describes the processes where a signal to be transmitted is initially transferred in the optical domain through the electro-optical (E/O) block within the central office (CO). Then, the waveform is launched to the optical fibre and converted in the electrical domain at the RU through an optoelectronic (O/E) component. As a further step, a mm-wave antenna allows the transmission of the RF waveform over the air that is finally detected by the wireless end-user (UE). The electrical-electrical (E/E) blocks at the RU and UE include high-speed RF components

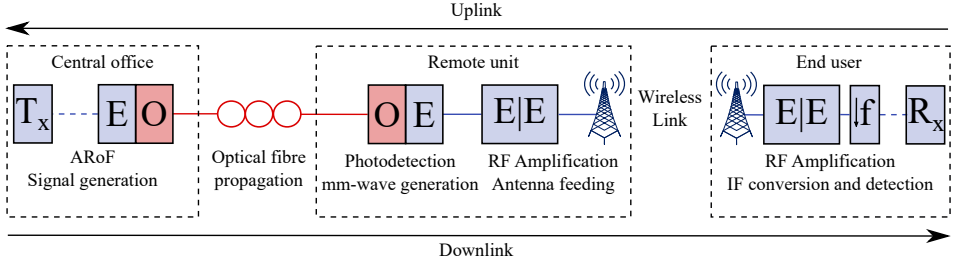


Figure 2.2: Generic block diagram of a hybrid photonic-wireless downlink/uplink.

responsible for the amplification of the mm-waves. Moreover, in the side of the UE there is an additional frequency down-conversion block reducing the processing complexity of the received signals.

Various techniques can be implemented towards the electrical up-conversion of the desired RF signals in the RU. A commonly employed method is initially based on the transfer of the optical waveform in baseband within the fibre [63]. Then, after photodetection within the RU, the signals are electrically assigned on a mm-wave frequency carrier through RF oscillators and mixers. However, this process is complex, bandwidth-limited and cost-inefficient in high frequencies. On the other hand, in the case where the mm-wave is generated through photonic heterodyning at the photodetector, the complexity of the RUs is decisively simplified. At the same time, by applying this technique, the network centralisation is further enabled following the 5G requirements [64], [65].

In the following subsections, all the key definitions will be provided in detail to support step by step the developed network scenario and experimental demonstrations presented in the Chapter. Section 2.1.1 introduces the evolution of the distributed radio access networks (D-RANs) to the fully centralised RAN (C-RAN) employing ARoF. Then, Sect. 2.1.2 shows various signal modulation formats employed in photonic-wireless links. Modulated electrical waves are converted in the optical domain through electro-optic components (Sect. 2.1.3). At a further step, the ARoF optical signal generation schemes, fibre propagation effects and heterodyne up-conversion methods are studied in Sect. 2.1.5, 2.1.6, and 2.1.7, respectively. Finally, the properties of the mm-wave wireless channel as well as the detection processes within the UEs are analysed in Sect. 2.1.8 and 2.1.9.

2.1.1 Beyond D-RAN towards 5G C-RAN employing ARoF

Figure 2.3 shows the evolution of network architectures supporting the high-capacity requirements of the UEs over the years. As illustrated in Fig. 2.3a), within the former generations of mobile networks, the payload data was transferred to the CO via internet protocol (IP) backhauling, whereas the baseband processing and signal up-conversion to an RF carrier were conducted in the RU [66]. Due

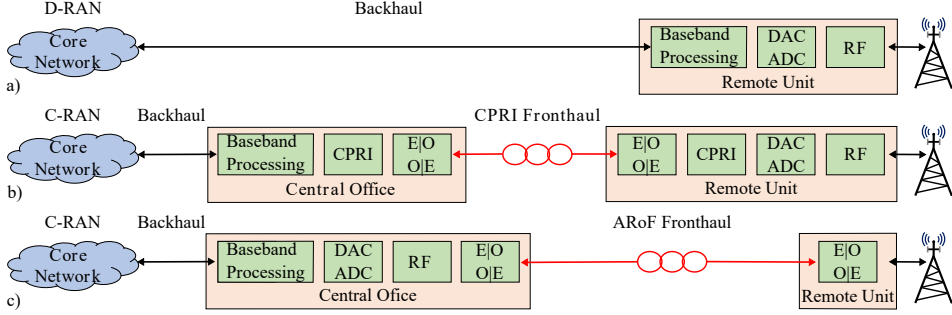


Figure 2.3: The evolution from D-RAN to the fully centralised C-RAN with ARoF where all processing functions are conducted in the central office.

to the distributed allocation of the remote units, this architecture is defined as distributed radio access network (D-RAN).

In the years that followed, the mobile access networks of Fig. 2.3b) were based on centralisation approaches involving electro-optic conversion and optical fibre connections to the RU. Within this C-RAN employing digital RoF (DRoF), multiple subsystems such as the broadband processing are partitioned between a centralised baseband unit (BBU) pool and the RU, reducing the remote unit's complexity, power consumption and maintenance costs [67], [68]. The optical fronthaul segment between the CO and RU is based on the common public radio interface (CPRI) [69], [70]. Digitised radio signals are transmitted through the optical domain to the RU to be transferred back in the electrical domain (O/E) while digital to analogue converters (DAC) further process the received waveforms before their RF frequency up-conversion [71].

However, CPRI cannot support the large volumes of wireless traffic and does not scale well with the high capacity requirements of the future 5G networks that demand the dense deployment of numerous RUs within an urban environment. Thus, the revolutionary architecture of Fig. 2.3c) is required showcasing the full centralisation of the network functions at the CO while simplifying the operations within the RU since no digital processing takes place, reducing their deployment costs and the communications latency. With analogue RoF, the RF carrier is already predefined through optical signal modulation techniques at the CO while the mm-wave is generated based on optical heterodyning [72], [73]. In the following subsections, all the key definitions comprising C-RAN networks employing ARoF will be analysed.

2.1.2 Modulation formats: From OOK to 5G-NR OFDM

Data encoding is one of the key parameters within a communications system [74]. A mm-wave carrier can transport information by modulating its amplitude, phase and frequency while modifying the information rate that can be transmitted over

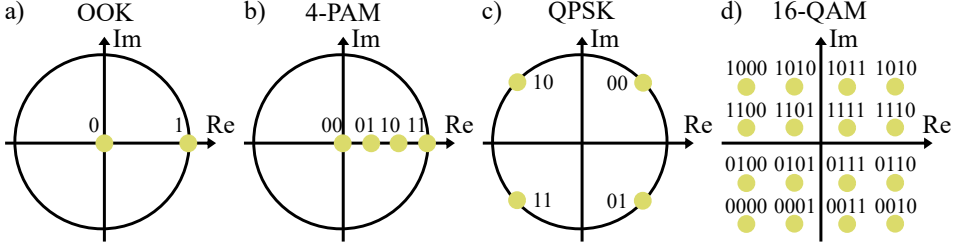


Figure 2.4: Constellation diagrams of various modulation formats: a) OOK; b) 4-PAM; c) QPSK; d) 16-QAM.

a given bandwidth, i.e., spectral efficiency (in bit/s/Hz) [75], [76]. In this section, various modulation formats that have been experimentally demonstrated and are considered for the implementation of ARoF fronthaul will be briefly described.

On-off keying (OOK) is the simplest form of non-return to zero (NRZ) amplitude modulation. The constellation diagram of an OOK signal is illustrated in Fig. 2.4a) [77]. Even though OOK waveforms are easy to encode, they lack in spectral efficiency since the number of bits per symbol is one and their data rate is equal to their occupied baseband bandwidth. On the other hand, by enhancing the complexity of modulation, the link capacity increases at the cost of additional and more elaborate digital signal processing (DSP). Comparing to OOK signals, multilevel (M-ary) amplitude modulation formats carry higher bit rates for the same used spectrum. One symbol of the four pulse amplitude modulation (4-PAM) in Fig. 2.4b) can carry $\log_2 4 = 2$ bits.

Moreover, phase modulation can be considered an alternative to transferring information with higher spectral efficiency and more robustness in channel power fading effects. However, carrier recovery techniques (e.g., Costas loop) are required within the processing blocks of the end-users [78], [79]. For example, phase-shift keying (PSK) modulation encodes symbols to be transmitted within the phase of the carrier. Moreover, a signal format combining the modulation in both phase and amplitude is quadrature amplitude modulation (QAM) [80]. The constellation chart of a 16-QAM signal is depicted in Fig. 2.4d). QAM modulation is widely employed in wireless communications and RoF links [81].

The presented single-carrier (SC) modulation techniques lack in terms of immunity to RF channel distortions such as small-scale channel fading (e.g., multipath effect) affecting the signal strength and phase [82], [83]. Therefore, complex equalisers in the receiver side are required for signal demodulation, especially when the channel response is much longer than the duration of the transmitted symbol [84]. Contrary to SC, with multi-carrier (MC) modulation, the transmission bandwidth is divided into multiple narrow subchannels, which are transmitted in parallel. Thus, each subchannel is narrow enough to minimise the fading it experiences [85]. Orthogonal frequency division multiplexing (OFDM) is a popular MC modulation format with high spectral efficiency that is widely applied

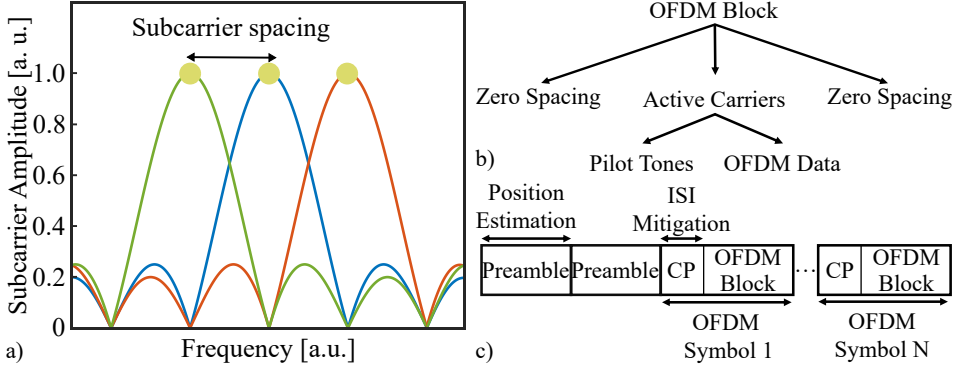


Figure 2.5: a) three OFDM subcarriers at a spacing of f_{scs} ; b) the structure of an OFDM block (frequency domain); c) an OFDM frame (time domain).

in RF bandwidth-limited communication systems [86]. These waveforms show robustness in signal impairments such as phase noise while allowing the efficient integration of multiple-input multiple-output (MIMO) systems [87].

Within an OFDM signal, QAM symbols are mapped on orthogonal subcarriers spaced by a frequency distance of $f_{scs} = 2^\mu \times 15$ kHz where, $\mu \in [0, 4]$ (Fig. 2.5a)). A multiple number of active subcarriers ($N_c^{act} \leq 3300$) synthesize an OFDM block of Fig. 2.5b) including active components carrying the QAM information while pilot tones can also be inserted at predefined intervals. These subcarriers are crucial for the inversion of the impact of the wireless channel at the receiver side during demodulation. Furthermore, zero padding is implemented in each block, allowing oversampling so that the total number of subcarriers (N_c^{tot}) is an exponentiation at the base of two (e.g., $N_c^{tot} = 4096 = 2^{12}$) [88]. After converting from the frequency to the time domain, a cyclic prefix (CP) is prepended to each OFDM symbol averting any inter-symbol interference (ISI). The total symbol duration, including the one of the CP is equal to $(66.67 + 4.69)/2^\mu \mu s$ [89]. OFDM frames are formed comprising of N_{symp} OFDM symbols each ($N_{symp} \leq 14$). Furthermore, a preamble equal to twice the size of a block may also be added, pinpointing the time location of each frame during reception. These OFDM frames are composed of different sets of subcarriers at different frequencies, hence constituting different bands. If multiple frames are summed in the time domain, then a single a multiband-OFDM (M-OFDM) signal is formed [90].

OFDM modulation will play a key role in future mobile communications since it complies with the key requirements for flexible 5G networks in small cell deployments that are low latency, high throughput and low power consumption. Moreover, by considering the fact that in mm-wave frequencies, the signals suffer from environment channel fading effects, the demand for more elaborate modulation techniques is increased [91]. Therefore, in order to achieve this, new spectrum assignments in the lower mm-wave range are being considered, which together with

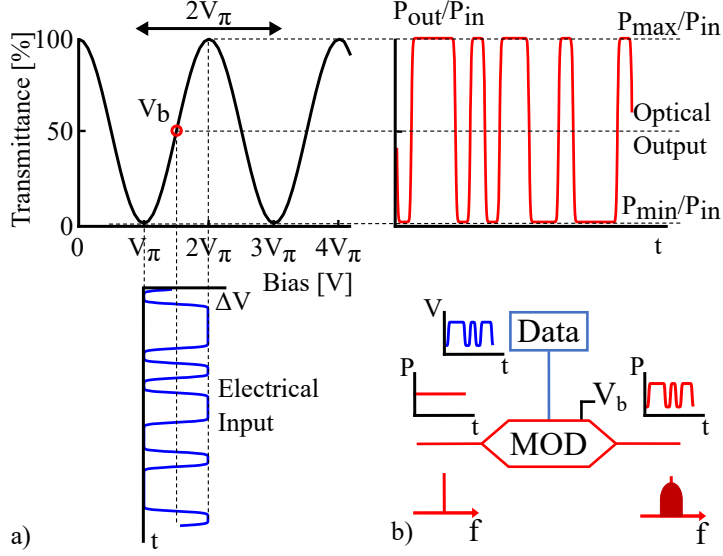


Figure 2.6: Amplitude modulation in optical communications: a) the transfer function of a Mach-Zehnder modulator; b) block diagram representation of an optical modulator.

a new radio interface and an adapted, and flexible numerology for OFDM are envisioned to successfully transmit peak user data rates in the Gbit/s range [92]. The waveforms studied in the experimental part of this Chapter in Sect. 2.3.2 and 2.3.3 are based on 5G new radio (5G NR) [93], [94].

2.1.3 The electro-optic conversion

An optical modulator allows the data generated in the electrical domain to be imposed on an optical beam originating from a continuous wave (CW) laser. The speed of this optoelectronic device defines the data rates of the optical communication systems. Various techniques for optical modulation have been widely realised based on directly modulated lasers (DML), electro-absorption modulators (EAM) and Mach-Zehnder modulators (MZM) [95]. Lithium niobate (LiNbO_3) MZM are always assumed in this dissertation and interconnected within the demonstrated experimental systems RoF links [96]. The simplest structural form of a MZM and principle of intensity modulation are shown in Fig. 2.6a,b).

The light beam (P_0) originating from an optical source centred at an angular frequency ω_c is split into the two branches of the MZM. The field in one branch is inserted into a phase modulator while the other either remains unmodulated (reference arm) or there is an additional phase shifter while push-pull control is used to regulate the phases inversely [97], [98]. The two fields interfere at the output leading to a constructive and destructive interference depending on the

applied electrical driven voltage (ΔV) and thereby leading to the optical intensity modulation. The output electric field (E_{mod}^{out}) and power transfer function (T_{mod}) of the modulator are shown in Eq. 2.1 and Eq. 2.2, respectively. The parameter T_{mod} is plotted in Fig. 2.6a) [99].

$$E_{mod}^{out} = \sqrt{P_0} \cos\left(\frac{\pi}{2} \frac{\Delta V}{V_\pi}\right) \cos(\omega_c t) \quad (2.1)$$

$$T_{mod} = \cos^2\left(\frac{\pi}{2V_\pi} \Delta V\right) \quad (2.2)$$

By applying different levels of bias voltage as well as opting for various types of MZM (e.g. dual drive, IQ MZM), a multitude of optical modulation formats can be synthesized [100]. In that case, ΔV consists of a direct current (DC) component (V_b) and the signal modulation ($s(t)$), i.e., $\Delta V = V_b + s(t)$. As an example, in order to achieve the optimal extinction of an OOK signal where the optical output is switched (i.e., voltage swing) from full transmission to full extinction, the DC component of ΔV is required to be equal to the switching voltage (V_π) where the relative phase change between the modulator arms is equal to π . Amplitude electro-optic conversion is applied in the experimental demonstrations of this Chapter, where the waveforms carrying advanced signal formats are already modulated in the electrical domain [101]. The signal inputs on the MZMs are provided by waveform generators (WGs) or DACs on field programmable gate array (FPGA) boards manipulating the intensity of the input light.

Moreover, in various RoF experimental links, the photonic up-conversion in the mm-wave domain is based on the principle of two tone generation with optical carrier suppression (OCS) [102]. Therefore, by inserting an RF tone at the electrical input of the modulator having an angular frequency ω_t , i.e., $\Delta V = V_b + V_s \cos(\omega_t t)$, and substituting it in Eq. 2.1 while implementing the trigonometric identities, then the output optical electric field ($E_{mod_{RF}}^{out}$) carrying the modulated signal is defined in Eq. 2.3 [103].

$$E_{mod_{RF}}^{out} \approx E_{mod}^{out}|_{\Delta V=V_b} - \sqrt{P_0} \frac{\pi V_s}{4V_\pi} \sin\left(\frac{\pi V_b}{2V_\pi}\right) \{\cos[(\omega_c - \omega_t)t] + \cos[(\omega_c + \omega_t)t]\} \quad (2.3)$$

In theory, by setting $V_b = V_\pi$ in $E_{mod_{RF}}^{out}$, then, $E_{mod}^{out} = 0$ and carrier suppression is achieved. Thus, in the optical spectrum, two tones are generated centred at $\omega_1 = 2\pi f_1 = \omega_c - \omega_t$ and $\omega_2 = 2\pi f_2 = \omega_c + \omega_t$ with a distance of $\Delta\omega = 2\omega_t = 2\pi\Delta f$. Once these tones heterodyne beat within a high-speed photodiode, they can potentially provide the mm-wave carrier at a frequency Δf . The implementation of the extracted derivations will be analysed in the following subsections.

2.1.4 Optical heterodyning for mm-wave generation

The millimetre wave generation in the optical domain has been widely studied and is based on optical heterodyning, i.e., the beating on a photodiode (PD) of two optical signals spaced at the desired RF frequency (f_{RF}). The expressions of the electric fields for both the signal (E_s) carrying modulated data and a co-propagating continuous wave (E_{LO}) local oscillator (LO) are expressed in Eq. 2.4 and Eq. 2.5, respectively.

$$E_s(t) = \sqrt{P_s} s(t) e^{-i(\omega_s t + \phi_s(t) + \phi_s^n)} \quad (2.4)$$

$$E_{LO}(t) = \sqrt{P_{LO}} e^{-i(\omega_{LO} t + \phi_{LO}^n)} \quad (2.5)$$

where the modulated signal in baseband carries information in amplitude ($s(t)$) and phase ($\phi_s(t)$), and P_s , P_{LO} are the optical signal powers. Both electric fields, oscillate at radial frequencies ω_s , ω_{LO} and carry phase components ϕ_s^n , ϕ_{LO}^n which also depend on the properties of the optical sources (e.g., laser linewidth). The equation describing electric field at the photodiode (E_{PD}) is derived as:

$$\begin{aligned} E_{PD}(t) &\propto |E_s(t) + E_{LO}(t)|^2 \\ &= [E_s(t) + E_{LO}(t)][\overline{E_s(t) + E_{LO}(t)}] \\ &= |E_s(t)|^2 + |E_{LO}(t)|^2 + E_s(t)\overline{E_{LO}(t)} + \overline{E_s(t)}E_{LO}(t) \end{aligned} \quad (2.6)$$

Thus, the generated photocurrent I_{PD} is proportional to:

$$I_{PD}(t) \propto P_s s^2(t) + P_{LO} + 2\sqrt{P_s P_{LO}} s(t) \cos[\omega_{RF} t + \phi_s(t) + (\phi_s^n - \phi_{LO}^n)] \quad (2.7)$$

with the desired RF signal defined as $2\sqrt{P_s P_{LO}} s(t) \cos(\omega_{RF} t + \phi_{RF}(t))$ at an angular frequency of $\omega_{RF} = |\omega_s - \omega_{LO}|$. The baseband components $P_s s^2(t) + P_{LO}$ of I_{PD} are filtered out by the RF modules connected to the mm-wave antenna. Furthermore, even though the additional high frequency terms $\nu(2\omega_s)$, $\nu(2\omega_{LO})$ and $\nu(\omega_s + \omega_{LO})$ can be mathematically extracted, they are centred within the range of approximately 400 THz which is too high to be physically generated by the photodiodes. Based on the above mentioned definitions, the term $\Delta\phi^n = \phi_s^n - \phi_{LO}^n$ affects the phase noise of the generated signal and needs to be minimised. That can be achieved by implementing coherent RoF schemes using a single optical laser source and OCS.

The presented method is commonly referred to as photonic up-conversion since any modulation present on the optical signals is transferred in the mm-wave domain. This efficient process allows the simplification of wireless transmitters since no high-frequency sources are required at the remote units to perform electronic up-conversion. Finally, based on the fact that the LOs can be generated at the central office, the C-RAN network topologies are enhanced even further simplifying the structures of the RUs and reducing their costs.

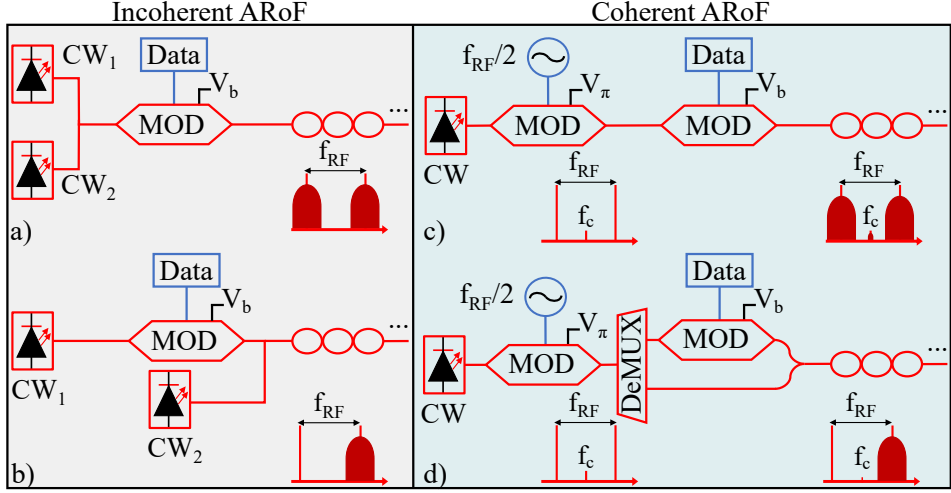


Figure 2.7: Summary of RoF signal generation schemes: a,b) incoherent schemes using two free running lasers (CW_1 and CW_2); c,d) coherent schemes based on a single laser, two tone generation and carrier suppression. Upper schematics: two modulated tones; lower schematics: modulated signal with a co-propagating local oscillator.

2.1.5 ARoF signal generation schemes

In accordance with the choice of a modulation format based on the end-user application, the selection of the signal generation scheme in the optical domain is also a fundamental aspect of the hybrid optical-wireless fronthaul links. Figure 2.7 provides with an overview of various ARoF generation structures. These systems can be divided based on the number of modulated signals launched at the optical fibre as well as their ability to preserve the phase information of the RF waves.

The block diagrams of the incoherent schemes in Fig. 2.7a,b) are based on the generation of two optical signals from two independent sources spaced by the desired radio frequency (f_{RF}). Once these waves heterodyne beat on a PD, an RF signal may be introduced in the wireless domain. However, such a process results in a mm-wave carrying the combined uncorrelated phase noise ($\Delta\phi^n$) of both laser sources. Therefore, there is a high probability of an output waveform with an exceedingly reduced quality due to increased linewidth, phase noise and carrier frequency drift that deviates from the international telecommunication union (ITU) regulations for radio carriers [104]. The negative impact of these effects can be improved by phase-locking the two lasers so that their wavelength difference and relative phase remains constant [105], [106]. These schemes can only be used for signals carrying intensity modulation formats (e.g., OOK) since any phase information is affected by the phase noise of the system.

Comparing to the incoherent ARoF systems, the block diagrams of Fig. 2.7c,d) have the advantage of using a single laser source providing a significantly improved

RF phase stability [107]. In both schemes, an externally driven sinusoid at $f_{RF}/2$ is applied at the electrical input of the modulator. At the same time, by biasing at the carrier suppression point V_π , the second-order harmonics are excited, leading to OCS and the generation of two optical tones at double of the sinusoid's frequency. Thus, the direct beating of the tones will lead to a new carrier at twice the frequency of the original sinusoid, i.e., at f_{RF} . This method is beneficial since the phase noise factor ($\Delta\phi^n$) from Eq. 2.7 on the two optical tones are correlated and therefore cancels in the beating leaving only the phase noise of the external RF synthesizer used. In addition, the required bandwidth for external oscillators that generate the RF tone is reduced by half.

After the electro-optic modulation and the transfer of the desired signal in the optical domain, the systems of Fig. 2.7a,c) suffer from in-band beat noise generated by the direct beating of the two sidebands [108]. Finally, the different amounts of dispersion that each modulated tone experiences within the fibre lead to RF power fading after the heterodyne beating [109], [110]. The equation and properties of this phenomenon will be analyzed thoroughly in Sec. 2.1.7 discussing the optoelectronic conversion and mm-wave generation. In this type of system, the effect of in-band beat noise can be ruled out by electrically moving the baseband signal to an intermediate frequency (f_{IF}) before the optoelectronic conversion by the second modulator [111].

A candidate to avoid the impact of dispersion and in-band beat noise is in Fig. 2.7b). This incoherent technique is one of the classical methods of optical heterodyning that is widely applied in optical communication systems [112], [113]. It includes an independent LO laser while only one modulated signal is present in the fibre and is spaced from the LO by f_{RF} . However, as previously mentioned, this type of system can be severely affected by phase noise and carrier instability.

Therefore, the valuable aspects of the systems in Fig. 2.7b,c) are combined in Fig. 2.7d). Once the two tones are generated; they are split by a demultiplexer (DeMUX). At a next step, one of the optical signals is modulated while it is recombined with the second that acts as an LO. Thus, all the aforementioned impairments are mitigated at the cost of more complex setups. This type of system is extremely beneficial since the signal phase information is preserved, allowing the generation of RF signals carrying complex modulation formats such as QAM [36]. In the demonstrated experimental processes, the results acquired from systems presented in Fig. 2.7b,c) and d) will be discussed in Sect. 2.3.1, 2.3.2 and 2.3.3, respectively.

2.1.6 Optical fibre propagation

Optical fibres constitute the cornerstone of RoF links, allowing the signal distribution from the central office to various optoelectronic conversion terminals where the mm-wave generation takes place. The propagation of a pulse with an envelope amplitude $A(z, t)$ within an optical fibre is governed by the nonlinear Schrödinger equation (NLSE) of Eq. 2.8 [114].

$$i \frac{\partial A(z, t)}{\partial z} = -\frac{i}{2} a A(z, t) + \frac{\beta_2}{2} \frac{\partial^2 A(z, t)}{\partial t^2} - \gamma |A(z, t)|^2 A(z, t) \quad (2.8)$$

The three terms on the right-hand side of the NLSE include parameters defining the fibre loss (a), dispersion (β_2) and nonlinearities (γ). Therefore, it is crucial to analyse these effects since they may cause the degradation of the optical signal quality that will eventually affect optoelectronic conversion.

Fibre attenuation and scattering effects

While optical signals propagate within a fibre, they experience power losses that depend on the fibre length L . If P_{in} is the power of a waveform launched at the input of a fibre, the measured output power is given in linear and logarithmic units based on Eq.2.9 and Eq.2.10 respectively [115]:

$$\frac{\partial P}{\partial z} = -a z|_{z=L} \Rightarrow P_{out} = P_{in} \exp(aL) \quad (2.9)$$

$$P_{out} = P_{in} - a_{\log} L \quad (2.10)$$

where a is the attenuation coefficient calculated in km^{-1} and a_{\log} is equal to $-4.343a_{\log}$ measured in dB/km.

Various factors contribute to fibre losses such as material intrinsic absorption (ultraviolet, infrared), extrinsic impurities (water vapour, transition metals), waveguide imperfections (Mie scattering, bending losses). However, these effects are negligible ($\simeq 0.03$ dB/km) comparing to the ones due to Rayleigh scattering $a_R \simeq 0.12..0.16$ dB/km. Rayleigh scattering is an elastic process where a spectral component is generated at the same carrier frequency of the signal opposite to the propagation direction. For standard single-mode fibres (SMFs), the attenuation constant is approximately 0.2 dB/km at 1550 nm [116].

An additional scattering effect causing power limitations is the inelastic phenomenon of stimulated Brillouin scattering (SBS). SBS is due to acoustic vibrations (electrostriction) induced by light travelling within the fibre, changing its refractive index. This effect leads to an up-shifted and a down-shifted backscattered spectral component (i.e., Stokes and anti-Stokes) displaced by approximately 11 GHz from the signal carrier. The amplitude of Brillouin reflections increases exponentially as a function of the input signal power. Once the signal level reaches a threshold, it is directly converted to Brillouin reflections defining maximum input power. However, this threshold limitation increases once a modulated signal propagates within the fibre due to its broadened transmitted spectrum [117].

Dispersion in optical communications

The refractive index (n) within an optical fibre is frequency dependent, and thus the spectral components of signal waveforms will propagate at different speeds (v_g), leading to their temporal broadening. Dispersive effects can be divided into different categories such as material, waveguide, modal, nonlinear and polarisation mode dispersion (PMD) [118]. The combined impact of both material and waveguide dispersion is defined as chromatic dispersion (CD). Fibre manufacturers quantify this effect based on the dispersion factor D ,

$$D = \frac{d}{d\lambda} \left(\frac{1}{v_g} \right) = -\beta_2 \frac{2\pi c}{\lambda^2}, \beta_2 = \frac{\lambda^3}{2\pi c^2} \frac{d^2 n}{d\lambda^2} \quad (2.11)$$

measured in ps/nm/km. Typically, for signal propagation within an SMF at 1550 nm, $D = 17$ ps/nm/km. Factor D is dependent on the second order wave propagation constant β_2 . The effect of dispersion can also be observed by implementing a Fourier transform to Eq. 2.8 while not taking account the nonlinearities, i.e., setting $\gamma = 0$.

$$\frac{\partial \tilde{A}(z, \omega)}{\partial z} = \frac{1}{2}(i\omega^2 \beta_2 - a)\tilde{A}(z, \omega) \Rightarrow \tilde{A}(z, \omega) = \tilde{A}(0, \omega) \exp\left[\frac{z}{2}(i\omega^2 \beta_2 - a)\right] \quad (2.12)$$

In Eq. 2.12, the phase change of the envelope at the fibre input ($\tilde{A}(0, \omega)$) is determined by β_2 corresponding to temporal broadening of $A(z, t)$ that is also attenuated by the factor a .

Moreover, fibre geometric imperfections introduce birefringence leading to minor differences of the refractive index between the two orthogonal axes of the fibre [119]. The changes in n lead to PMD which is a stochastic process introducing a wavelength-dependent polarisation rotation. In comparison to CD that is deterministic and scales linearly with the fibre length, the stochastic properties of PMD follow a random walk principle so that the accumulated PMD scales with \sqrt{L} . Thus, PMD-induced pulse broadening is relatively small compared with the chromatic dispersion effects [120]. Overall, CD and PMD may cause severe impairments in microwave photonic links since they lead to power fading of the generated millimetre waves.

Nonlinear effects

Except for its frequency dependence, the refractive index is also affected by optical powers [121], [122]. The parameter γ is dependent on the nonlinear refractive index that is directly related to the third order susceptibility ($\chi^{(3)}$) of silicon [123]. For further analysis, by setting $A(z, t) = |A(z, t)| \exp(i\phi(z, t))$ in Eq. 2.8 while assuming $\beta_2 = 0$ then,

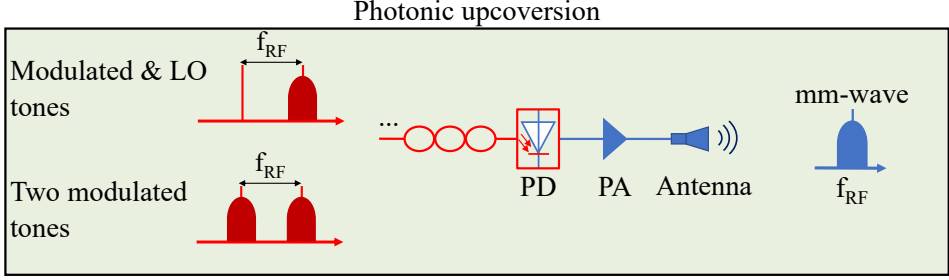


Figure 2.8: ARoF optical signal detection and photonic upconversion on a photodiode leading to the mm-wave generation and transmission through an antenna while amplification is implemented.

$$\begin{aligned}
 \frac{\partial |A(z, t)| \exp(i\phi(z, t))}{\partial z} &= \frac{a}{2} |A(z, t)| \exp(i\phi(z, t)) + i\gamma |A(z, t)|^3 \exp(i\phi(z, t)) \\
 \Rightarrow A(z, t) &= |A(0, t)| \exp\left(-\frac{a}{2}z\right) \exp(i\gamma |A(0, t)|^2 L_{eff})
 \end{aligned}
 \tag{2.13}$$

The nonlinear phase shift ($\phi_{NL} = i\gamma |A(0, t)|^2 L_{eff}$) is dependent on the envelope at the fibre input $A(0, t)$ as well as the effective length ($L_{eff} = [1 - \exp(-az)]/a$) corresponding to the minimum propagation distance required in order for the impact of the nonlinear effects to start becoming significant. Once high power signals are launched within a fibre, then ϕ_{NL} is induced by the signal itself, leading to spectral broadening that is defined as self-phase modulation (SPM) or Kerr effect [124]. In addition, if multiple channels propagate in the optical channel, several phenomena contribute to nonlinear behaviours such as cross-phase modulation (XPM) and four-wave mixing (FWM) [125]. These effects as well as SBS confine the maximum fibre input powers (P_{in}) while setting an upper limit to the power budget calculations of the photonic-wireless links.

2.1.7 Optoelectronic conversion and mm-wave generation

This section will evaluate the photonic upconversion and the fading phenomena that occur during the generation of mm-waves. As indicated by the simplified block diagram of Fig. 2.8, once the two tones (single or double sideband) reach the remote unit, they heterodyne beat within the photodiode generating the desired mm-wave with a power level related to the optical input powers, i.e., $P_{PD} \propto P_s P_{LO}$. At a further step, a power amplifier (PA) increases its amplitude by G_{PA} before arriving at the transmitting antenna exhibiting a gain of $G_{AntennaTx}$. If the connector losses are taken into account (L_{Tx}), the maximum amount of the mm-wave power (P_{Tx}) that could be radiated from the antenna is given in Eq. 2.14 as

$$P_{Tx} = P_{PD} + G_{PA} - L_{Tx} + G_{Antenna_{Tx}} \quad (2.14)$$

For link power budget calculations, it is useful to have a rough estimation of the optical input power to the photodiode (P_{PD}^{op}) as a function of the electrical output (P_{PD}) or vice versa. It is assumed that the PD has a responsivity R_{op} and is terminated by a 50Ω load R_L . A detailed analysis on the physical properties and functions of PDs is given in Chapter 3. The proportionalities in Eq. 2.15 show that any change in the electrical domain affects the input optical powers by a factor of two ($|\Delta P_{PD}| = 2|\Delta P_{PD}^{op}|$) in logarithmic scale (dB).

$$P_{PD}^{op} = 10 \log \sqrt{\frac{10^{\frac{P_{PD}}{10}} + 3}{R_{op}^2 R_L}} = 6.5 - 10 \log R_{op} + P_{PD}/2 \quad (2.15)$$

$$P_{PD} = 10 \log (R_{op}^2 R_L 10^{\frac{2P_{PD}^{op}}{10} - 3}) = -13.01 + 20 \log R_{op} + 2P_{PD}^{op}$$

Dispersion induced RF fading

As previously mentioned, optical fibre dispersion may cause RF power losses to the generated mm-waves. These effects need to be taken into consideration when opting for and implementing an ARoF scheme with two optical modulated waves since they may have an impact on its reliability.

Chromatic dispersion affects the microwave photonic systems of Fig. 2.7a,c) due to the fact that the two optical sidebands experience different amounts of CD at the output of the fibre resulting in a beating product falling onto the same frequency but having different phase [126]. The same principle applies to the case of employing intermediate frequency (IF) modulation in the system of Fig. 2.7c), where each optical tone carries two modulated sidebands at a distance of f_{IF} . This results in two electrical signals at the photodiode's output centred at f_{RF} after the beating with an unmodulated carrier. By taking CD into account, these two waves can be out of phase and interfere destructively. This fading effect is quantified in Eq. 2.16 [127]:

$$P_{CD_{Loss}} = \cos^2 \left[\frac{\pi D L (f_{RF} \lambda_0)^2}{c} \right] \quad (2.16)$$

In Fig. 2.9, the $P_{CD_{Loss}}$ is calculated for a 10 km SMF at 1550 nm with $D = 17$ ps/nm/km for RF frequencies ranging within Ka and V bands. As an example, at 50.7 GHz the two modulated tones beat destructively at the PD leading to a null of the curve. In literature, thorough research has been conducted in order to reduce the impact of this effect involving the interconnection of dispersion-compensating fibres or chirped fibre Bragg gratings with an optical circulator [128]. The curve of $P_{CD_{Loss}}$ can be used as a map to avoid the negative effects of dispersion on the generated mm-waves. This has been applied in the experimental setup of Sec. 2.3.3 where $P_{CD_{Loss}}$ was minimal for the selected frequency carrier.

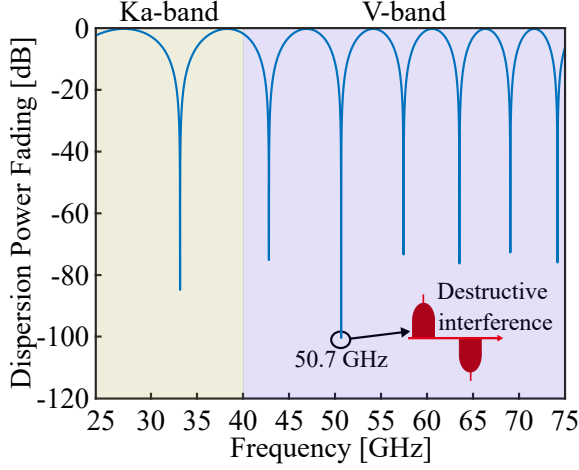


Figure 2.9: Effect of dispersion induced power fading on the RF frequency response of a 10 km single mode fibre with a dispersion factor of 17 ps/nm/km in Ka- and V-bands.

2.1.8 Wireless channel propagation

Despite their advantageous contribution on increasing the capacity of the future wireless communications, mm-wave radio signals suffer from losses due to the properties of the wireless channels [129], [130]. Before arriving at the receiving antenna, the powers of the transmitted waveforms (P_{Tx}) experience channel fading from high path loss and reduced coverage for non-line-of-sight (NLoS) connections. Figure 2.10a) provides a comparison of free space path loss (FSPL) between several bands of the traditional global system mobile (GSM: [821 – 960] MHz, [1710.2–1989.8] MHz) [131], [132] and long-term evolution (LTE, LTE-A: [1900–3800] MHz) [133], [134] as well as in mm-wave Ka-([26.5–40] GHz) and V-([40–75] GHz) communication frequency bands [135]. The calculation of the line-of-sight (LoS) FSPL is given in Eq. 2.17 [136].

$$FSPL_{dB} = 20 \log\left(\frac{c}{4\pi f_{RF} d}\right) \quad (2.17)$$

It can be observed that signals in the mm-wave domain suffer at least a 20 dB increased FSPL compared to systems operating in LTE bands. These derivations in Fig. 2.10a) correspond to ideal LoS transmission. However, some additional parameters need to be taken into account for the power budget link calculations. More specifically, when the carrier signal frequency coincides with the mechanical resonant frequencies of the gas molecules in the atmosphere, then high attenuation occurs [137]. Atmospheric absorption (a_{atm}) is due to the absorption of oxygen and water vapour gases in the atmosphere creating a high power fading peak of 15.2 dB/km at 60.9 GHz [138]. This effect is added in the solid lines of Fig. 2.10b).

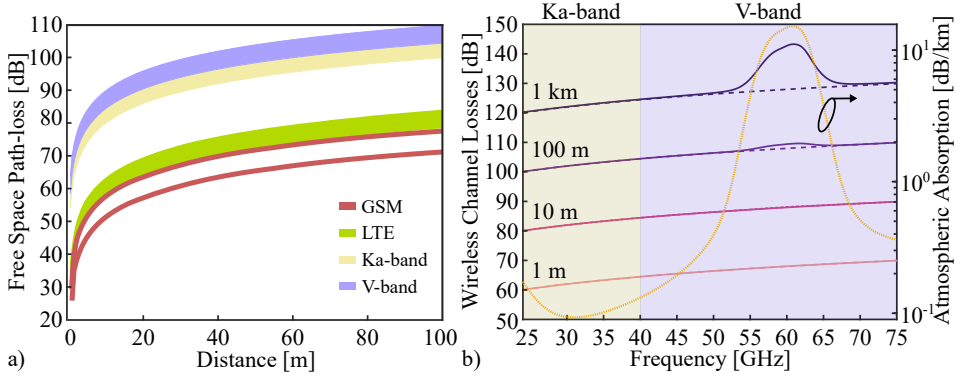


Figure 2.10: The impact of power fading of the wireless channel: a) comparison of free-space path loss between the traditional RF communication bands and mm-wave bands; b) wireless channel loss due only to FSPL (dashed lines) and including the effect of atmospheric absorption (solid lines) for different transmission distances. The graph of atmospheric attenuation is also calculated (yellow straight line) in the right hand side assuming 7.5 g/m^3 of water vapor density and 15°C .

The contribution of the atmospheric absorption peak becomes more significant in V-band. It is calculated that for short-range wireless links, the channel losses follow the FSPL curve. However, as the distance between the transmitter and receiver increases, a_{atm} becomes the dominant loss factor. The unlicensed 7 GHz spectrum around 60 GHz received a lot of attention by the industry since it allows wireless transmission of broadband mm-wave communication signals within picocells leading to a wide variety of indoor communication applications [139], [140].

GSM and LTE communication signals can penetrate through obstacles (e.g. walls, furniture) with relatively low loss allowing wide signal coverage. However, that is not the case in the mm-wave domain due to the fact that at these frequencies, the wavelengths are much smaller compared to the interfering objects leading to low diffraction [141], [142]. As previously mentioned, radio signals suffer from high path loss due to rain fading and foliage attenuation in outdoor links since the wavelength of the mm-waves are comparable to the size of rain droplets. Thus, it is challenging to recover the received signals. Consequently, the end-users can experience high-quality services by interconnecting to the systems high gain amplifiers with antenna systems incorporating beamforming that compensate for the FSPL while considering the atmospheric losses. It needs to be mentioned that in Sec. 2.2, a network scenario will be analysed, including a mm-wave antenna capable of compensating the increased values of FSPL while using phased antenna arrays, analogue beamforming and power amplification.

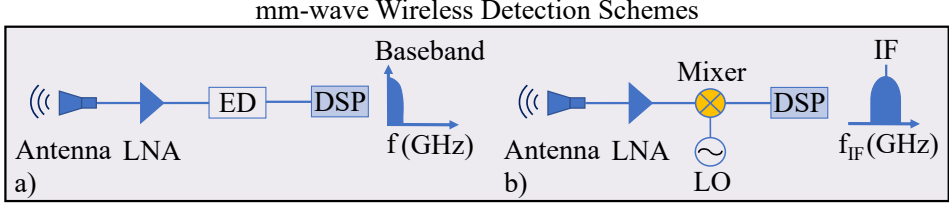


Figure 2.11: Millimetre wave signal detection, amplification and downconversion schemes: a) envelope detection of the signal and reception in baseband; b) down-conversion to an intermediate frequency by mixing with a local oscillator and further DSP processing of the IF waveform.

2.1.9 End-user detection

After wireless propagation, the mm-waves arrive at the end-users (e.g., vehicles, buildings) for further processing and evaluation. The electrical detection in the side of the UE includes a receiving antenna and a low noise amplifier (LNA) while the downconversion in lower frequencies can be divided in two main schemes.

The first system in Fig. 2.11a) employs an envelope detector (ED) based on Schottky diodes extracting the envelope of the mm-wave signal moving it directly to baseband (e.g., OOK modulation) [143]. Then, by implementing DSP techniques, the quality of the received waveforms are evaluated. Such a process limits the number of active components required for reception at the cost of losing phase information. Therefore, this scheme is applicable for intensity modulated signals [144]. Figure 2.11b) illustrates a down-conversion method detecting the desired signal at an intermediate frequency (f_{IF}) after mixing with an LO. This process preserves the phase integrity and, thus, complex modulation formats can be detected by a more complex DSP block requiring processing at IF frequencies. By considering the downconversion and connector losses in both schemes (L_{Rx}), the received power for LoS signal components at the input of the DSP block is equal to:

$$P_{Rx} = P_{Tx} - (FSPL_{dB} + a_{atm}d) + G_{Antenna_{Rx}} + G_{LNA} - L_{Rx} \quad (2.18)$$

In both presented cases, the DSP can be conducted either offline through signal processing software or in real-time by interconnecting analogue to digital converters (ADC) implementing advanced processes such as signal equalisation, non-linearities compensation, and probabilistic shaping [145]. Furthermore, other aspects affecting the noise of the signals have to be taken into account, such as the noise originating from the ED or the added phase noise as a result of the downconversion from the LO source. Finally, it is crucial to underline that the interconnected RF electronics are required to be chosen optimally in terms of their noise figure (NF) and phase noise so that their contribution to the received noise levels is minimised.

2.2 Signal multiplexing with ARoF architectures for flexible 5G communications

At mm-wave frequencies, the radio signals suffer from high path loss and reduced coverage for NLoS connections. Thus, from a network perspective, one possible solution to this impediment is the size reduction of the current cells and the increase in the number of network nodes located in a specific area. Passive optical networks (PONs) [146] are candidates for being the backbone to support connections in small cells with coverage areas of radius equal to 10-200 m. The antennas within are required to have increased gain and achieve effective radiated powers high enough to compensate for the extensive path loss [147].

Nonetheless, the current structure of PONs does not allow them to handle the vast amount of connections needed towards 5G because of limited data rates and small power splitting ratios [148]. The same applies for the optical channel splitting of the wavelength division multiplexing (WDM) PONs where the channel sizes are very wide (e.g., 50 or 100 GHz) [149]. Therefore, the transformation of the current PONs to ultra dense wavelength division multiplexing (UDWDM) PONs is crucial for enabling the support of a very high number of wavelengths available to be designated to the large amount of end-users within different small cells [150]. This means that such architecture uses ultra narrow spacing between optical wavelengths in order to assure wireless connections within the highly dense networks while implementing a mm-wave fronthaul based on 5G requirements [151]. Furthermore, the interface between the optical network unit (ONU) and the mm-wave antenna needs to be redesigned to support the new 5G numerology for OFDM.

WDM PONs are most commonly associated with fibre to the x (FTTx) applications, where x=home, curb, or building [152]. UDWDM is the next step to the evolution of optical access networks since the wavelengths of each channel that are multiplexed within a single fibre are spaced either by 6.25 GHz or 12.5 GHz. The implementation of the infrastructure of Fig. 2.1 is shown in Fig. 2.12 proposing the use of a ring architecture interconnecting multiple UDWDM PONs. This structure also allows the optical line terminals (OLTs) to interchange information through optical add drop multiplexers (OADMs). Moreover, by properly combining the modules (both passive and active) of the networks, fast and reliable connections are provided between the PONs and the end-users [153]. Finally, the activation of the dark fibres within the existing infrastructures increase the cost effectiveness of the implementation while allowing the support of the vast amount of connections towards the impending evolution to 5G.

To truly expand wireless communications into the outer limits of radio technology, the optical network approaches towards 5G need to be connected to novel phased array antenna systems offering a promising approach for 5G mobile communications. Such systems achieve multiple-beam generation with highly focused beam characteristics reducing hardware complexity as well as signal processing

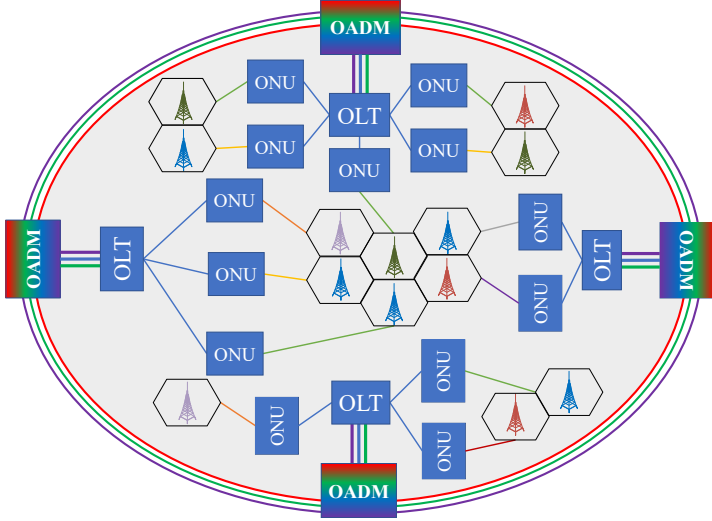


Figure 2.12: The ring infrastructure of the UDWDM PON based on the proposed network scenario.

requirements. Hence, by combining the optical network concept with a novel antenna approach within the future remote units, an improved user experience can be provided.

2.2.1 Analogue fronthaul radio access network scenario based on UDWDM PON and SDM

The core of the concept of the proposed network architecture is that the mm-wave RoF links will be integrated with the already installed PONs and their future versions (e.g., UDWDM PONs). A basic description of the suggested network is shown in Fig. 2.13. Within the central office, the signal generation, distribution and control of channel interleaving is conducted. The CO is highly centralised with a pool of virtualised BBUs [154]. Combining optical-wireless fronthaul with flexible carrier aggregation (e.g., OFDM signal generation) allows optimum resource utilisation, and since no framing and digitisation are involved for the ARoF signal generation, the network may operate with low latency.

Closely spaced optical signals propagate through optical fibres, and depending on the needs of the users of each cell, they are split and allocated by a wavelength splitter (e.g., array waveguide grating-AWG). Narrow-width optical filters are used in order for the noise introduced by the network to be discarded. Moreover, power splitters divide the selected signals and disseminate them to the ONUs. These signals are converted into the electrical domain and transmitted by the antennas to the end-users within a small cell.

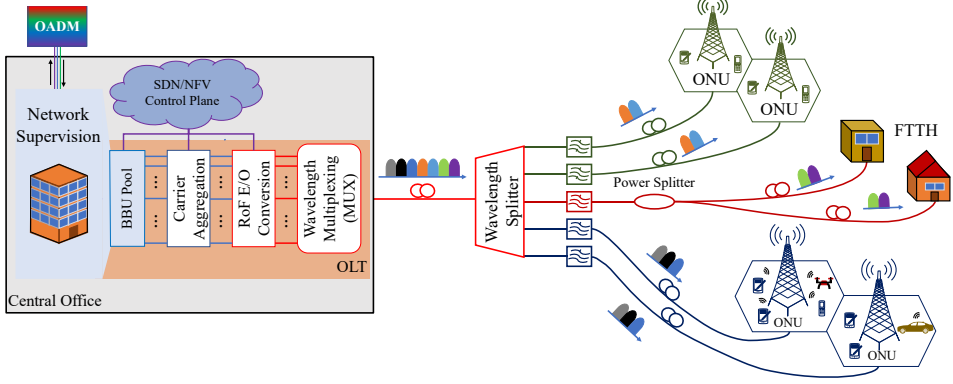


Figure 2.13: A block diagram of the network proposed where optical signals are delivered from the OLT to the ONUs supporting multiple wireless users within a cell or fixed connections to the home.

A virtual orchestrator offers the resource management and allocation within the network based on a centralised control plane defined by software defined networking (SDN) and network function virtualisation (NFV) [155]. With SDN, the control plane of the network is decoupled from the data plane, which is responsible for forwarding the data traffic. This gives the ability to centralise the control of the network using transparent interfaces. In addition, with NFV, all the hardware-based network services and functions are moved to a virtualised environment. 5G networks will be supported and controlled by cloud orchestrators and virtual machines that use both SDN and NFV. The centralisation of the RANs leads to a more flexible routing as well as it allows the reduction of the complexity within the ONUs increasing control and minimising the communications latency even further.

Optical tone generation within the OLTs

The OLTs are responsible for the transmission of data that need to be converted from the electrical to the optical domain. This is implemented in the overall structure that is shown in Fig. 2.14 where multiple optical sources generate light at densely spaced wavelengths [156]–[158]. The lasers are tuned by a centralised wavelength locker combined with a high-performance thermo-electric cooler prohibiting the frequency drift of the sources [159], [160]. Some wavelengths are input to optical modulators where their electrical inputs are the aforementioned data that may be encoded in different modulation formats. The rest of the lasers generate unmodulated optical tones that will function as local oscillators to the mm-wave generation within the ONUs. By assigning UDWDM channel slots and interleaving between modulated and unmodulated tones, flexible selection of the resulting RF frequency is possible, as shown in Fig. 2.14 [161], [162]. The wavelengths en-

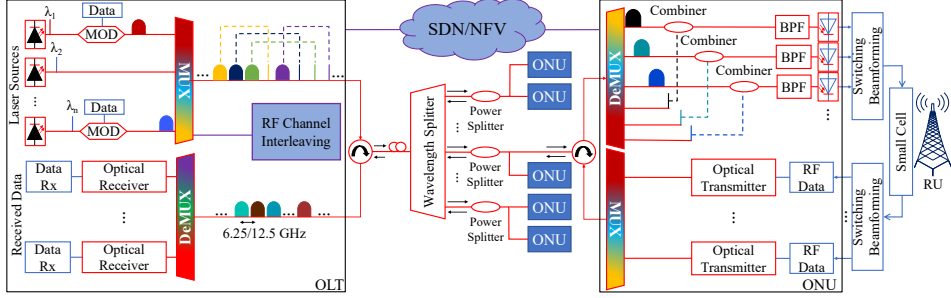


Figure 2.14: Block diagram illustrating the basic functions of OLTs and ONUs as well as the optical distribution network; the OLT contains UDWDM signal generation and reception, while the ONU performs conversion between optical and RF domains and connects to a beamforming network and antenna.

ter an optical multiplexer (MUX) and travel through an optical circulator which allows bidirectionality inside the transmission of the fibre.

Instead of using multiple laser sources that may cause phase noise and RF carrier drifting, a comb source can be introduced that simplifies the tone generation. In that case, after this source block, an extra demultiplexer needs to be added into the OLTs before the modulators since it will be responsible for separating the tones of the comb. The DeMUX may be dependent on external tuning if it is based on active filters such as Fibre Brag grating (FBG) filters [163] or passive in the case of a photonic integrated AWG. In some branches between the DeMUX and MUX, optical modulators are connected, and to others, the tones propagate (unmodulated) directly to the MUX. It needs to be mentioned that in both approaches, the input electrical signals at the optical modulators are not necessarily in baseband. To achieve a more flexible RF frequency selection and higher tunability in the case of the comb, signals can be already modulated electrically at an intermediate frequency based on IF over fibre (IFoF) [164].

The synthesis of the OLTs is currently cost-inefficient and power-consuming due to the complexity for the generation and splitting of the UDWDM signals, as well as the increased tunability and cooling requirements that such terminal designs demand. In order to carve a roadmap depicting the timescale and financial viability of this scenario, the advancements and solutions provided by photonic integration should be taken into account. As an example, the scientific achievements on integrated microring resonators on silicon allow the design of microring modulators that can be used after the frequency comb as an alternative to the second DeMUX [165]. Photonic integration may lead to massive production of both multi-tone sources and narrow wavelength selective devices on a compact footprint, scaling down the fabrication costs and allowing this concept to be integrated with the existing infrastructures.

Table 2.1: Performance parameters of the presented network concept, where each ONU is capable of generating four RF signals.

UDWDM Channel Spacing (GHz)	12.5	6.25
Number of UDWDM Channels	320	640
Power per Channel (dBm)*	-4	-7
Wavelength Splitting Ratio	1:20	1:40
Number of Connected ONUs	20	40
Generated RF Signals	80	160
Fibre attenuation (dB/km)		0.3
Insertion loss per 1:20/1:40 AWG (dB)		5.5
Insertion loss per UDWDM MUX and DeMUX (dB)		6
Booster Gain within OLTs (dB)		2-6
Receiver sensitivity (dBm)		-18

*Expected power level after modulation and multiplexing in Fig. 2.14

Signal propagation within the UDWDM PON

The signals at the output of the OLT have a frequency separation that is based according to the ITU-T recommendation G.694.1 of 2020 [166]. The fixed-grid will evolve to the flex-grid allowing channel slots equal to 12.5 GHz and the next step will lead to a spacing down to 6.25 GHz. Therefore, two consequent optical tones would have a frequency separation of either 6.25 GHz or 12.5 GHz. Such narrow spacing may increase the probability of channel crosstalk. However, the use of complex modulation formats allows the transmission of multiple bits per symbol, increasing significantly the spectral efficiency. Consequently, only a narrow bandwidth fraction of each UDWDM channel is used to ferry the desired optical signal. Therefore, channel crosstalk between two adjacent channels can be mitigated.

At a further step, within the PON, a UDWDM passive splitter dictates the separation of wavelengths travelling to a specific ONU. Such a component can be an AWG separating the overall UDWDM signal into 20 or 40 sub-bands. The calculations made in Tab. 2.1 summarise some of the important parameters of the proposed UDWDM PON [167]–[169]. It is assumed that 320 or 640 channels are active and that each ONU is capable of generating four RF signals [170]. Furthermore, some of the tones will be feeding optical modulators within the optical transmitters of the ONUs.

The RF signal is generated in the ONU illustrated on the right-hand-side of Fig. 2.14. The modulated optical signals and LOs get separated through a demultiplexer. Channel interleaving regulated by the SDN/NFV plane allows the proper combination of an optical signal with its corresponding unmodulated tone. As it already has been demonstrated, the frequency distance between the two wavelengths is equal to a desired RF signal frequency. The two wavelengths go through an optical bandpass filter (BPF) able to reject unwanted noise such as ampli-

fied spontaneous emission (ASE originating from optical boosting amplifiers [171], [172]. After the heterodyne beating at the PD, the output of the ONU can be wirelessly transmitted using the mm-wave antenna that may be equipped with beamforming solutions. There are multiple PDs at the outputs of the ONUs, the number of which depends on the structure of the antenna array and the signal demand inside a cell. Before being transmitted, the RF signals are connected to a switching and beamforming network.

In the uplink, the same process as described in the transmission part of the OLTs is achieved where multiple optical signals can be generated by broadband optical modulators based on the UDWDM principle. These signals go in the opposite direction. Starting from the lower part of the ONU in Fig. 2.14, depending on the bandwidth of the optical modulators, the received RF information is either downconverted to an f_{IF} or directly to f_{RF} . Signals converted in the optical domain travel through the MUX combiner and the circulator leading to the fibre and finally to the OLT [173]. Once more, the received information at the OLT will be demultiplexed and then the data will be extracted from an optical heterodyne receiver. Based on the values of Tab. 2.1, the optical transmission distance can reach 20 km which is sufficient for 5G fronthaul in dense deployments [174]. In the case that reach extenders are available, the fibre length may exceed 60 km.

Scaling to SDM and multicore fibres

A further upgrade in the presented concept accommodating the traffic increase for the next 20 to 30 years could be achieved by harnessing the advantageous capabilities of "space" as a variable of freedom [175]. Space division multiplexing (SDM) using multi-core fibre (MCF) technologies shows tremendous potential to keep up with the network capacity requirements of the future generation of communication services at the cost of crosstalk between the fibre cores [176], [177]. However, this impediment can be evaded by applying innovative processes during the fibre fabrication as well as digital crosstalk cancellation techniques on the received signal waveforms [178], [179].

Therefore, the network presented in Fig. 2.14 is updated in Fig. 2.15a) [180]. Multiple OLTs provide input to spatial MUX/DeMUX units referred to as fan-in/fan-out that dynamically couple light from the single mode fibres to each core of the MCF and vice versa [181], [182]. MCF with different types of cores can be used as shown in Fig. 2.15b) [183]. The combination of SDM applying MCFs and UDWDM may achieve a network capacity 300 times higher than it is feasible by the SMF-based WDM networks [184]. Moreover, C-RANs will be able to support a high amount of end-users while techniques such as optical beamforming with photonic integrated circuits will be enabled [185], [186].

In order to expand the application of importing SDM to UDWDM PONs even further, an additional process that can be beneficial for the reception of mm-wave signals in the side of the ONUs is illustrated in Fig. 2.15c). One dedicated OLT may generate multiple optical LOs that propagate within one core of the MCF.

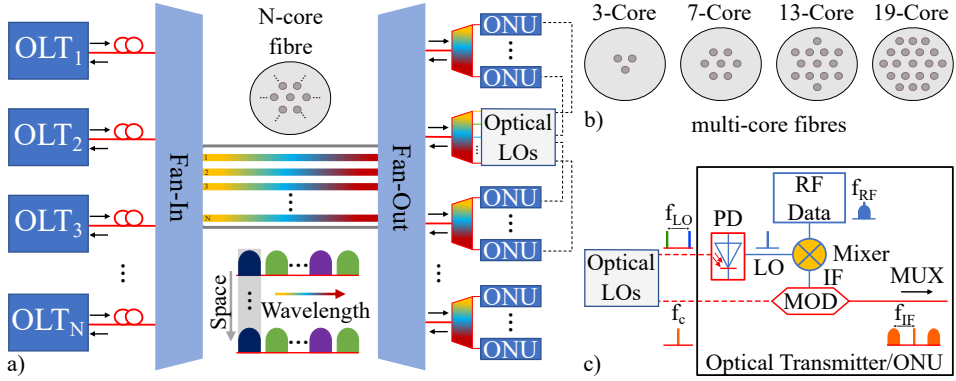


Figure 2.15: Merging the advantageous properties of SDM with UDWDM PONs: a) the network structure; b) various multicore fibres; c) the provision of unmodulated tones from a bank of optical LOs to the ONUs as input of modulators and frequency downconversion of the received mm-waves.

Once they reach the DeMUX these tones can be assigned to various ONUs from a block implementing channel interleaving. A primary application of this bank of optical LOs resides on providing the input for the modulators within the optical transmitters of the ONUs [187]. This process will simplify the complexity of those units since no additional laser sources would be needed to feed the modulators enhancing the network centralisation. Then, if two optical tones would be selected at a distance of f_{LO} and beat within a PD, they can generate an RF local oscillator accommodating the signal downconversion of the mm-waves within the ONUs. In such way, cost-inefficient RF sources would no longer be required while lower bandwidth driver amplifiers and modulators can be interconnected performing the electro-optical conversion in f_{IF} while employing IFoF for the uplink direction. The concept presented in Fig. 2.15c) is experimentally evaluated in Sec. 2.3.3.

2.2.2 Enabling phased array antenna systems for mobile communications

With every scientific advancement in mobile communications, antenna systems have become more complex. As summarised in [188], within the early communications systems, antennas were rather simple with an omni-directional radiation pattern in the horizontal plane. Sector antennas later replaced these devices and in the latest generation by MIMO antenna systems (in, e.g., WiFi, WiMAX, LTE). MIMO multiplies system capacity since numerous signals can be transmitted and received simultaneously by the RUs [189]–[191].

For the next step forward, the idea of MIMO will be extended by increasing the number of antenna elements to massive MIMO systems [192]. This becomes feasible in mobile communications due to the plan to utilise higher frequencies,

in particular, mm-waves. Massive MIMO is achieved by applying hybrid digital (e.g., DBF applying precoding) and analogue beamforming (ABF) techniques in the baseband and RF domains, respectively. Hybrid beamforming (HBF) offers simplicity, low-cost and high-performance [193]. More specifically, in the RF domain, analogue beamforming is implemented by adding a phase shift to a copy of each mm-wave signal and thus, phased arrays (PhA) are synthesised, allowing the steering of each generated beam towards a specific end-user [194], [195]. The implementation of massive MIMO with HBF and PhA antennas have the potential to improve the system capacity and spectral efficiency while keeping the power consumption low [196]. One reason for this is that multiple steerable beams can be generated, providing a strong signal to a certain user while keeping the interference to other users low. Another benefit of massive MIMO is the interconnection of inexpensive and energy-efficient silicon-based amplifiers, which becomes only applicable if a large number of antennas are used due to their low output power at mm-waves. However, using single active antenna elements (e.g., microstrip patch antennas [197]) may result in low efficiency. Hence, several elements have to be combined to sub-array feeds. By applying amplitude and phase tapering, a beam with high efficiency pointing at a certain direction can be generated [198], [199].

Figure 2.16 illustrates such a system where an ABF antenna is connected to the outputs and inputs of the ONU. The interface between the two networks is located right after the PD in transmit mode and before the electro-optical modulator in receive mode. In transmit mode, the optical system feeds multiple PDs, where each provides the signal of a single beam. Hence, the number of PDs equals the maximum number of independent beams that can be generated simultaneously. Therefore, it is necessary to be able to transfer the signals of each PD to all sub-arrays. To do so, each photodiode is connected to a series of controllable switches (SW) where the number and constellations depend on the number of sub-arrays and the amount of outputs per switch.

There are various types of commercially available controllable switches operating in Ka-band. Each switch in series adds an insertion loss that can be compensated by the gain of the ABF chips near the antenna elements. Furthermore, each switch needs supply and digital control voltage that has to be considered in the design. Hence, increasing the flexibility of the board comes along with a higher DC feeding complexity. The accumulated signals of each sub-array are then fed to ABF chips via a circulator, which is used to separate transmit and receive signals. The ABF chips are used to tune amplitude and phase to provide an optimal sampling, which is vital to achieving a high antenna efficiency. The number and constellation of the ABF network depend on the sub-array size. The advantage of this feeding network is that accurate field sampling can be provided by a small ABF network while the signals are distributed via a more inexpensive SW network. This makes it also possible to generate multiple beams for each user to obtain spatial multiplexing gain if, due to multi-path phenomena, multiple directions are possible. On the other hand, in receive mode, all signals can be received simultaneously and are highly separated due to the use of sub-arrays. An

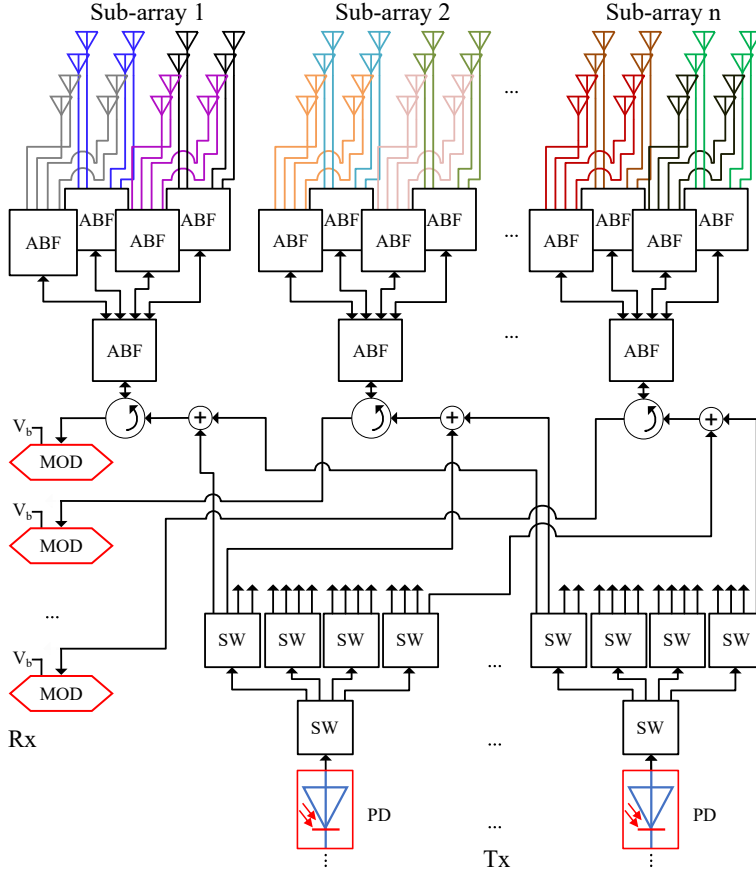


Figure 2.16: Phased array antenna system with a sub-array configuration connected to the UDWDM PON interface via switches (SW) and analogue beamformer (ABF) electronic chips.

experimental demonstration of such a PhA antenna type employing ABF that is interconnected with optical fronthaul will be discussed in Sec. 2.3.3.

To expand even further the beneficial capabilities of phased array antennas, the concept of adding a reflector has been introduced. Phased array fed (PAF) reflector systems exhibit a large effective antenna aperture and, therefore, achieve large antenna gain [200]. This allows the reduction of the number of antenna elements as well as the hardware complexity. The advantage of PAF reflectors is that only a sub-set of elements contributes to a beam in a specific direction. This attribute makes the use of sub-arrays, which are fed by the ABF network, feasible to reduce the number of RF paths, for instance, by using predefined beams [201], [202]. Taking advantage of the controllable ABF chips makes it possible to combine

sub-array signals to enable adaptive beamforming.

2.3 Experimental validation of ARoF schemes

After pinpointing the theoretical aspects of hybrid photonic-wireless links as well as analysing the fundamental requirements from a network scenario perspective, the experimental demonstrations will allow the evaluation of possible preconditions for their actual deployment. Therefore, in this section, three experimental setups will be presented, examining numerous characteristics of ARoF links towards their future integration with the 5G based UDWDM PONs. Various mm-wave signal generation and detection schemes are analysed fitting to a corresponding application based on the 5G KPIs.

2.3.1 Broadband fibre-wireless access to rural areas

High speed communications access with optical fibres is a major challenge to some rural areas. Physical obstacles such as mountains and forests render fibre deployment either prohibitively expensive or impossible. Thus, a dynamic way to achieve these connections is by employing versatile photonic-wireless links operating in the lightly licensed millimetre wave bands allowing transmission of large bandwidth signals. A leading method for the mm-wave generation is based on RoF links, providing fibre-wireless access (FWA) to remote units over long distances.

A Ka-band RoF link is demonstrated based on incoherent heterodyne photonic upconversion supported by two independent light sources [203]. The optical signal modulation is provided by a commercial small form-factor pluggable (SFP+) module increasing the cost efficiency of the setup [204]. Indoor transmission is achieved at 2.5 Gbit/s for different RF frequencies (f_{RF}) with low bit error rate ($BER < 10^{-6}$). Humidified obstacles are put in the path of the wireless link, replicating a rain forest environment, and the impact on BER is examined.

Experimental Setup

As depicted in Fig. 2.17, a pulse pattern generator PPG is connected to a commercial SFP+ module emitting at f_s . The PPG provides a 2.5 Gbit/s non-return to zero (NRZ) signal based on a pseudo random bit sequence (PRBS15) that has a length equal to $2^{15}-1$ bits. In addition, an external cavity laser at f_{LO} is employed acting as a tunable local oscillator with the frequency distance between the two tones to be equal to the desired RF frequency ($f_s - f_{LO} = f_{RF}$).

The two optical signals are transmitted through a 10 km single mode fibre (SMF). The heterodyne photonic upconversion is realised on a PD, with an input optical power P_{PD}^{op} that is controlled by a variable optical attenuator (VOA). The generated RF current is directly proportional to P_{PD}^{op} and depends on the responsivity (R_{op}) of the PD. The RF signal is amplified by a medium power

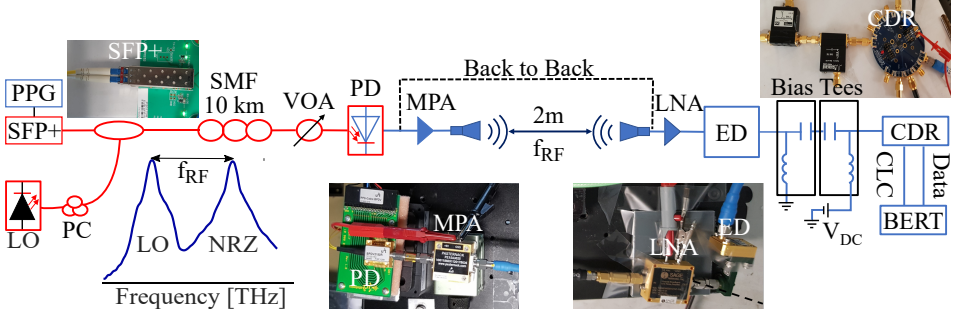


Figure 2.17: The hybrid photonic-wireless link including the spectrum of the two optical tones.

amplifier (MPA) providing a gain of 30 dB before being transmitted over a 2 m wireless link, for which a pair of horn antennas with a gain of 18 dBi each is used.

At the receiver, a low noise amplifier (LNA) boosts the RF signal by 40 dB, and an envelope detector (ED) downconverts it to baseband. The baseband signal goes through two bias tees which remove the DC components and add another DC component (V_{DC}) compatible with the operation voltage of the clock data recovery (CDR) module. The CDR extracts both the data and the clock (CLC) of the signal, and the bit-error rate tester (BERT) records the BER. This photonic-wireless link is characterised by low complexity in both the optical and RF domain while the total cost is minimised since for the optical signal generation, a commercial SFP+ module is used.

Experimental Results

Hybrid optical-wireless transmission is achieved over 10 km of optical fibre and a 2 m wireless link. Three different RF frequencies (26.5 GHz, 32.5 GHz and 38.5 GHz) are tested across Ka-band. For each frequency, six sets of measurements take place. The back to back connection is tested by attaching the output of the PD to the LNA, and the BER is measured while the P_{PD}^{op} is increased. Then, the complete wireless link is assessed with a line of sight between the antennas. Finally, four measurement sets are conducted where highly humidified paper sheets (623.7 cm^2 sheet) dipped into water are put in between the antennas. The wet paper sheets mainly consist of cellulose fibres from wood and calcium carbonate resembling the cellulose soft fibre structure of plant leaves. If it is assumed that the calcium carbonate embodied in the sheets does not add a significant attenuation, this process may give a rough estimate of the transmission quality of mm-wave signals that propagate through forest areas and plantations.

Figures 2.18(a), (b) and (c) show the BER as a function of P_{PD}^{op} at the PD. Exponential fitting is used to model the measured data. Based on the back to back curve, the receiver's sensitivity for different BER values can be calculated by

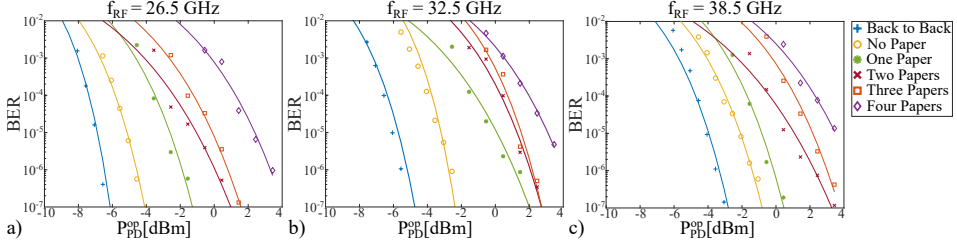


Figure 2.18: Three figures of BER vs. Optical Power (P_{PD}^{op}) at the PD for three different RF frequencies (f_{RF}) within Ka-band for back to back, LoS and transmission with obstacles.

converting the P_{PD}^{op} into the electrical domain. In Fig. 2.18a), the second curve to the right depicts the LoS wireless transmission measurement. By employing the wet sheets, an additional layer of attenuation is added to the RF signal. Thus, in order to achieve the same BER levels, higher P_{PD}^{op} are needed, and therefore the BER curves are displaced to higher optical powers. Moreover, these six curves are further displaced (with a relatively small error offset) to the right in Fig. 2.18b) and c) due to the path losses that increase at higher frequencies.

Experimental summary

An incoherent ARoF link based on an off-the-shelf SFP+ module is proposed. RF signals successfully propagated through humid sheets that mimic tree leaves of a rain forest, and low BER was obtained. The minimised complexity and cost-effective design of the total system will facilitate its implementation in remote rural areas and tropical forests where fibre infrastructure deployment is impractical or deficient.

The optical multichannel transmission of these types of signals that have a 2.5 GHz bandwidth can be achieved by allocating 6.25 GHz channels (numerology compatible to UDWDM). The additional 3.75 GHz is a guard band between channels allowing the laser sources to drift without any channel interference [205]. Thus, this scheme can be compatible with UDWDM technologies enabling the seamless extension of the existing passive optical networks to enable fronthaul or backhaul radio access units based on these commercial SFP+ modules.

Even though the proposed solution is beneficial for rural environments fitting with Fig. 2.1f), the transmission of NRZ signals with a drifting frequency carrier becomes ineffective in dense areas where multiple users need to be supported by the mm-wave wireless networks. Therefore, more advanced modulation formats are required to increase the capacity of the communication systems, while an alternative coherent ARoF setup needs to be implemented in order to deal with the phase noise and frequency drifting of the RF carriers.

2.3.2 Coherent ARoF mm-wave generation transmitting carrier aggregated 5G OFDM signals

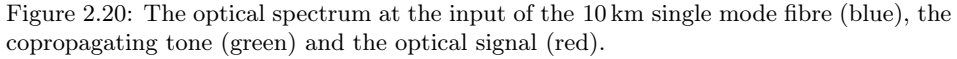
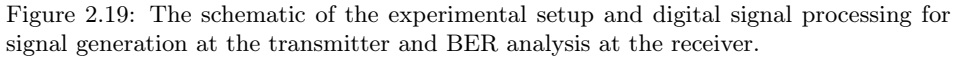
To alleviate the larger signal bandwidths required in a centralised radio access network architecture, analogue optical fronthaul with flexible carrier aggregation, signal generation, and distribution has been suggested. Thus, optimum resource utilisation is achieved, enabling the centralisation of network complexity at the central office [206], [207]. The transmission of carrier aggregated OFDM signals following the 5G new radio numerology is demonstrated over a millimetre wave coherent 2.2 m ARoF link in Ka-band. Signals with different parameters are generated and evaluated for their BER performance after optical and wireless transmission on a 28 GHz frequency carrier.

Experimental setup

The experimental setup for ARoF transmission of multiband OFDM (M-OFDM) signals is shown in Fig. 2.19, including the digital signal processing both at the transmitter and receiver side. At the transmitter, the M-OFDM signal is synthesised by mapping QAM symbols generated from a random bit stream onto the OFDM subcarriers spaced at f_{scs} of 60 kHz. The OFDM blocksize is either 2048 or 4096—with 1650 and 3300 active subcarriers, respectively. On every 12th subcarrier a pilot tone is inserted. After converting to the time domain using an inverse fast Fourier transform (IFFT), a cyclic prefix (CP) with a size of 6.25 % of the blocksize is prepended to each OFDM symbol in order to prevent inter-symbol interference. OFDM frames are formed of 14 OFDM symbols each and attached to a preamble equal to twice the blocksize. The complex baseband signal is split into its real and imaginary components, upsampled and pulse shaped by a raised cosine filter, before being upconverted to the target band frequency using a local oscillator. The resulting signals for the different bands are summed in the time domain, generating the final M-OFDM signal. In the experiment, the modulation order of the QAM symbols is equal to 4 and 16 and the number of OFDM bands is varied between 1 and 8.

Figure 2.19 also shows the block diagram of the ARoF link where two optical tones are generated by modulating the signal from an external cavity laser (ECL) with a MZM biased at its minimum transmission point and driven with a sinusoid at $f_{RF}/2$ from a vector signal generator (VSG). Consequently, two tones are created with a suppressed carrier and a frequency distance of f_{RF} . An erbium doped fibre amplifier (EDFA) amplifies the two tones and a wavelength selective switch (WSS) separates them. One of the tones is modulated with the M-OFDM signal in a second MZM. A VOA regulates the power of the co-propagating unmodulated tone (i.e., LO) before it is recombined with the data-carrying signal.

Both waves are boosted by another EDFA before being launched into a span of 10 km standard SMF. The optical spectrum at the input of the SMF as well as the signals at the output ports of the WSS are illustrated in Fig. 2.20. The



The receiver DSP uses a Costas loop to perform carrier and phase recovery and convert the IF signal to baseband. Next, the signal is downsampled, and a bank of band pass filters isolates the bands. In each band, the preamble is used for time synchronization and discarded. From each of the 14 symbols, the CP is discarded, and the fast-Fourier transform (FFT) is performed. The received

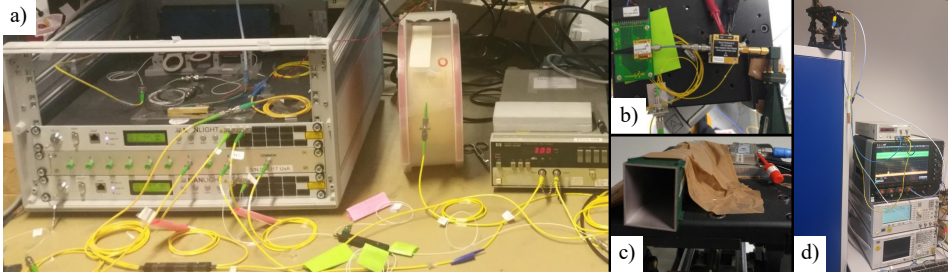


Figure 2.21: The experimental setup: a) optical signal generation and fibre transmission; b) PD and MPA connected to the transmitting antenna; c) receiving antenna connected to the LNA; d) the VSG and the DSO capturing the received signal traces.

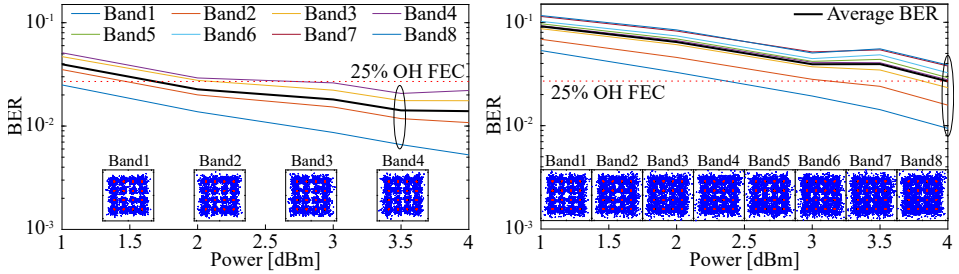


Figure 2.22: BER against optical power for a 4 and 8 band M-OFDM signal using 16 QAM symbols versus the input power at the PD; the constellation diagrams are depicted for optical powers of 3.5 dBm and 4 dBm respectively.

pilot tones, P_{Rx} , are compared to the transmitted ones, P_{Tx} , giving the channel response $H_{Ch} = P_{Rx}/P_{Tx}$ which is used to reverse the impact of the channel [208]. The received symbols are demodulated for BER evaluation.

Experimental results

The analogue RoF fronthaul link is evaluated by measuring BER after wireless transmission of the M-OFDM signals. Figure 2.22 shows BER with respect to power for $M_{QAM} = 16$ and 4 or 8 bands. It also shows the received constellation diagrams for all bands, while Table 2.2 shows a summary of the obtained results for different signal combinations as a function of the BER limits of 3.8×10^{-3} and 1.32×10^{-2} corresponding to forward error correction (FEC) with 7 % (hard decision FEC) and 25 % (soft decision FEC) overhead (OH).

For configurations with few bands, lower BERs are observed, as signal power is spread over fewer bands, and hence the received signal has a better signal to noise ratio (SNR). Similarly, as with larger blocksizes, the symbol duration is reduced, the received power per symbol—and thus the SNR—is lower. Both show the

Table 2.2: Required FEC overhead for the different M-OFDM signal configurations.

Block Bands	2048		4096	
	4-QAM	16-QAM	4-QAM	16-QAM
1	7%	7%	7%	25%
2	7%	7%	7%	25%
4	7%	7%/25%	7%/25%	25%
8	7%/25%	25%	7%/25%	25%

system to be SNR limited, and thus any increase in available transmitter power can be expected to result in an improved BER performance or to allow longer transmission distances. For the evaluated signal with four bands in Fig. 2.22, a BER below the limit for 25 % overhead FEC is achieved, allowing a data rate of 1.2 Gbit/s within a bandwidth of 491.5 MHz. Similarly, for the 8 band signal, a bit rate of 2.4 Gbit/s is transmitted over a bandwidth of less than 1 GHz while with an increased blocksize, the data rate becomes 4.8 Gbit/s with a bandwidth of 1.96 GHz.

These results are promising in terms of capacity and data rate. However, as noted above, there is a trade-off between power, bandwidth and data rate. This may be overcome by providing additional transmitted power or through further optimization of the system with regard to the efficiency of RF signal generation. Consequently, it is expected that more bands will be transmitted carrying OFDM symbols that contain higher-order QAM modulated symbols.

Conclusions

The transmission of carrier aggregated OFDM signals following the 5G numerology over a 28 GHz ARoF fronthaul link is demonstrated, finding bit error rates below the limit for a 25 % overhead FEC after wireless transmission over 2.2 m. Data rates between 1.2 Gbit/s and 4.8 Gbit/s are achieved over respective bandwidths of 491.5 MHz and 1.96 GHz. The observed results showcase ARoF as a candidate for 5G, providing maximum flexibility in the fronthaul segment and achieving multi-Gbit/s performance over limited bandwidths.

The investigated setup can be implemented in 5G applications with a static transmitter and receiver such as the illustrated links of Fig. 2.1b,c,g). However, the offline DSP processing as well as the interconnection of the transmitter with gain horn antennas are required to be replaced by more elaborate techniques and components converging to a more realistic 5G network scenario. This is achieved in the following section.

2.3.3 High capacity real-time hybrid optical wireless 5G fronthaul with dynamic beam steering

As already analysed in Fig. 2.15, apart from the introduction to ARoF, optical space division multiplexing with multicore fibres increases the capacity of radio access networks as it employs the synchronous transfer of signals centred at equal wavelengths within different cores of the same MCF [209]. Once the optoelectronic conversion takes place at the RU, and the RF waveforms are generated, antenna systems providing beam generation and precise steering are required to serve end-users in various locations, as shown in the network scenario of Fig. 2.1a,d,c). However, mm-wave signals suffer from excess propagation losses and building blockages, leading to disruptions of the wireless links. Therefore, high-gain smart antennas with beamforming capabilities would overcome these impediments [O1].

In this section, the combined scientific output of two EU Horizon 2020 projects blueSPACE and SILIKA is experimentally demonstrated [210], [211]. An optical distribution network developed by blueSPACE that encompasses the generation of real-time 5G new radio signals and transmission over 10 km 7-core MCF feeds an 8×4 SILIKA phased array antenna that employs analogue beamforming. The transmitted mm-wave signals arrive at the receiving antenna that is also linked to the RU for concept validation since an end-user is not included in the investigated setup. A successful wireless transmission of up to 1.4 Gbit/s 5G OFDM signals at 26.9 GHz (Ka-band) is achieved while the receiver is moved within an arc of 90° verifying the beam steering capabilities of the SILIKA array.

Experimental Setup

The performance evaluation of the system is achieved by the experimental setup in Fig. 2.23a). At the CO, an ARoF-BBU maps M-QAM ($M \in [4, 256]$) symbols originating from a random bit stream onto 4096 OFDM subcarriers (3196 of which are active) with a spacing of $\Delta f = 120$ kHz. Furthermore, the BBU includes DAC and an ADC, generating and receiving in-phase and quadrature (IQ) baseband signals, respectively. An intermediate frequency (IF) unit incorporates an IQ modulator and demodulator ($\text{IQ}_{\text{MOD/DMOD}}$) and a tunable vector signal generator performing frequency up- and downconversion between baseband and f_{IF} . For the conducted experiment, four different 5G OFDM waveforms are generated and detected centred at a fixed $f_{IF} = 5.2$ GHz with $M = [4, 16]$ and IF bandwidths of 200 and 400 MHz.

A CW laser is used as an optical source, feeding a Mach-Zehnder modulator biased at the null transmission point and driven by a sinusoidal tone of 10.85 GHz. Thus, optical two-tone generation takes place resulting in two spectral lines with a spacing of 21.7 GHz (f_{LO}). The output of the MZM is boosted by an EDFA and divided in two branches through a 70:30 optical splitter. The 30 % branch is directly transmitted via one of the cores of the MCF to the RU and detected by a PIN photodiode (PIN-PD2). This signal, after electrical amplification by a 30 dB

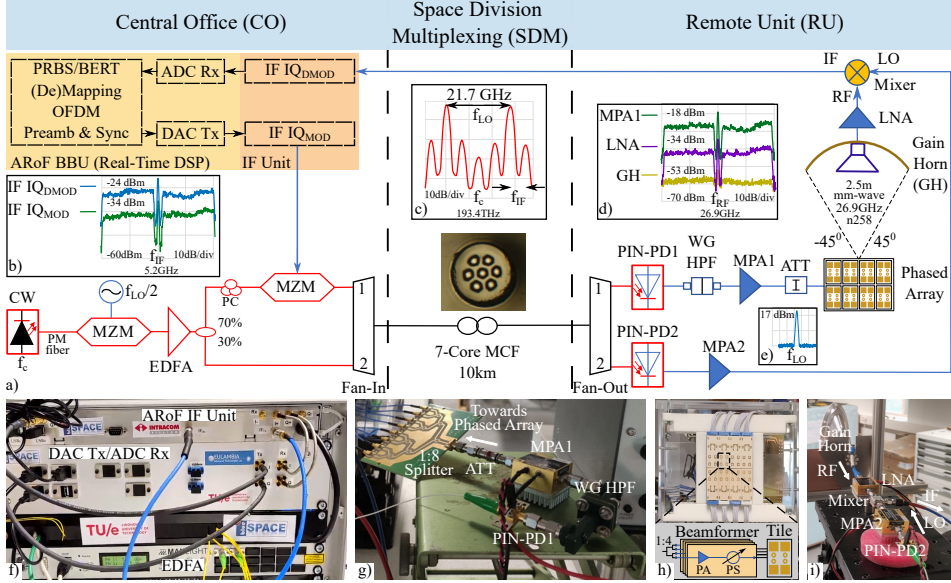


Figure 2.23: Summary of the experimental demonstration and signal spectra of a 16-QAM 5G OFDM signal with 400 MHz IF bandwidth: a) schematic of experimental setup, b) transmitted and received IF signal spectrum, c) optical spectrum of the signal at the output of the MCF, d) spectrum of the RF signal at the output of MPA1, LNA and GH at 0°, e) spectrum of photonic generated LO after MPA2, f)-i) photographs of laboratory setup: f) ARoF BBU, g) RU with optoelectronic conversion, filter, amplification and 1:8 split towards the phased array, h) antenna module at the RU with a block diagram of the analog beamforming network, i) receiver antenna with LNA, and IF downconversion with a photonic generated LO.

medium power amplifier (MPA2) acts as the LO for the electrical downconversion of the received mm-wave signal. The 70 % branch is fed through a polarization controller (PC) to a second MZM biased in quadrature and electrically driven by the IF 5G OFDM. The modulated output (its spectrum is shown in Fig. 2.23c)) arrives at the RU through a different core of the MCF, showcasing the advantageous properties of SDM, allowing the seamless transfer of both signals, despite being carried by the same wavelength.

The mm-wave generation is based on the optical heterodyning of the two modulated tones on the PIN-PD1 at the RU. In order to isolate the desired OFDM signal centred at $f_{RF} = f_{LO} + f_{IF} = 26.9$ GHz from the low frequency beating products, a waveguide high pass filter (WG HPF) is added. Then, the RF waveform is amplified by 30 dB in MPA1 while a 5 dB attenuator (ATT) reduces its output power in order for the boosted mm-wave to meet the power limitations of the phased array module. This module consists of a 1:8 splitter linked to 8 beamforming tiles where each tile splits the signal and feeds four antenna elements

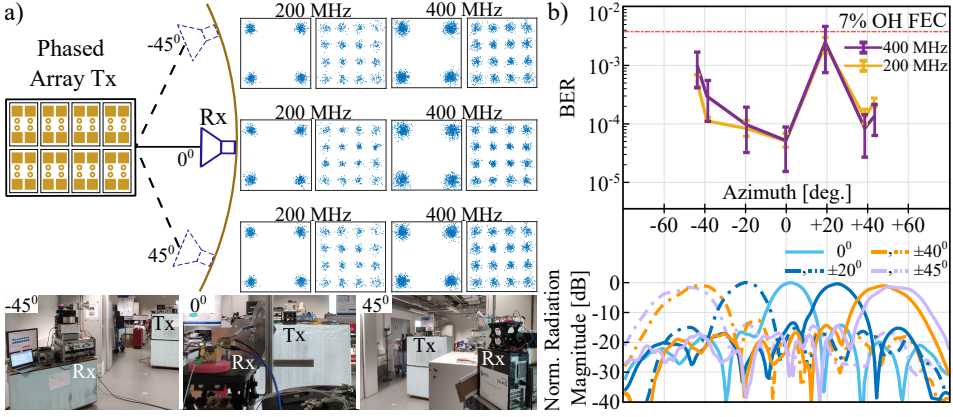


Figure 2.24: a) The constellation diagrams of QPSK and 16-QAM 5G OFDM signals at an IF bandwidth of 200 and 400 MHz measured in the laboratory at -45° , 0° and 45° , b) upper: the BER curves of received 16-QAM 5G OFDM signals at an IF bandwidth of 200 and 400 MHz for a receiver moving between $\pm 45^\circ$, lower: the normalised radiation magnitude of the phased array antenna module measured in the anechoic chamber at the same angles as the BER measurements.

that are individually controlled. Every antenna element with a gain of 5.5 dBi has the capability to adjust amplitude and phase since it is connected with a phase shifter (PS) and a power amplifier (PA) delivering a gain of up to 20 dB, compensating for the connector and splitting losses [212]. The mm-wave is transmitted at 26.9 GHz within the 3GPP n258 band and received by a gain horn (GH) antenna exhibiting a gain of 24 dBi and a compact size due to an attached lens. Then, the output is amplified by a 40 dB low-noise amplifier before being fed to a mixer for downconversion to f_{IF} and then back to the IF unit and the ARoF-BBU for real-time signal processing. The phased antenna array is chosen to have a steering range covering one quadrant (90°) and the data that are analysed correspond to angles equal to $[0^\circ, \pm 20^\circ, \pm 40^\circ \text{ and } \pm 45^\circ]$ where at 0° no beam steering is performed. For all measurements, the wireless distance is kept constant at 2.5 m with the receiver always facing towards the transmitter in line of sight. It is important to note that only the receiver is radially moved within the quadrant while the transmitter is kept at the same position and orientation.

Transmission Results & Discussion

The ARoF link is evaluated based on the resulting real-time bit error rates and their corresponding signal constellations. Figure 2.24a) shows the laboratory environment and the received averaged constellations at $\pm 45^\circ$ and 0° for the four different 5G OFDM waves. The measured BER for (QPSK) is error-free for all angles and IF bandwidths.

In Fig. 2.24b), the BER curves for the two 16-QAM based OFDM signals are assessed for various angles. The average BER over 25 samples is below the 7% OH FEC, BER limit for all angles, while the sample variance is also indicated by the vertical stubs. Moreover, the normalised magnitudes of the radiation patterns of the phased array module are measured in the anechoic chamber for the corresponding steering angles. The obtained maximum radiation magnitude decreases for increasing angles and thus justifying the BER degradation. In addition, the asymmetric behaviour of the BER curves around 0° is caused by the laboratory environment that is also asymmetric due to the presence of various objects such as metallic cabinets and windows. At 20° there is an abrupt increase of BER for both curves that may be due to the destructive interference of reflections at the receiver for the specific position deteriorating the signal quality. Furthermore, since high bandwidth waveforms are more affected by the reflections of the wireless channel and the noise of receiver electronics, the BER variance for the 400 MHz wide signals is higher compared to the ones with a bandwidth of 200 MHz. The presented results allow longer transmission distances in the case where laboratory space limitation is not an obstacle for moving the receiver within a wider arc.

Experimental Conclusions

Successful real-time multi-Gbit/s transmission of carrier aggregated 5G OFDM signals through a 2.5 m Ka-band hybrid photonic-wireless link with dynamic analogue beam steering was demonstrated, using a smart, high gain 8×4 antenna module capable of steering the generated beams towards a moving receiver. The implemented ARoF link with MCF fronthaul transport achieved data rates of up to 1.4 Gbit/s with measured average BER below the limit for a 7% OH FEC. The achieved transmission performance and dynamic beam steering showcase ARoF using SDM with multicore fibres and smart phased arrays employing analogue beamforming as key enablers for the seamless transport of 5G signals to end-users with increased capacities and high quality of service.

2.4 Summary

5G communications will accommodate groundbreaking applications using wide wireless channels that are capable of providing data rates within the Gbit/s range. That can only be supported by operating within the mm-wave bands through a new framework for 5G, alongside with a novel concept of fronthaul architecture. The use of traditional methods for digitised fronthaul and electrical up-conversion of baseband signals to mm-waves is inefficient, complex and for large bandwidths becomes economically prohibitive. Therefore, hybrid photonic-wireless links are a promising solution allowing full centralisation of the network hardware and functions to the central office as well as the simplification of the remote units.

In this Chapter, the building blocks synthesising an ARoF system are discussed, including theoretical derivations, component analysis and signal modulation techniques. Moreover, the concept of a highly centralised RAN with a pool of potentially virtualised BBUs in combination with analogue RoF fronthaul over UDWDM not only offers maximum flexibility for capacity assignment but also seamlessly enables SDN and NFV—and hence network slicing. This network is drastically enhanced in terms of capacity by implementing spatial multiplexing in the optical domain using multi-core fibres while enabling novel techniques such as the use of optical beamforming networks.

Several aspects of the presented network scenario are experimentally evaluated. Initially, a 2.5 Gbit/s low complexity Ka-band hybrid optical-wireless link based on a commercial SFP+ module is demonstrated, showcasing an economical and efficient solution for access provisioning to rural areas. Thus, the benefits of implementing incoherent ARoF schemes that can be directly integrated with UDWDM PONs are reported. In order to avoid phase noise and carrier drift, a coherent system setup is explored. This scheme, combined with the propagation of carrier aggregated 5G OFDM signals lead to improved link quality and phase stability. Therefore, multi-Gbit/s data rates are transmitted through analogue radio-over-fibre fronthaul in limited bandwidth over 2.2 m in Ka-band. As a final step and in order to approach a more realistic 5G based network structure, a real-time mm-wave hybrid photonic-wireless system is demonstrated where up to 1.4 Gbit/s 5G OFDM signals propagate through a MCF to an 8×4 antenna array employing analogue beamforming to radially track a moving receiver.

In order to move towards the realisation of 5G networks operating in mm-wave bands, the future remote units are required to be located far and wide within the urban environments supporting a broad wireless coverage to the end-users while compensating for the increased channel losses. Based on the pictures taken from the experimental systems, if multiple RF transmitter and receiver devices are put together, then the RUs become bulky, cost-ineffective and power consuming. Thus, alternative processes towards the miniaturisation of the components comprising the interface between the photonic and wireless domain are required. The advancements in photonic and electronic integrated components need to be examined to be interfaced together on a replicable, low-cost system on-chip that guarantees a smooth transition while operating on higher carrier frequency communications.

Research Question:

How can the antenna, the amplifier and the photodiode be incorporated to a single system on chip ?

High-speed photodiodes for mm-wave generation

The generation and transmission of millimetre wave signals for 5G applications require the use of broadband and high output power photodetectors to bridge from optical to electronic domains. This matter was discussed in the previous Chapter, where efficient photodiode modules played a pivotal role in the mm-wave generation within the hybrid photonic-wireless systems. However, the solutions reviewed so far were based on bulky and packaged components that are on a much larger scale compared to the desired application of this work which is the design of a compact device that can be deployed on the numerous 5G remote units within the small cells.

The advances in photonic integration allow the miniaturisation and mass production of such components, making them accessible for many applications in telecommunication services. This Chapter explores the enormous potential of untravelling carrier photodiodes (UTC-PDs), including a presentation of their physical aspects and an overview of their characterisation processes. Moreover, the deep knowledge of the equivalent circuit properties of these devices is vital since it provides crucial information about their RC-bandwidth as well as reveals if there was a process issue on the wafer where the diode chips are fabricated. Therefore, a detailed review on the extraction of the full-equivalent circuit of UTC-PDs based on reflection coefficient and bandwidth measurements is also examined. Finally, various de-embedding methods that analytically remove the parasitic effects of the electrical transmission lines allowing the accurate analysis of their active region and calculation of the series resistance and junction capacitance with lumped elements, are thoroughly investigated, presented and compared. The methods, experimental work and results shown in this Chapter are related to publications [J2], [J3], [C4], [C5].

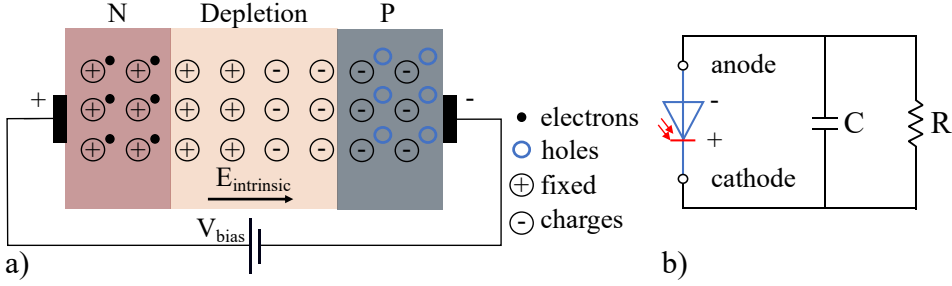


Figure 3.1: A block diagrams of a PN junction in reverse bias showing a) the material mechanisms and b) simplified equivalent circuit representation including the accumulative resistance (R) and capacitance (C).

3.1 Properties of photodetecting devices

The operation principle of a photodiode is based on the properties and functionality of a PN junction in reverse bias as indicated in Fig. 3.1a) [213]. Since a positive potential is applied to the n-type semiconductor layer of the device and a negative to the p-layer, oppositely charged carriers (electrons and holes, respectively) are attracted. Thus, the length of the depletion region is increased while not allowing any current to flow except for a negligible parasitic defined as dark current.

Once the depleted region absorbs photons, electron-hole pairs are generated and swept by the electric field ($E_{intrinsic}$) through the junction, inducing a photocurrent (I_{PD}). In order to achieve this effect, the incident photons are required to have energy levels (hf) higher than the bandgap of the absorbing semiconductor material [214]. Photodetectors that are incorporated in optical communication systems operating at 1550 nm are widely based on the promising and mature III-V compound semiconductor technologies employing materials with direct bandgap (e.g., InP, GaAs, InGaAs, InGaAsP) [215], [216].

3.1.1 Fundamental definitions

Responsivity

A fundamental parameter of a PD is the responsivity (R_{opt}) calculating the ratio between the generated photocurrent (I_{PD}) versus the input optical power (P_{opt}). The responsivity is given in Eq. 3.1 where q is the charge of the electrons, h is the Planck's constant, c is the speed of light, and λ is the wavelength of the incident light. Furthermore, R_{opt} is strongly dependent on the quantum efficiency (η) of the device describing the probability of generating an electron-hole pair per absorbed photon.

$$R_{opt} = \frac{I_{PD}}{P_{opt}} = \frac{\eta q \lambda}{hc} \quad (3.1)$$

In the ideal case when $\eta = 1$, the maximum level of responsivity of a PD at 1550 nm is 1.25 A/W [217]. However, this value is obtained once the quantum efficiency of the device is optimal. For a standard single mode waveguide PD, η is calculated based on Eq. 3.2. The internal quantum efficiency (η_{int}) depends on the absorption coefficient (a) of the carrier generating semiconductor, L is the length of the PD, and Γ is the optical confinement factor. In addition, η_{int} needs to be multiplied by the coupling efficiency (η_{cpl}), taking into account the additional loss factors of the device, such as coupling losses with the optical fibre.

$$\eta = \eta_{int} \times \eta_{cpl}, \eta_{int} = 1 - e^{-\Gamma a L} \quad (3.2)$$

Nevertheless, with a low electric field applied, the carrier-collector region of a PD may become undepleted, leading to carrier recombination since the generated electrons and holes recombine, not allowing them to diffuse to the contacts, resulting in reduced efficiency. Thus, the reverse bias is a crucial factor ensuring that the carrier escape time to the contacts is shorter than the recombination time.

Dark current

Except for the induced photocurrent, there is an additional parameter that is due to the random generation of electrons and holes within the depletion region of the PD originating from stray light or thermal generation effects [218]. The amplitude of this noise source defined as dark current (I_{dark}), resides within the range of nA.

Frequency response

Apart from the static parameters of a photodiode, the frequency response of the device is also critical. The calculation of the 3 dB bandwidth (f_{3dB}) of a PD is presented in Eq. 3.3 and consists of two elements. The first is determined by the RC time constant ($\tau_{RC} = 2\pi\sqrt{RC}$) shown in Fig. 3.1b) that depends on the accumulative resistance (R) and capacitance (C) of the PD, including the junction capacitance, the series resistance and all the parasitics added to it from the waveguide pads. The second parameter of Eq. 3.3 is a function of the transit time of the carriers (τ_{tr}) generated in the absorption layer of the PD that varies based on its type and will be introduced at a further step. By determining the properties of semiconductor materials, altering the number of layers or modifying the material doping, the f_{3dB} can be optimised. The frequency response of a PD regulates its speed and its ability to generate mm-waves at high frequency carriers [219].

$$f_{3dB} = \sqrt{\frac{1}{\frac{1}{f_{RC}^2} + \frac{1}{f_{tr}^2}}} \quad (3.3)$$

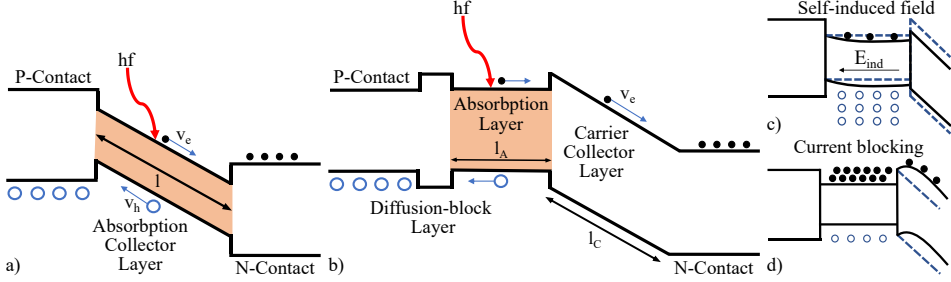


Figure 3.2: The block band diagrams of: a) PIN photodiode; b) UTC photodiode; c) the impact of the self-induced field (E_{ind}) leading to the band-bending (black line) of the absorber with thickness l_A ; d) the effect of current-blocking (space charge effect) caused by high input optical powers leading to band-bending of the collector area.

RF power saturation

Power saturation to a photodetector occurs once its RF output reaches a maximum level as a function of increasing optical input (i.e., I_{PD}). In saturation, negative space charge effects caused by additional generated carriers do not allow them to travel within the junction [220]. Thus, once higher powers are injected, the temperature rises leading to increased heat transfer and eventually to permanent damage of the component.

3.1.2 Photodetecting structures

The layerstack that defines a photodetecting device directly affects its speed parameters presented in Eq. 3.3. There are several photodiode topologies used for high-speed communications such as the PIN, avalanche (APD) and uni-travelling carrier [221]. In the following subsections, the properties of PIN and UTC-PDs are evaluated in order to determine the most suitable structure for the design and co-integration of the high-speed mm-wave transmitter.

PIN photodiodes

As shown in Fig. 3.2a), a PIN-PD consists of three different types of semiconductors. A p-type collects the photogenerated holes, an undoped intrinsic semiconductor that acts as the photon absorption layer and an n-type material receiving the generated electrons. Based on the principle of the PN junction, if a reverse bias is applied, the intrinsic region becomes fully depleted while the electric field at the junction accelerates the generated carriers (electrons, holes) that drift towards the contacts of the device.

The speed of the carriers is proportional to their mobility (μ) measured in $\text{cm}^2/(\text{Vs})$ [222] and the electric field applied (E). When E is sufficiently high, the carriers' speed reaches saturation. The saturation velocity of the electrons (v_e) is

higher than the one of the holes (v_h), and thus, the transit time of the holes defines the speed of the device. The f_{tr} is calculated in Eq. 3.4 and is proportional to v_h while it is inverse proportional to the length (thickness) of the absorption layer (l). A short l increases the f_{tr} while the junction capacitance becomes higher, reducing the f_{RC} . Thus, in PIN-PDs, there is a trade-off between f_{RC} and f_{tr} while l is required to be chosen optimally so that the f_{3dB} is maximised.

$$f_{tr} = \frac{1}{2\pi\tau_{tr}} = \frac{3.5v_h}{2\pi l} \quad (3.4)$$

High input optical powers lead to the space-charge effect due to the photogeneration of an excessive amount of electrical carriers. This carrier accumulation within the absorption region decreases the net electric field leading to power saturation, as well as reduces the carrier drift velocity and therefore the f_{3dB} [223].

UTC photodiodes

A block diagram of the overall structure of a UTC-PD is presented in Fig. 3.2b). The carrier generation takes place at an absorption layer. The holes are directly swept to the p-contact within the dielectric relaxation time of the p-doped region ($> \text{THz}$ bandwidth) [224], [225]. In addition, a diffusion block layer supports the unidirectional motion of electrons towards the n-contact [226].

Thus, the speed of the device is defined by the τ_{RC} and the τ_{tr} that is dominated by the transit time of the electrons within the structure. The transit time constant of electrons is equal to the summation of the diffusion time through the absorber (τ_A), and the drift time within the carrier-collector layer (τ_C) [217]. The diffusion time (τ_A) in Eq. 3.5 is affected by Fick's law on the probability of the electrons diffusing towards the intrinsic region and the thermionic transport with velocity v_{th} . Since the saturation velocity of the electrons in the carrier-collector layer is much higher than the velocity of the holes in the absorption layer ($v_e > v_h$), it is easier than in PIN structures to increase the collection layer thickness without excessively raising the transit time and alleviating for the compromise between $f_{tr} = 1/[2\pi(\tau_A + \tau_C)]$ and f_{RC} [227].

$$\tau_A = \frac{l_A^2}{3D_e} + \frac{l_A}{v_{th}} \quad (3.5)$$

$$\tau_C = \frac{l_C}{3.5v_e} \quad (3.6)$$

In Eq. 3.6, it is assumed that the electrons travel with saturation velocity within the carrier-collector layer. However, by adjusting the length of the collector and applying an optimal bias, the electrons purely accelerate, reaching an overshoot velocity (v_e) that is at least two times higher than saturation (typically equal to $v_e = 3 - 5 \times 10^7 \text{ cm/s}$) [228]. Consequently, this effect can significantly decrease τ_C , affecting f_{tr} of the UTC-PD and thus its total bandwidth.

Except for the velocity overshoot, another effect able to increase the bandwidth of the UTC-PDs occurs in the absorption layer while it is illuminated by high optical powers. As illustrated in Fig. 3.2c), the surplus of the generated holes that drift within this region induces an electric field defined as the self-induced field (E_{ind}) [229]. This results in the band-bending of the absorption region, accelerating the photogenerated electrons and decreasing their diffusion time (τ_A). Based on this aspect, an electric field can also be introduced independently of power by using doping or material gradient (bandgap variation) in the absorber [230].

The saturation of output power within a UTC-PD occurs when the excessively high amount of electrons at the carrier-collector layer causes band-bending blocking the electrons at the absorber [231]. The space-charge effect is illustrated in Fig. 3.2d). Furthermore, very large photocurrents lead to the abrupt drop of the effective voltage ($V_{eff} = V_{bias} - V_{DC} - V_{AC}$) applied to the junction due to a DC voltage drop in the series resistance of the device (V_{DC}) as well as an AC voltage drop (V_{AC}) in the load resistance. Therefore, the reduction of V_{eff} may undeplete the intrinsic region and decrease the speed, i.e., the bandwidth of the UTC-PD. Finally, the lack of heat dissipation within the device leads to high temperatures caused by the high input powers [232]. Thermal heat-up may cause an additional dark current generation due to the thermal runaway effect and eventually the destruction of the PDs.

Compared to PIN-PDs, the power saturation of UTC-PDs occurs at much higher power levels. Moreover, the overshoot velocity leads to high output saturation RF currents and reduced space charge effects [233]. Consequently, these devices show great potential in microwave photonics applications and act in accordance with the purpose of this thesis.

3.1.3 Modelling a UTC-PD with lumped circuit elements

In order to characterise the important aspects of a UTC-PD, the extraction of the series resistance (R_s) and junction capacitance (C_j) is crucial [234]. As illustrated in Fig. 3.3, the accumulation of the resistive effects within the doped layers of the PD can be represented by R_s . Furthermore, within the depleted active region of the device (collector), the value of C_j contributes to thorough performance analysis of the photodiodes through the calculation of the bandwidth. Insight into these processes is valuable for device design, as they are used to verify that the parasitics between the designed model before and after fabrication are low. Also, it is important to mention that the junction capacitance provides information on the optimal amount of reverse bias voltage that needs to be applied in order to fully deplete the intrinsic region of the UTC-PD [235].

Essential information towards the analysis of the electrical equivalent circuit of a UTC-PD is calculated by the reflection coefficient at the input of these devices (Γ_m) shown in Fig. 3.4. Γ_m is acquired at the output of the electrical transmission line (TML), which is the interface between the active region and the measurement point of UTC-PDs. If the S-parameters of the TML $S_{TML} = [S_{ij}]$, $i, j = \{1, 2\}$ are

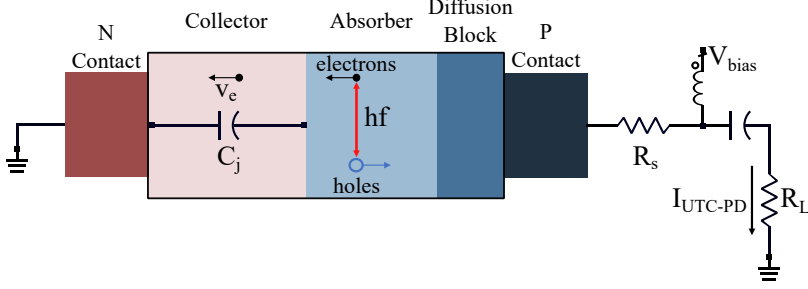


Figure 3.3: A UTC-PD capable of generating current at its load (R_L) due to the creation of electron-hole pairs by the absorption of photons with energy hf .

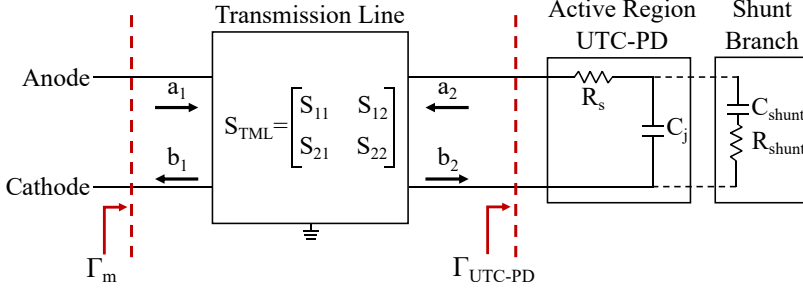


Figure 3.4: A circuit model for the measurements of the UTC-PDs showing the point of the input reflection coefficient Γ_m and the active region of the diodes including the transmission line parasitics (S_{TML}).

known, then the reflection coefficient of the active region as well as of the shunt branch between the active area and the contacts within the UTC-PD (Γ_{UTC-PD}) can be extracted analytically based on Eq. (3.7).

$$\Gamma_{UTC-PD} = \frac{S_{11} - \Gamma_m}{S_{11}S_{22} - S_{22}\Gamma_m - S_{12}S_{21}} \quad (3.7)$$

The TML properties are not always easy to measure, and thus either full equivalent circuit methods or de-embedding techniques are employed in order to move the reference measurement plane to the active region of the UTC-PDs, i.e., isolate Γ_{UTC-PD} [236]. The advantageous aspects of both processes will be analysed in the following sections.

3.2 UTC-PD measurement processes

Figure 3.5 shows a broadband, low-cost, and high-responsivity evanescent waveguide uni-travelling carrier photodiode (UTC-PD) fabricated at III-V Lab using all

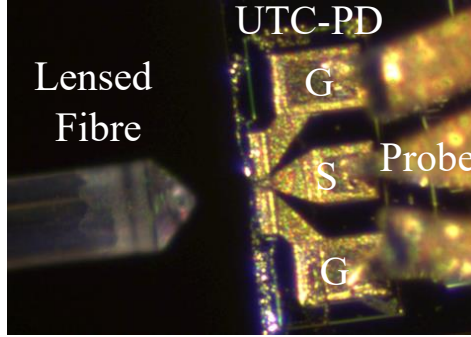


Figure 3.5: A high-speed UTC-PD fabricated at III-V Lab connected to characterisation equipment through an RF probe with $150\ \mu\text{m}$ pitch while its optical waveguide is coupled to a lensed fibre.

2-in InP processing, including etched facet with on-wafer anti-reflection coating. The input optical waveguide can be coupled with a $3.5\ \mu\text{m}$ -mode diameter lensed fibre for inserting light into the UTC-PD [237]. The generated electrical signals are guided to the output through a conductor backed coplanar waveguide (CB-CPW) where the ground pads of the CB-CPW are connected to the n-contact of the photodiode.

All measurements are conducted with the support of a probe station where high frequency equipment such as an RF power meter (for saturation power, frequency response) or a vector network analyser (VNA), for reflection coefficient measurements) are connected to the pads of this single-port device via a bias-tee enabling the application of reverse DC bias to the UTC-PDs. One RF port of the bias-tee is linked to the equipment and the second to a ground-signal-ground (GSG) microwave probe.

3.2.1 Experimental Measurements of UTC-PDs

Measurement setup

The complex characterisation setup shown in Fig. 3.6 can provide a multitude of measurements such as responsivity, saturation current, reflection coefficient and bandwidth of the photodiodes. Two optical tones that are generated by a laser source set at a fixed frequency f_1 and a second at a variable frequency f_2 are combined through a 3 dB coupler. One of the coupler outputs injects the two tones to a commercial photodiode where the two tones heterodyne beat, generating a DC component and an electrical RF tone at a frequency of $\Delta f = f_1 - f_2$. This electrical signal is monitored by an electrical spectrum analyser (ESA). Moreover, at the input of the ESA, there is a DC-block removing the generated DC component. The optical segment that is connected to the second output of the 3 dB coupler is

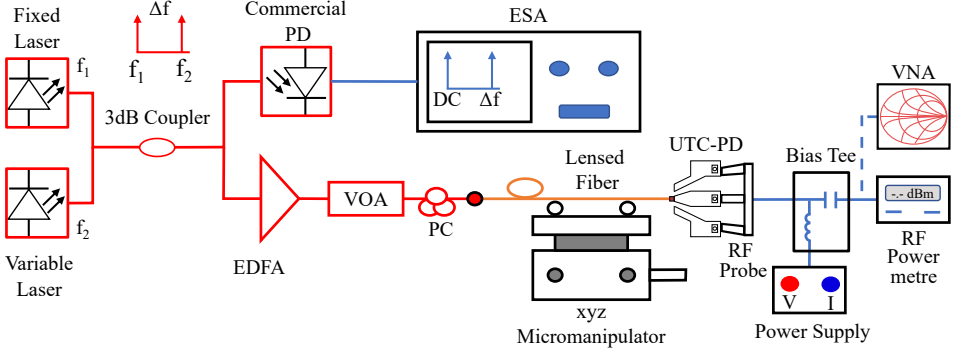


Figure 3.6: Block diagram of the setup providing the measurement results shown in this Chapter.

connected to an EDFA with an output power of 25 dBm. A VOA and a polarisation controller regulate the input to the lensed fibre that emits light to the UTC-PD. The fibre is positioned using a micromanipulator. As previously described, at the pads of the diode under test, there is an RF probe connected to a bias tee. The bias tee's DC terminal provides the junction's reverse bias, and the RF part is connected to an RF power metre or a VNA.

Responsivity and dark current

For responsivity measurements, the variable laser is turned off, and the power originating from the fixed laser is measured at the output of the lensed fibre with a free-space optical power metre so that it equals to 0 dBm. Based on the equation $R_{op} = I_{PD}/P_{op}$, if P_{op} is 1 mW, then the indication of the DC current at the power supply directly gives the responsivity of the photodiode under test. Furthermore, once the VOA is off and no light is injected into the device, the dark current of the photodiode can be obtained. As an example, a device with a size of $4 \times 15 \mu\text{m}^2$ is measured with a responsivity of 0.7 A/W and a dark current in the level of 5 nA.

Bandwidth measurement

The bandwidth measurements (S_{21}) are achieved by controlling the frequency f_1 of the tunable laser as well as registering data from the ESA and the RF power metre. Therefore, for each frequency step Δf , the RF power is registered, synthesising a power over frequency diagram. The obtained data are de-embedded by implementing correction files based on the reflection coefficient parameters of the probe, the bias tee and the UTC-PD.

In addition, the f_{3dB} is affected by the input optical power to the photodiode. This is confirmed by the results calculated in Fig. 3.7a) where the values of f_{3dB} for a $4 \times 15 \mu\text{m}^2$ at -2V are measured as a function of the DC component of the

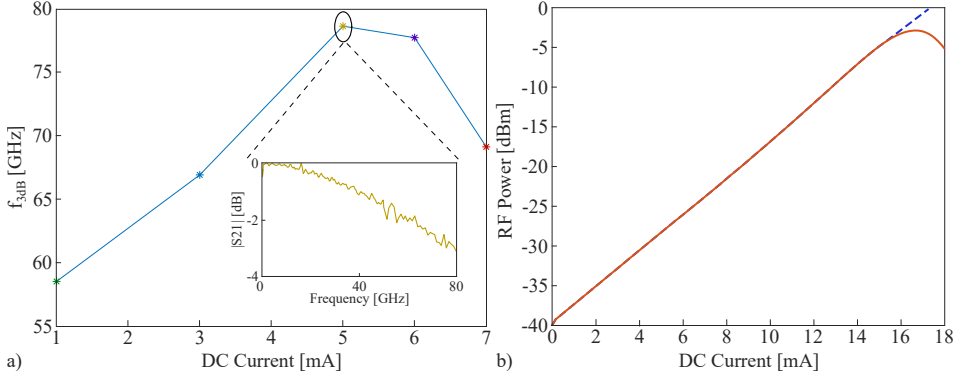


Figure 3.7: a) The measured 3-dB bandwidth (f_{3dB}) of the $4 \times 15 \mu\text{m}^2$ diode for a reverse bias voltages of -2 V for increasing input optical powers (i.e., I_{PD}^{DC}) while the frequency response is shown for a DC current of 5 mA ; b) The saturation current of a $4 \times 15 \mu\text{m}^2$ diode for a reverse bias voltage of -2 V at 46 GHz .

generated photocurrent (I_{PD}^{DC}). By increasing the I_{PD}^{DC} , i.e., increasing the optical power at the input of the UTC-PD, the self-induced electric field (E_{ind}) becomes higher at the absorber, accelerating the speeds of the electrons that propagate within the intrinsic region of the device. As mentioned in the theoretical part of this Chapter, this effect leads to lower electron transit times (τ_{tr}) and thus, higher f_{3dB} . As the input power increases even further, it is expected that the f_{3dB} will drop as a result of the current blocking in the absorber leading to the decrease of the velocity of electrons that transcend from the overshoot to the saturation state. At 5 mA of I_{PD}^{DC} the 3dB frequency response of the examined UTC-PD (78.67 GHz) exceeds the limits of V-band, making it a promising candidate for being co-integrated within the mm-wave transmitter providing the interface between optics and electronics.

Saturation power

During the saturation power measurements, the tunable laser is manually set to a constant frequency (i.e., Δf fixed). A computer program measures the DC current at the power supply and the indication of the RF power metre while controlling the input power to the UTC-PD from the VOA. Therefore, data of RF power versus DC current can be obtained, resulting in saturation power curves. Such a result is given in Fig. 3.7b) for a lower bandwidth $4 \times 15 \mu\text{m}^2$ UTC photodiode at a frequency of 46 GHz . As previously described, the impact of band-bending is observed for DC currents above saturation where the RF output power drops due to the space-charge effect for $I_{PD}^{DC} > 16.5\text{ mA}$.

3.2.2 Reflection coefficient measurements with a VNA

VNA calibration

In order to optimise the experimental processes for the reflection coefficient extraction of UTC-PDs, VNA calibration is performed, allowing the elimination of errors on the measured S-parameters that stem from the VNA and the interconnected RF components due to losses and reflections [238]–[240]. This procedure can be complex for optoelectronic devices due to the different nature of their ports (optical input, electrical output) [241], [242]. However, the goal in this work is the acquisition of S_{11} parameters and the electrical characterisation of UTC-PDs under the dark regime where no optical illumination is applied. Thus, the calibration is conducted on a commercial wafer substrate provided by the GSG probe vendor where the standards used are open, short, and load (OSL) [243]. Through the OSL correction technique of the VNA, the reference measurement plane is moved to the tip of the microwave probe [244]. All the data described are based on the exact OSL calibration ensuring a fair comparison between the presented circuit analysis methods. An alternative solution to the performed process is based on the techniques of the open and load with two additional offset shorts [245], [246]. The three-offset shorts (SSS) approach is capable of achieving single-port calibration on transmission media where it is challenging to realise loads or opens. It is important to note that this method is highly frequency dependent and band limited [247]. Moreover, each short should have a unique length that is precisely known, and it is not proportional to multiples of $\lambda/2$ [248], [249].

Retrieving data from InP on-wafer structures

Once calibrated, the VNA acquires information on the reflection parameters of a photodiode (Γ_m) that is illustrated in Fig. 3.8a). Γ_m shows a capacitive behaviour, and the blue curve confirms this on the Smith chart of Fig. 3.8c) for a measured $5 \times 25 \mu\text{m}^2$ UTC-PD at a reverse bias of -2 V. Moreover, measurements of the TML while it is terminated by an open (open test structure, Γ_{OC}) and by a short circuit (short test structure, Γ_{SC}) are also conducted. The block diagrams of these components are depicted in Fig. 3.8b). Based on the Smith chart of Fig. 3.8c), Γ_{OC} (in red) has a capacitive behaviour and Γ_{SC} (in yellow) has an inductive behaviour. Both Γ_{SC} and Γ_{OC} provide information on the transmission line parameters of the device that contributes to the curvature of Γ_m .

Ideally, the retrieved reflection coefficient curves of both the short and open should coincide with the outer circle of the Smith chart where the load impedances $Z_L = 0$ and $Z_L = \infty$ are located, respectively. However, since the on-wafer components are not ideal, the measured parameters have a deviation that is also visible in the magnitude and phase of Γ_{OC} and Γ_{SC} in Fig. 3.9a). Optimally, it is expected that both magnitudes to be equal to 1 for all frequencies. Nonetheless, losses in the conductors arise due to the metals' finite conductivity, leading to the decrease

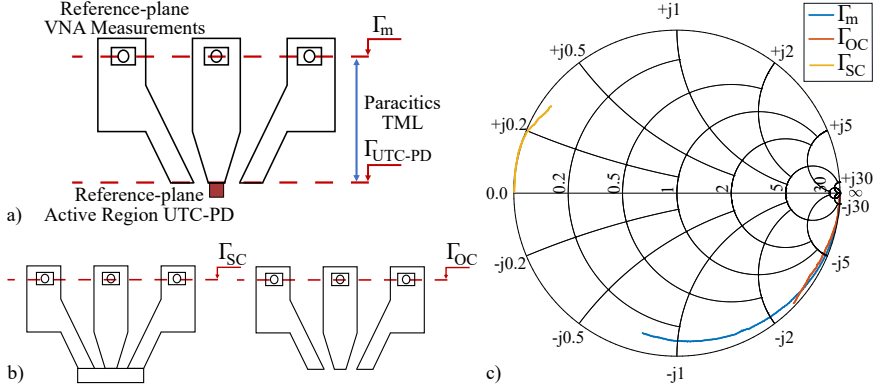


Figure 3.8: a) A block diagram of the active region of an on-wafer UTC-PD connected to the waveguide pads to be de-embedded; b) the short and open circuit structures; c) the reflection coefficients mapped on a Smith chart for open (Γ_{OC}) and short (Γ_{SC}) structures as well as for a $5 \times 25 \mu\text{m}^2$ UTC photodiode at a reverse bias of -2 V .

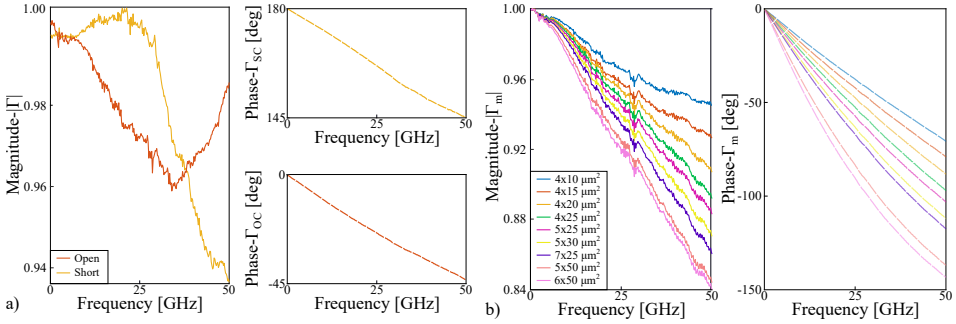


Figure 3.9: a) The magnitude and phase of Γ_{OC} and Γ_{SC} ; b) the magnitude and phase of Γ_m for measurements of diodes with different sizes at a reverse bias of -2 V .

of $|\Gamma|$. In addition, the Γ_{OC} curve shows a reduction in magnitude for lower frequencies while it reverts to higher values over 30 GHz. This may indicate radiation losses and parasitic coupling with neighbouring on-wafer structures that are closely spaced or direct coupling between the structures and the GSG probe [250], [251]. Moreover, multiple reflections may occur before the signal reaches the end of the design as a result of impedance mismatch between the probe tip and the on-wafer design [252]–[254]. Another cause can be due to material characteristics as well as fabrication imperfections on the InP substrate. Thus, the representation of the TML with lumped components becomes more complex, making the de-embedding techniques a compelling solution for extracting the active region properties.

Figure 3.9b) shows the magnitude and phase of Γ_m for UTC-PDs with different sizes at an applied bias voltage of -2 V . It is observed that the negative slope

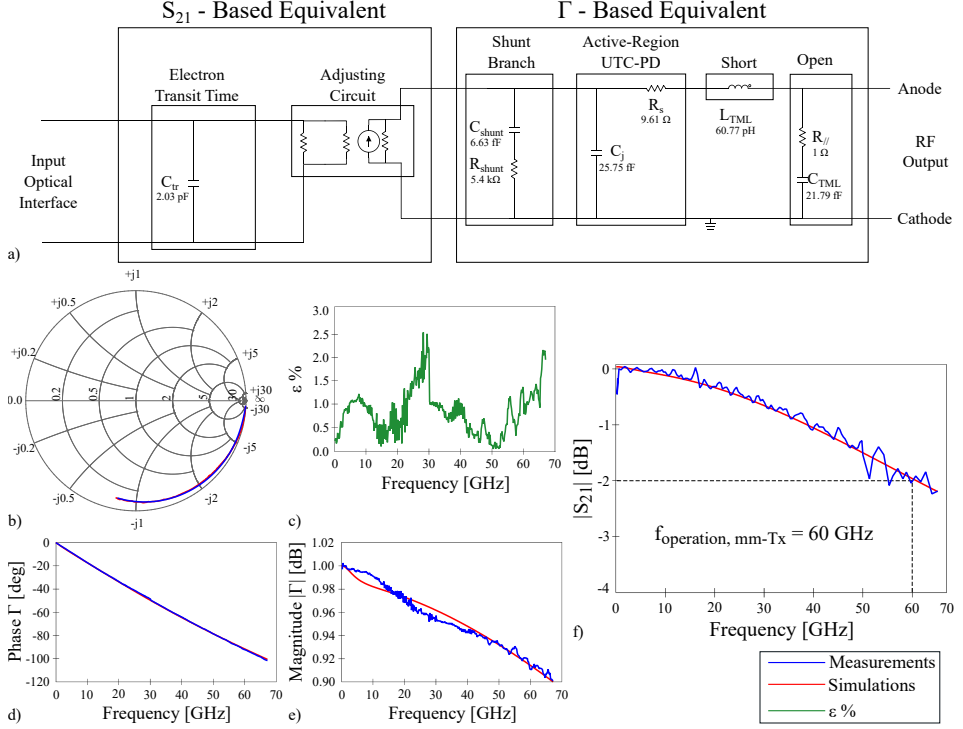


Figure 3.10: Data obtained from the full equivalent circuit simulations and measurements of a $4 \times 15 \mu\text{m}^2$ UTC-PD biased at -2 V : a) the full equivalent circuit including all the extracted component values; b) the measured and simulated Smith charts; c) the percentage error between measurements and simulations; d,e) the magnitude and phase of the measured and simulated reflection coefficients; f) measured and simulated device bandwidth.

increases for diodes with wider surfaces. This is due to the fact that the values for the real part of the reflection coefficients ($\text{Re}[\Gamma_m]$) are higher for smaller devices due to their larger series resistance [255]–[257]. Moreover, the imaginary part of the Γ_m values ($\text{Im}[\Gamma_m]$) also show the same trend where the capacitive behaviour of the active region is more dominant for wider structures comparing to the parasitics of the TML [258]–[260]. The opposite occurs for small diodes (e.g. size of $4 \times 10 \mu\text{m}^2$) where the TML principally influences the magnitude and phase of Γ_m that is equal to $\sqrt{(\text{Re}[\Gamma_m])^2 + (\text{Im}[\Gamma_m])^2} \angle (\text{Re}[\Gamma_m], \text{Im}[\Gamma_m])$.

3.2.3 Full Equivalent Circuit Analysis

The equivalent circuit extraction process of a $4 \times 15 \mu\text{m}^2$ photodiode at -2 V and 5 mA , shown in Fig. 3.10a), is divided in three major steps. First, the waveguide connected to the active region of the photodiode is simulated based on reflection

coefficient measurements of the short and open on-wafer structures. Then, the UTC-PD junction capacitance and series resistance are extracted from the Γ_m parameters. Finally, through bandwidth (S_{21}) measurements, the electron transit time circuit is derived and linked to the Γ -based equivalent via an adjusting block. This voltage to current transformer symbolizes the optoelectronic conversion and photocurrent generation. Additionally, it allows the independent simultaneous optimization and adjustment of the lumped elements based on the measured transmission and reflection coefficient data. The values of the equivalent components can be calculated either analytically or through a circuit simulations software.

The short on-wafer circuit structure has an inductive behaviour, and therefore the measured waveguide Γ_{OC} parameters can be matched with an inductor (L_{TML}). The same process models the open circuit represented by a capacitance (C_{TML}). Moreover, a resistor ($R_{//}$) is added in series to C_{TML} to correct for the non-ideal performance of the open structure (e.g., potential leakage to the substrate). In some cases, $R_{//}$ is small and can be omitted. Furthermore, analytical methods provide the magnitude for both $C_{TML} = 1/(j\omega Z_{OC})$ and $L_{TML} = Z_{SC}/(j\omega)$ with very good precision once the impedances of the short (Z_{SC}) and open (Z_{OC}) structures are calculated.

The properties of the waveguides connecting the photodiode to the external world are important, as they can affect the response. After obtaining these parameters, the junction capacitance and series resistance are assessed. The lumped elements for C_j and R_s are obtained by using the optimisation feature of a circuit simulations software that is able to minimise the error difference (ϵ) between the extracted data, i.e., Γ_m and the reflection coefficient of the circuit model (Γ_{model}) where $\epsilon = |\Gamma_{UTC-PD} - \Gamma_{model}|/|\Gamma_{UTC-PD}|$ [261]. For the parametric estimation of these elements, the Γ_m data of the measured diodes are inserted in the software that calculates the two unknown elements (i.e., R_s and C_j). To achieve the optimal matching between the measurements and the circuit model, a shunt resistor R_{shunt} and capacitor C_{shunt} are connected in parallel to C_j . The impedance of this part is high (in the range of $k\Omega$), and in most of the simulations presented in the literature, this parallel branch is considered open. Alternatively, these elements can be directly derived from the asymptotic behaviour of the Γ_m [262].

The bandwidth of the Γ -based equivalent is very high and does not match with experimental S_{21} parameter measurements. This is due to the fact that the bandwidth of a UTC-PD is based on both the RC-time constant ($\tau_{RC} = 0.88$ ps) of the device as well as the transit time ($\tau_{tr} = 1.82$ ps) of the majority carriers (electrons) through the junction. Thus, the transit time can be approximated as an additional RC cut-off time [263]. In this case, the value of the lumped element C_{tr} is evaluated based on the experimental S_{21} curves. In addition, the adjusting circuit able to adapt the amplitude of the imported S_{21} parameters without changing any of the properties of the measured curve interfaces the two equivalents of the UTC-PD. Using this S_{21} equivalent, a UTC-PD can be fully modelled with lumped circuit elements while perfect matching between measurements and simulations is achieved with an error percentage calculated below 3 %.

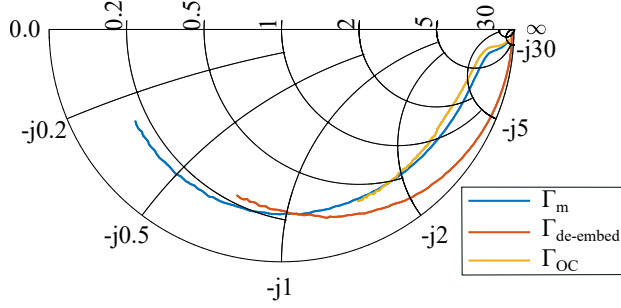


Figure 3.11: Example of a $5 \times 25 \mu\text{m}^2$ UTC-PD where due to a fabrication there is leakage on the substrate; this error is fully removed by implementing a de-embedding method.

3.3 De-embedding Techniques

The synthesis of the full equivalent circuit with lumped components based on reflection coefficients (Γ) is a prevalent solution for analysing the measured diodes. However, the simulation of the elements composing the total equivalent is not always a feasible task. The measured reflection coefficient data of the UTC photodiodes include additional information about the pads and the on-wafer transmission lines, which are used to interconnect the intrinsic devices for probing measurements [264]. Even an ideal TML, if not simulated accurately, may lead to a circuit that does not precisely represent the physical characteristics of the device under test (DUT). Additionally, parasitic phenomena that may occur –such as signal leakage on the substrate– increase the complexity of the circuit structures and impede the extraction of the values of the components representing the active region of UTC-PDs. Therefore, in order to isolate these elements, there are several de-embedding techniques that remove the impact of the unwanted parasitic effects added to the DUT [265].

The valuable information extracted for Γ_{OC} , Γ_{SC} and Γ_m are inserted to de-embedding equations calculating the reflection coefficient of the photodiodes' Γ_{UTC-PD} . At a further step, Γ_{UTC-PD} is introduced to the software-based circuit model where the active region of the diodes can be simulated as indicated in Fig. 3.4. It is worth noting that the shunt branch, including a capacitor in series with a resistor, can be added in parallel to C_j [266]. This part is not removed from the de-embedding but, due to its high impedance, is considered as open and can be omitted without an impact on the measured data [267]. As already mentioned, the lumped elements for C_j and R_s are obtained using the optimisation feature of the software able to minimise the error difference (ϵ) between the extracted data, i.e., Γ_{UTC-PD} and the reflection coefficient of the circuit model (Γ_{model}).

An example of the beneficial impact of these processes is shown in Fig. 3.11. The Smith plot of the open pad has a behaviour that is not purely capacitive but is more complex, indicating the existence of signal leakage to the substrate confirming

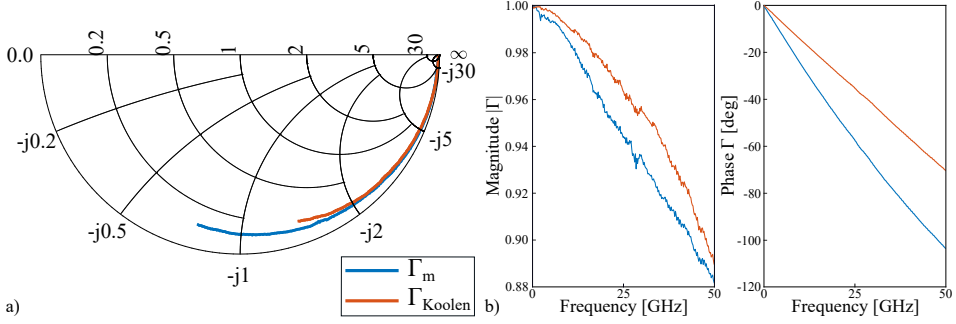


Figure 3.12: a) The impact of the open-short method on a $5 \times 25 \mu\text{m}^2$ UTC-PD leading to the removal of the waveguide parasitics at -2 V reverse bias plotted on a Smith chart; b) the magnitude and phase of Γ_m and Γ_{Koolen} .

that the TML directly affects the curvature of the UTC-PD and is impossible to simulate. This effect is fully removed in $\Gamma_{de-embed}$ by employing de-embedding equations that provide the intrinsic diode response which allow their modelling and at a later step lead to the design optimisation for future fabrications. In the following subsections three different de-embedding techniques will be analysed and compared, the open-short, corrected and S-parameter based.

3.3.1 The open-short de-embedding

The open-short method introduced by Koolen [268] is based on the conversion of all measured S-parameters into admittances (Y) and calculates the impedance of a DUT by implementing Eq. (3.8) [269].

$$Z_{Koolen} = (Y_m - Y_{OC})^{-1} - (Y_{SC} - Y_{OC})^{-1} \quad (3.8)$$

This technique is applied to a $5 \times 25 \mu\text{m}^2$ UTC-PD, and the Smith chart of Fig. 3.12a) is obtained. It is evident that the de-embedded (red) curve of Γ_{Koolen} also has a capacitive behaviour while the parasitics introduced by the waveguide are removed. The differences between the two reflection coefficients are also calculated in Fig. 3.12b) based on magnitude and phase. As previously stated, the added parasitics from the TML increase the negative slope of the Γ_m comparing to the de-embedded Γ_{Koolen} .

In regards to the lumped equivalent circuit of the active region, it is expected that $Z_{Koolen} = Z_{UTC-PD}$. However, in order to acquire a perfect optimisation in the circuit simulations software and minimise ϵ , an inductor (L_p) needs to be added in series with the Z_{UTC-PD} of Fig. 3.4 after the transmission line. This additional element contradicts the predicted circuit model of the active area within a photodiode [270]. The origin of L_p is thoroughly analysed in the following section.

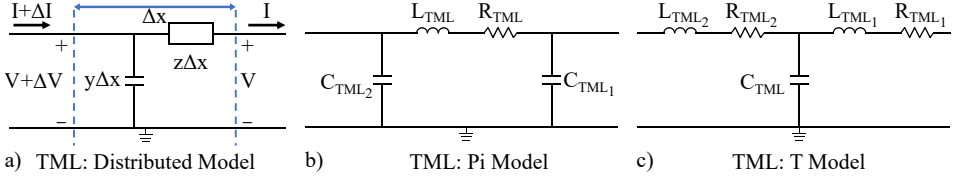


Figure 3.13: Three representations of the transmission line based on the: a) distributed Model; b) Pi lumped equivalent model; c) T equivalent model.

Analysis of the inaccuracies introduced by the open-short method

In order to verify the existence and magnitude of the additional inductance, the open-short de-embedding is investigated analytically. As depicted in Fig. 3.13a), the TML connected to the DUT can be based on the distributed model. The transfer matrix for this type of ideal waveguide with length l is given by Eq. 3.9, with a propagation constant $\gamma = \sqrt{zy}$ and $z = R + j\omega L \approx j\omega L$, $y = j\omega C$ [271]. Finally, $Z_c = \sqrt{z/y}$ is the characteristic impedance of the line. Each variable is measured in units per transmission length.

$$T = \begin{bmatrix} A & B \\ C & D \end{bmatrix} = \begin{bmatrix} \cosh(\gamma l) & Z_c \sinh(\gamma l) \\ \frac{\sinh(\gamma l)}{Z_c} & \cosh(\gamma l) \end{bmatrix} \quad (3.9)$$

$$Z_m = \frac{AZ_{DUT} + B}{CZ_{DUT} + D}, \quad Z_{OC} = \frac{A}{C}, \quad Z_{SC} = \frac{B}{D}$$

Converting the impedances of this symmetric model ($S_{11} = S_{22}$) in Eq. (3.9) to admittances through inversion and placing them into Eq. (3.8) results in:

$$Z_{Koolen} = Z_{DUT} \cosh^2(\gamma l) \quad (3.10)$$

The term $\cosh^2(\gamma l)$ can be approximated with a Taylor series and thus,

$$Z_{Koolen} = \frac{1}{2} Z_{DUT} \left[1 + \sum_{n=0}^{\infty} \frac{(2\gamma l)^{2n}}{(2n)!} \right] \quad (3.11)$$

$$Z_{Koolen} = Z_{DUT} [1 + (\gamma l)^2] + R_2$$

is extracted. The residual error (R_2) for this Taylor approximation is presented in Eq. (3.12). It is a constant, that multiplied by an impedance, results in negligible values and therefore can be omitted.

$$R_2 = \sum_{n=2}^{\infty} (-1)^n (10)^{-9n} \left[\frac{2^{2n}}{(2n)!} \right] \quad (3.12)$$

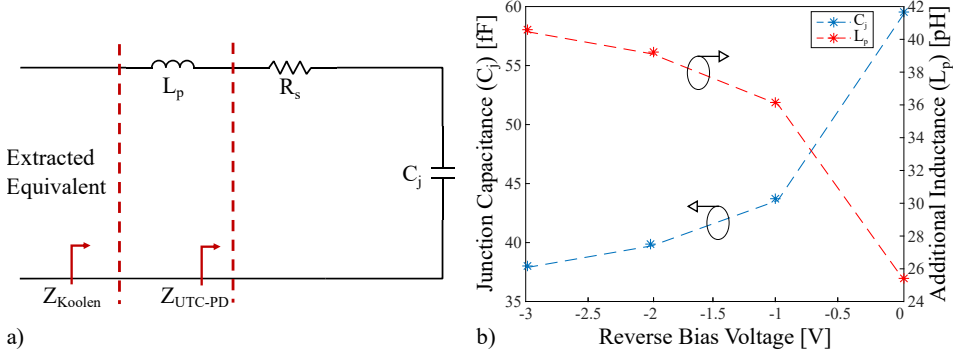


Figure 3.14: a) The resulting equivalent circuit extracted by the open-short method; b) The descending behaviour of the additional inductance (L_p) extracted from the open-short method of a $5 \times 25 \mu\text{m}^2$ UTC-PD as a function of the applied reverse bias that is inverse to the curve for the junction capacitance.

If the DUT is a UTC-PD, i.e., $Z_{UTC-PD} = R_s - j \frac{1}{\omega C_j}$, and by replacing it in Eq. (3.11),

$$Z_{Koolen} = Z_{UTC-PD} - R_s(\gamma l)^2 + j\omega \frac{LC}{C_j} l^2 \quad (3.13)$$

is obtained. Consequently, Eq. (3.13)a) agrees with the previous statement that Z_{Koolen} is not directly equal to Z_{UTC-PD} for both the real and imaginary parts of the UTC-PD. For low frequencies, the real parasitic term $|R_s(\gamma l)^2| = |R_s \omega^2 L C l^2|$ that depends on the characteristics of the transmission line (L, C, l) can be omitted ($< 1 \text{ m}\Omega$). However, in higher frequencies, its quadratic impact increases, reducing the series resistance. The additional inductance ($L_p = \frac{LC}{C_j} l^2$) that is calculated is inversely proportional to the junction capacitance of the device. The exact same result for L_p is measured if the equation of the open-short method is implemented to the Pi and T equivalent models of a waveguide in Fig. 3.13b) and c) [272]. Based on this process, it is proven that a systematic error is added to Z_{DUT} while using the Koolen de-embedding technique. In principle, since the device model of Fig. 3.4 is related to different types of diodes such as PN, PIN and Schottky, it is expected that the same error would occur if the open-short technique is applied [273]–[275].

These analytical calculations concerning the additional inductance are confirmed through circuit simulations based on experimental data for diodes with a different reverse bias applied, sizes, and frequency of operation. In theory, the value of $C_{jth} = \epsilon A_j / l_j$ is proportional to the junction area (A_j) and inversely proportional to the junction length that is directly linked to the reverse bias. In the case where the bias is not enough to fully deplete the active region of a UTC-PD, l_j decreases while C_j increases. In addition, since the declining junction area of a photodiode reduces the value of C_j , it is observed that L_p of Fig. 3.14a) increases.

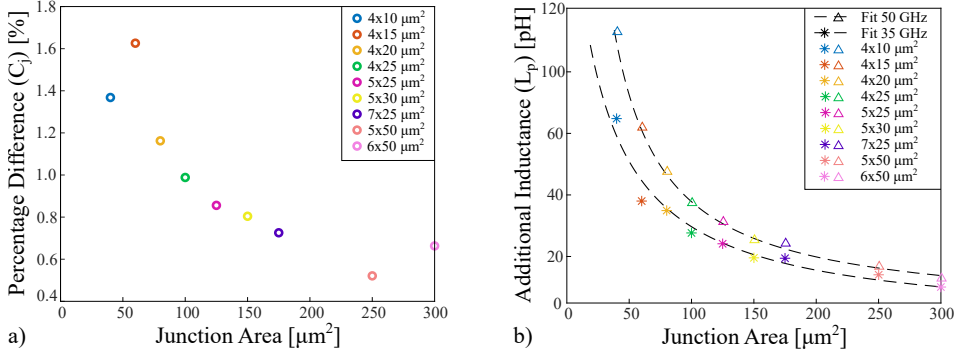


Figure 3.15: a) The percentage of difference between the values of C_j extracted up to 35 and 50 GHz affecting the calculation of L_p ; b) the additional inductance (L_p) introduced by the open-short technique as a function of area at a reverse bias voltage of -2 V for different UTC-PDs up to 35 and 50 GHz.

In Fig. 3.14b), the junction capacitance and inductance of a $5 \times 25 \mu\text{m}^2$ UTC-PD are extracted for different values of the reverse bias. As expected, the form of the curve of C_j (blue) is approximately a reflection of L_p (red) as a reference to the x -axis, verifying the previous observations on the inverse proportional relationship between these two lumped components.

Furthermore, in the ideal case, the values of the junction capacitance are expected to be constant as a function of frequency. However, since C_j is extracted based on S-parameter measurements, it is expected to show a slight deviation for different frequencies with C_j being higher at low frequencies due to parasitic effects [276]. This deviation (in percentages) is depicted in Fig. 3.15a) where for the same diodes, the junction capacitance calculated over the range $0 - 35$ GHz shows higher values compared to the data measured between $0 - 50$ GHz. The maximum percentage of difference at 1.65% is obtained for a diode with a size of $4 \times 15 \mu\text{m}^2$. This directly affects the calculation of L_p that is plotted in Fig. 3.15b) as a function of increasing A_j for different measured UTC-PDs at a bias of -2 V. Then, a hyperbolic curve fitting is used in order to show the inverse proportionality of L_p to the sizes of the diodes while LCl^2 is constant. As previously discussed, this curve is shifted upwards for higher frequencies.

3.3.2 A correction to the open-short method

To eliminate the additional inductive behaviour of Eq. (3.13), a correction to the open-short technique needs to be introduced, isolating Z_{UTC-PD} . Therefore, the term $\cosh^2(\gamma l)$ in Eq. (3.10) is expressed as a function of the two known variables imported from the open (Y_{OC}) and short (Y_{SC}) structures from Eq. 3.9.

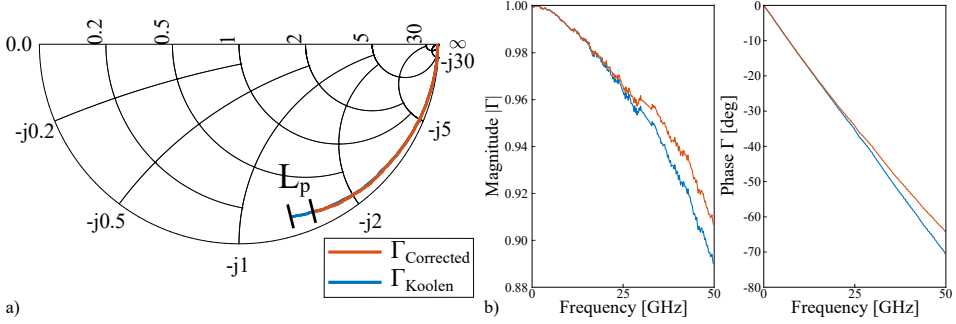


Figure 3.16: a) The impact of the corrected method to a $5 \times 25 \mu\text{m}^2$ UTC-PD leading to the removal of the waveguide parasitics at -2 V reverse bias depicted on a Smith chart; the corrected curve is compared to Γ_{Koolen} showing the additional inductance L_p ; b) the magnitude and phase of Γ_{Koolen} and $\Gamma_{Corrected}$.

$$Y_{OC} + Y_{SC} = \frac{\sinh(\gamma l)}{Z_c \cosh(\gamma l)} + \frac{\cosh(\gamma l)}{Z_c \sinh(\gamma l)} = \frac{\cosh^2(\gamma l) + \sinh^2(\gamma l)}{Z_c \sinh(\gamma l) \cosh(\gamma l)} \quad (3.14)$$

Calculating $Y_{OC} + Y_{SC}$ in Eq. (3.14), as well as taking into account $\cosh^2(\gamma l) + \sinh^2(\gamma l) = 2\cosh^2(\gamma l) - 1$ of the hyperbolic trigonometric identities and Eq. (3.10), results in Eq. (3.15) which introduces a correction forming an impedance based de-embedding capable of removing the systematic error imported in Eq. (3.8) for any single-port DUT.

$$Z_{Corrected} = Z_{OC} \frac{Z_m - Z_{SC}}{Z_{OC} - Z_m} \quad (3.15)$$

The de-embedded reflection coefficients based on the open-short technique and its correction are calculated and plotted in the Smith chart of Fig. 3.16a) for the same $5 \times 25 \mu\text{m}^2$. The curves for Γ_{Koolen} and $\Gamma_{Corrected}$ overlap while the one for the open-short is longer due to L_p added by the method itself. A similar observation can be extracted from Fig. 3.16b) where the magnitude and phase of the two obtained reflection coefficients are plotted. Consequently, Eq. (3.15) is capable of isolating the active region of a UTC-PD leading to the valid design of its circuit model matching the impedance Z_{UTC-PD} and can be expanded to all devices using open and short structures for de-embedding.

3.3.3 The S-parameter based de-embedding method

An alternative process that can be implemented in order to de-embed the parasitics of the UTC-PDs is the S-parameter based (SPb) method. This mathematical approach relies primarily on reducing the unknown S-parameter variables of the

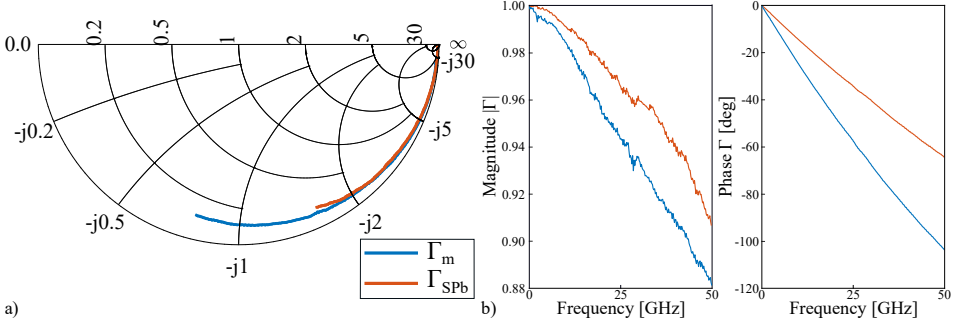


Figure 3.17: a) The impact of the S-parameter based method to a $5 \times 25 \mu\text{m}^2$ UTC-PD leading to the removal of the waveguide parasitics at -2 V reverse bias mapped on a Smith chart; b) the magnitude and phase of Γ_{SPb} and Γ_m .

TML (S_{TML}) in Eq. (3.7) from four to two. This is initially accomplished by implementing the property of passive behaviour of the TML connected to the UTC-PD where $S_{12} = S_{21}$. Moreover, by assuming the symmetry of the TML, the equality between S_{11} and S_{22} is acquired. The validity of this hypothesis is substantial and it will be investigated even further through simulation processes in the following section.

The de-embedding equation is finally derived in Eq. (3.16) as a function of Γ_m , Γ_{OC} and Γ_{SC} by replacing and rearranging the variables in Eq. (3.7) from the data obtained for the open structure, $\Gamma_{DUT} = 1, \Gamma_m = \Gamma_{OC}$ and for the short $\Gamma_{DUT} = -1, \Gamma_m = \Gamma_{SC}$. The Smith chart of Fig. 3.17a) and b) presents the impact of the S-parameter based method on a $5 \times 25 \mu\text{m}^2$ UTC-PD where the TML parasitics are removed in the curve of Γ_{SPb} .

$$\Gamma_{SPb} = \frac{\Gamma_{OC} + \Gamma_{SC} - 2\Gamma_m - \Gamma_m(\Gamma_{OC} - \Gamma_{SC})}{2\Gamma_{OC}\Gamma_{SC} + \Gamma_{SC} - \Gamma_{OC} - \Gamma_m(\Gamma_{OC} + \Gamma_{SC})} \quad (3.16)$$

3.3.4 Evaluating the asymmetry assumption for the TML

It is essential to extract an estimation of the error that is introduced due to the asymmetry assumption of the TML connected to the DUT introduced in the de-embedding processes. This is achieved through the simulation where a photodiode is connected to a transmission line that is based on the Pi-model of Fig.3.13b) and shown in the upper part of Fig. 3.18a) that is designed with lumped components ($C_{TML_1} = 21.3 \text{ fF}$, $L_{TML} = 55.6 \text{ pH}$, $R_{TML} = 0.3 \Omega$).

The TML of the circuit exhibits 100% of symmetry if $C_{TML_1} = C_{TML_2}$, i.e., $S_{11} = S_{22}$. Asymmetry can be introduced by setting $C_{TML_2} = (1-a)C_{TML_1}$ where a is a scaling factor varying between 0 and 1 where 1 represents a fully asymmetric TML. The values of the lumped components for these simulations are chosen based

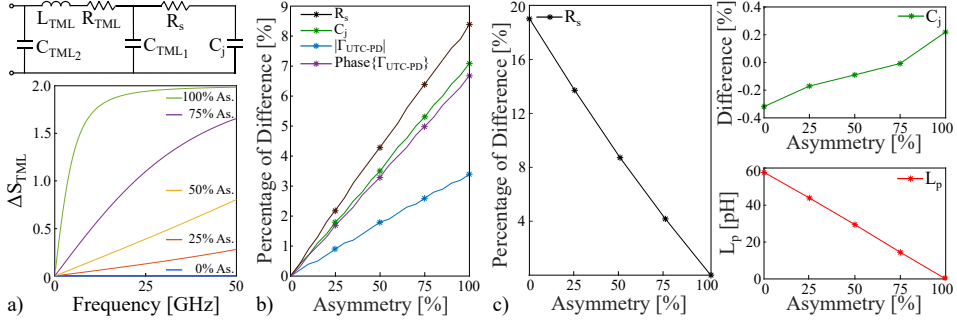


Figure 3.18: a) The simulated circuit and ΔS_{TML} as function of frequency for different asymmetry values; b) the percentage difference of C_j , R_s and of the characteristic properties of Γ_{UTC-PD} between the S-parameter based and direct methods as a function of the increasing TML asymmetry; c) the percentage difference of C_j , R_s and L_p between the open-short and direct methods as a function of the increasing TML asymmetry.

on measurements of a $5 \times 25 \mu\text{m}^2$ UTC-PD ($C_j = 37.7$ fF, $R_s = 14.9 \Omega$). The circuit simulator is used to calculate the S_{TML} as well as the reflection coefficients of the TML while it is terminated by a short (Γ_{SC}) and by an open circuit (Γ_{OC}) reproducing the test structures on a real wafer for frequencies up to 50 GHz.

The first figure of merit that is tested is the effect of the asymmetry on the S_{11} and S_{22} parameters of the TML. Therefore, $\Delta S_{TML} = |S_{11} - S_{22}|/S_{11}$ is introduced comparing the magnitude of the reflection coefficient S_{11} to S_{22} [277]. The ΔS_{TML} is calculated for an ascending value of the asymmetry factor a . The results are provided in Fig. 3.18a) where it is evident that the asymmetry of a transmission line affects its S-parameters. At a further step, the impact of increasing a is implemented in order to investigate its effect on the de-embedding equations (3.8), (3.15) and (3.16).

Asymmetry dependence in S-parameter based method

Figure 3.18b) examines the percentage of difference between the junction capacitance and series resistance both extracted by Eq. (3.7) that provides the exact values of C_j and R_s and the resulting lumped elements calculated by Eq. (3.16) as a function of the increasing asymmetry. The curves are linear and maximum difference reaches 7.1% for C_j and 8.2% for R_s once $a = 1$. Similar behaviour is demonstrated in the percentage differences in the mean values of magnitude, phase, real and imaginary parts of the diode's reflection coefficients (Γ_{UTC-PD}).

Thus, the extracted data confirms that the transmission line symmetry influences the S-parameters (Γ_{SPb}) of the de-embedded circuits as well as the values of the lumped components C_j and R_s . However, the percentage of difference does not exceed the 8.2% for all tested variables, while the technique's performance

improves once the additional branch is added to the TML. Identical values are observed once the equation for the corrected method ($Z_{Corrected}$) is used. Since there is no effective divergence between the de-embedded elements and the original data, the S-parameter based method can be considered an alternative de-embedding that removes the transmission line parasitics from a DUT.

Asymmetry dependence in open-short method

A similar procedure is applied while implementing the open-short de-embedding in order to analyse the impact of asymmetry. The results of this process are shown in Fig. 3.18c) for the series resistance, junction capacitance and additional inductance. While the percentage of difference on the extraction of C_j is low, varying between -0.33% to 0.21% , the real part of the intrinsic region ($Re[Z_{UTC-PD}]$) is directly affected by the type of the transmission line linked to the active area of the UTC-PD. The value for R_s is 19.1% lower than the actual once the C_{TML_2} rises. This percentage linearly reduces for increasing a due to the decrease of the factor LC in the real part of Eq. 3.13. The same trend is presented for L_p .

These results show that the open-short technique is capable of successfully removing the TML parasitics. However, once a second parallel branch with increasing admittance is shunt in the line model, the process starts demonstrating errors that become significant for low a . It is essential to underline that the increasing L_p for high values of C_{TML_2} can be a good indication of the type of transmission line that is experimentally measured as well as on the effectiveness of the open-short especially for the calculation of R_s . As an example, if the open-short method is applied on diodes with a leaking TML on the substrate, an imprecise value of R_s would be extracted as well as high L_p .

Therefore, the additional inductance is not only dependent on the diode size, reverse bias voltage applied and the frequency of operation (Fig. 3.14, Fig. 3.15b)) but also on the type of the TML. Finally, this simulation validates the mathematical analysis of Eq. 3.13 on this series component, i.e., L_p , added by the process.

3.3.5 S-parameter comparison between de-embedding methods

This section provides a good insight on the behaviour of the de-embedding techniques based on circuit simulation level. However, it is of the essence to compare the discussed techniques on their analytical equations and their impact on the measured de-embedded lumped equivalent data.

Comparison S-parameter based - corrected

In order to compare the de-embedding methods for the corrected and S-parameter based techniques, the de-embedded S-parameters for $\Gamma_{Corrected}$ and Γ_{SPb} of the Fig. 3.16 and Fig. 3.17 respectively are superimposed on a Smith chart leading

to an overlap between the two red curves. Moreover, the error difference between the magnitudes of the two reflection coefficients is negligible. That is due to the fact that both the techniques in Eq. 3.15 and Eq. 3.16 are extracted based on the symmetry of the transmission lines. With further mathematical analysis the conversion equation from Z to S parameters in Eq. 3.17 [278] is implemented.

$$Z = \sqrt{Z_0}(1 - \Gamma)^{-1}(1 + \Gamma)\sqrt{Z_0} \quad (3.17)$$

By substituting Eq. (3.17) to Eq. (3.15) then,

$$Z_0 \frac{1 + \Gamma_{Corrected}}{1 - \Gamma_{Corrected}} = Z_0 \frac{1 + \Gamma_{OC}}{1 - \Gamma_{OC}} \frac{\frac{1 + \Gamma_m}{1 - \Gamma_{OC}} - \frac{1 + \Gamma_{SC}}{1 - \Gamma_{SC}}}{\frac{1 + \Gamma_{OC}}{1 - \Gamma_{OC}} - \frac{1 + \Gamma_m}{1 - \Gamma_m}} \quad (3.18)$$

is obtained.

If Eq. 3.18 is rearranged and $\Gamma_{Corrected}$ is extracted, the corrected method becomes identical to the S-parameter based ($\Gamma_{Corrected} = \Gamma_{SPb}$). Therefore, the two de-embedding processes converge and both Z and S parameters can be used to calculate a valid equivalent for the active area of UTC-PDs.

Comparison Koolen - corrected

A similar process is conducted for the comparison between the open-short and the corrected method. As a first step, Eq. 3.8 is analysed based on Z -parameters in Eq. 3.19.

$$Z_{Koolen} = Z_{OC}^2 \frac{Z_m - Z_{SC}}{(Z_{OC} - Z_{SC})(Z_{OC} - Z_m)} \quad (3.19)$$

Then, the error ratio of difference between Z_{Koolen} and $Z_{Corrected}$ is expressed in Eq. 3.20 as a function of Z_{OC} and Z_{SC} .

$$\frac{Z_{Koolen} - Z_{Corrected}}{Z_{Corrected}} = \frac{Z_{SC}}{Z_{OC} - Z_{SC}} = \alpha + j\beta \quad (3.20)$$

In the ideal case where the ratio is a real number, i.e., $\beta = 0$ the relationship between the lumped elements for R_s and C_j extracted by the two methods is given in Eq. 3.21.

$$\begin{aligned} C_{j,Koolen} &= (1 + \gamma^2)C_{j,Corrected} \\ R_{s,Koolen} &= \frac{1}{1 + \gamma^2}R_{s,Corrected} \end{aligned} \quad (3.21)$$

For the two techniques, both R_s and C_j are dependent on the propagation constant of the waveguide (γ) with $C_{j,Koolen} > C_{j,Corrected}$ and $R_{s,Koolen} < R_{s,Corrected}$. However, the measurement results contradict with the ideal scenario since it is calculated that $R_{s,Koolen} > R_{s,Corrected}$ clarifying that it is

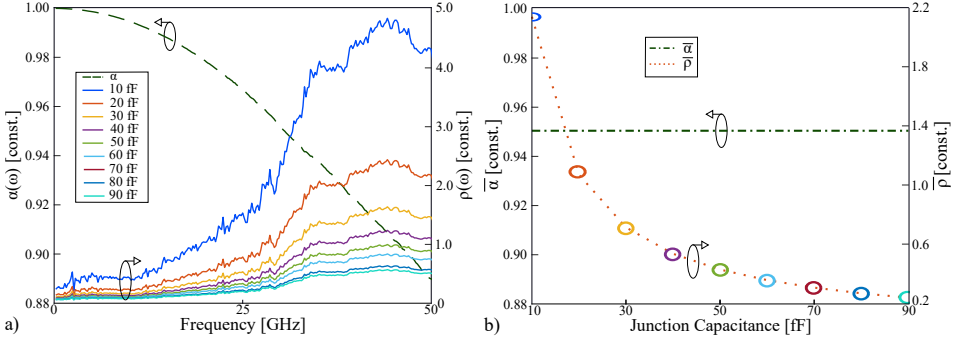


Figure 3.19: a) The $\alpha(\omega)$ and $\rho(\omega)$ as a function of increasing frequency for different diode capacitances; b) $\bar{\alpha}$ and $\bar{\rho}$ as a function of C_j .

important to take into account the impact of the imaginary part of Eq. 3.20, i.e., $\beta \neq 0$. This is because, as shown in Fig. 3.9a), the open and short circuit curves are not ideal. Therefore, by taking into account that the product $\beta\omega R_{s,Corrected}C_{j,Corrected} \approx 10^{-6}$ the results of Eq. 3.22 are obtained.

$$\begin{aligned}
 C_{j,Koolen} &= \frac{C_{j,Corrected}}{\alpha(\omega) - \beta\omega R_{s,Corrected}C_{j,Corrected}} \\
 &\approx \frac{C_{j,Corrected}}{\alpha(\omega)} \\
 R_{s,Koolen} &= \alpha(\omega)R_{s,Corrected} + \frac{\beta}{\omega C_{j,Corrected}} \\
 &= \alpha(\omega)R_{s,Corrected} + \rho(\omega, C_j)
 \end{aligned} \tag{3.22}$$

This analysis confirms that the relationship of R_s and C_j between the two methods is more complex and it depends on both $\alpha(\omega)$ and $\rho(\omega, C_j)$ that includes the parameter β and the $C_{j,Corrected}$ that is directly connected to the UTC-PD's area (A_j). In Fig. 3.19a), the factors $\alpha(\omega)$ and $\rho(\omega, C_j)$ are plotted as a function of frequency showing that $\alpha(\omega)$ decreases at higher frequencies while the opposite occurs to $\rho(\omega, C_j)$. In order to get a better perspective on the impact of the different photodiode sizes to the magnitude of these factors, averaging over frequency is implemented removing ω from the variables of freedom in α and ρ . Thus, $\alpha(\omega)$ as well as each curve of $\rho(\omega, C_j)$ is represented by a single value. Figure 3.19b) shows that $\bar{\alpha}$ remains constant as a function of increasing C_j while $\bar{\rho}(C_j)$ decreases exponentially. Therefore, based on the calculated data it is expected that $C_{j,Koolen} \approx C_{j,Corrected}$ while $R_{s,Koolen} > R_{s,Corrected}$ since the impact of the of $\bar{\rho}$ is high especially for smaller junctions.

These characteristics are verified in Fig. 3.20a) where the percentage of difference between the lumped components of the active region (C_j, R_s) for the

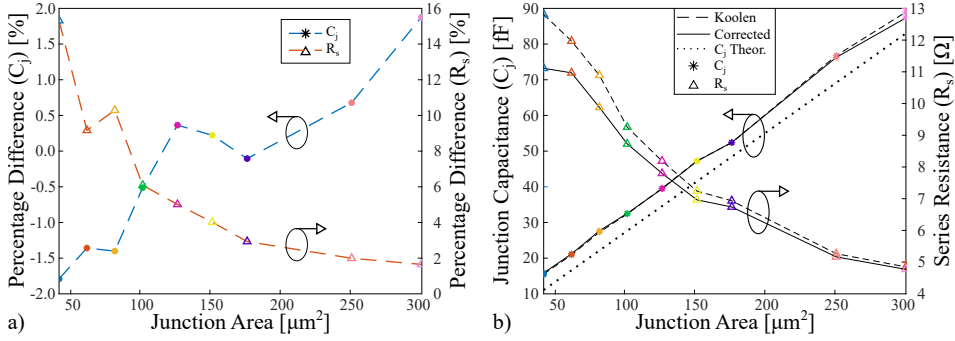


Figure 3.20: a) The percentage of difference of the lumped element components between the open-short and corrected methods; b) the impact of the corrected method to a $5 \times 25 \mu\text{m}^2$ UTC-PD leading to the removal of the waveguide parasitics at -2 V reverse bias.

open-short and the corrected method are plotted using real measurements for diodes with different sizes. The percentage of error difference between $C_{j,Koelen}$ and $C_{j,Corrected}$ increases as a function of size not exceeding the absolute value of 1.8%. The negative percentage implies that the lumped element has a higher magnitude in the corresponding junction area once it is obtained by the corrected method. Concerning the series resistance, the difference between the two methods starts with a significant difference of 15.2% and decreases to values of approximately 1.6% for large devices such as a $6 \times 50 \mu\text{m}^2$ UTC photodiode.

The extracted data of these elements are also shown in Fig. 3.20b) for the different de-embedding techniques. Furthermore, the theoretical curve of the junction capacitance (C_{jth}) is also calculated. It can be observed that for all the different junction areas, the theoretical curve is shifted downwards by a value varying in the range of 4 to 7.1 fF. The difference between the dotted line for C_{jth} and the actual measurement data can be caused due to a parasitic capacitance generated by leakage of electric field at the edges of the diodes' intrinsic region towards the neighbouring layers of the collector layer forming a fringe capacitor in parallel to C_j [279]–[281].

In summary, the classical Koelen method of open-short provides both the R_s and C_j at the price of adding a virtual inductance (L_p) with reduced values for R_s in high frequencies leading to an imprecise circuit model of the intrinsic area within the photodetectors. This error is fixed by using an updated method (corrected) and its equivalent S-parameter based technique. The difference between these three methods in terms of the accuracy of the equivalent circuit and its component magnitudes are mainly based on the assumptions made for the equation calculations, the TML characteristics, the frequency of operation as well as the quality and precision of the on-wafer measurements conducted with the VNA [282]. Overall, the use of these de-embedding methods provides with a good estimation for the values of the lumped elements within the active region of the diodes that are a

valuable tool for the characterization and analysis of their physical properties.

3.4 Summary

In this Chapter, the important aspects of UTC photodiodes have been presented and investigated. Initially, the basic principles of the PIN and UTC photodetectors are reported providing a useful background for the analysis of the obtained results. UTC-PDs have been chosen to play an important role in the fabrication of the mm-wave transmitter since they provide high sensitivity, broad bandwidth and high saturation power due to the unidirectional motion of electrons (as the only active carriers) within their intrinsic region.

The characterisation setup at III-V Lab that is used in order to extract the crucial parameters and functionalities of the fabricated chips is explained in detail. Based on the measured data, a $4 \times 15 \mu\text{m}^2$ UTC-PD is distinguished to be implemented for millimetre wave applications due to its high saturation powers and 3dB bandwidth that exceeds the limits of V-band. Furthermore, all the procedures for synthesising the full equivalent circuit of this device are analysed, including the effect of carrier transit time and the RC-time constant.

At a further step, the Chapter investigates three de-embedding methods contributing to the characterisation of the active region within the uni-travelling carrier photodiodes that remove the parasitic effects of the waveguides connected to the active area of these devices, allowing the calculation of their series resistance and junction capacitance. The open-short method is examined where a systematic error introduced by the technique is identified. This error is analytically extracted, and a correction is implemented. The properties of an S-parameter based de-embedding are also obtained through simulation approaches. Finally, the lumped components calculated and verified by these processes are compared for diodes with different sizes.

Research Question:

How would it be possible to amplify and wireless transmit the generated mm-waves from the UTC photodiodes ?

Broadband RF Components

In the previous Chapter, a thorough analysis of the properties of UTC photodiodes has been discussed. As a further step, the advancements in integrated electronic components need to be investigated to allow interfacing them in a replicable, cost-effective system-on-chip guaranteeing a smooth transition while operating on higher carrier frequencies [283]. Figure 4.1 illustrates such a device, including a photodiode where the optoelectronic conversion takes place, and a mm-wave is generated based on optical heterodyning. Then, the RF signal is boosted by a broadband, high-gain amplifier interconnected to an integrated planar end-fire antenna element transmitting the mm-wave over the air.

In Sec. 4.1, the properties of high frequency transistors are provided, showcasing their characteristics in both the DC and RF domains. Multiple transistors can be combined to form a transimpedance amplifier (TIA) architecture which is a prevailing candidate for interfacing the optoelectronic components. Crucial parameters defining the gain and noise are studied, underlining the leading role of TIAs over different amplifier architectures. A TIA in emitter-follower transistor configuration is simulated, fabricated, and measured. This amplifier provides satisfactory gain and bandwidth to boost the mm-waves from UTC-PDs towards the integrated antenna.

Then in Sec. 4.2, the design and measurement results of a V-band coplanar Vivaldi antenna that can be employed within the future beyond-5G remote unit are presented. The permitted substrate thicknesses for operating in these frequencies is calculated while the optimal value is chosen. Moreover, a balun design allowing the transition from the unbalanced coplanar transmission line to slotline feeding the antenna is analysed. In addition, a comb structure inspired by integrated optical grating couplers is added, improving the component's gain. Finally, the simulation and experimental results are discussed and thoroughly compared, finding good agreement. This Section validates an essential element for future

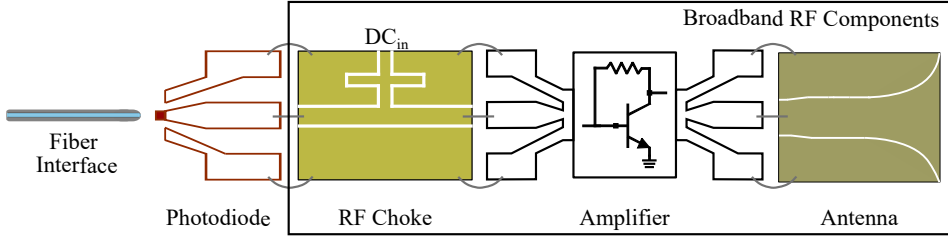


Figure 4.1: Block diagram of a 5G photonics-enabled millimetre wave transmitter including a fibre interface, a high-speed photodiode followed by an RF choke and a broadband amplifier interconnected with a planar antenna.

beyond-5G remote units with the implemented antenna as part of the proposed transmitter design.

In the last part of the Chapter, a three-port structure on a printed circuit board (PCB) is designed and fabricated to be placed in between the active components, i.e., the UTC-PD and the TIA. This device provides the reverse bias voltage to the UTC-PD from its DC port while “choking” the RF signals. Thus, mm-waves are not allowed to propagate towards the DC path. The RF choke exhibits broadband properties in V-band centred at 60 GHz with a total bandwidth exceeding 10% of the carrier frequency. The presented broadband RF components demonstrate a promising potential towards the co-integration and synthesis of the photonics-enabled mm-wave transmitter.

4.1 A mm-wave transimpedance amplifier

The transimpedance amplifier acts as the first element after the optoelectronic generation. More specifically, such device converts the mm-wave photocurrent to amplified voltages providing input to the broadband antenna. While various technologies have been used to fabricate these types of amplifiers such as CMOS and GaAs substrates with high electron mobility transistors (HEMTs) as well as GaAs with heterojunction bipolar transistors (HBTs), the InP HBTs support high power and broadband operation [284]–[287]. Designing TIAs based on InP double-HBTs (DHBTs) can be an ideal technology to deploy ultra-wideband and highly linear devices [288]. Therefore, the fabricated circuit is based on InP/In-GaAs DHBTs allowing the operation in a frequency range including V-band while exhibiting sufficient gain to boost the desired 5G-NR signals towards the end-users.

In the following sections, a theoretical background on transistor functionality, amplifier architectures and TIA properties is provided, while thorough argumentation justifies the selection of the fabricated and measured amplifier between various TIA topologies. Several aspects on the TIA properties and interconnection with optoelectronic devices that are discussed in this section are covered in [C5], [O2].

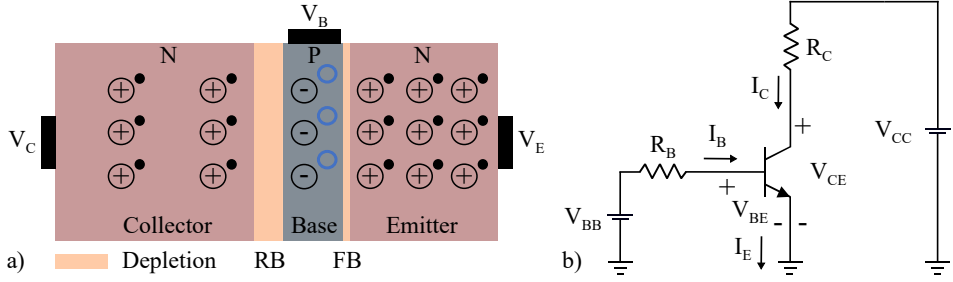


Figure 4.2: An overview of the basic functions of an NPN transistor in active configuration: a) the semiconductor block diagram of a transistor showcasing the depletion regions of the base-collector in reverse bias (RB) and the base-emitter junction in forward bias (FB); b) the circuit representation of a common-emitter transistor.

4.1.1 HBT transistor principles

An NPN transistor is a three terminal semiconductor device that can be used as an amplifier in analogue electronic applications. Based on Fig. 4.2a) it consists of three doped regions, an n-doped emitter, a p-doped base and an n-doped collector [289]. Both electrons and holes contribute to the current flow of the device and generally it can be modelled as two interconnected PN junctions. Regarding the carrier doping concentration, the emitter is heavily doped supplying the electrons, the very thin base area is lightly doped with holes while the moderately doped collector is wider so that it can support the ultra-high supply of electrons from the emitter.

If a transistor is used as an amplification unit, it is regulated in the active regime where the base-emitter region is forward biased (FB) and the base-collector in reverse bias (RB). Therefore, once applied, the voltage of the base (V_B) is higher than the one of the emitter (V_E) and the one of the collector (V_C) is required to be higher than V_B , i.e., $V_C > V_B > V_E$ [290]. Since the emitter is heavily doped, a large amount of electrons will be pushed towards the base. At a further step, there are two possible paths that the electrons can follow, either towards the base or the collector terminal. Within the lightly p-doped thin area, the recombination probability is very small due to the reduced number of holes. Thus, based on the PN junction principle in reverse bias, the electrons arriving at the base become the minority charge carriers and are swept towards the collector.

Heterojunction bipolar transistors, i.e., HBTs, use semiconductor materials with different bandgaps in order to control the flow and distribution of carriers within the devices [291]. The beneficial aspect provided by the wide-gap emitter within an HBT is the capability of increasing current gain by controlling the trade-off between base and emitter dopings as well as optimising the device's geometry [292], [293]. The following simulation and design analysis are based on the Ferdinand Braun Institute (FBH) transferred-substrate InP-DHBT technol-

ogy [294]. Double finger transistors are applied with 500 nm InP emitter width stacked above an InGaAs base [295]. The designs showcase tolerance to high temperature effects and low thermal resistance without limiting their output power capabilities. Thus, these DHBTs can be interconnected with mm-wave components. Moreover, the applied DC biasing voltages and currents presented follow the recommendations of the foundry. These transistors are the fundamental elements for the design and fabrication of the TIA discussed in this Chapter [296].

Common emitter configuration analysis

Even though there are various ways to configure a transistor, the common emitter (CE) is widely used for designing high-gain amplifiers [297]. In this work, the CE configuration is selected where the emitter terminal is shared between the input and the output. Therefore, the input is applied between the base and the emitter, while the output is measured between the collector and the emitter. The circuit diagram including the direction of the current flowing within a CE configured transistor are shown in Fig. 4.2b) [298].

Concerning the supply voltages where V_{BB} and V_{CC} are the source voltages for the base and the collector controlled by the resistor values R_b and R_c , respectively. Moreover, V_{BE} is the difference between the base and emitter terminal at the input side and V_{CE} is measured with respect to the collector terminal at the output. As previously defined, $V_{BE}, V_{CE} > 0$ since the base-emitter and base-collector junctions are in forward and reverse bias, respectively. In addition, by applying Kirchhoff's laws, $I_E = I_C + I_B$ and $I_C = \alpha_t I_E$, where α_t defines the fraction of the emitter current flowing to the collector. Since $I_B \ll I_C$ then, α_t is close to one. In CE configuration, the base is used as the input and the collector is device's output. By controlling I_B , then I_C is regulated and related to the base current as $I_C = \alpha_t / (1 - \alpha_t) I_B = \beta_t I_B$, where β_t is the current gain of the transistor [299].

InP DHBT transistor characteristics

By calculating and plotting the DC characteristics of a DHBT a useful tool is provided for properly understanding the transistor's DC bias, gain, and power consumption capabilities. As a first step, by assuming that V_{CE} is constant, the input characteristics of the transistors can be extracted by showing the relationship between I_C and V_{BE} . Figure 4.3a) calculates the $I_C - V_{BE}$ characteristic with an exponential behaviour identical to the one of the PN junction in forward bias [300]. For low values of V_{BE} , the depletion region between the base and the emitter does not allow any electrons to flow. Typically a $V_{BE} \approx 0.9$ V is required in order for the depletion region to disappear, leading to the exponential increase of I_C .

Similarly, the output properties are in reference to the behaviour of I_C as a function of V_{CE} for various values of I_B shown in Fig. 4.3b). The curves can be divided into two parts the active region and the saturation. Concerning the saturation part, for low V_{CE} , the voltage of the collector is smaller than the one

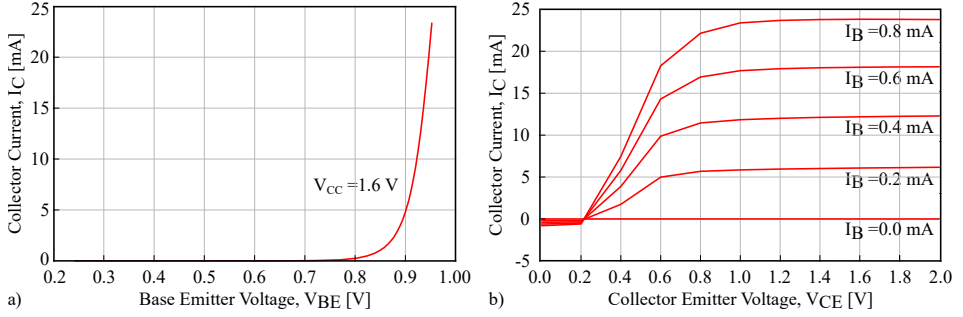


Figure 4.3: The input and output characteristics of a double finger InP/DHBT fabricated at FBH: a) the collector current as a function of base-emitter voltage for $V_{CC} = 1.6$ V following the foundry rules for maximum gain provision by the HBTs; b) the collector current as a function of collector-emitter voltage for various values of I_B .

of the base leading to forward biasing of the collector-base junction. Thus, the electrons of the collector diffuse towards the base, decreasing the total net current. In the active area of the transistor where the base-collector is in reverse bias and $V_{CE} > 0.9$ V, the DHBT provides amplification while I_C is constant independently of the increase of (V_{CE}). In addition, as the base current increases, the collector current also increases proportionally to β_t . In this work, the supply to the collector is equal to $V_C = 1.6$ V and $I_B = 0.6$ mA leading to an $I_C = 18.1$ mA and a gain $\beta_t = 30.2$ [301], [302]. The selected values provide an optimal gain and sufficient thermal stability while guaranteeing that the amplified current would not cause damage in the collector region.

In terms of RF figures of merit, it is important to mention that the cut-off frequency (f_T) equal to 350 GHz defines the point where the short-circuited current gain reaches unity. Moreover, the maximum frequency of oscillation, i.e., $f_{max} = 450$ GHz, provides the value at which the maximum available power gain (MAG) reaches unity [303], [304]. The theoretical curve of MAG simulated within V-band is shown in Fig. 4.4a). In addition, the output power (P_{out}) as a function of the input matched at 50Ω is provided in Fig. 4.4b) at a carrier frequency of 60 GHz with an RF transistor gain of 17.2 dB. The 1 dB compression point (P_{1dB}) where P_{out} decreases by 1 dB from its theoretically expected value ($P_{out,th}$) is at the level of 1.2 dBm for $P_{in} = -15$ dBm [305]. In addition, saturation is reached at an output value of $P_{sat} = 9.2$ dBm. Higher levels of P_{1dB} can be achieved by designing a matching network extracted by load-pull contour calculation techniques while compromising for the transistor gain.

Finally, once multiple transistors synthesise an amplifier, it has to demonstrate unconditional stability indicating a non-oscillatory behaviour for the operating bias and frequency [306]. Amplifier stability can be extracted by the factor K that is an absolute value required to be higher than one [307]. Furthermore, these devices add time delays to the amplified electrical signals affecting their phase.

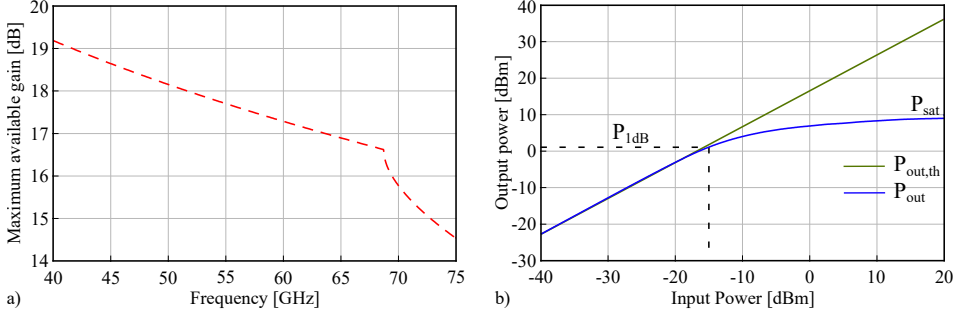


Figure 4.4: RF characteristics of InP/InGaAs double finger DHBTs fabricated at FBH: a) the maximum available gain of the DHBTs simulated in V-band; b) the simulation of the output power (P_{out}) as a function of input (P_{in}) indicating the P_{1dB} and P_{sat} at 60 GHz.

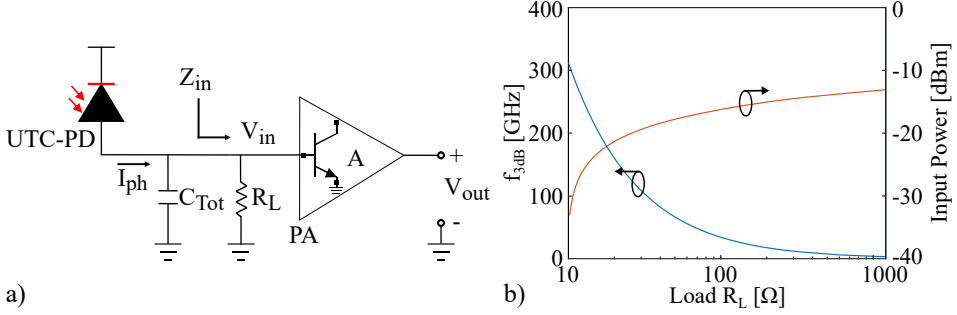


Figure 4.5: a) Optoelectronic conversion including UTC-PDs and power amplifiers with an input load R_L ; b) the influence of the value of R_L on the 3 dB bandwidth and input power to the amplifier (PA) with $C_{Tot} = 51$ fF.

This metric can be derived through the deviation from the linear phase (ϕ_{dev}) identifying the difference between the measured phase and an ideal phase as a function of frequency. Values for ϕ_{dev} ranging within $\pm 15^\circ$ provide a low time jitter [308]. It needs to be underlined that all the characteristics mentioned earlier are considered for the fabrication and synthesis of the mm-wave TIA.

Current to voltage conversion architectures

Once the optoelectronic generation takes place, the photocurrent has to be converted into a voltage signal that its RF power is large enough to be transmitted over the air. Thus, an amplification unit is required to employ the transformation of the mm-wave while also increasing its strength. Figure 4.5a) depicts a simplified architecture of such interconnection where a voltage amplifier with a gain of A (i.e., open-loop gain) is linked to a UTC-PD through a shunt load (R_L) responsi-

ble for the current to voltage conversion [309]. The total input capacitance to the amplifier (C_{Tot}) is the sum of C_j of the UTC-PD, the TML capacitance (C_{TML}) and the input capacitance of the base of the transistor (C_B).

As calculated in Fig. 4.5b) based on Ohm's law, for a high value of R_L , the input powers to the amplifier increase while the amount of thermal noise is minimised since $I_{th} \propto \sqrt{1/R_L}$. However, in that case, the 3 dB bandwidth of this architecture calculated as $f_{3dB} = 1/(2\pi R_L C_{Tot})$ with $C_{Tot} = 51$ fF, decreases significantly once $R_L > 100$. An equaliser can be used in baseband optical communication receivers as a countermeasure at the output of the amplifier enhancing sensitivity at the cost of increasing the systems' complexity [310], [311]. On the other hand, in the case where the circuit noise of the front-end is not a primary concern, a limiting amplifier with low R_L can be linked [312]. However, even with high amplification gain, the low voltage levels at R_L may not provide enough boost at the output of the unit to support applications requiring high signal sensitivity such as baseband optical receivers [313], [314]. Therefore, an amplifier design is required, able to optimally compromise the relationship between gain, noise and f_{3dB} .

4.1.2 The transimpedance amplifier

The transimpedance amplifier is commonly used in optical communication systems requiring broad bandwidth and high sensitivities. A simplified TIA architecture is shown in Fig. 4.6 where a UTC-PD is connected to the input of an amplifier with a negative shunt feedback resistor (R_f) [315]. The TIA circuit is a current to voltage converter receiving the mm-wave signal from the photodiode as current. It then converts it into an amplified voltage to be compatible at the output with equipment that in most cases is designed to be matched to 50Ω . TIAs are more broadband compared to high impedance topologies with the same gain. Moreover, they provide increased sensitivity levels contrary to low impedance amplifiers. TIAs possibly present stability issues and higher noise levels compared to the high R_L amplifiers [316], [317]. Nevertheless, an equalisation circuit is not required, and more elaborate feedback techniques can be implemented to mitigate instability effects [318], [319]. The definitions analysed in these sections provide valuable information on the results obtained in the TIA simulations and measurements.

An important metric defining the crucial aspects of a TIA is the transimpedance gain (Z_T) calculated as the ratio between the output voltage (V_{out}) over the input current (I_{ph}) and can be measured in linear units, i.e., Ω or dB Ω based on Eq. 4.1 [320].

$$Z_T^{lin} = \frac{V_{out}}{I_{ph}}, Z_T = 20 \log\left(\frac{Z_T^{lin}}{1 \Omega}\right) \quad (4.1)$$

The term transimpedance stems from the fact that the current and voltage defining Z_T are measured at two different ports. Furthermore, the input impedance (Z_{in}^{lin}) of the TIA needs to match the output of the UTC-PDs that can be lower

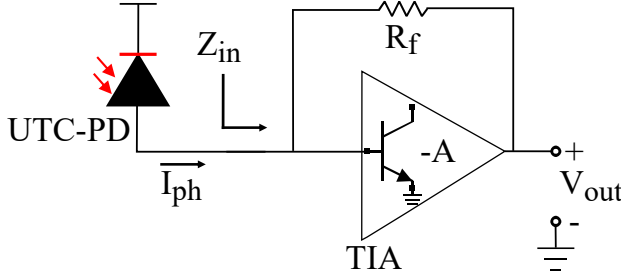


Figure 4.6: An overview of the architecture combining a UTC-PD and a TIA supporting the generation of mm-waves.

than $50\ \Omega$. Based on Fig. 4.6, Z_T^{lin} and Z_{in}^{lin} are calculated in Eq. 4.2 and Eq. 4.3, respectively as:

$$Z_T^{lin} = -\frac{A}{A+1}R_f \quad (4.2)$$

$$Z_{in}^{lin} = -\frac{1}{A}Z_T^{lin} = \frac{R_f}{A+1} \quad (4.3)$$

where A corresponds to the open loop gain amplifier. As shown in Eq. 4.2, while designing such amplifiers, the gain A needs to be optimised in order to maximise the transimpedance. Moreover, high values of A lead to increased Z_T^{lin} and lower Z_{in}^{lin} allowing the impedance matching between the TIA and the UTC-PDs. In the ideal case where A is infinite, Z_T^{lin} depends only on the R_f . However, in terms of the 3dB bandwidth of the TIA, in Eq. 4.4, there is a trade-off between A , C_{Tot} and R_f [321]. For example, with a constant A , low values of the feedback resistor and C_{Tot} lead to increased f_{3dB} .

$$f_{3dB} = \frac{1+A}{2\pi R_f C_{Tot}} \quad (4.4)$$

Therefore, transimpedance amplifiers show increased flexibility in terms of controlling several of their properties. Consequently, depending on the application, these parameters can be selected accordingly. Finally, even though the presented generic model is ideal and not feasible to be applied in actual designs, these equations provide a comprehensive overview of the basic function of TIAs.

Input noise current calculation

Concerning the noise calculations of TIAs, the input-referred noise current is an important metric for this type of amplifier [322], [323]. As illustrated in Fig. 4.7a), this current is defined such that it acts as a noise source to an ideal (noiseless) TIA which is able to reproduce the same noise levels as the actual TIA (including noise) [324]. The input-referred noise current can be measured in three ways:

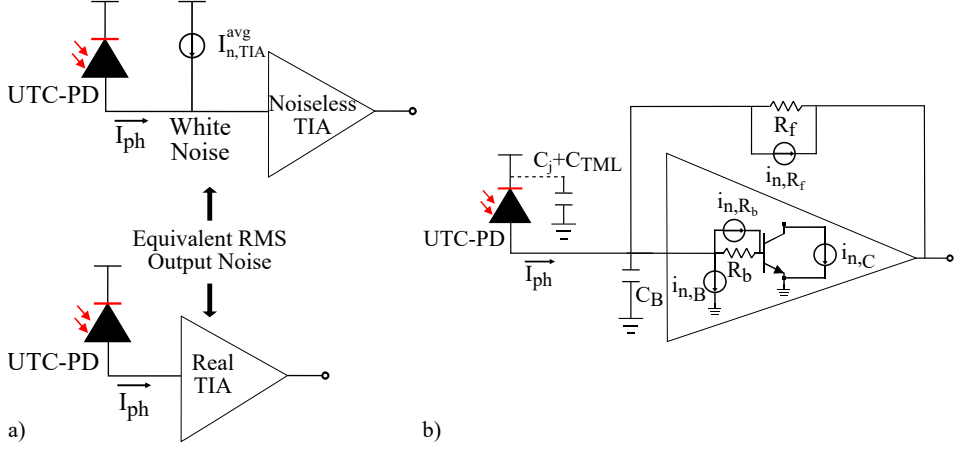


Figure 4.7: a) Definition of the input-referred noise current; b) the noise sources of a TIA that includes HBT transistors.

- *Input-referred noise current power spectral density (PSD).* The PSD ($I_{n,TIA}^2$) of the input-referred noise current measured in pA^2/Hz and the noise current density ($\sqrt{I_{n,TIA}^2}$) in pA/\sqrt{Hz} . As illustrated in Fig. 4.7b), the TIA includes a transistor which acts as the open-loop amplifier in this case and a feedback resistor. There is a multitude of noise sources contributing to $I_{n,TIA}^2$, including the thermal noise of the feedback resistance and the noise currents at the base and collector of the transistor [325], [326]. Therefore, this PSD is not white and it cannot be provided by a single number [327]. A theoretical estimation of $I_{n,TIA}^2$ is given in Eq. 4.5 [328], [329],

$$I_{n,TIA}^2(f) \approx \frac{4kT}{R_f} + \frac{2qI_C}{\beta} + 2qI_C \frac{(2\pi C_{Tot})^2}{g_m^2} f^2 + 4kTR_b (2\pi C_j)^2 f^2 \quad (4.5)$$

including the Boltzmann's constant (k), the equivalent resistance of the base (R_b) and the transconductance of the DHBT (g_m) [330]. As shown in Fig. 4.8a), the $\sqrt{I_{n,TIA}^2}$ consists of a low frequency region described by $1/f$ due to the shot noise in the base and collector [331]; a white noise component and two high frequency (f^2) terms that are directly affected by both $C_{Tot} = C_j + C_{TML} + C_B$ and the junction capacitance of the photodiode that plays an important role on the TIA noise levels [332]. The dependence of C_j to $I_{n,TIA}^2$ is investigated in Fig. 4.8b) for a single-feedback TIA based on Eq. 4.5 with R_f at the level of 205Ω and $\beta = 30.2$, $I_C = 18.1 \text{ mA}$, $g_m = 0.38 \text{ S}$ with $R_b = 40 \Omega$. By increasing C_j , the $I_{n,TIA}^2$ increases exponentially at

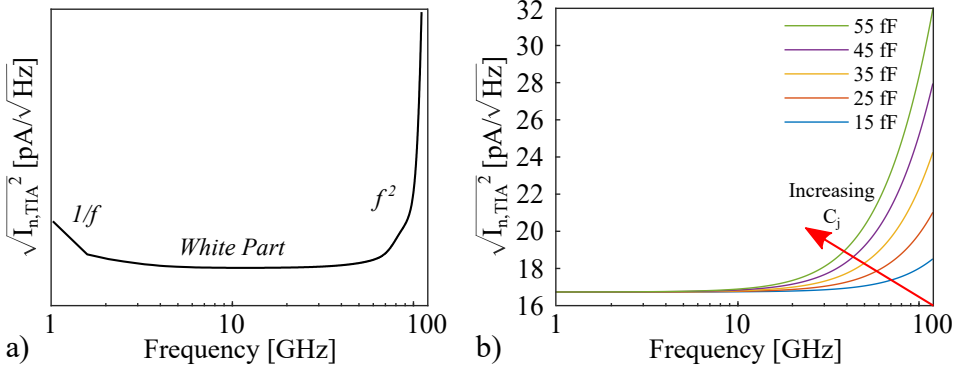


Figure 4.8: a) The typical curve of the noise current spectral density of a TIA; b) the impact of the increasing junction capacitance of a UTC-PD to the PSD noise $\sqrt{I_{n,TIA}^2}$.

higher frequencies. Thus, in the case where a combined module of a UTC-PD and TIA is designed, C_j is required to be as low as possible so that its noise contribution to be minimised.

- *Input-referred RMS noise current.* It is an RMS value ($i_{n,TIA}^{rms}$) given by a single number (in nA or μA) and is extracted from the ratio of the RMS output noise voltage ($v_{n,TIA}^{RMS}$) over the midband transimpedance value of the TIA [333]. The analytical equation is provided in Eq. 4.6,

$$i_{n,TIA}^{RMS} = \frac{1}{Z_T} \sqrt{\int_0^{2\Delta f_1} v_{n,TIA}^{RMS} df} = \frac{1}{Z_T} \sqrt{\int_0^{2\Delta f_1} |Z_T(f)|^2 I_{n,TIA}^2(f) df} \quad (4.6)$$

where the term $\Delta f_1 = \frac{\pi}{2} f_{3dB}$ is the 1st order equivalent noise bandwidth of the TIA and is dependent on the f_{3dB} of the device [334]–[336].

- *Averaged input-referred RMS noise current density.* This noise current definition ($I_{n,TIA}^{Avg}$) is measured in $\text{pA}/\sqrt{\text{Hz}}$ and obtained by the ratio:

$$I_{n,TIA}^{Avg} = \frac{i_{n,TIA}^{rms}}{\sqrt{\Delta f_1}} \quad (4.7)$$

as presented in Fig. 4.7a), it is interpreted as the white noise source that needs to be connected to the input of a noise free TIA in order to reproduce the RMS output voltage noise of the real TIA [337], [338].

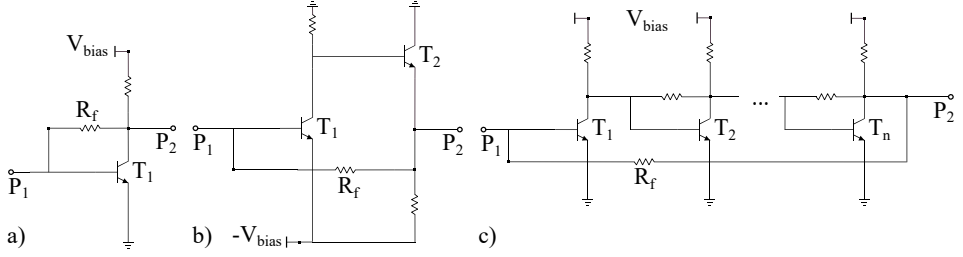


Figure 4.9: Various implementations of shunt-series feedback TIA: a) common-emitter amplifier with feedback resistor (S-TIA); b) emitter follower TIA (EF-TIA); c) multi-stage TIA (MS-TIA).

TIA configurations with shunt resistive feedback

Up to this point, the theoretical demonstrations and calculations concern a general open-loop amplifier with a shunt negative resistive feedback. Figure 4.9 shows three standard shunt-feedback TIA configurations that are widely used namely the single-stage (S-TIA), the emitter follower (EF-TIA) and multi-stage (MS-TIA), respectively [339]–[341].

Moving from the left side to the right of Fig. 4.9, the topologies exhibit higher gain and lower bandwidth while higher values of required R_f result in increased input current noise levels [342]. Moreover, in terms of DC biasing, the MS-TIA needs higher biasing voltage values compared to EF-TIA. Regarding gain and amplifier stability, an S-TIA or an EF-TIA in series with a buffer amplifier are more stable related to an MS-TIA [343], [344]. Therefore, by opting for a compromise between the crucial parameters of a transimpedance amplifier, an EF-TIA linked to a buffer amplifier is chosen to be simulated and fabricated as the interstage amplification unit of the proposed mm-wave transmitter [345]. Finally, the EF-TIA architecture can be modified so that a negative voltage (V_{bias}) to be applied, making the device compatible with the biasing regime of UTC-PDs, promoting the device's co-integration.

4.1.3 Fabrication of an emitter follower TIA

Towards the analysis and design of the proposed TIA, a lot of focus is given to the optimisation of five prominent figures of merit, i.e., broad bandwidth, high transimpedance gain, as well as low values of noise, deviation from linear phase, and dc power consumption [346], [347]. Since the UTC-PDs interconnected to the mm-wave Tx are matched to $50\ \Omega$, the input stage of the TIA is adjusted to match these requirements accordingly with the additional advantage of straightforward characterisation measurements with $50\ \Omega$ devices. However, as previously shown in the theoretical section, Z_{in}^{lin} is a versatile variable and can be adjusted to interface

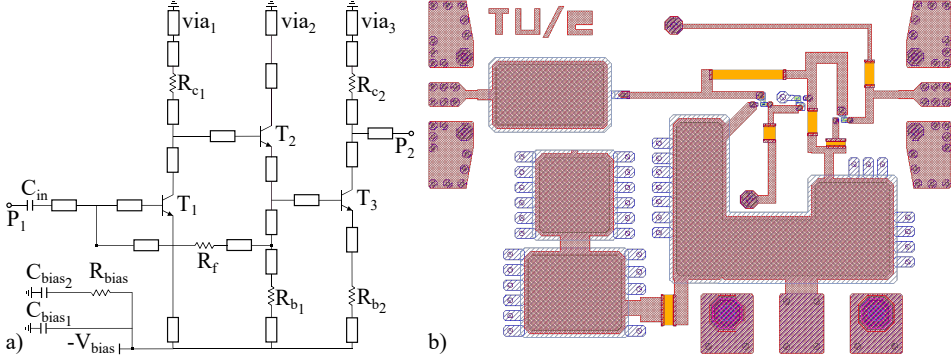


Figure 4.10: An emitter follower TIA linked to a buffer transistor that is synthesised based on the FBH component libraries [348]: a) the TIA equivalent circuit; b) the final TIA layout with a size of $0.51 \times 0.82 \text{ mm}^2$.

the characteristic impedance of various components. The circuit of the fabricated EF-TIA is presented in Fig. 4.10a).

The coupling capacitor (C_{in}) connected at the input port P_1 prohibits the flow of DC current from the UTC-PD towards the TIA, ensuring that the employed transistors are not driven out of their operating point, guaranteeing stability (i.e., $K > 1$). Therefore, the $C_{in} = 3.7 \text{ pF}$ acts as a high pass filter with low cut-off frequency able to effectively eliminate the DC component without significantly affecting the f_{3dB} and MAG of the DHBTs [349]. The transistors T_1 and T_2 are interconnected in the emitter follower implementation within the shunt feedback TIA stage. At the next step, the common-emitter stage transistor T_3 acts as the post-amplifier that further increases the gain and drives the generated mm-wave at the output port P_2 to the transmitting antenna. The resistors R_{b1} , R_{b2} as well as R_{c1} and R_{c2} set the bias voltage for each individual transistor originating from a single bias network consisting of the components R_{bias} , C_{bias1} and C_{bias2} . The feedback resistor (R_f) is tuned to a value of 205Ω providing the optimum trade-off between simulated transimpedance gain and f_{3dB} . Furthermore, by varying the sizes (length, width) of the transmission lines within the design, the f_{3dB} can be increased even further due to inductive peaking [350], [351]. The bias voltage is set to $V_{bias} = -2.3 \text{ V}$ with total current consumption of $I_{DC} = 34 \text{ mA}$ and $P_{DC} = 98 \text{ mW}$. The layout of the fabricated EF-TIA is shown in Fig. 4.10b) with an overall dimension equal to $0.51 \times 0.82 \text{ mm}^2$.

Simulation and measurement results

A uniform transimpedance gain ($Z_T = Z_{21}$) of approximately $55.5 \text{ dB}\Omega$ is obtained from the simulated straight line of Fig. 4.11a) with an f_{3dB} bandwidth of 111 GHz between $1.5 - 112.5 \text{ GHz}$. The measurements are conducted between DC to 67 GHz with a VNA and are presented with the dashed curve. It is observed that the

Table 4.1: EF-TIA component values and biasing characteristics.

Input Capacitor [pF]	C_{in} 3.7	
Feedback resistor [Ω]	R_f 205	
Base resistors [Ω]	R_{b1} 62	R_{b2} 5.1
Collector resistors [Ω]	R_{c1} 28	R_{c2} 63.2
Bias capacitors [pF]	C_{bias1} 10	C_{bias2} 6.9
Bias resistor [Ω]	R_{bias} 7.5	
Bias points	V_{bias} [V] -2.3	I_{DC} [mA] 34

fabricated transistors provide less gain compared to the expected values leading to lower Z_T , limiting the total bandwidth. That implementation penalty between the actual measurements and simulations may be due to the fabrication tolerance in the cleanroom. In addition, the abrupt drop of the Z_T curve can also be caused by a potential inaccurate transfer of an element of the TIA (e.g., in terms of size) between the circuit design and the layout that may have enhanced the reported gain issue. Nevertheless, within the measured frequencies in V-band (40–67 GHz), Z_T decreases between from 50.3 to 48.5 dB Ω ensuring amplification of the generated mm-wave photocurrents. Furthermore, as it is also presented, within the bandwidth of interest, a low deviation from the linear phase (ϕ_{dev}) ranging between $\pm 2.5^\circ$ minimises the phase instability added to the waveforms.

The limited transistor gain is also imprinted on the S-parameter measurements of Fig. 4.11b). The average deviation between measured and simulated $|S_{21}|$ is equal to 5 dB. However, the $|S_{21}|$ curve is quite uniform for the measured frequencies while the reflection parameters S_{11} and S_{22} remain below -10 dB. Furthermore, the simulated S_{11} starts increasing above 87 GHz reaching a value of -5.7 dB at 113 GHz. Based on the experimental data, the extracted stability factor is equal to values ranging above $K > 10$ indicating the unconditional stability of the amplifier between 1.5 – 67 GHz. It needs to be mentioned that S_{12} is below -40 dB and thus it is not included in the figure. In theory, a simulated $P_{1dB} = 4.2$ dBm at $P_{in} = -9.5$ dBm is acquired with $P_{sat} = 7$ dBm. Nonetheless, the data on DC biasing of the TIA in Fig. 4.11c) show a mean DC input current difference of 6 mA underlining that the 1 dB compression and saturation powers are expected to be lower. This DC current value variation also affects the f_{3dB} .

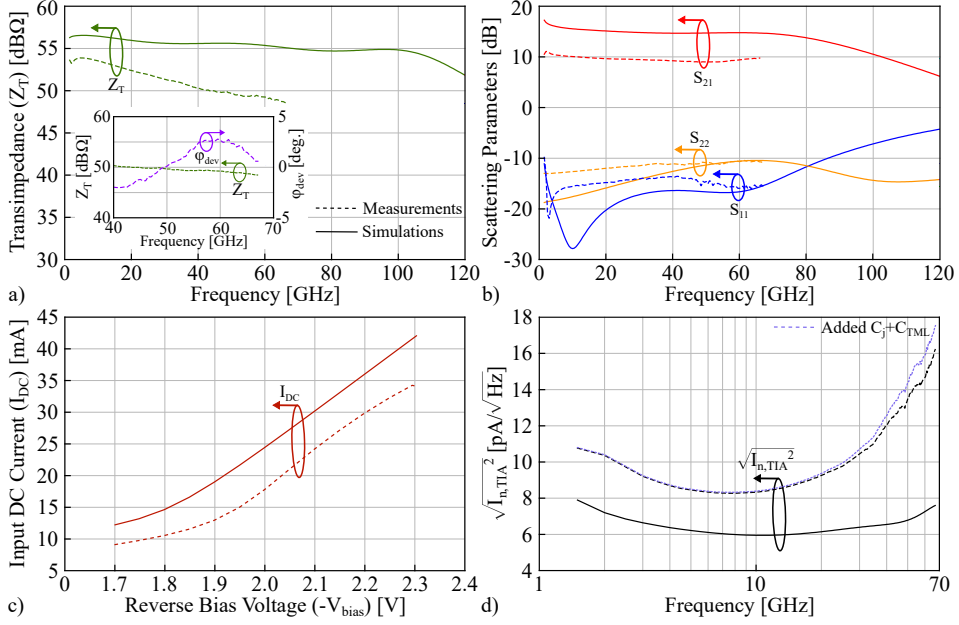


Figure 4.11: The simulated (straight lines) and measured data (dashed lines) of an emitter follower TIA linked to a buffer transistor: a) the transimpedance of the fabricated TIA as a function of frequency including the deviation from linear phase (ϕ_{dev}) in V-band (40 – 67 GHz); b) the S-parameter information of the EF-TIA; c) the DC current (I_{DC}) as a function of the reverse bias applied at the biasing network (V_{bias}); d) the spectral noise current density of the TIA including the added negative impact of an additional shunt capacitive element.

For future characterisation measurements, a power analysis of the fabricated TIA will pinpoint the exact P_{sat} and P_{1dB} .

The values of input noise current need to be approximated (between 40 to 67 GHz) since, at the point where the chip characterisation processes were conducted, such a current noise measurement setup was not available. Therefore, the Eq. 4.6 and Eq. 4.7 are applied using the simulated and measured Z_T while the $I_{n,TIA}^2$ stems from the very accurate transistor simulation models of FBH. Figure 4.11d) shows that the measured noise current spectral density is shifted upwards compared to the simulated results. Moreover, the $i_{n,TIA}^{RMS} = 3.3 \mu A$ and $I_{n,TIA}^{Avg} = 16.1 pA/\sqrt{Hz}$ extracted from the measured scattering parameters are higher by $6.3 pA/\sqrt{Hz}$ and $0.9 \mu A$, from the simulations, respectively. Furthermore, in Fig. 4.11d) the impact of shunting a 36 fF capacitor to the EF-TIA (i.e., $C_j = 15 fF$, $C_{TML} = 21 fF$) is approximated with the violet dashed line confirming the effect of noise increase and the calculations performed in the theoretical part of this section. As previously underlined, the obtained discrepancies between

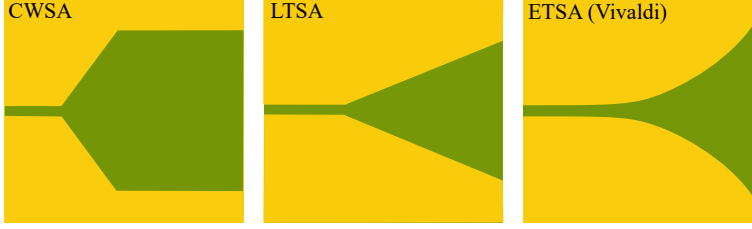


Figure 4.12: Various types of tapered slot antennas.

measurements and simulations may be due to the possible errors in the fabrication process [352]. On the other hand, even though higher than expected, the noise input current values are comparable with TIA circuit implementations in literature [353]–[355].

While improvements can be achieved in future designs in terms of gain and input noise current, this fabricated TIA can be interconnected with the first generation of the mm-wave Tx. Thus, a sufficient amount of amplification can be provided to the mm-waves supporting the planar integrated antenna that transmits the 5G based waves over the air towards the wireless end-users.

4.2 A photonics-enabled V-band Vivaldi antenna

Tapered slot antennas (TSAs) integrated on copper laminated materials (e.g., PCB) have planar geometries and end-fire radiation. At the same time, they are easy and low-cost to fabricate, allowing their mass production [356]. As illustrated in Fig. 4.12, the common types of TSAs are constant width (CWSAs), linear (LTSA), and nonlinear taper slot antennas including the exponential TSAs (ETSA) [357]. While TSAs have similar radiation mechanisms (i.e., radiation parallel to substrate material), each type has specific advantages for selecting depending on the application. Moving from left to right of Fig. 4.12, the beamwidth and bandwidth become higher while the opposite trend occurs for the sidelobe level suppression and size [358], [359]. Thus, a broadband ETSA design with high gain is the optimum choice promoting the device miniaturisation, which is one of the goals in this work. The exponentially tapered slot antenna, i.e., Vivaldi antenna has predominant radiation characteristics such as low side lobes, high gain and constant beamwidth over an ultra-wide bandwidth [360].

This section presents the fabrication and experimental measurements of a V-band Vivaldi antenna that can be interconnected with a photonics-enabled mm-wave transmitter within the future remote units. Initially, the permitted substrate thicknesses allowing the seamless operation of a planar antenna in V-band are extracted. Then, a mode converter enables the transition of the electric field from coplanar to slotline feeding the antenna. In order to increase the antenna gain

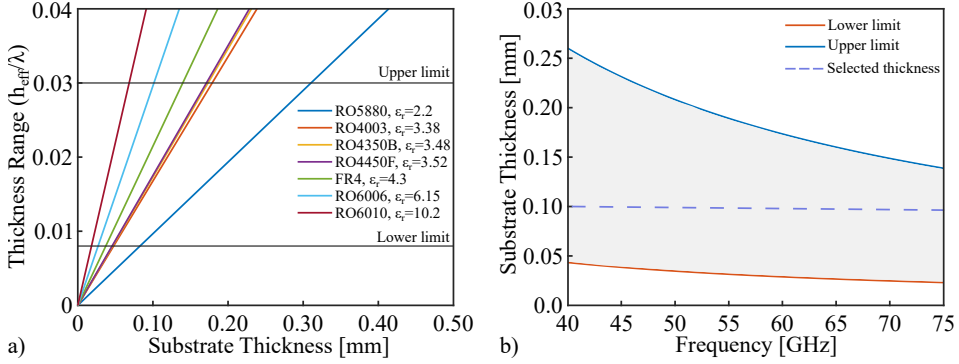


Figure 4.13: a) Dielectric substrate thickness range (h_{eff}/λ) calculation for various materials at a carrier of 60 GHz [361]–[364]; b) acceptable PCB thickness range for a TSA formed over a RO4350B dielectric material operating in V-band.

levels, a comb structure inspired by integrated optical grating couplers is designed. Finally, the simulation and measurement results are compared, resulting in good agreement verifying its ability to play an essential role in the mm-wave wireless transmission within the beyond-5G remote units. The antenna design, simulations, experimental processes and results covered in this section are discussed in [C6].

4.2.1 The antenna structure

Tapered slot antennas are shaped by applying slot etching techniques over a dielectric material. Electric field waves propagate between the gradually widened metal slots of the component enabling end-fire radiation in parallel the dielectric substrate. The operation of a TSA on PCB is affected by its thickness linked to the electrical effective thickness $h_{eff} = h(\sqrt{\epsilon_r} - 1)$. The optimal range of substrate thickness (h) guaranteeing the good operation of a TSA is based on the experimental approximation in [356], provided in Eq. (4.8).

$$0.005 \leq \frac{h_{eff}}{\lambda} \leq 0.03 \Rightarrow \frac{0.005\lambda}{\sqrt{\epsilon_r} - 1} \leq h \leq \frac{0.03\lambda}{\sqrt{\epsilon_r} - 1} \quad (4.8)$$

If h_{eff}/λ is below the minimum point, it is observed that the beamwidth of the main radiation lobe is increased, leading to lower antenna directivity, while if it exceeds the maximum, then unwanted substrate modes may propagate causing performance degradation of the TSA. The ratio h_{eff}/λ is calculated in Fig. 4.13a) for different substrates at the carrier frequency of 60 GHz allowing the choice of the material based on the commercially available thicknesses. By taking into account the extracted results, Rogers 4350B ($\epsilon_r = 3.48$) is selected for the antenna design. This dielectric is characterised by its ceramic reinforcement enabling bond-wire interconnections between the antenna and the optoelectronics while preventing

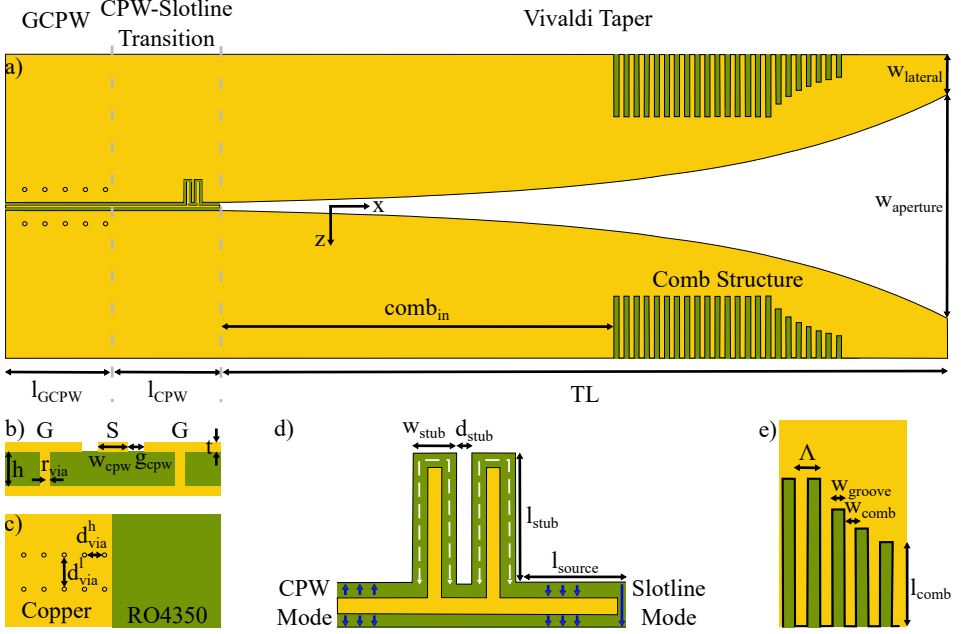


Figure 4.14: A V-band Vivaldi antenna fabricated on RO4350B: a) top view of the structure; b) cross section of the GCPW; c) the bottom of the design; d) the CPW to slotline transition; e) the comb structure enhancing the directivity of the antenna.

the potential bending of the fabricated component. At a further step, Fig. 4.13b) provides the recommended substrate thickness limits for designing planar RF antennas on RO4350B within V-band. A laminate thickness h of 0.1 mm is chosen for the integrated antenna design complying with both upper and lower limits of Eq. 4.8 while covering the whole band.

Significant improvement in terms of narrowing the main beam as well as reducing the side lobe level can be achieved once the substrate within the antenna taper is partially or totally removed [365]. Therefore, a high precision laser is used to remove the substrate inside the tapered slot, as shown in Fig. 4.14a). The final Vivaldi antenna design can be optimised for various frequency bands and mainly consists of four parts: a grounded coplanar-waveguide (GCPW), a coplanar-waveguide (CPW) to slotline transition, the Vivaldi taper and a comb structure for gain enhancement.

Grounded coplanar-waveguide

The input of the antenna in Fig. 4.14b) includes a GCPW with a signal trace width of w_{CPW} and gap width g_{CPW} . It is a uni-planar structure with both the signal and ground conductors on the same side of the substrate, allowing various

devices to be easily mounted in a series configuration on the GCPW. As depicted in Fig. 4.14c), the antenna structure includes plated through vias in order to connect to the ground plane on the backside of the PCB, which also serves as a heatsink [366]. The vias are placed close to the gaps of the GCPW suppressing the parallel plate modes [367]. Their plating thickness, dimensions and distribution ($t_{plating}$, r_{via} , d_{via}^l , d_{via}^h) comply with the relevant manufacturing design rules.

To fit the size of the input of the planar antenna with the small GSG pad dimensions of the integrated mm-wave amplifier, the values of the signal trace and gap have to reach the minimum allowed PCB fabrication limits. Therefore, the feed-point impedance to the antenna is equal to $70\ \Omega$, increasing reflections when interconnecting with $50\ \Omega$ matched devices. This effect is taken into account in the design optimisation processes so that the reflection coefficient of the antenna remains below -10 dB within V-band. Thus, in the following sections, the design values of all the components presented in Fig. 4.14 are finely tuned so that the Vivaldi antenna is matched within the desired band of operation [368]–[371].

CPW to slotline transition

As previously mentioned, for the application showcased in Fig. 4.1, the Vivaldi antenna must be connected to electronic devices with a CPW interface. This is an incompatibility issue that needs to be addressed since the Vivaldi antenna tapers have slotline inputs. Therefore, a CPW to slotline converter is required to provide a smooth transition between these two different types of transmission lines. Thus, as shown in Fig. 4.14d), the GCPW is followed by a CPW leading to a balun that adds a 180° phase shift to the upper slot of the antenna (negative z direction) [372]. This is achieved by increasing the total relative path difference of the two slot modes by $\lambda_{eff}/2$. The effective wavelength (λ_{eff}) is calculated in Eq. (4.9).

$$\lambda_{eff} \approx \frac{\lambda_0}{\sqrt{\epsilon_{eff}}}, \epsilon_{eff} \approx \frac{\epsilon_r + 1}{2} \quad (4.9)$$

The designed CPW to slotline transition in Fig. 4.14d) has two stubs with a length of $\lambda_{eff}/8$ each, converting the CPW modes at the input to slotline modes allowing them to propagate within the Vivaldi taper [373]. The transition is designed to achieve a maximum conversion at $f_0 = 60$ GHz. The parameters of this structure such as the stub length (l_{stub}), source length (l_{source}), stub width (w_{stub}) and distance between stubs (d_{stub}) are optimised to achieve the results of Fig. 4.15. Figure 4.15a) illustrates the phase shifting by 180° of the upper slot modes at 60 GHz so that they are in the same phase with the lower slot at the output of the transition (i.e., arrows of both gaps point in the same direction). Furthermore, Fig. 4.15b) shows the simulated scattering parameters of the coplanar modes (S_{21}^{cc}) to slotline (S_{21}^{cs}) [374]. The goal is to maximise S_{21}^{cs} while minimising S_{21}^{cc} at frequencies around f_0 while guaranteeing low levels of S_{11}^{cc} , i.e., $S_{11}^{cc} < 10$ dB. The simulation results are normalised to a $50\ \Omega$ input impedance.

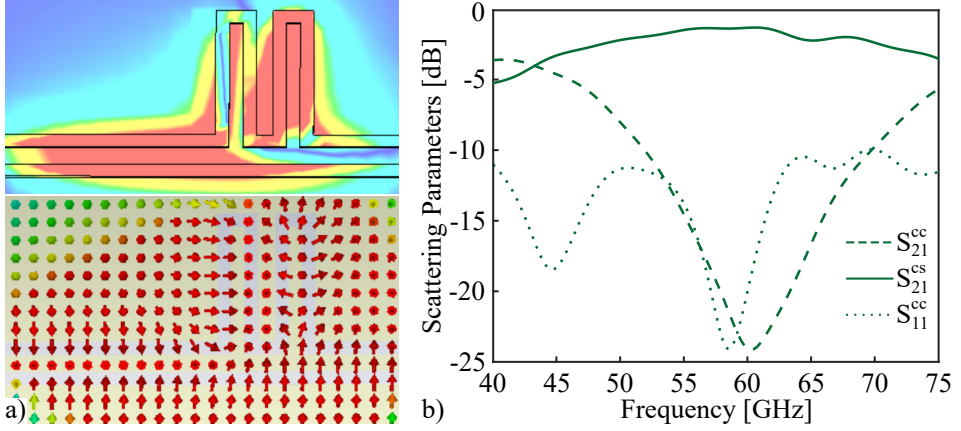


Figure 4.15: Simulation results for a CPW to slotline transition based on two stubs: a) the simulated electric field including the absolute value (upper) as well as the phase (lower) in form of arrows showcasing the 180° phase shift of the upper slot modes at 60 GHz at the output of the transition; b) scattering parameter results including the calculated transmission and reflection of the CPW modes (S_{21}^{cc} , S_{11}^{cc}) as well as the CPW to slotline conversion (S_{21}^{cs}).

The Vivaldi taper

This type of antenna is characterised by a very broad bandwidth [375], [376]. Its slotline width varies progressively, and thus for a given frequency, only a fraction of the metal taper efficiently radiates, contributing to the broadband properties of this design. The equations determining the exponential tapering of the Vivaldi antenna are given by [377]:

$$\begin{aligned}
 z(x) &= A_1 e^{rx} + A_2 \\
 A_1 &= \frac{1}{2} \frac{w_{aperture} - (w_{CPW} + 2g_{CPW})}{e^{-rTL} - 1} \\
 A_2 &= \frac{1}{2} \frac{(w_{CPW} + 2g_{CPW})e^{-rTL} - w_{aperture}}{e^{-rTL} - 1}
 \end{aligned} \tag{4.10}$$

where $(w_{CPW} + 2g_{CPW})$ is equivalent to the initial width of the antenna aperture, i.e., the slotline. Moreover, TL and $w_{aperture}$ correspond to the length and width at the end of the aperture approximated as $3.6\lambda_0$ and $1.1\lambda_0$, respectively (Fig. 4.14). These parameters need to be carefully selected since they decisively affect the directivity and the sidelobe levels of the design. Furthermore, r is the aperture rate of the exponential profile of the Vivaldi, which is a crucial element regulating its gain, beamwidth and operation bandwidth.

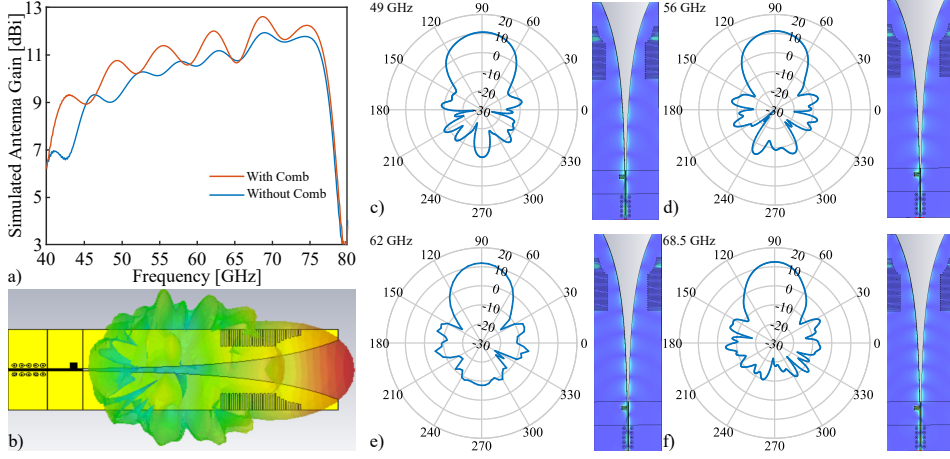


Figure 4.16: Gain simulations of the Vivaldi antenna: a) Realised gain comparison between the antenna designed with and without a comb structure; b) 3D far field radiation pattern of Vivaldi antenna at 68.5 GHz where the maximum gain is achieved; the simulated radiation patterns and electric fields of the antenna captured at frequencies that correspond to the peaks of the red gain curve at c) 49 GHz, d) 55.5 GHz, e) 62 GHz, f) 68.5 GHz, where the electric field modes are efficiently blocked by the comb improving the antenna directivity.

The comb structure

To extend the lower end frequency of operation and increase the gain of the antenna, the comb structure of Fig. 4.14 e) includes multiple quarter-wave transformers added to the Vivaldi taper [378]. This blocks electric field modes that may propagate along the edge of the PCB, improving the impedance match and directivity across a large frequency band [379].

The comb structure in this work is inspired by optical grating couplers with varying apodised gratings [380], [381]. The grating period ($\Lambda = w_{comb} + w_{groove}$) and the fill factor ($FF = w_{comb}/\Lambda$) are constant following the PCB manufacturer's guidelines [382]. Within the total number of comb lines (N_{tot}) there is a number of lines (N_d) at the beginning that have a constant length ($\lambda_d/4$) while the rest have a parabolic length decrease. The wavelength λ_d corresponds to a frequency of 49.5 GHz which is the point where the conversion parameter S_{21}^{cs} is simulated to have a magnitude above -2 dB. Moreover, the input position of the comb on the taper ($comb_{in}$), as well as the parameters N_d and N_{tot} are optimised such that the gain is increased while keeping the magnitude of the input reflection coefficient at a minimum.

The realised gain improvement by adding the comb comparing to the same design without it is shown in Fig. 4.16 a). The red line remains above the blue for almost all simulated frequencies while the impact of the comb lines appears as

Table 4.2: Antenna characteristics and dimensions measured in [mm].

Rogers 4350	ϵ_r 3.48	ϵ_{eff} 2.24	h 0.1	t 0.02
GCPW/CPW	w_{CPW} 0.075	g_{CPW} 0.06	l_{GCPW} 2.8	l_{CPW} 2.5
Vias	$t_{plating}$ 0.01	r_{via} 0.05	d_{via}^h 0.4	d_{via}^l 0.75
CPW to Slotline	w_{stub} 0.18	d_{stub} 0.075	l_{stub} 0.5	l_{source} 0.45
Comb	w_{comb} 0.125	d_{comb} 0.125	l_{comb}^{min} 0.55	l_{comb}^{max} 1.53
Vivaldi taper	r 0.186	TL 18.1	$w_{lateral}$ 1.0	$w_{aperture}$ 5.52

peaks on the curve, providing for each peak a gain improvement approximated to be equal to 1 dB. In a future design, an increased variation of stub lengths will allow further flattening and decrease the gain variations calculated on the red curve. The three dimensional radiation pattern at 68.5 GHz is provided in Fig. 4.16 b) where the maximum gain is extracted. In addition, the radiation patterns and electric field distribution on the device are calculated in Fig. 4.16 c)–e) corresponding to the four main peaks of the red gain curve. In all the electric field measurements, the impact of adding the comb lines can be observed. An ultra-wide 3 dB gain bandwidth of 30.5 GHz is simulated between 46.9 to 77.4 GHz covering a major part of V-band with a maximum gain of 12.6 dBi at 68 GHz. The final antenna dimensions are provided in Tab. 4.2 where all values except for the constants (ϵ_r , ϵ_{eff} , r) are measured in [mm].

4.2.2 Antenna measurement results

Figure 4.17a,b) show the measurement setup for the characterisation of the antenna prototypes. On a probe station, two antenna copies are placed on top of metallic chucks at a distance L . High frequency absorbers are placed on the table between the antennas to decrease the amount of additional reflections. The electronic microscope supports the placement of the devices so that only the GCPW is on top of the metal chuck. Furthermore, due to the suction provided by the chucks, the components are stabilised. The ports of an Agilent E8361A vector network analyser (VNA) operating at frequencies up to 67 GHz are connected through RF cables with two high frequency GSG probes that are landed on the Vivaldi antennas. The VNA was calibrated using two single port calibrations entailing *open*, *short* and *load* standards on a calibration substrate of the probe vendor, but without *thru* calibration to avoid issues due to the movement of the cables. Therefore,

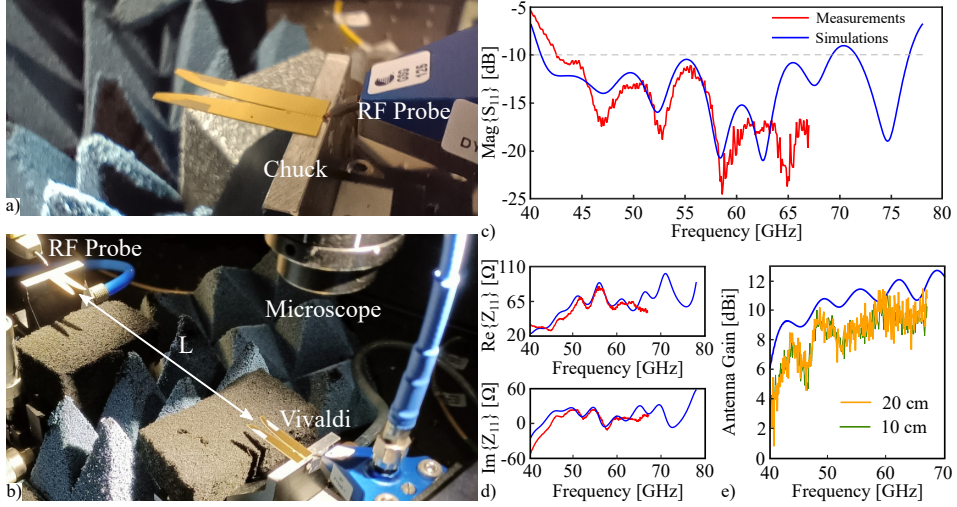


Figure 4.17: a) The GSG probe landing at the input of the device; b) the total experimental setup measuring reflection coefficients and gain; the experimental results extracted from a fabricated Vivaldi antenna: c) the reflection coefficient parameters; d) the real and imaginary part of the input impedance; e) the gain measurement approximation.

this allows for reflection coefficient measurements and gain approximation.

Figures 4.17 c) and d) calculate the reflection coefficient measurements of the antenna as well as the real and imaginary parts of the input impedance. The simulation results are also given in the graph up to 78 GHz to provide a reference. The measurement and simulations show good agreement. The differences may be caused by the imprecise placement of the antenna on the metallic chuck leading to distortions on the reflection coefficient properties of the CPW to slotline transition. Furthermore, errors stemming from non-ideal high frequency calibration and potential asymmetric physical contact of the GSG probe on the GCPW need to be considered while evaluating the measurements.

Since no *thru* calibration is available, the gain of the antennas is approximated. Therefore, during this process, the transmission parameters of the total system (S_{21}^{full}) are obtained for two antenna distances L (10 and 20 cm) without applying calibration. This measurement includes cable and probe losses (S_{21}^{loss}), the wireless channel free space path loss (FSPL) and the combined gain (G) of the two identical antennas. Then, the two probes are put close and in contact with a *thru* transmission line of the calibration substrate. Thus, a non-calibrated *thru* transmission measurement provides information on S_{21}^{loss} . At a further step, by de-embedding the losses of the *thru* line (1 dB), the S_{21}^{loss} as well as the free space path loss from S_{21}^{full} and dividing by two, the gain approximation for a single antenna can be provided in Fig. 4.17 e). It is observed that at both distances, the curves follow the same pattern with a maximum gain measured to be equal

to 10.6 dBi at 60 GHz. The impact of the gain curve ripples mainly stemming from the uncalibrated S_{21}^{full} response cause deviation from the linear phase that may affect a wideband communication system. However, this impairment can be compensated by DSP through signal equalization applying channel estimation and compensation techniques at the side of the wireless receiver. It should be noted that this is a rough estimation since there may have been additional reflections, antenna misalignment and errors in the calculations that are not taken into account. Further verification and accurate analysis of the radiation patterns of the Vivaldi antenna would require measurements in an anechoic chamber.

Therefore, ultra-wideband characteristics are achieved with a 3 dB gain bandwidth of 30.5 GHz, helped by a comb structure along the edge of the antenna. A maximum simulated gain of 12.6 dBi is achieved, compensating for the high path losses in mm-wave frequencies and especially in the unlicensed V-band. Measurements of the reflection coefficient and gain of the antenna are consistent with the simulations, showing that it can be a viable solution to be embedded within the future remote units supporting increased numbers of 5G end-users.

4.3 Active component interconnection

So far, the integrated broadband RF components providing the generation, amplification and wireless transmission over the air have been presented. The next step towards the assembly of the mm-wave transmitter is the study of the RF interconnection between the active components, i.e., the UTC-PD and the TIA. Thus, the design and measurement of a V-band RF choke for DC biasing of the photodiode will be presented.

4.3.1 RF choke design

In order to guarantee the reverse bias provision to the UTC-PD, an additional connection is essential to tap into the RF path towards the TIA. However, such a process will cause leakage of the mm-wave in the direction of the DC input. Therefore, a structure on PCB delivering the bias voltage to the photodiode while not allowing the high frequency waveforms to be diverted is required [383].

This is accomplished by synthesising the three-port GCPW-based RF choke of Fig. 4.18. Theoretically, within the DC path of the device, a parallel $\lambda_0/4$ open circuit stub is added for each slot of the GCPW leading to a virtual RF short circuit that is then transformed to an open by a quarter-wave transformer optimised to operate in V-band [384], [385]. In addition, the metal-plated vias are placed close to the gap of the GCPW as well as around the periphery of the RF stubs on the DC path following the PCB manufacturer's rules.

Similar to the Vivaldi antenna, the thickness and substrate properties of the final design are based on Rogers 4350b with laminate thickness h of 0.1 mm. The RF signal trace and gap widths have the same sizes as the ones of the antenna in

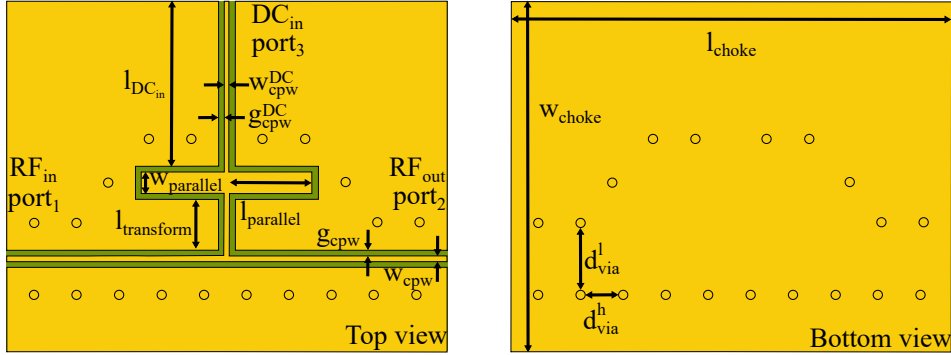


Figure 4.18: A V-band RF choke fabricated on RO4350B: a) top view of the structure; b) the bottom of the design.

Table 4.3: RF choke characteristics and dimensions measured in [mm].

Rogers 4350	ϵ_r 3.48	ϵ_{eff} 2.24	h 0.1	t 0.02
GCPW	w_{CPW} 0.075	g_{CPW} 0.06	w_{GCPW}^{DC} 0.06	g_{CPW}^{DC} 0.06
Vias	$t_{plating}$ 0.01	r_{via} 0.05	d_{via}^h 0.4	d_{via}^l 0.75
DC Path	l_{DCin} 2.0	$l_{transform}$ 0.61	$w_{parallel}$ 0.21	$l_{parallel}$ 0.92
Dimensions	l_{choke} 5.18		w_{choke} 4.14	

order to approach the GSG pad dimensions of both the UTC-PD and the TIA. The parameters of this structure reported in Tab. 4.3, such as the length of the DC input (l_{DCin}), length and width of the parallel stubs ($l_{stub}, w_{parallel}$), as well as the quarter-wave transformer length ($l_{transform}$) are adjusted to provide maximum isolation towards the DC in frequencies around 60 GHz.

Simulation results

The RF choke simulations of the scattering parameters are calculated in Fig. 4.19a) reporting the insertion loss ($-S_{21}$), return loss ($-S_{11}$) and RF isolation ($-S_{31}$) of the module. Due to the symmetry of the design $S_{11} = S_{22}$ and $S_{31} = S_{32}$. It can be observed that the insertion losses vary between 2 to 1.3 dB while the return losses remain higher than 10 dB (i.e., $S_{11} < -10$ dB) above 53 GHz. In addition, the isolation towards the DC port ranges above 25 dB between 53 to 68.5 GHz,

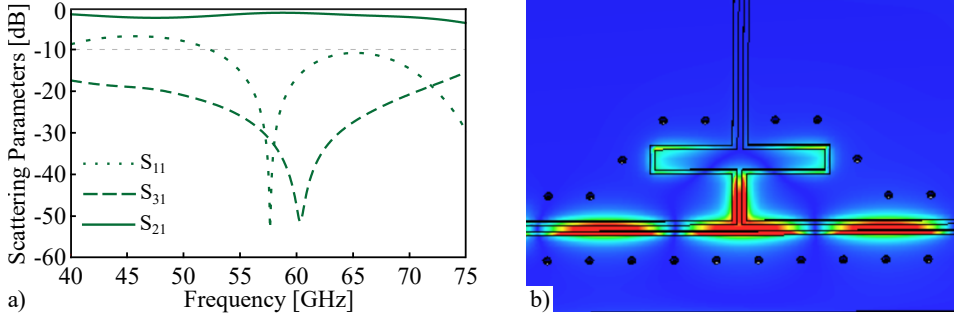


Figure 4.19: Simulation results of the RF choke with $50\ \Omega$ matched ports: a) transmission, isolation and reflection parameters within V-band; b) the simulated electric field showing isolation towards the DC input at 60 GHz.

reaching a maximum at 60 GHz where the DC line is virtually invisible to the mm-waves generated by the photodiode. Moreover, this observation is verified by the simulation of the electric field in Fig. 4.19b) where the propagating waveform is confined within the RF path of the structure.

Measurement processes

As demonstrated with the Vivaldi antenna measurements, once the design is fabricated, it is placed on the probe station and connected to the VNA. The two high frequency GSG probes land on two ports of the choke, and scattering parameter measurements are conducted. During the measurement, the VNA calibration is based on the commercial wafer substrate where the standards applied are open, short, load and thru (OSLT). The OSLT calibration technique moves the measurements reference plane to the tip of the microwave probes enabling the direct extraction of the S-parameters of the RF choke.

In addition, scattering parameters are acquired between the two RF ports as well as of each RF port with the DC input. However, since for all measurements, one of the three ports had to remain open, the simulations are also repeated for frequencies up to 67 GHz in accordance with the same measurement regime. Figure 4.20 shows that the simulations and measurements are in good agreement. The device is matched, i.e., $S_{11} < -10\text{ dB}$ for frequencies between 55 to 65 GHz while the RF isolation in the DC path is above 25 dB for the same frequency band. The RF transmission losses remain below 2 dB for the corresponding bandwidth with the minimum difference between measurements and simulations reaching 0.4 dB at 60 GHz.

The described processes leading to this biasing design on PCB are versatile, and once the presented parameters are modified, it can be applied in various frequency bands. The fabricated RF choke provides a 10 GHz RF isolation corresponding to a bandwidth higher than 10% of the carrier frequency (i.e., 60 GHz). Even though,

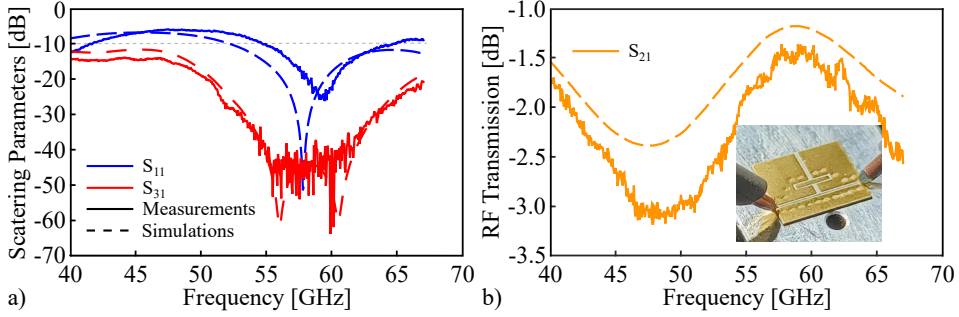


Figure 4.20: VNA measurements and simulations of the fabricated RF choke: a) reflection (DC port open) and RF isolation towards the DC path (RF output port open); b) RF transmission parameters (DC port open).

while co-integrated, the component partially limits the broadband capabilities of the rest of the presented devices, it still shows promising potential for biasing the UTC-PD within the mm-wave wireless transmitter.

4.4 Summary

Once optoelectronic conversion takes place, and the mm-waves are generated, additional high-frequency devices are required to successfully realise the wireless signal propagation towards the 5G end-users. Therefore, in this Chapter, three broadband RF components have been studied and discussed allowing the amplification and transmission of mm-waves while enabling a low RF loss bias provision to the UTC photodiodes.

As a first step, the beneficial aspects of including an amplification stage to the device is discussed by describing the physical concepts of NPN InP/InGaAs DHBTs. Then, the advantages of interfacing optoelectronic components with TIAs compared to various amplifier architectures are analysed. Definitions such as transimpedance gain and input noise current are studied since these derivations are applied to the modelled amplifier. An emitter-follower TIA able to offer a compromise between gain, bandwidth and noise is designed and fabricated. Despite the implementation penalty between the simulations and measurements, the gain ($Z_T = 50 \text{ dB}\Omega$) of the EF-TIA will significantly contribute to the amplification of the mm-waves compensating for the high FSPL occurring in the V-band.

In the following section, a Vivaldi antenna design for beyond-5G base station applications operating within V-band is demonstrated. This device can be used for interfacing with radio-over-fibre links and optoelectronic components through a coplanar waveguide to slotline transition. Simulations show end-fire radiation with a 3dB gain bandwidth ranging between 46.9-77.4 GHz combined with the reflection coefficients remaining below -10 dB for the same frequency range. A comb

structure inspired by optical grating couplers is added, providing an increased maximum gain of 12.6 dBi at 68.5 GHz. Measurement results validate the promising characteristics of the planar antenna. Furthermore, the Chapter presents an RF choke interconnected between the UTC-PD and the TIA based on the same type of substrate as the one of the antenna. Simulation and measurement results reveal that the device is centred at 60 GHz with a bandwidth of 10 GHz enabling the biasing of the UTC-PD while it prevents RF signal loss towards the DC path.

Ground-signal-ground pads interface with the input and output ports of the TIA and UTC-PD. Thus, the designed RF choke and antenna follow the same configuration approaching the sizes of the active devices that despite the impedance mismatch, the S_{11} remains below -10 dB for a considerable segment of V-band based on component parameter optimisation mitigating for this impediment. Consequently, since all the presented individual integrated structures in Fig. 4.1 are fabricated and measured, the interconnection processes are required to be investigated, leading to the realisation of the mm-wave transmitter.

Research Question:

What processes need to be followed in order to co-integrate the UTC-PD with the broadband RF components in a single module ?

A broadband, highly integrated, hybrid photonic-wireless mm-wave transmitter module

In Chapters 3 and 4, the characteristics and properties of a UTC-PD, an RF choke, an EF-TIA and a Vivaldi antenna targeting the optoelectronic conversion, amplification and transmission of mm-waves in V-band were analysed. Therefore, as a next step, the co-integration of all individual components in a single module is proposed, and a full design is provided. This process initially requires the investigation of techniques for device interconnection and the provision of bias stability. Thus, the properties of various wirebonding methods and high-frequency noise bypassing are briefly discussed. Then, the design of a PCB network biasing the UTC-PD and EF-TIA while defining the position of all components is described. A metal plate in the bottom of this architecture acts as the ground reference and common link for all chips.

Once all the components are attached through conductive adhesives to the base of the mm-wave transmitter, their interconnection through wirebonding will be investigated. The amount of RF and DC wirebonds is listed, and an approximation of their lengths and equivalent inductances is extracted. Moreover, suggestions on improving the final design of the co-integrated system on-chip are provided. As a final step, two experimental setups are proposed that primarily allow the small-signal characterisation of the assembly and then verify its ability to be embedded within a 5G system. That is achieved through an experimental photonic-wireless mm-wave link transmitting 5G waveforms in a simplified optical back-to-back regime (i.e., without including the optical fibre). Therefore, this Chapter showcases a complete and compact solution for combining high-speed photonics and electronics supporting future broadband high-frequency applications.

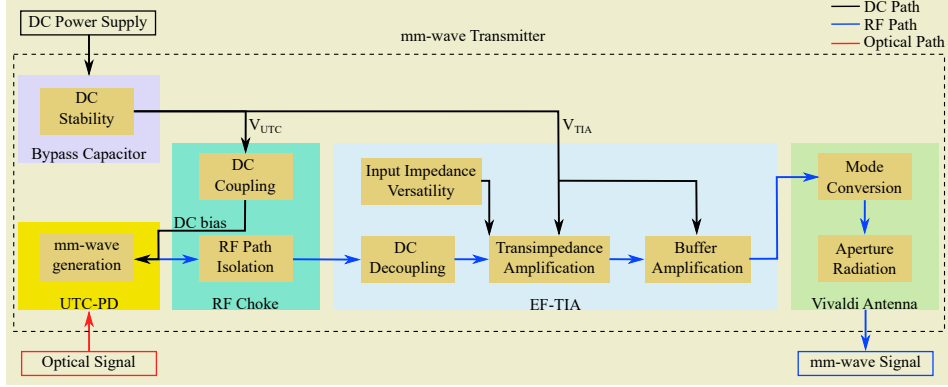


Figure 5.1: The functional design of the proposed mm-wave transmitter module including all the RF components and the DC biasing method.

5.1 The functional design of the mm-wave Tx

The mm-wave transmitter is comprised of four main RF components. As illustrated in Fig. 5.1, the functional processes of the device are divided based on the properties of each element that contributes to its seamless performance. These functions are summarised as follows:

- DC voltage connectivity:** The biasing of the active UTC-PD and EF-TIA is crucial, enabling the optimal optoelectronic conversion and amplification of the generated mm-waves. Thus, a DC power supply with high quality is required prohibiting any voltage fluctuations that may cause instability and even permanent damage to the transmitter. Furthermore, voltage ripples can also be generated from RF currents flowing towards the power supply. Therefore, bypass capacitors need to be co-integrated to send such high frequency currents to the ground.
- UTC-PD:** As discussed in Chapter 3, it is the interface between the photonic and electronic domains. Once optical signals are inserted into the device, mm-waves are generated through the process of optical heterodyning analysed in Sec. 2.1.4. Coplanar mm-wave modes spread over the contact pads and travel to the following stages of the co-integrated Tx device. However, since this photodiode is a single-port electronic block, an additional component needs to be added, allowing to apply a DC bias.
- RF choke:** The design of Sec. 4.3 enables the application of reverse bias (V_{UTC}) on the UTC photodiode by adding a DC interconnection that intersects the RF path between the UTC-PD and the TIA. Moreover, it guarantees the isolation of the RF path, prohibiting the mm-waves from flowing

in the direction towards the power supply that would potentially lead to increased losses around the frequencies of operation.

- *EF-TIA*: The functions of this device provided in Sec. 4.1 are divided into three processes. As a first step, a decoupling block secures the stability of the transistors by preventing the flow of any additional DC currents originating from the UTC-PD to enter the amplifier. Then, a transimpedance amplification stage amplifies generated photocurrents. This block is versatile in terms of input impedance (Z_{in}). During the design of this component, the parameter Z_{in} can be adjusted to match the impedance of the device placed at its input ($50\ \Omega$ in this case). Finally, the output voltages receive a final boost by a buffer amplifier.
- *Vivaldi antenna*: Once the amplified waveforms exit the EF-TIA block, they need to provide input to an element allowing their transmission over the air. Therefore, the antenna component in Sec. 4.2 employs a mode conversion block transforming the CPW electric modes to slotline compatible with a planar antenna module. At a further step, the slotted electric waves enter the device's aperture that enables their wireless transmission. The radiation gain is also aided through the comb structures in the far-end part of the antenna.

Once the main characteristics of each module are described and summarised, it is vital to elaborate on the practical assembly processes of the device. In the following section, the co-integration techniques and an assembly design are synthesised and illustrated. This will allow the definition of the test benches supporting the characterisation procedures of the final component.

5.2 Co-integration of all integrated devices

After identifying the building blocks contributing to the synthesis of the mm-wave device, it is crucial to elaborate on the techniques guaranteeing the component's bonding and DC bias stability and initiate the co-integration procedures of the final design. Furthermore, the assembly will be conducted by state-of-the-art packaging equipment provided by Ferdinand Braun Institute. The dimensions of the devices (measured in mm) that contribute to the processes within the mm-wave transmitter are mentioned in Tab. 5.1. In addition to the already described and analysed components, supplementary structures are listed, including the metal base placed in the bottom of the mm-wave Tx maintaining mechanical stability and realising a common ground, a PCB design for circuit biasing, two bypass capacitors and four DC pin heads.

Table 5.1: The list components included within the mm-wave Tx including their dimensions measured in [mm].

Component	length×width×thickness
Metal Base	9.4×8.3×10
PCB Biasing Network	9.5×11.5×0.7
Uni-travelling Carrier Photodiode (UTC-PD)	0.23×0.5×0.1
Emitter follower transimpedance amplifier (EF-TIA)	0.82×0.51×0.65
V-Band RF choke	5.2×4.1×0.15
V-Band Vivaldi antenna	23.3×7.5×0.15
DC bypass capacitor	0.25×0.25×0.1
DC pin head	2.54×2.54×11.6

5.2.1 Seamless chip interconnection techniques

Wirebonding integrated circuits

Wirebonding is a popular procedure linking multiple devices to form a single module [386]. Gold wires are to be selected since they are not prone to oxidation and tarnishing and thus, maintain their conductivity and are less prone to break. There are two main methods of wirebonding, namely, ball and wedge bonding.

During the ball bonding process of Fig. 5.2a), a capillary that is a tool threading the gold wire forms a ball at its end by melting the gold (100-200 °C). This ball is roughly two times the diameter of the wire. At a further step, the capillary securely couples the ball to the surface of a metal pad. By applying pressure, high temperature, and ultrasonic energy (thermo-sonic wiring technique), a weld is formed between the pad and the ball, creating a bonding shape that depends on the dimensions of the capillary. Then, the wire is moved towards the next bonding location, creating a loop. It needs to be mentioned that the bonding equipment controls the loop's length, shape, and height. A stitch is created once the bond reaches the final location, i.e., a link to the other pad below the capillary. Once the connection is completed, the wire breaks and the capillary is lifted, moving to the following bonding location.

The wedge bonding process in Fig. 5.2b) uses a gold wire or ribbon fed by a tool in a needle or a stylus shape. The bond between the wire and the area to be connected is formed by combining pressure and ultrasonic vibration. The shape and dimensions of the wedge are determined by the dimensions of the geometry of the needle guiding the wire to the second bonding location while forming the loop. In the same way, the second bond is forged by applying pressure and ultrasonic energy. Then, the wire is broken with the needle moving towards the next location where interconnection is required.

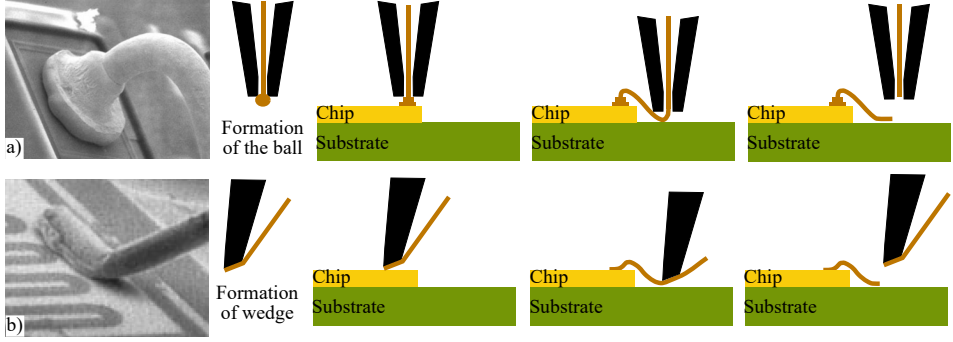


Figure 5.2: Illustration of the different stages of wirebond interconnections using: a) ball bonding; b) wedge bonding [387].

For both processes, the wirebond inductance (L_{WB}) depends on the width (w_{WB}) and thickness (t_{WB}) of the gold wire and is calculated in Eq. 5.1 [388]. In addition, the smaller the length of the wirebond, the lower its reactance, minimising the attenuation levels in high frequencies. This suggests that it is important to keep the distances between the RF components at a minimum, decreasing L_{WB} .

$$L_{WB} = 5.08 \times 10^{-3} \times l_{WB} \times \ln\left(\frac{l_{WB}}{w_{WB} + t_{WB}}\right) + 1.19 + 0.22 \times \left(\frac{w_{WB} + t_{WB}}{l_{WB}}\right) \quad (5.1)$$

Conducting adhesive

In several electronic applications, electrically conducting adhesives provide an alternative to soldering where they are applied in assemblies to interconnect circuits with PCB tracks [389]. An adhesive, i.e., glue, offers high reliability, thermal stability, and structural bonding except for electrical contact. The majority of these materials include silver particles offering conductivity levels higher than 80%. Thus, such adhesives are recommended to attach the independent integrated chips to a DC biasing base and will be used on the components presented in this work.

Bypass capacitor

Based on the investigation of the previous Chapters, DC stability is crucial for biasing the active devices. Any unexpected variation of the bias voltage may cause the shrinking of the depletion region of a UTC-PD or transistor instability of an amplifier, leading to permanent damage. As illustrated in Fig. 5.3a) high frequency current signals ($i(t)$ in blue) may induce voltage fluctuations (ΔV) to the DC bias provision within an IC. As shown in Eq. 5.2, the amplitude of ΔV (in red) is proportional to L_{WB} .

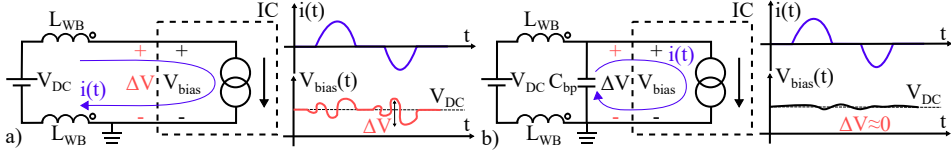


Figure 5.3: The interconnection of an IC circuit with a DC power source including an example of current and bias voltage graphs with a) and without b) a bypass capacitor.

$$\Delta V = L_{WB} \frac{di(t)}{dt} \quad (5.2)$$

An effective method limiting this voltage ripple is accomplished by shunting a bypass capacitor between the source and the IC as depicted in Fig. 5.3b) [390]. The capacitance (C_{bp}) has a low value such that it presents a low impedance $Z_c = 1/(j\omega C_{bp})$ to mm-waves that follow this branch towards the ground and therefore, $V_{bias}(t) \approx V_{DC}$. This process will be proven beneficial for biasing the UTC-PD and the EF-TIA, ensuring constant junction (C_j) and transistor stability (K), respectively. For the investigated application, a wirebondable vertical low-profile Si capacitor with C_{bp} of 100 pF is selected.

5.2.2 Base design and housing the integrated circuits

The DC biasing network of Fig. 5.4a) will be synthesised on a PCB. Its structure includes copper pads where the RF components are to be bonded with a conducting adhesive. All pads and DC lines have minimum separation and width of 0.06 mm following the design rules of the PCB manufacturer and the tolerances of the assembly equipment. On all presented pads, there are additional plated through holes ensuring the transfer of the ground plane on the metal base used as a ground reference directly to all mm-wave devices. Table 5.2 records the properties of the copper pads on the structure.

Based on the dimensions of the components, it is observed that the TIA has the highest thickness compared to the rest of the devices. To avoid long wirebonds in the RF path between the EF-TIA with the RF choke and the antenna, a square hole on the DC biasing PCB must be made to attach the EF-TIA directly to the metal base. Therefore, by opting for a PCB thickness of approximately 0.5 mm the UTC-PD, RF choke and antenna will be brought at the same level as the EF-TIA. As previously indicated, the PCB network will be glued on top of the metal base that has a thickness of 50 mm that allows mechanical stability as well as smooth handling during measurements. Figure 5.4b) shows that the PCB extends beyond the metal base allowing for the DC pins to be placed and soldered, providing seamless biasing by an external source.

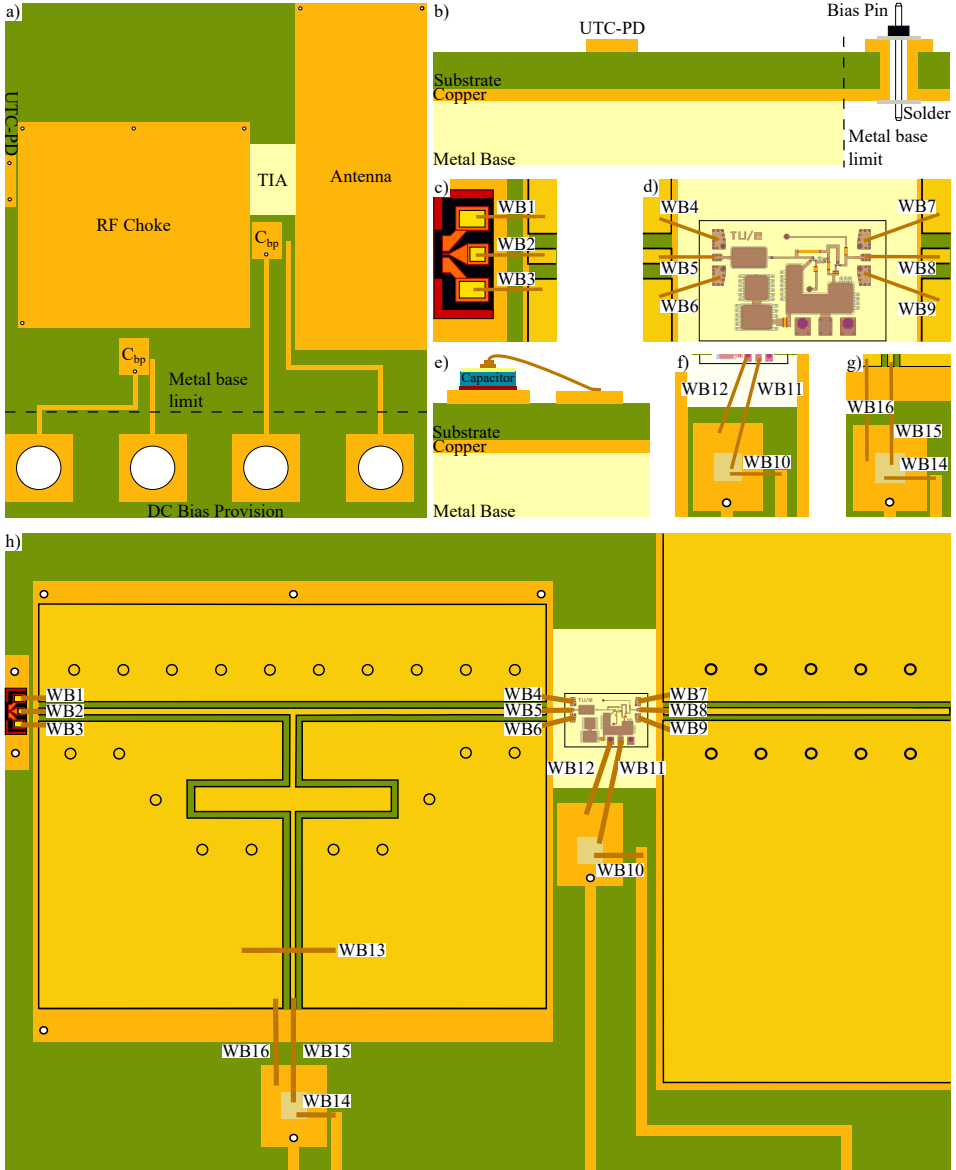


Figure 5.4: a) A laminate based design housing the integrated components for the mm-wave Tx that takes into account the DC biasing of the active integrated circuits, i.e., the UTC-PD and TIA; b) the cross-section of the metal base at the input showing the metal base and the biasing processes through the biasing pins that are interconnected through soldering; c) the wirebonds between the UTC-PD and the RF choke; d) the wirebonds interconnecting the TIA placed directly on the metal base with the RF choke and the antenna; e) the process for wirebonding the bypass capacitors with the TIA f) and the RF choke g); h) overview of the components' placement with the wirebonds.

Table 5.2: The dimensions of the pads included to the PCB biasing network.

Component	length×width
UTC-PD Pad	0.23×1.1
RF choke Pad	5.2×4.6
Antenna Pad	2.9×7.7
EF-TIA Gap	1.0×1.6
Bypass capacitor Pad	0.65×0.81
DC Pad	1.5×1.5
Via radius	0.05
DC via radius	0.5

Placement of the devices

Once the attachment of the PCB network on the base is successful, the interconnection of the mm-wave components will be followed. Initially, the UTC-PD chip will be glued on top of the copper after placing conductive adhesive. It needs to be mentioned that the UTC-PD has to be added at the very edge of the biasing network allowing the light at the output of a lensed fibre to reach its optical waveguide. Furthermore, since the chip is photosensitive, it is crucial to protect and not to cover the optical waveguide of the chip while spreading the glue. At the next step, the RF choke will be installed in the middle of its corresponding pad on the PCB biasing network after adding the adhesive, as indicated by the figure. The EF-TIA is connected to the metal base within the square aperture and is placed closer to the RF choke, where the DC pad's distance is minimal. In addition, once the antenna is attached, its copper ground has to cover the PCB's pad fully. At a final step, the bypass capacitors will be added and the four metal soldered DC biasing pins.

Wirebonding and co-integrating components

The wirebonds will attach all the RF components and realise the DC biasing of the UTC-PD and TIA chips. A total of sixteen wirebonds are required for the RF interconnects. Three wires (ground, signal, ground) will be placed in between the RF chips (Fig. 5.4c,d)) while two in the DC path of each active component (Fig. 5.4f,g)). More specifically, the DC connection process that involves the wire bonding of the bypass capacitors on the PCB base is shown in Fig. 5.4e). As an example, the signal DC pad of the EF-TIA is wirebonded (WB12) vertically with the upper part of the capacitor. Then, WB11 connects the capacitor with the DC signal line of the PCB biasing network. Finally, WB12 links the left ground DC pad of the EF-TIA with the ground line of the biasing network. A similar

Table 5.3: The list of wirebonds within the mm-wave Tx including their length and approximated equivalent inductance.

Wirebond [#]	Length [mm]	Inductance [nH]
WB1, WB2, WB3	0.2	0.09
WB4, WB5, WB6	0.23	0.11
WB7, WB8, WB9	0.3	0.16
WB10	0.5	0.31
WB11	1.05	0.8
WB12	0.65	0.43
WB14	0.5	0.31
WB15	1.05	0.8
WB16	0.75	0.52
WB13	1.2	0.95

procedure will be conducted on adding the WB14, WB15 and WB16 to the RF choke. Finally, WB13 will be placed between the DC ground planes of the RF choke, securing a common ground between its two sides. A general overview of the wirebond placement on the mm-wave transmitter is provided in Fig. 5.4h). An approximation of the WB lengths and inductances are calculated in Tab. 5.3 by assuming $w_{WB} = 100 \mu\text{m}$ and $t_{WB} = 3 \mu\text{m}$.

Final assembly of the mm-wave Tx module

Figure 5.5a) illustrates the circuit schematic of the complete assembly pinpointing the location of the wirebonds. Moreover, it demonstrates the flow of the optical, mm-wave and DC signals within the final component. The total block diagram of the first generation of the mm-wave Tx is shown in Fig. 5.5b) that is based in Fig. 5.4h) while serving the functions of Fig. 5.1. The input to the co-integrated device is provided by a lensed fibre guided by a micropositioner that delivers the optical input. It is crucial to measure the output of the fibre, and therefore, a free-space optical power metre needs to be available. In addition, the power supply applies the reverse bias to the UTC-PD (V_{UTC}) and EF-TIA (V_{TIA}) through the DC biasing pin heads.

In order to eliminate the requirement of a station for chip characterisation, the following generations of the device need to take into account electromagnetic compatibility (EMC) shielding and permanent fibre installation leading to an independent module that can be interconnected with any commercially available optical equipment. However, this first prototype will be very useful for the initial experimental processes acting as a proof of concept that will be further upgraded.

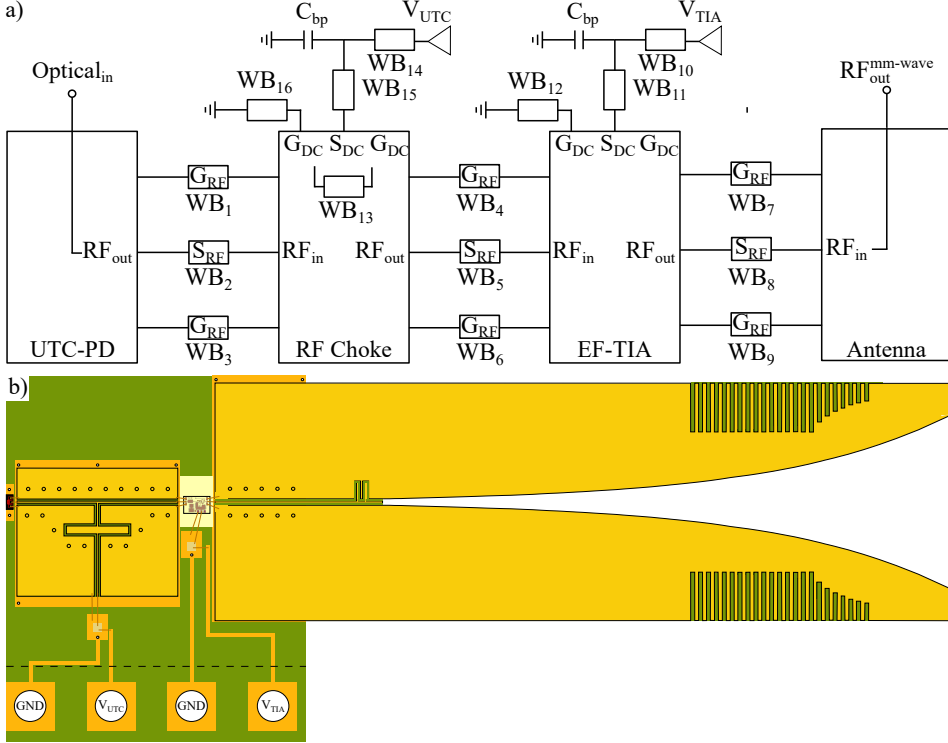


Figure 5.5: A fully integrated mm-wave transmitter including a high-speed UTC-PD, an RF choke, a transimpedance amplifier and a V-band Vivaldi antenna: a) the circuit diagram; b) the components interconnected to the PCB and metal base.

5.2.3 Assembly simulation results

In the previous section, a general overview of the device under fabrication has been presented. As a next step, all the blocks synthesising the mm-wave transmitter are concatenated into a system-level circuit simulation, including the equivalent of the UTC photodiode showcased in Chapter 3 and the measured S-parameter data of the broadband RF components of Chapter 4. This simulation is in reference to the schematic presented in Fig. 5.5a) following the RF path starting from the mm-wave generation within the UTC-PD, the RF choke and the EF-TIA while terminated by the feed-point impedance of the measured Vivaldi antenna. All subsystems are interconnected with bond-wires represented as lumped inductors with values equal to the ones calculated in Tab. 5.3. The approximated evaluation is conducted step-by-step to investigate and analyse the impact of wirebonding and impedance mismatch between the succeeding components on the device's performance.

At the first stage, once the photodiode equivalent circuit (in Fig. 3.10) is directly terminated by the feed point impedance of the RF choke, then the transmis-

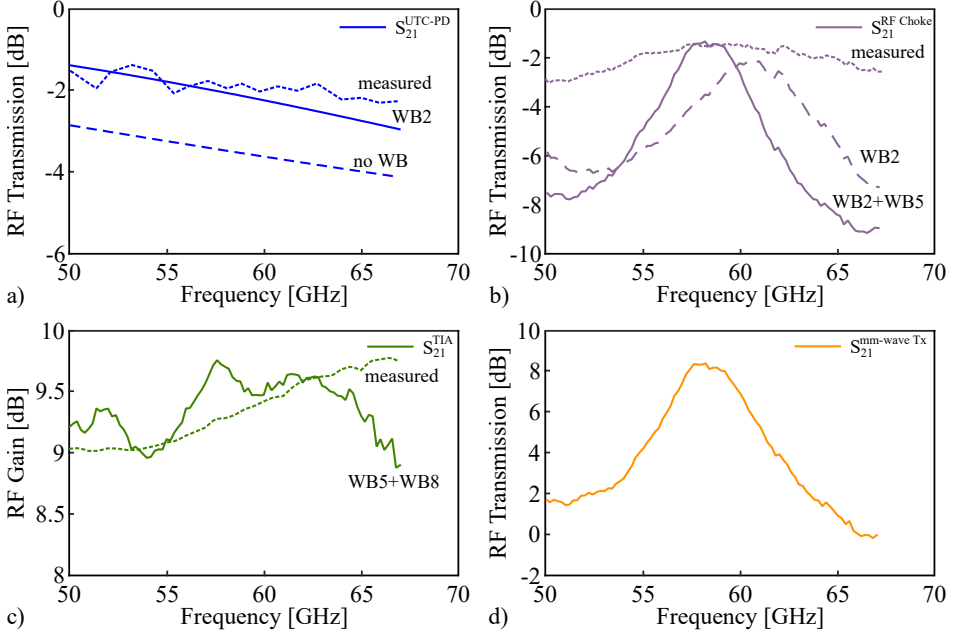


Figure 5.6: Simulation results of the RF transmission path of the mm-wave transmitter including comparisons between the measured data of the individual components (straight lines) and the impact of their interconnection (dashed lines) within the device to be assembled: a) the impact of inductive peaking on the transmission curve of the $4 \times 15 \mu\text{m}^2$ UTC-PD; b) the performance degradation of the transmission capabilities of the RF Choke due to the wirebond inductances compared to the individual device measurements; c) the gain calculation of the EF-TIA due to impedance mismatch and interconnection of the wirebonds; d) the transmission parameters of the mm-wave transmitter (the total aggregate takes the effect of each wirebond once).

sion curve of Fig. 5.6a) (no WB) is shifted downwards in reference to the measured one (dashed line, matched at 50Ω) due to the impedance mismatch between the two devices. However, once the wirebond is added, the RLC network formed between WB2 and the UTC-PD equivalent leads to inductive peaking. Therefore, part of the capacitive influence of the circuit is counteracted by the introduced inductor leading to the amplitude elevation and extension of the device's bandwidth. This is shown in the straight line of Fig. 5.6a) displaced such that it is approximately at the same level of the measured frequency response of the UTC-PD. Then, the impact of adding the RF choke is obtained in Fig. 5.6b) and compared with the measured data extracted from testing the component individually (i.e., Fig. 4.18). Once the passive structure is interconnected with the PD, the shape of the RF transmission curve is substantially affected since the added inductor introduces unwanted resonances in the transmission band. This effect becomes more

apparent once WB5 is also linked at the choke's output, causing deeper resonant falls into the working band, limiting its width and shifting the peak transmission by 1.8 GHz. Furthermore, it needs to be mentioned that additional gain peaking is achieved where the reactive part of WB5 interacts with the capacitive behaviour of the photodiode forming an LC resonator shifting the curve to a higher level.

The EF-TIA gain is also examined to observe the impact of wirebonding, and the impedance mismatch between the 50 Ω matched amplifier and the input and output point impedances of the RF choke and Vivaldi antenna, respectively. Therefore, the added resonant effects lead to the gain curve of Fig. 5.6c) that is comparable to the measured data with a maximum gain difference of 0.6 dB at 67 GHz. Once all the devices are connected, it is evident that the characteristic of the RF Choke dominates the response of the total system exhibiting a 3 dB bandwidth of 5.5 GHz centred at 58.2 GHz with a link gain equal to 8.2 dB. By assuming the generation of a mm-wave at the output of the UTC-PD with a power level of -7 dBm at the central carrier frequency and approximately $I_{PD}^{DC} = 4.5$ mA, an 18 % optoelectronic conversion efficiency is derived [391], and it is a reference point for future improvement processes.

These preliminary results showcase the challenges in terms of link gain and bandwidth limitations arising while interconnecting various devices into a single module. Therefore, in the next generation of fabricated components, these calculations will be beneficial since it is necessary to consider the impact of the electrical properties of RF interconnections and packaging to adjust their design accordingly. On the other hand, the simulated system bandwidth corresponds to a 9.4 % of the frequency carrier and will be verified experimentally. Thus, the mm-wave Tx remains a promising integrated solution to provide optoelectronic conversion, mm-wave amplification and wireless transmission for 5G applications.

5.3 Device characterisation processes

As it has already been shown in Chapters 3 and 4, once a component is fabricated, then its properties need to be experimentally validated¹. Thus, in the following sections, the small-signal measurements and wireless transmission of 5G-NR signals as summarised in Fig. 5.7a,b) will be discussed. In all cases, optical heterodyning will be employed for the mm-wave generation.

5.3.1 Small-signal parametric response measurements

A first step to measure the characteristics of the assembled mm-wave Tx is based on the setup of Fig. 5.7a) allowing the extraction of useful information on the frequency response of the device. A CW laser provides input to a Mach-Zehnder

¹The fabrication of the mm-wave Tx was not finalised by the time of the completion of this manuscript due to delays introduced by the global pandemic. However, the assembly plans have currently been completed based on the guidelines indicated in this Chapter.

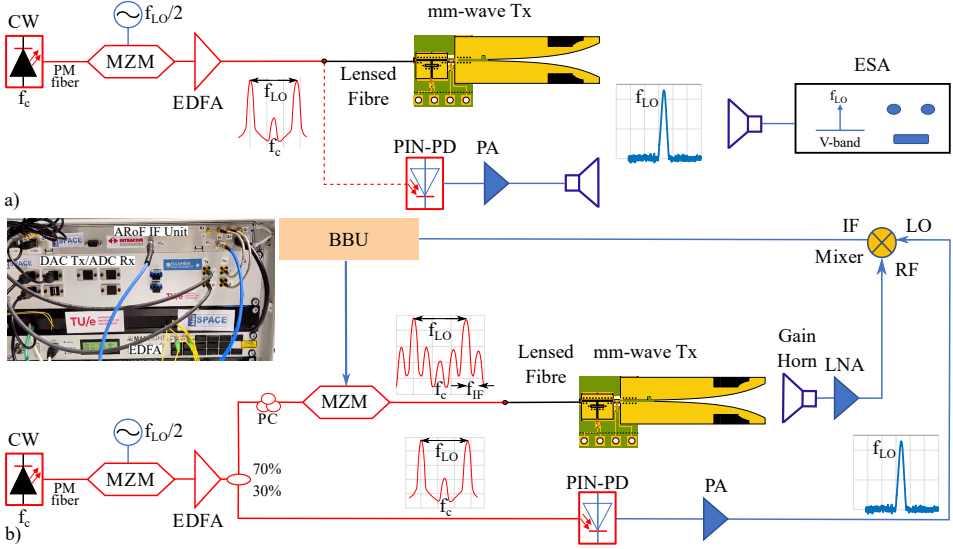


Figure 5.7: Experimental testing of the co-integrated mm-wave Tx: a) small-signal parameter extraction by monitoring the mm-wave tone generation based in amplitude and phase, while comparing the capabilities of the transmitter with off-the-shelf V-band components; b) schematic of the experimental setup testing the wireless modulation capabilities of the mm-wave Tx without including the optical fibre (optical back-to-back) involving a real-time transmission and reception through an ARoF BBU.

modulator (MZM) biased at the null transmission point and driven by a sinusoid with a sweeping frequency between 20 to 40 GHz covering the entire range of V-band and beyond. Therefore, two spectral lines are induced with a spacing of f_{LO} equal to twice the frequency of the sinusoid. The output of the MZM is amplified by an EDFA that is interconnected through a lensed fibre to the mm-wave Tx, transmitting a single tone at f_{LO} . The amplitudes of the tones are recorded by an ESA linked to a receiving 25 dBi gain horn (GH) antenna. Thus, a power over frequency diagram may be calculated. To conduct a qualitative comparison, the same process can be replicated with off-the-shelf components, i.e., a 90 GHz PIN-PD in series with a 10 dB V-band power amplifier (PA) and another 25 dBi GH. This experiment effectively acts as normalisation for the initial measurement relating the performance of the synthesised transmitter to that from well-known bulk devices. A successful correlation is achieved based on the link budget by securing that the transmitter's output power is the same for both regimes.

5.3.2 Transmission of 5G NR OFDM signals in V-band

The evaluation of the mm-wave transmitter in terms of wireless transmission of modulated signals is illustrated in the setup of Fig. 5.7b). The link is based

on optical back-to-back since no fibre will be included. As already exhibited in Sec. 2.3.3, within the ARoF BBU, various 5G-based OFDM waveforms would be generated at an $f_{IF} = 3.2$ GHz. Furthermore, based on the previous schematic, the sinusoid frequency is set at 27.5 GHz and thus, $f_{LO} = 55$ GHz. Then, the output of the EDFA is divided by the 70:30 optical coupler. The low output power feeds directly the 90 GHz PIN-PD generating a mm-wave tone at f_{LO} that is amplified by a 25 dB V-band PA and serves as the LO for the electrical downconversion of the received RF waveforms. The 70 % output of the coupler provides optical input to the second MZM that is biased in quadrature and is electrically fed by the OFDM signal generated at the BBU. The mm-wave Tx interconnected with the MZM through a lensed fibre produces, amplifies and transmits in the wireless domain the 5G-NR OFDM signals centred at $f_{RF} = f_{LO} + f_{IF} = 58.2$ GHz. At the next step, after wireless propagation, the waves are received by the 25 dBi GH and amplified by a 35 dB V-band LNA interconnected to a mixer for downconversion to the f_{IF} . Finally, the OFDM waves are sent back to the BBU for real-time processing evaluating the received signal quality. Therefore, BER measurements can be conducted for various signal modulations, bandwidths and link distances.

5.4 Summary

This Chapter described the assembly of multiple components into a broadband mm-wave transmitter interfacing with the photonic-wireless links. Furthermore, concepts, techniques and processes supporting the device were presented. It investigated the two main methods of wirebonding, namely, wedge and ball bonding, as well as showed the impact of applying conducting adhesives for attaching chips on PCBs. In addition, the beneficial effect of interconnecting an 100 pF bypass capacitor was analysed, guaranteeing the stability of DC voltage provided to the UTC-PD and EF-TIA. A DC biasing network on PCB directly attached to a metal base was designed to house all the presented components. Its thickness was chosen such that the UTC-PD, RF choke and antenna were levelled with the thick amplifier circuit chip connected directly to the base. Once the conducting adhesive attaches all the chips, sixteen wirebonds may provide the direct RF and DC interconnection between components leading to the final assembly. System-level simulation results showcase the impact of interconnecting all devices to a single module while a bandwidth equal to 5.5 GHz centred at a frequency carrier of 58.2 GHz is calculated. The capabilities of the co-integrated system on-chip are to be tested through small-signal and 5G-NR modulation experimental setups. In that way, the characteristics of a miniaturised and replicable system on-chip will be presented. Such a device will exhibit considerable potential supporting communication links operating in frequencies within the unlicensed V-band.

Conclusions and future outlook

6.1 Summary and conclusions

The presented work contributed to the state-of-the-art on hybrid photonic wireless systems in two main sub-topics. First, it involved the analysis and experimental demonstration of ARoF links in Ka-band that have been identified as the prominent candidate to support the impending 5G wireless communications. Various concepts were discussed, including the provision of high-speed connections in rural areas where fibre deployment is financially prohibitive, as well as systems employing ARoF to transmit 5G based signals while presenting analogue beamforming properties. In a further step, integrated elements on-chip, namely a uni-travelling carrier photodiode for optoelectronic conversion, an RF-choke for DC biasing, a high-gain transimpedance amplifier and a broadband antenna, were individually analysed, fabricated and characterised. The overall design of a flexible, low-cost and scalable mm-wave transmitter on-chip in V-band is synthesised by interconnecting these components in order to provide high capacity wireless access in point-to-point links.

The introductory part of the dissertation underlined the issues arising from the exponentially increasing mobile IP traffic requirements. Due to the advent of popular and compelling applications in terms of capacity, such as virtual reality gaming and ultra-high definition streaming, the evolution of the existing wireless networks is necessary. Thus, sub-6 GHz communications are insufficient to sustain these demands, and they need to be allocated in frequency carriers beyond Ka-band supporting multi-Gbit/s data rates. Despite the remarkable benefits in these frequencies, the propagation of wireless signals in the mm-wave domain is not straightforward due to propagation loss. Phenomena such as free-space path loss and atmospheric absorption affect the power budget calculations towards the realisation of mm-wave systems. Thus, point-to-point links in the line of sight regime

while using high gain antennas may grant valuable effectiveness. This work focuses on systems operating in Ka [26.5-40 GHz], V [40-75 GHz] and W [75-110 GHz] bands supporting wireless users in indoor and outdoor applications within small cells such as 5G mobile communications and broadband WiFi connections (e.g., 802.11ay). Furthermore, it focuses on solutions using the hybrid interconnection of photonic and electronic devices, showcasing the dynamic potential of co-integration to achieve flexible and low-cost systems on-chip.

The essential aspects of microwave photonics and mm-wave generation based on optical heterodyning were provided in Chapter 2. The beneficial characteristics of employing ARoF-based networks in terms of deployment costs, management and end-to-end latency make them prime candidates for providing mm-wave wireless connections. The building blocks describing the ARoF signal generation, wireless transmission and end-user detection within these links were presented, including the synthesis of complex modulation formats that follow the 5G standards and decisively boost system capacity. Broadband components and high data rate modulation techniques allow the consideration of a 5G UDWDM network concept that is highly centralised since it enables resource allocation with SDN and NFV. In addition, the capacity is drastically increased by including space division multiplexing in multicore fibres as an optical variable of freedom to the optical network properties. Moreover, with SDM, novel methods such as the interconnection of integrated optical beamforming networks can be realised. A variety of characteristics of the presented scenario are tested by demonstrating three hybrid photonic wireless systems. As a first step, a simplified 2.5 Gbit/s ARoF Ka-band 2 m link based on a commercial SFP+ module was analysed, realising a low-cost method for high-speed access to rural areas where fibre deployment is financially prohibitive. Then, a coherent ARoF experimental architecture was used to evade increased phase noise and potential carrier drifting. This scheme combined with 5G signal numerology provides higher capacities to the UEs. The transmission of carrier aggregated multiband 5G OFDM signals over coherent ARoF was experimentally analysed, achieving data rates of 1.2 Gbit/s and 4.8 Gbit/s over 2.2 m. Towards a more realistic 5G based network scenario, a real-time mm-wave hybrid photonic-wireless system was also demonstrated transmitting up to 1.4 Gbit/s 5G-NR OFDM waveforms through a 7-core MCF to an 8×4 antenna array utilising analogue beamforming tracking moving receivers. The experimental results indicate that flexible solutions can be provided depending on the end-user application and capacity requirements, each supported by a different ARoF scheme.

The crucial parameters describing the photodetecting devices responsible for optoelectronic conversion were described and analysed in Chapter 3. Integrated uni-travelling carrier photodiodes (UTC-PDs) fabricated at III-V Lab were chosen among various types of these components to be considered in this work due to their increased sensitivity, broad bandwidth and high saturation powers caused by the unidirectional motion of electrons within their active region. Measurements of these essential characteristics verified the presented theoretical background. More importantly, a $4 \times 15 \mu\text{m}^2$ UTC-PD was identified to be interconnected for the

mm-wave application of this thesis since its frequency bandwidth, i.e., S_{21} , exceeds the limits of V-band. Thus, the full equivalent circuit of this structure was extracted, including the effect of carrier transit time and the RC-time constant. Moreover, the second part of the Chapter focused on investigating three de-embedding methods contributing to the characterisation of the active region within the UTC photodiodes. De-embedding removed the parasitic effects of the waveguides connected to the active area. A systematic error introduced by the standard open-short method was identified, and a correction was proposed. At the same time, an S-parameter based process was also examined through simulation techniques. Finally, the methods were compared by calculating the junction capacitance (C_j) and series resistance (R_s) for diodes with different sizes.

The amplification and transmission over the air of the generated mm-wave signals are conducted by the broadband RF components presented in Chapter 4. More specifically, a transimpedance amplifier, a Vivaldi antenna and an RF choke centred at 60 GHz were fabricated and experimentally tested. Concerning the amplification, the fundamental functions of transistors were shown. TIAs interconnected with optoelectronics have a competitive advantage over various amplifier architectures due to their low additive current noise and input impedance versatility, enabling optimal matching. Thus, an emitter-follower TIA was fabricated in FBH and a transimpedance gain of $50 \text{ dB}\Omega$ was measured between 40 to 67 GHz exhibiting RMS and averaged RMS input noise current density equal to $i_{n,TIA}^{RMS} = 3.3 \text{ }\mu\text{A}$ and $I_{n,TIA}^{Avg} = 16.1 \text{ pA}/\sqrt{\text{Hz}}$, respectively. Even though an implementation penalty between measurements and simulations was identified, the fabricated TIA can boost the high-frequency waveforms within the mm-wave transmitter. In addition, a Vivaldi antenna in V-band was designed and measured, including a coplanar to slotline transition input and a comb-based structure able to increase its gain. The antenna has an increased 3dB gain bandwidth of 30.6 GHz that reaches a maximum of 12.6 dBi at 68.5 GHz. Finally, an interface between the UTC-PD and the TIA was manufactured, allowing for the biasing of the photodiodes while evading increased losses in the RF path between the two active devices. This RF choke has an operation bandwidth of 10 GHz and is centred at 60 GHz. Therefore, all the pieces synthesising the mm-wave transmitter were characterised towards the assembly processes.

A complete transmitter module design based on the assembly of all the individual examined components was presented in Chapter 5. On a metal plate, a DC biasing network on PCB was synthesised to define the location of all four fabricated components and the position for the bypass capacitors. These elements protect the interconnected active components from possible fluctuations originating from the power supplies. Furthermore, the importance of limiting the wirebond lengths was underlined while its equivalent inductance was calculated for every connection within the mm-wave transmitter. Then, a circuit formed by the equivalent of the UTC-PD interconnected through wirebonds with the measured data of the RF choke and EF-TIA terminated by the feedpoint impedance of the Vivaldi antenna was simulated providing a bandwidth equal to 5.5 GHz centred at a frequency

carrier of 58.5 GHz. Two experimental processes were described that first would allow the small-signal characterisation of the assembly and then would verify its large-signal capabilities through the wireless transmission of 5G-NR waveforms in a simplified back to back (i.e., without interconnecting the optical fibre) hybrid photonic wireless link.

6.2 Recommendations and Future Outlook

This work experimentally demonstrates the synthesis of three hybrid photonic-wireless links guaranteeing the provision of 5G based signals to end-users and analyses the synthesis of a mm-wave optoelectronic transmitter based on four integrated components discussed individually. However, vital challenges still exist, and research effort is still required to optimise the RoF systems as well as to provide a mature, compact, and low-cost integrated solution supporting mm-wave wireless access. Various aspects of these topics that need to be addressed for further development are detailed in the recommendations sections listed below.

6.2.1 Analysis and improvement processes

Hybrid photonic-wireless links

The valuable characteristics of ARoF systems towards ultra-broadband access for 5G were verified by three experimental demonstrations that, once upgraded, can show great potential in terms of capacity and communication distance. Regarding the setup that included the SFP+ module for mm-wave generation and real-time detection, further investigation and analysis of the RF frequency stability are required to allow seamless integration with the existing PON infrastructure. This method will provide constructive feedback in case active control and temperature management need to be considered to minimise the drift of the mm-wave carrier. Furthermore, the data rates can be potentially doubled if 4PAM is applied as a modulation format instead of NRZ. In addition, the capabilities of the ARoF link with a single laser and two-tone generation using M-OFDM signals may also be enhanced. By providing boosted waveforms from the WG to the modulator through a driver amplifier at the CO, while including a higher gain LNA and improved signal processing techniques (e.g., upgrading the Costas loop algorithm, phase noise compensation methods [392]) at the receiver, increased data rates and link distances can be achieved. Both wireless links were point-to-point; thus, by further optimisation of the antenna gain, the distance between the antennas can be potentially extended even further. Finally, the realised experimental demonstration that combined the significant research outputs of the EU projects blueSPACE and SILIKA included a remote unit that also played the role of the end-user. To emulate a more realistic 5G scenario, a bidirectional link that consists of an independent UE able to receive and transmit signals would also add significant value to the investigated

concept. Furthermore, the experiment can be conducted outdoors, allowing the receiver to move over wider arcs, increasing the link transmission distance. Finally, novel technologies and solutions can be included in the experimental schemes such as SDN for perceptive control and optimisation of the interconnected components within the RU as well as reconfigurable intelligent surfaces (RIS) supporting NLoS mm-wave wireless communications [393], [394].

Analysis of UTC photodiodes

Uni-travelling carrier photodiodes offer an advantageous solution for co-integration with mm-wave electronics since they allow the generation of high-frequency carriers. For further recommendations, the full equivalent of a UTC-PD has to be upgraded to an adaptive RC-circuit that depending on the applied reverse bias and input optical power, the exact junction capacitance will be calculated. Moreover, the impacts of overshoot velocity and saturation may also be imprinted on the equivalent circuit by monitoring the change of C_j for different optical input powers while measuring with a lightwave component analyser (LCA). In addition, the value of C_j can contribute to the optimisation of the intrinsic region (e.g., in terms of dimensions) since as it was already mentioned it can be identified if there was a process error during fabrication. This will result in future integrated UTC-PD chip generations with higher output powers, f_{3dB} and total efficiencies. Furthermore, the de-embedding equations should be applied on devices such as PIN-PDs and Schottky diodes as well as optical modulators, verifying the assumption that these techniques are valid for various single-ended devices.

Optimising the RF broadband components

Improvements to the designed and fabricated RF components will deliver an optimal interface between the UTC-PDs and the wireless domain. Based on the measurement results of the fabricated EF-TIA, additional testing and possibilities for future development can be arranged. The saturation powers and the third-order intercept point (IP3), where the output power of the intermodulation lines becomes equal to that of the fundamental, have to be acquired for the existing designs contributing to a more concrete evaluation of the TIA. These type of large signal measurements can be conducted with a performance network analyser (PNA). Towards the next generation of the amplifier, the transimpedance gain can be increased as well as the bandwidth while minimising the input current noise even further. Since both the EF-TIA and the UTC-PDs operate at comparable bias points, an upgraded design can provide the DC input to the photodiodes (e.g., add an RF choke circuit within the design). Moreover, instead of a buffer transistor at the output of the TIA, a distributed amplifier can be cascaded, offering increased gain bandwidth product and output powers.

Concerning the components on laminate technologies, polymer materials with very low dielectric constant and reduced losses can replace the Rogers substrates

that are currently used [395], [396]. For both passive components, the impedance mismatch issue can be resolved if the designs are submitted to a foundry incorporating technologies that allow the fabrication of chips with resolutions lower than $50\text{ }\mu\text{m}$. An alternative idea that has yet to be implemented is a two-stage device manufacture where the antenna and the RF-choke designs are sent to a PCB commercial foundry without including the signal paths. Then, gold signal layers are added posterior to fabrication with equipment employing nm resolution plating that leads to signal and gap widths of the CPW matched to $50\text{ }\Omega$. Also, for the RF choke design, in the case that materials with lower dielectric constants are used, slot ring resonators instead of the current structure with the $\lambda/4$ stubs would decrease the size of the chip even further [397], [398]. Finally, additional fine-tuning of the designed comb and CPW to slotline transition on the Vivaldi antenna will increase its 3dB gain bandwidth.

Towards a fully-packaged and pigtailed mm-wave transmitter

The previously presented co-integration of all components is sufficient to provide a proof of concept. However, further improvements can be implemented to the assembly of the mm-wave transmitter to mimic an off-the-shelf solution. Towards the optimisation techniques of the chips' interconnection, flip-chip transitions can replace the wirebonds. Such transition can be designed for arbitrary impedance levels leading to an optimum match between optical devices and customised electronics. In addition, thermoelectric cooling (e.g., Peltier element) needs to be considered for thermal stability. Also, electromagnetic compatibility (EMC) shielding using ceramics or metals will protect the transmitter from any RF interference. At the same time, a robust package will preserve the included chips from any corrosion or oxidation. Finally, a lensed fibre must be permanently attached to the assembly, offering a solution able to be interfaced with commercial optical components (e.g., optical fibre spools).

6.2.2 Enhancing the functions of the integrated system

Monolithic integration of multiple components

In order to avoid the losses, any potential impedance mismatches caused by the wirebonds as well as the high costs from the device fabrication and assembly in different foundries, monolithic integration of multiple devices of the proposed system on a single chip can provide a solution towards a more compact device. As a first step towards this direction, an optoelectronic component is designed on the InP membrane on silicon (IMOS) in Fig. 6.1a) [399]. The device consists of an RF choke built in IMOS that is matched to $50\text{ }\Omega$ and operates between 45 to 70 GHz. The design is monolithically co-integrated with a $2 \times 5\text{ }\mu\text{m}^2$ UTC-PD and is currently under fabrication. Due to the versatility of the proposed bandpass UTC photodiode, it can be interconnected with any type of V-band amplifier

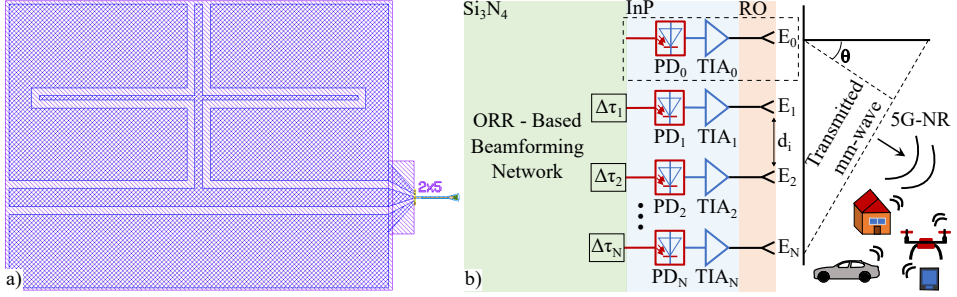


Figure 6.1: Suggestions expanding the functions of the mm-wave system on chip: a) a $2 \times 5 \mu\text{m}^2$ UTC-PD monolithically integrated with a V-band RF choke in IMOS; b) a Si₃N₄ chip placed before an array of the proposed mm-wave transmitters showcasing the operating principle of optical true-time delay allowing beamforming, targeting 5G UEs.

(e.g., TIA, LNA, PA) or directly to a planar antenna. The latter applies when the transmitter can be used for low-power applications (e.g., mm-wave sensing). In future, the next step forward would entail the design of the UTC-PD, RF choke and the TIA on the same substrate.

Adding a beamforming network

As demonstrated in the ARoF experimental processes, analogue beamforming was conducted within the SILIKA wireless antenna structure. The mm-wave was split into multiple copies, whereas their amplitudes and phases were tuned before launching into the antenna array elements. Therefore, the propagating electromagnetic waves constructively interfered only at the desired location in the far-field, leading to a steerable radiation pattern able to follow the end-users. However, the steerability of the beams is highly dependent on the type of antenna used in order to form the phased array. Antennas with high gain are unable to provide an extensive scanning range due to the trade-off between directivity and beamwidth. Thus, an ETSA can be embedded within arrays for applications requiring low steering range (e.g., 40° arc [400]) or fixed wireless access while patch antennas with broader patterns in massive MIMO applications showcased in Chapter 2.

Concerning the beamforming techniques, the showcased phase-shifting can also be achieved in the optical domain through true time delays (OTTDs) based on off-the-shelf or integrated chip solutions [401]. Integrated photonic networks split the optical path into multiple branches and add time delays $\Delta\tau$ to each branch using optical ring resonators (ORRs). ORRs grown on silicon-nitride (Si₃N₄) are widely used to achieve this goal [402]. A prominent alternative to the SRR chip that can be interconnected is an optical beamforming network (OBFN) integrated module offering multi-beam transmission by implementing blaz gratings in the optical domain [403]. As illustrated in Fig. 6.1b), multiple copies of the suggested mm-wave transmitter can be put in parallel at a distance d_i . Once an optical

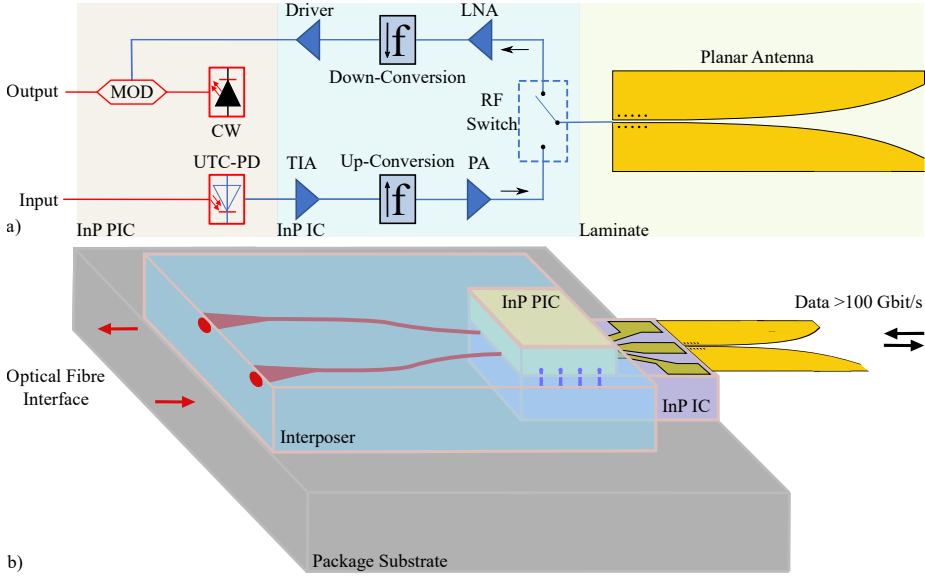


Figure 6.2: The smart wireless pluggable (SWP): a) a block diagram of the components comprising the SWP; b) illustration of photonic-electronic InP-on-InP SWP using flip-chip processes and an interposer for both high frequency operation and interfacing optical signals capable of transmitting and receiving mm-waves above W-band.

signal copy delayed by $\Delta\tau_i$ heterodyne beats within the photodiode, then, a wave is generated with an angle equal to $\theta_i = \arcsin(c\Delta\tau_i/d)$. The beamforming chip can be either directly linked within the RU or at the CO in the case where the optical networks are based on SDM and MCF, increasing the centralisation of 5G networks even further.

A Smart Wireless Pluggable enabling bidirectionality

As it has already been observed with the sub-6 GHz bands, the communications' congestion of the investigated mm-wave bands (e.g., Ka-, V-) is inevitable due to the continuous and growing requirement for bandwidth consuming applications and services. Therefore, wireless connections above 110 GHz are currently under investigation. Towards that direction, a schematic that is an upgrade of the designed mm-wave transmitter is illustrated in Fig. 6.2a). The component is also enhanced by adding bidirectionality based on time-division duplexing (TDD). In the downstream direction, within this smart wireless pluggable (SWP), the mm-wave is generated by a UTC-PD based on optical heterodyning and amplified by the TIA. Then, upconversion takes place to an even higher band. This process can be performed in a mixer. An additional PA compensates for the conversion losses by boosting the mm-waves further before entering an endfire antenna through a

broadband RF switch. For the upstream, the switch allows the received waveforms to enter an LNA. At a further step, downconversion within an envelope detector or a mixer occurs, and a driver provides the required voltage swing to an interconnected optical modulator with an input originating from a CW laser. Towards this end, three integrated chips can be fabricated, including a PIC with the CW, the UTC-PD and the modulator, an electronic IC and the planar antenna. In addition, the PIC and IC can also be monolithically integrated on a single component based on the previous recommendations. A suggested packaging strategy is shown in Fig. 6.2b), allowing the co-integration of IC and PIC devices on an interposer interconnecting the components while the antenna can be flip-chipped on the InP IC [404]. This method is based on low electrical-optical losses, reduced complexity and packaging costs. Therefore, by transmitting mm-waves carrying modulation formats (e.g., 8/16-PAM, OFDM) beyond W-band frequencies (e.g., the unlicensed part of D-band [141-174.8 GHz]), very high data rates can be achieved [405]. Such devices can be deployed and interconnected with the existing optical networks compensating for the high FSPL in these bands, while due to their small sizes, they can be placed in multiple locations providing a promising solution for the future end-users.

6.2.3 The road to 5G and beyond

In conclusion, this dissertation investigated and experimentally tested various milestones paving the path towards high capacity wireless communications while elaborating on the synergy between photonics and electronics. More specifically, this work justified that even though ultra-high frequencies and speeds define photonics, they require electronics to drive them, strengthening the plethora of future broadband applications and services.

Technology never stops growing, and thus the beyond the fifth generation of mobile networks will emerge in the following decade, establishing and even advancing the technologies introduced by 5G (e.g., smart cities, IoT, industry 4.0). Therefore, the proliferation of mm-wave communications will be guaranteed while expanding to sub-THz and THz frequencies. Consequently, the synthesis of devices with exceptional potential will be enabled in terms of increased capacity, compactness and low-cost supporting the Tbit/s hybrid photonic-wireless transmission systems in the road to the impending beyond-5G era.

Bibliography

- [1] A. A. Huurdeman, *The Worldwide History of Telecommunications* (Wiley - IEEE). Wiley, 2003.
- [2] L. Atzori, A. Iera, and G. Morabito, “The internet of things: A survey,” *Computer Networks*, vol. 54, no. 15, pp. 2787–2805, 2010. DOI: 10.1016/j.comnet.2010.05.010.
- [3] D. Rainer and H. Alexander, “Industrie 4.0: hit or hype?” *IEEE Industrial Electronics Magazine*, vol. 8, no. 2, pp. 56–58, 2014. DOI: 10.1109/MIE.2014.2312079.
- [4] M. Masoudi, M. G. Khafagy, A. Conte, *et al.*, “Green Mobile Networks for 5G and Beyond,” *IEEE Access*, vol. 7, pp. 107 270–107 299, 2019. DOI: 10.1109/ACCESS.2019.2932777.
- [5] Cisco, “Cisco Visual Networking Index: Forecast and Trends, 2017–2022,” Tech. Rep., 2018.
- [6] Cisco, “Cisco Annual Internet Report (2018–2023),” Tech. Rep., 2020.
- [7] C. E. Shannon, “A mathematical theory of communication,” *The Bell System Technical Journal*, vol. 27, no. 3, pp. 379–423, 1948. DOI: 10.1002/j.1538-7305.1948.tb01338.x.
- [8] B. Sklar, “Defining, designing, and evaluating digital communication systems,” *IEEE Communications Magazine*, vol. 31, no. 11, pp. 91–101, 1993. DOI: 10.1109/35.256888.
- [9] F. Gunnarsson, “Fundamental limitations of power control and radio resource management in wireless networks,” *Wireless Communications and Mobile Computing*, vol. 4, no. 5, pp. 579–591, 2004. DOI: <https://doi.org/10.1002/wcm.198>.
- [10] R. N. Clarke, “Expanding mobile wireless capacity: The challenges presented by technology and economics,” *Telecommunications Policy*, vol. 38, no. 8, pp. 693–708, 2014. DOI: 10.1016/j.telpol.2013.11.006.
- [11] D. Lee, H. Sasaki, H. Fukumoto, K. Hiraga, and T. Nakagawa, “Orbital Angular Momentum (OAM) Multiplexing: An Enabler of a New Era of Wireless Communications,” *IEICE Transactions on Communications*, vol. E100.B, no. 7, pp. 1044–1063, 2017. DOI: 10.1587/transcom.2016SCI0001.

- [12] E. Halepovic, C. Williamson, and M. Ghaderi, "Wireless data traffic: a decade of change," *IEEE Network*, vol. 23, no. 2, pp. 20–26, 2009. DOI: 10.1109/MNET.2009.4804332.
- [13] Y. Ghasempour, C. R. C. M. da Silva, C. Cordeiro, and E. W. Knightly, "IEEE 802.11ay: Next-Generation 60 GHz Communication for 100 Gb/s Wi-Fi," *IEEE Communications Magazine*, vol. 55, no. 12, pp. 186–192, 2017. DOI: 10.1109/MCOM.2017.1700393.
- [14] W. Hong, Z. H. Jiang, C. Yu, *et al.*, "The Role of Millimeter-Wave Technologies in 5G/6G Wireless Communications," *IEEE Journal of Microwaves*, vol. 1, no. 1, pp. 101–122, 2021. DOI: 10.1109/JMW.2020.3035541.
- [15] A. Morales Vicente, "Towards optical beamforming systems on-chip for millimeter wave wireless communications," English, Proefschrift., Ph.D. dissertation, Electrical Engineering, 2020.
- [16] "IEEE Standard Letter Designations for Radar-Frequency Bands," *IEEE Std 521-2019 (Revision of IEEE Std 521-2002)*, pp. 1–15, 2020. DOI: 10.1109/IEEESTD.2020.8999849.
- [17] E. Ojefors, M. Andreasson, T. Kjellberg, *et al.*, "A 57-71 GHz Beamforming SiGe Transceiver for 802.11 ad-Based Fixed Wireless Access," in *2018 IEEE Radio Freq. Integr. Circuits Symp. (RFIC)*, 2018, pp. 276–279. DOI: 10.1109/RFIC.2018.8428976.
- [18] A. Stöhr, "Photonic millimeter-wave generation and its applications in high data rate wireless access," in *2010 IEEE International Topical Meeting on Microwave Photonics*, 2010, pp. 7–10. DOI: 10.1109/MWP.2010.5664246.
- [19] X. Wang, L. Kong, F. Kong, *et al.*, "Millimeter wave communication: A comprehensive survey," *IEEE Communications Surveys & Tutorials*, vol. 20, no. 3, pp. 1616–1653, 2018. DOI: 10.1109/COMST.2018.2844322.
- [20] L. Ren, B. Lu, F. Lu, and Y. Shu, "Modular and Scalable Millimeter-Wave Patch Array Antenna for 5G MIMO and Beamforming," in *2020 50th European Microwave Conference (EuMC)*, 2021, pp. 336–339. DOI: 10.23919/EuMC48046.2021.9338130.
- [21] V. Reddy and L. Jolly, "Radio over Fiber (RoF) Technology an Integration of Microwave and Optical Network for Wireless Access," *IJCA Proceedings on International Conference and Workshop on Emerging Trends in Technology*, vol. ICWET 2015, no. 1, pp. 8–13, May 2015.
- [22] D. Wake, A. Nkansah, and N. J. Gomes, "Radio Over Fiber Link Design for Next Generation Wireless Systems," *Journal of Lightwave Technology*, vol. 28, no. 16, pp. 2456–2464, 2010. DOI: 10.1109/JLT.2010.2045103.
- [23] J. Yao, "Microwave photonics," *Journal of Lightwave Technology*, vol. 27, no. 3, pp. 314–335, 2009. DOI: 10.1109/JLT.2008.2009551.
- [24] S. Rommel, "Millimeter Wave Hybrid Photonic Wireless Links for High-Speed Wireless Access and Mobile Fronthaul," English, Ph.D. dissertation, 2017.
- [25] T. Maloney and J. Frey, "Transient and steady-state electron transport properties of GaAs and InP," *Journal of Applied Physics*, vol. 48, pp. 781–787, Mar. 1977. DOI: 10.1063/1.323670.

- [26] M. Smit, K. Williams, and J. van der Tol, "Past, present, and future of InP-based photonic integration," *APL Photonics*, vol. 4, no. 5, p. 050901, 2019. DOI: 10.1063/1.5087862.
- [27] T. Nagatsuma, G. Ducournau, and C. C. Renaud, "Advances in terahertz communications accelerated by photonics," *Nature Photonics*, vol. 10, no. 6, pp. 371–379, 2016. DOI: 10.1038/nphoton.2016.65.
- [28] L. A. Samoska, "An Overview of Solid-State Integrated Circuit Amplifiers in the Submillimeter-Wave and THz Regime," *IEEE Transactions on Terahertz Science and Technology*, vol. 1, no. 1, pp. 9–24, 2011. DOI: 10.1109/TTHZ.2011.2159558.
- [29] A. Muhsin, L. E. Garcia Muñoz, M. C. Lo, R. Cruzoe Guzmán, and G. Carpintero, "mmWave photonic emitter featuring a UWB fermi tapered slot antenna," in *2017 International Conference on Electromagnetics in Advanced Applications (ICEAA)*, 2017, pp. 1789–1792. DOI: 10.1109/ICEAA.2017.8065645.
- [30] X. Li, J. Yu, and J. Xiao, " 100^3 (100Gb/s \times 100m \times 100GHz) optical wireless system," in *European Conference on Optical Communication (ECOC)*, IEEE, Valencia, Spain, 2015, pp. 1–3. DOI: 10.1109/ecoc.2015.7341829.
- [31] X. Li, J. Xiao, and J. Yu, "Long-distance wireless mm-wave signal delivery at W-band," *Journal of Lightwave Technology*, vol. 34, no. 2, pp. 661–668, 2015. DOI: 10.1109/JLT.2015.2500581.
- [32] H. Shams, M. J. Fice, L. Gonzalez-Guerrero, C. C. Renaud, F. van Dijk, and A. J. Seeds, "Sub-THz Wireless Over Fiber for Frequency Band 220–280 GHz," *Journal of Lightwave Technology*, vol. 34, no. 20, pp. 4786–4793, 2016. DOI: 10.1109/jlt.2016.2558450.
- [33] T. Umezawa, K. Kashima, A. Kanno, *et al.*, "100-GHz Fiber-Fed Optical-to-Radio Converter for Radio- and Power-Over-Fiber Transmission," *IEEE Journal of Selected Topics in Quantum Electronics*, vol. 23, no. 3, pp. 23–30, 2017. DOI: 10.1109/JSTQE.2016.2611638.
- [34] X. Li and J. Yu, "Generation and Heterodyne Detection of >100 -Gb/s Q-Band PDM-64QAM mm-Wave Signal," *IEEE Photonics Technology Letters*, vol. 29, no. 1, pp. 27–30, 2016. DOI: 10.1109/lpt.2016.2625042.
- [35] F. C. Abrecht, R. Bonjour, S. Welschen, *et al.*, "Pre-equalization technique enabling 70 Gbit/s photonic-wireless link at 60 GHz," *Optics Express*, vol. 24, no. 26, pp. 30350–30359, 2016. DOI: 10.1364/oe.24.030350.
- [36] R. Puerta, S. Rommel, J. J. Vegas Olmos, and I. Tafur Monroy, "Optically generated single side-band radio-over-fiber transmission of 60Gbit/s over 50m at W-band," in *2017 Optical Fiber Communications Conference and Exhibition (OFC)*, 2017, pp. 1–3.
- [37] X. Li, J. Yu, K. Wang, *et al.*, "Delivery of 54-Gb/s 8QAM W-Band Signal and 32-Gb/s 16QAM K-Band Signal Over 20-km SMF-28 and 2500-m Wireless Distance," *Journal of Lightwave Technology*, vol. 36, no. 1, pp. 50–56, 2017. DOI: 10.1109/jlt.2017.2755402.
- [38] M. Jenkins, E. Soto, and R. DeSalvo, "144 Gb/s dual-polarization photonic wireless link operating in the V-band," in *IEEE Photonics Conference (IPC)*, IEEE, Orlando, USA, 2017, pp. 149–150. DOI: 10.1109/ipcon.2017.8116045.

- [39] Z. K. Weng, Y. C. Chi, H. Y. Kao, C. T. Tsai, H. Y. Wang, and G. R. Lin, "Quasi-color-free LD-based long-reach 28-GHz MMWoF With 512-QAM OFDM," *Journal of Lightwave Technology*, vol. 36, no. 19, pp. 4282–4297, 2018. DOI: 10.1109/JLT.2018.2820167.
- [40] H. T. Huang, C. S. Sun, C. T. Lin, *et al.*, "Direct-Detection PDM-OFDM RoF System for 60-GHz 2×2 MIMO Wireless Transmission Without Polarization Tracking," *Journal of Lightwave Technology*, vol. 36, no. 17, pp. 3739–3745, 2018. DOI: 10.1109/JLT.2018.2840102.
- [41] X. Li, J. Yu, L. Zhao, *et al.*, "1-Tb/s millimeter-wave signal wireless delivery at D-band," *Journal of Lightwave Technology*, vol. 37, no. 1, pp. 196–204, 2018. DOI: 10.1109/JLT.2018.2871472.
- [42] F. Li, Z. Li, D. Zou, *et al.*, "Optical I/Q modulation utilizing dual-drive MZM for fiber-wireless integration system at Ka-band," *Optics Letters*, vol. 44, no. 17, pp. 4235–4238, 2019. DOI: 10.1364/ol.44.004235.
- [43] P. T. Dat, A. Kanno, F. Rottenberg, J. Louveaux, N. Yamamoto, and T. Kawanishi, "80 Gb/s 2 × 2 MIMO Fiber–Wireless Integrated System in W Band Using IFoF Transmission," in *2019 International Topical Meeting on Microwave Photonics (MWP)*, 2019, pp. 1–4. DOI: 10.1109/MWP.2019.8892135.
- [44] A. Muhsin, A. Jankowski, R. Cruzoe Guzmán, L. E. Garcia Muñoz, F. van Dijk, and G. Carpintero, "Photonics-based Compact Broadband Transmitter Module for E-band Wireless Communications," in *2019 49th European Microwave Conference (EuMC)*, 2019, pp. 808–811. DOI: 10.23919/EuMC.2019.8910781.
- [45] W. Zhou, L. Zhao, J. Zhang, *et al.*, "135-GHz D-Band 60-Gbps PAM-8 Wireless Transmission Employing a Joint DNN Equalizer With BP and CMMA," *Journal of Lightwave Technology*, vol. 38, no. 14, pp. 3592–3601, 2020. DOI: 10.1109/jlt.2020.2979070.
- [46] I. Dan, P. Szriftgiser, E. Peytavit, *et al.*, "A 300-GHz Wireless Link Employing a Photonic Transmitter and an Active Electronic Receiver With a Transmission Bandwidth of 54 GHz," *IEEE Transactions on Terahertz Science and Technology*, vol. 10, no. 3, pp. 271–281, 2020. DOI: 10.1109/TTHZ.2020.2977331.
- [47] W. Zhou, J. Yu, L. Zhao, *et al.*, "Few-subcarrier QPSK-OFDM wireless Ka-band delivery with pre-coding-assisted frequency doubling," in *Optical Fiber Communications Conference and Exhibition (OFC)*, OSA, San Diego, USA, 2020, Th2.A.45. DOI: 10.1364/ofc.2020.th2a.45.
- [48] Z. X. Xie, B. J. Lin, P. X. Ding, *et al.*, "81.37-Gbps 2times2 MIMO 60-GHz OFDM-RoF System Employing I/Q Nonlinear Compensation Filtering Algorithm," in *Optical Fiber Communications Conference and Exhibition (OFC)*, OSA, San Diego, USA, 2020, W2A.38. DOI: 10.1364/OFC.2020.W2A.38.
- [49] S. Jia, L. Zhang, S. Wang, *et al.*, "2 × 300 Gbit/s Line Rate PS-64QAM-OFDM THz Photonic-Wireless Transmission," *Journal of Lightwave Technology*, vol. 38, no. 17, pp. 4715–4721, 2020. DOI: 10.1109/JLT.2020.2995702.

- [50] P. T. Dat, A. Kanno, F. Rottenberg, J. Louveaux, N. Yamamoto, and T. Kawanishi, "101 Gb/s 2×2 End-to-End MIMO Fiber-Wireless System in W Band Using WDM Radio-over-Fiber," in *2020 International Topical Meeting on Microwave Photonics (MWP)*, 2020, pp. 25–28. DOI: 10.23919/MWP48676.2020.9314618.
- [51] S. Nellen, S. Lauck, E. Peytavit, P. Szriftgiser, G. Ducournau, and B. Globisch, "Wireless communication link at 300 GHz with up to 160 GBit/s," in *2020 45th International Conference on Infrared, Millimeter, and Terahertz Waves (IRMMW-THz)*, 2020, pp. 01–01. DOI: 10.1109/IRMMW-THz46771.2020.9370556.
- [52] P. T. Dat, A. Kanno, N. Yamamoto, and T. Kawanishi, "1024-QAM Analog Waveform Transmission Over a Seamless Fiber-Wireless System in W Band," in *IEEE INFOCOM 2021 - IEEE Conference on Computer Communications Workshops*, 2021, pp. 1–2. DOI: 10.1109/INFOCOMWKSHP51825.2021.9484620.
- [53] H. Yasuda, T. Suzuki, H. Y. Kao, *et al.*, "Demonstration of 28-GHz Band Radio Signal Transmission into Vehicle by Analog Radio over Multi-Mode Fiber," Optical Society of America, 2021, W1J.4.
- [54] N. Singh, G. Torfs, J. van den Kerrebrouck, C. Caillaud, P. Demeester, and X. Yin, "60 GHz Resonant Photoreceiver With an Integrated SiGe HBT Amplifier for Low Cost Analog Radio-Over-Fiber Links," *Journal of Lightwave Technology*, vol. 39, no. 16, pp. 5307–5313, 2021. DOI: 10.1109/JLT.2021.3095522.
- [55] 5G STEP FWD. "5G System Technological Enhancements Provided by Fiber Wireless Deployments (5G STEP FWD), This project has received funding from the European Union's Horizon 2020 research and innovation programme under the Marie Skłodowska Curie grant agreement No: 722429." (2017), [Online]. Available: <https://www.5gstepfwd.eu/>.
- [56] F. Mazda, *Telecommunications Engineer's Reference Book*. Focal Press, 1998.
- [57] M. Denker, "Remote Radio Head systems - Requirements and concept of lightning and overvoltage protection," in *Intelec 2013; 35th International Telecommunications Energy Conference, SMART POWER AND EFFICIENCY*, 2013, pp. 1–5.
- [58] C. W. Chow and C. H. Yeh, "Recent advances in hybrid access networks: From long-reach (LR) to short-reach (SR) systems," in *10th International Conference on Optical Communications and Networks (ICOON 2011)*, 2011, pp. 1–2. DOI: 10.1049/cp.2011.1333.
- [59] P. McClusky and J. L. Schroeder, "Fiber-to-the-antenna: Benefits and protection requirements," in *Intelec 2012*, 2012, pp. 1–6. DOI: 10.1109/INTLEC.2012.6374502.
- [60] F. Haque, S. J. Chowdhury, S. S. Ahsan, Z. Rahman, and M. Z. Ali, "Fiber to the Antenna: Solution in integrated optical and wireless networks," in *The 8th International Conference on Software, Knowledge, Information Management and Applications (SKIMA 2014)*, 2014, pp. 1–8. DOI: 10.1109/SKIMA.2014.7083549.

- [61] U. Habib, A. E. Aighobahi, T. Quinlan, S. D. Walker, and N. J. Gomes, “Analog Radio-Over-Fiber Supported Increased RAU Spacing for 60 GHz Distributed MIMO Employing Spatial Diversity and Multiplexing,” *Journal of Lightwave Technology*, vol. 36, no. 19, pp. 4354–4360, 2018. DOI: 10.1109/JLT.2018.2832028.
- [62] *Report FG IMT-2020: Report on Standards Gap Analysis*. International Telecommunication Union, 2016.
- [63] E. Tangdiongga, A. M. Trinidad, N. Tessema, M. Morant, and R. Llorente, “Compact photonic chip assisted by multi-core fiber for radio beamsteering in 5G,” in *Broadband Access Communication Technologies XIII*, B. B. Dingel, K. Tsukamoto, and S. Mikroulis, Eds., International Society for Optics and Photonics, vol. 10945, SPIE, 2019, pp. 29–34. DOI: 10.1117/12.2514715.
- [64] A. Checko, H. L. Christiansen, Y. Yan, *et al.*, “Cloud RAN for Mobile Networks—A Technology Overview,” *IEEE Communications Surveys Tutorials*, vol. 17, no. 1, pp. 405–426, 2015. DOI: 10.1109/COMST.2014.2355255.
- [65] M. Xiao, S. Mumtaz, Y. Huang, *et al.*, “Millimeter wave communications for future mobile networks,” *IEEE Journal on Selected Areas in Communications*, vol. 35, no. 9, pp. 1909–1935, 2017. DOI: 10.1109/JSAC.2017.2719924.
- [66] G. E. Gonçalves, G. L. Santos, L. Ferreira, *et al.*, “Flying to the Clouds: The Evolution of the 5G Radio Access Networks,” in *The Cloud-to-Thing Continuum: Opportunities and Challenges in Cloud, Fog and Edge Computing*, T. Lynn, J. G. Mooney, B. Lee, and P. T. Endo, Eds. Springer International Publishing, 2020, pp. 41–60. DOI: 10.1007/978-3-030-41110-7_3.
- [67] D. Harutyunyan and R. Riggio, “How to Migrate From Operational LTE/LTE-A Networks to C-RAN With Minimal Investment?” *IEEE Transactions on Network and Service Management*, vol. 15, no. 4, pp. 1503–1515, 2018. DOI: 10.1109/TNSM.2018.2876666.
- [68] S. Kuwano, Y. Suzuki, Y. Yamada, and K. Watanabe, “Digitized Radio-over-Fiber (DROF) System for Wide-Area Ubiquitous Wireless Network,” in *2006 International Topical Meeting on Microwave Photonics*, 2006, pp. 1–4. DOI: 10.1109/MWP.2006.346570.
- [69] A. de la Oliva, J. A. Hernandez, D. Larrabeiti, and A. Azcorra, “An overview of the CPRI specification and its application to C-RAN-based LTE scenarios,” *IEEE Communications Magazine*, vol. 54, no. 2, pp. 152–159, 2016. DOI: 10.1109/MCOM.2016.7402275.
- [70] L. M. P. Larsen, A. Checko, and H. L. Christiansen, “A Survey of the Functional Splits Proposed for 5G Mobile Crosshaul Networks,” *IEEE Communications Surveys Tutorials*, vol. 21, no. 1, pp. 146–172, 2019. DOI: 10.1109/COMST.2018.2868805.
- [71] S. S. Jaffer, A. Hussain, M. Qureshi, and W. S. Khawaja, “Towards the Shifting of 5G Front Haul Traffic on Passive Optical Network,” *Wireless Personal Communications*, vol. 112, pp. 1549–1568, 2020. DOI: 10.1007/s11277-020-07115-6.

- [72] Y. Tian, K. L. Lee, C. Lim, and A. Nirmalathas, "60 GHz Analog Radio-Over-Fiber Fronthaul Investigations," *Journal of Lightwave Technology*, vol. 35, no. 19, pp. 4304–4310, 2017. DOI: 10.1109/JLT.2017.2740436.
- [73] C. Lim, Y. Tian, C. Ranaweera, A. Nirmalathas, E. Wong, and K. L. Lee, "Evolution of Radio-Over-Fiber Technologies: Past and Present," in *2018 European Conference on Optical Communication (ECOC)*, 2018, pp. 1–3. DOI: 10.1109/ECOC.2018.8535106.
- [74] P. Massoud Salehi and J. Proakis, *Digital Communications*. McGraw-Hill Education, 2007.
- [75] P. Banelli, S. Buzzi, G. Colavolpe, A. Modenini, F. Rusek, and A. Ugolini, "Modulation Formats and Waveforms for 5G Networks: Who Will Be the Heir of OFDM?: An overview of alternative modulation schemes for improved spectral efficiency," *IEEE Signal Processing Magazine*, vol. 31, no. 6, pp. 80–93, 2014. DOI: 10.1109/MSP.2014.2337391.
- [76] J. M. Kahn and K. P. Ho, "Spectral efficiency limits and modulation/detection techniques for DWDM systems," *IEEE Journal of Selected Topics in Quantum Electronics*, vol. 10, no. 2, pp. 259–272, 2004. DOI: 10.1109/JSTQE.2004.826575.
- [77] P. J. Winzer and R. J. Essiambre, "Advanced optical modulation formats," *Proceedings of the IEEE*, vol. 94, no. 5, pp. 952–985, 2006. DOI: 10.1109/JPROC.2006.873438.
- [78] N. K. Mallat and S. O. Tatu, "Carrier recovery loop for millimeter-wave heterodyne receiver," in *2008 24th Biennial Symposium on Communications*, 2008, pp. 239–242. DOI: 10.1109/BSC.2008.4563247.
- [79] B. Shamla and D. K. G. Gayathri, "Design and implementation of Costas loop for BPSK demodulator," in *2012 Annual IEEE India Conference (INDICON)*, 2012, pp. 785–789. DOI: 10.1109/INDCON.2012.6420723.
- [80] *Recommendation G.992.3-200904-I sec: Asymmetric digital subscriber line transceivers 2 (ADSL2)*. International Telecommunication Union, 2009.
- [81] E. Ruggeri, A. Tsakyridis, C. Vagionas, *et al.*, "A 5G Fiber Wireless 4Gb/s WDM Fronthaul for Flexible 360° Coverage in V-Band massive MIMO Small Cells," *Journal of Lightwave Technology*, vol. 39, no. 4, pp. 1081–1088, 2021. DOI: 10.1109/JLT.2020.3029608.
- [82] T. S. Rappaport, *Wireless Communications: Principles and Practice* (Electrical engineering). Prentice Hall PTR, 1996.
- [83] D. D. Durgin and T. S. Rappaport, "Theory of multipath shape factors for small-scale fading wireless channels," *IEEE Transactions on Antennas and Propagation*, vol. 48, no. 5, pp. 682–693, 2000. DOI: 10.1109/8.855486.
- [84] T. Pollet, M. Moeneclaey, I. Jeanclaude, and H. Sari, "Comparison of Single-Carrier and Multi-Carrier QAM System Performance in the Presence of Carrier Phase Jitter," *Wireless Personal Communications*, vol. 8, no. 2, pp. 205–218, 1998. DOI: 10.1023/A:1008881323119.

- [85] M. S. Yee, M. Sandell, and Y. Sun, "Comparison study of single-carrier and multi-carrier modulation using iterative based receiver for MIMO system," in *2004 IEEE 59th Vehicular Technology Conference. VTC 2004-Spring (IEEE Cat. No.04CH37514)*, vol. 3, 2004, 1275–1279 Vol.3. DOI: 10.1109/VETECS.2004.1390458.
- [86] J. A. C. Bingham, "Multicarrier modulation for data transmission: An idea whose time has come," *IEEE Communications Magazine*, vol. 28, no. 5, pp. 5–14, 1990. DOI: 10.1109/35.54342.
- [87] J. Pérez Santacruz, S. Rommel, U. Johannsen, A. Jurado-Navas, and I. Tafur Monroy, "Candidate Waveforms for ARoF in Beyond 5G," *Applied Sciences*, vol. 10, no. 11, 2020. DOI: 10.3390/app10113891.
- [88] Y. Al-jawhar, K. Ramli, M. Taher, N. S. Mohd Shah, L. Audah, and M. Sami, "Zero-padding techniques in OFDM systems," *International Journal on Electrical Engineering and Informatics*, vol. 10, pp. 704–725, Jan. 2019. DOI: 10.15676/ijeei.2018.10.4.6.
- [89] A. A. Zaidi, R. Baldemair, M. Andersson, S. Faxér, V. Molés-Cases, and Z. Wang, "Designing for the future: the 5G NR physical layer," *Ericsson Technology Review*, 2017.
- [90] Y. G. Li and G. L. Stuber, *Orthogonal Frequency Division Multiplexing for Wireless Communications* (Signals and Communication Technology). Springer US, 2006.
- [91] J. D. Vega Sánchez, L. Urquiza-Aguiar, and M. C. Paredes Paredes, "Fading channel models for mm-wave communications," *Electronics*, vol. 10, no. 7, 2021. DOI: 10.3390/electronics10070798.
- [92] S. Redana, A. Kaloxylou, A. Galis, *et al.*, "View on 5G Architecture," 2016. DOI: 10.13140/RG.2.1.3815.7049.
- [93] 3GPP TS 38.104, *Base Station (BS) radio transmission and reception*. Version 16.3.0, Mar. 2020.
- [94] 3GPP TS 38.211, *Nr; physical channels and modulation*. Version 15.7.0, Sep. 2019.
- [95] A. Chen and E. J. Murphy, *Broadband Optical Modulators: Science, Technology, and Applications*. Taylor & Francis Group, 2020.
- [96] M. Doi, M. Sugiyama, K. Tanaka, and M. Kawai, "Advanced LiNbO₃ optical modulators for broadband optical communications," *IEEE Journal of Selected Topics in Quantum Electronics*, vol. 12, no. 4, pp. 745–750, 2006. DOI: 10.1109/JSTQE.2006.876192.
- [97] S. Akiyama and T. Usuki, "High-speed and efficient silicon modulator based on forward-biased pin diodes," *Frontiers in Physics*, vol. 2, p. 65, 2014. DOI: 10.3389/fphy.2014.00065.
- [98] T. Berceli and N. Badraoui, "Parasitic phase modulation in single drive mach-zehnder optical modulator," in *2017 19th International Conference on Transparent Optical Networks (ICTON)*, 2017, pp. 1–4. DOI: 10.1109/ICTON.2017.8025020.

- [99] J. Xiao, C. Tao, J. Li, *et al.*, “Design and modeling of Mach-Zehnder type electro-optic modulators: balanced and unbalanced interferometers,” in *Optoelectronic Devices and Integration IX*, X. Zhang, B. Li, C. Yu, and X. Zhang, Eds., International Society for Optics and Photonics, vol. 11547, SPIE, 2020, pp. 33–41. DOI: 10.1117/12.2573717.
- [100] W. Wang, F. Li, Z. Li, Q. Sui, and Z. Li, “Dual-Drive Mach-Zehnder Modulator-Based Single Side-Band Modulation Direct Detection System Without Signal-to-Signal Beating Interference,” *Journal of Lightwave Technology*, vol. 38, no. 16, pp. 4341–4351, 2020. DOI: 10.1109/JLT.2020.2992046.
- [101] S. Rommel, L. Yi, M. Shi, I. Tafur Monroy, and J. J. Vegas Olmos, “Demonstration of 4Gbit/s Duobinary Ka-Band Hybrid Photonic-Wireless Transmission,” in *Asia Communications and Photonics Conference 2015*, Optical Society of America, 2015, ASu1J.2. DOI: 10.1364/ACPC.2015.ASu1J.2.
- [102] J. Yu, G. K. Chang, Z. Jia, *et al.*, “Cost-Effective Optical Millimeter Technologies and Field Demonstrations for Very High Throughput Wireless-Over-Fiber Access Systems,” *Journal of Lightwave Technology*, vol. 28, no. 16, pp. 2376–2397, 2010. DOI: 10.1109/JLT.2010.2041748.
- [103] Y. Wu, X. B. Xie, J. H. Hodiak, S. M. Lord, and P. K. L. Yu, “Multioctave high dynamic range up-conversion optical-heterodyned microwave photonic link,” *IEEE Photonics Technology Letters*, vol. 16, no. 10, pp. 2332–2334, 2004. DOI: 10.1109/LPT.2004.834454.
- [104] *Recommendation ITU-R SM.1045-1: Frequency tolerance of transmitters*. International Telecommunication Union, 1997.
- [105] R. .-. Braun, G. Grosskopf, D. Rohde, and F. Schmidt, “Low-phase-noise millimeter-wave generation at 64 GHz and data transmission using optical side-band injection locking,” *IEEE Photonics Technology Letters*, vol. 10, no. 5, pp. 728–730, 1998. DOI: 10.1109/68.669405.
- [106] L. A. Johansson and A. J. Seeds, “Millimeter-wave modulated optical signal generation with high spectral purity and wide-locking bandwidth using a fiber-integrated optical injection phase-lock loop,” *IEEE Photonics Technology Letters*, vol. 12, no. 6, pp. 690–692, 2000. DOI: 10.1109/68.849086.
- [107] J. Yu, Z. Jia, L. Yi, Y. Su, G. K. Chang, and T. Wang, “Optical millimeter-wave generation or up-conversion using external modulators,” *IEEE Photonics Technology Letters*, vol. 18, no. 1, pp. 265–267, 2006. DOI: 10.1109/LPT.2005.862006.
- [108] S. Ahmadi, “Chapter 5 - New Radio Access RF and Transceiver Design Considerations,” in *5G NR*, Academic Press, 2019, pp. 655–745. DOI: <https://doi.org/10.1016/B978-0-08-102267-2.00005-1>.
- [109] S. Iezekiel, “Measurement of microwave behavior in optical links,” *IEEE Microwave Magazine*, vol. 9, no. 3, pp. 100–120, 2008. DOI: 10.1109/MM.2008.919935.

- [110] R. Hofstetter, H. Schmuck, and R. Heidemann, "Dispersion effects in optical millimeter-wave systems using self-heterodyne method for transport and generation," *IEEE Transactions on Microwave Theory and Techniques*, vol. 43, no. 9, pp. 2263–2269, 1995. DOI: 10.1109/22.414574.
- [111] S. Rommel, D. Dodane, E. Grivas, *et al.*, "Real-Time Demonstration of ARoF Fronthaul for High-Bandwidth mm-Wave 5G NR Signal Transmission over Multi-Core Fiber," in *2020 European Conference on Networks and Communications (EuCNC)*, 2020, pp. 205–208. DOI: 10.1109/EuCNC48522.2020.9200921.
- [112] O. E. DeLange, "Optical heterodyne detection," *IEEE Spectrum*, vol. 5, no. 10, pp. 77–85, 1968. DOI: 10.1109/MSPEC.1968.5215385.
- [113] R. Puerta and I. Tafur Monroy, "Single Photodiode, Single Wavelength, and Single Polarization 65 Gb/s 16-QAM and QPSK Coherent Transmission," in *2018 10th International Conference on Advanced Infocomm Technology (ICAIT)*, 2018, pp. 56–60. DOI: 10.1109/ICAIT.2018.8686726.
- [114] G. P. Agrawal, "Nonlinear fiber optics: Its history and recent progress," *J. Opt. Soc. Am. B*, vol. 28, no. 12, A1–A10, Dec. 2011. DOI: 10.1364/JOSAB.28.0000A1.
- [115] A. Pedersen Tegtmeier, L. Gruner-Nielsen, and K. Rottwitt, "Measurement and Modeling of Low-Wavelength Losses in Silica Fibers and Their Impact at Communication Wavelengths," *Journal of Lightwave Technology*, vol. 27, no. 10, pp. 1296–1300, 2009. DOI: 10.1109/JLT.2008.2012001.
- [116] T. Miya, Y. Terunuma, T. Hosaka, and T. Miyashita, "Ultimate low-loss single-mode fibre at 1.55 μm ," *Electronics Letters*, vol. 15, no. 4, pp. 106–108, 1979. DOI: 10.1049/el:19790077.
- [117] M. Ferrario, L. Marazzi, P. Boffi, A. Righetti, and M. Martinelli, "Impact of Rayleigh Backscattering on Stimulated Brillouin Scattering threshold evaluation for 10Gb/s NRZ-OOK signals," in *2008 Conference on Lasers and Electro-Optics and 2008 Conference on Quantum Electronics and Laser Science*, 2008, pp. 1–2. DOI: 10.1109/CLEO.2008.4551335.
- [118] G. P. Agrawal, *Fiber-optic communication systems*, Fourth Edition. John Wiley & Sons, 2010, ch. 2.
- [119] B. Saleh and M. Teich, *Fundamentals of Photonics*, Third Edition. John Wiley & Sons, 2019.
- [120] G. P. Agrawal, *Nonlinear Fiber Optics*, Fifth Edition. Academic Press, 2013. DOI: 10.1016/C2011-0-00045-5.
- [121] K. Rottwitt and P. Tidemand-Lichtenberg, *Nonlinear Optics: Principles and Applications* (Optical Sciences and Applications of Light). Taylor & Francis, 2014.
- [122] T. Sato, S. Makino, Y. Ishizaka, T. Fujisawa, and K. Saitoh, "A rigorous definition of nonlinear parameter γ ; and effective area A_{eff} for photonic crystal optical waveguides," *J. Opt. Soc. Am. B*, vol. 32, no. 6, pp. 1245–1251, Jun. 2015. DOI: 10.1364/JOSAB.32.001245.
- [123] R. del Coso and J. Solis, "Relation between nonlinear refractive index and third-order susceptibility in absorbing media," *J. Opt. Soc. Am. B*, vol. 21, no. 3, pp. 640–644, Mar. 2004. DOI: 10.1364/JOSAB.21.000640.

- [124] R. H. Stolen and C. Lin, "Self-phase-modulation in silica optical fibers," *Phys. Rev. A*, vol. 17, pp. 1448–1453, 4 Apr. 1978. DOI: 10.1103/PhysRevA.17.1448.
- [125] S. Singh and N. Singh, "Nonlinear effects in optical fibers: Origin, management and applications," *Progress in Electromagnetics Research-pier - PROG ELECTROMAGN RES*, vol. 73, pp. 249–275, Jan. 2007. DOI: 10.2528/PIER07040201.
- [126] U. Gliese, S. Norskov, and T. N. Nielsen, "Chromatic dispersion in fiber-optic microwave and millimeter-wave links," *IEEE Transactions on Microwave Theory and Techniques*, vol. 44, no. 10, pp. 1716–1724, 1996. DOI: 10.1109/22.538964.
- [127] J. Park, A. F. Elrefaie, and K. Y. Lau, "Fiber chromatic dispersion effects on multichannel digital millimeter-wave transmission," *IEEE Photonics Technology Letters*, vol. 8, no. 12, pp. 1716–1718, 1996. DOI: 10.1109/68.544729.
- [128] G. H. Smith, D. Novak, and Z. Ahmed, "Overcoming chromatic-dispersion effects in fiber-wireless systems incorporating external modulators," *IEEE Transactions on Microwave Theory and Techniques*, vol. 45, no. 8, pp. 1410–1415, 1997. DOI: 10.1109/22.618444.
- [129] M. Weiss, M. Huchard, A. Stohr, B. Charbonnier, S. Fedderwitz, and D. S. Jager, "60-GHz Photonic Millimeter-Wave Link for Short- to Medium-Range Wireless Transmission Up to 12.5 Gb/s," *Journal of Lightwave Technology*, vol. 26, no. 15, pp. 2424–2429, 2008. DOI: 10.1109/JLT.2008.927604.
- [130] S. Deng, M. K. Samimi, and T. S. Rappaport, "28 GHz and 73 GHz millimeter-wave indoor propagation measurements and path loss models," in *2015 IEEE International Conference on Communication Workshop (ICCW)*, 2015, pp. 1244–1250. DOI: 10.1109/ICCW.2015.7247348.
- [131] H. F. Huang and W. Zhao, "Planar triple-band antenna for LTE/GSM/UMTS and WLAN/WiMAX mobile device applications," *Microwave and Optical Technology Letters*, vol. 57, Oct. 2015. DOI: 10.1002/mop.29315.
- [132] Wikipedia. "GSM frequency bands." (2021), [Online]. Available: https://en.wikipedia.org/wiki/GSM_frequency_bands.
- [133] K. Yu, Y. Li, X. Luo, and X. Liu, "A modified E-shaped triple-band patch antenna for LTE communication applications," in *2016 IEEE International Symposium on Antennas and Propagation (APSURSI)*, 2016, pp. 295–296. DOI: 10.1109/APS.2016.7695856.
- [134] Y. H. Cui, R. Li, and P. Wang, "Novel Dual-Broadband Planar Antenna and Its Array for 2G/3G/LTE Base Stations," *IEEE Transactions on Antennas and Propagation*, vol. 61, no. 3, pp. 1132–1139, 2013. DOI: 10.1109/TAP.2012.2229377.
- [135] N. Al-Falahy and O. Y. K. Alani, "Millimetre wave frequency band as a candidate spectrum for 5G network architecture: A survey," *Physical Communication*, vol. 32, pp. 120–144, 2019. DOI: 10.1016/j.phycom.2018.11.003.
- [136] C. A. Balanis, *Antenna theory: analysis and design*, Fifth Edition. John Wiley & Sons, 2016.
- [137] M. Marcus and B. Pattan, "Millimeter wave propagation: Spectrum management implications," *IEEE Microwave Magazine*, vol. 6, no. 2, pp. 54–62, 2005. DOI: 10.1109/MMW.2005.1491267.

- [138] *Recommendation ITU-R P.676-12: Attenuation by atmospheric gases and related effects, Series P: Radiowave Propagation*. International Telecommunication Union, 2019.
- [139] P. Smulders, “Exploiting the 60 GHz band for local wireless multimedia access: prospects and future directions,” *IEEE Communications Magazine*, vol. 40, no. 1, pp. 140–147, 2002. DOI: 10.1109/35.978061.
- [140] C. Park and T. S. Rappaport, “Short-Range Wireless Communications for Next-Generation Networks: UWB, 60 GHz Millimeter-Wave WPAN, And ZigBee,” *IEEE Wireless Communications*, vol. 14, no. 4, pp. 70–78, 2007. DOI: 10.1109/MWC.2007.4300986.
- [141] R. Schulpen, A. B. Smolders, and U. Johannsen, “5G Millimeter-Wave Beam Adaptation for Indoor Moving Users,” in *2019 49th European Microwave Conference (EuMC)*, 2019, pp. 424–427. DOI: 10.23919/EuMC.2019.8910760.
- [142] Z. Pi and F. Khan, “An introduction to millimeter-wave mobile broadband systems,” *IEEE Communications Magazine*, vol. 49, no. 6, pp. 101–107, 2011. DOI: 10.1109/MCOM.2011.5783993.
- [143] S. Rommel, L. C. P. Cavalcante, A. G. Quintero, A. K. Mishra, J. J. Vegas Olmos, and I. Tafur Monroy, “W-band photonic-wireless link with a schottky diode envelope detector and bend insensitive fiber,” *Opt. Express*, vol. 24, no. 11, pp. 11 312–11 322, May 2016. DOI: 10.1364/OE.24.011312.
- [144] S. Rommel, L. C. P. Cavalcante, J. J. Vegas Olmos, I. Tafur Monroy, and A. K. Mishra, “Requirements for bend insensitive fiber in millimeter-wave fronthaul systems,” in *2015 International Topical Meeting on Microwave Photonics (MWP)*, 2015, pp. 1–4. DOI: 10.1109/MWP.2015.7356674.
- [145] X. L. J. Yu and G. K. Chang, “Photonics-Assisted Technologies for Extreme Broadband 5G Wireless Communications,” *Journal of Lightwave Technology*, vol. 37, no. 12, pp. 2851–2865, 2019. DOI: 10.1109/JLT.2019.2906498.
- [146] J. Sung, C. Chow, C. Yeh, Y. Liu, and G. Chang, “Cost-Effective Mobile Backhaul Network Using Existing ODN of PONs for the 5G Wireless Systems,” *IEEE Photonics Journal*, vol. 7, no. 6, pp. 1–6, Dec. 2015. DOI: 10.1109/JPHOT.2015.2497222.
- [147] A. H. Jafari, D. López-Pérez, H. Song, H. Claussen, L. Ho, and J. Zhang, “Small cell backhaul: Challenges and prospective solutions,” *EURASIP Journal on Wireless Communications and Networking*, vol. 2015, no. 1, p. 206, Aug. 2015. DOI: 10.1186/s13638-015-0426-y.
- [148] M. Fujiwara, K. Suzuki, N. Yoshimoto, M. Oguma, and S. Soma, “Increasing Splitting Ratio of 10Gb/s-Class PONs by Using FW-DMF that Acts as Low Loss Splitter for Upstream and Conventional Splitter for Downstream,” in *Optical Fiber Communication Conference*, Optical Society of America, 2014, Tu2C.5. DOI: 10.1364/OFC.2014.Tu2C.5.
- [149] J. Segarra, V. Sales, J. Prat, and L. Kazovsky, “Flexible coherent UDWDM-PON adapting dynamically to different bandwidths,” in *2017 19th International Conference on Transparent Optical Networks (ICTON)*, 2017, pp. 1–6. DOI: 10.1109/ICTON.2017.8024857.

- [150] Z. Dong, X. Li, J. Yu, Z. Cao, and N. Chi, “ 8×9.95 -Gb/s Ultra-Dense WDM-PON on a 12.5-GHz Grid With Digital Pre-Equalization,” *IEEE Photonics Technology Letters*, vol. 25, no. 2, pp. 194–197, Jan. 2013. DOI: 10.1109/LPT.2012.2233467.
- [151] J. S. Vardakas, I. Tafur Monroy, L. Wosinska, *et al.*, “Towards high capacity and low latency backhauling in 5G: The 5G STEP-FWD vision,” in *19th International Conf. on Transparent Optical Networks (ICTON)*, Jul. 2017, pp. 1–4. DOI: 10.1109/ICTON.2017.8025130.
- [152] J. S. Vardakas, E. Kartsakli, S. Papaioannou, *et al.*, “Quality of Service Provisioning in High-Capacity 5G Fronthaul/Backhaul Networks,” in *Interactive Mobile Communication Technologies and Learning*, M. E. Auer and T. Tsiatsos, Eds., Springer International Publishing, 2018, pp. 797–804. DOI: 10.1007/978-3-319-75175-7_78.
- [153] P. E. Green, “Fiber to the home: The next big broadband thing,” *IEEE Communications Magazine*, vol. 42, no. 9, pp. 100–106, Sep. 2004. DOI: 10.1109/MCOM.2004.1336726.
- [154] S. Abdelwahab, B. Hamdaoui, M. Guizani, and T. Znati, “Network function virtualization in 5G,” *IEEE Communications Magazine*, vol. 54, pp. 84–91, 2016. DOI: 10.1109/MCOM.2016.7452271.
- [155] T. Muciaccia and V. Passaro, “Future Scenarios for Software-Defined Metro and Access Networks and Software-Defined Photonics,” *Photonics*, vol. 4, p. 1, Jan. 2017. DOI: 10.3390/photonics4010001.
- [156] H. Weng, Y. Yang, J. Wu, *et al.*, “Dual-mode microcavity semiconductor lasers,” *IEEE Journal of Selected Topics in Quantum Electronics*, vol. 25, no. 6, pp. 1–8, Nov. 2019. DOI: 10.1109/JSTQE.2019.2918165.
- [157] P. Brochard, S. Bilicki, A. Shehzad, S. Schilt, and T. Sudmeyer, “Laser linewidth optimization in a feedback loop,” in *2017 European Conference on Lasers and Electro-Optics and European Quantum Electronics Conference*, 2017, pp. 4–3.
- [158] C. F. Wu, X. S. Yan, J. Q. Huang, J. W. Zhang, and L. J. Wang, “Phase noise reduction by optical phase-locked loop for a coherent bichromatic laser based on the injection-locking technique,” *Review of Scientific Instruments*, vol. 89, no. 1, p. 013 103, 2018. DOI: 10.1063/1.4993262.
- [159] S. Pachnicke, J. Zhu, M. Lawin, *et al.*, “Novel WDM-PON System with Shared Wavelength Locking and Full C-Band Tunability,” in *Photonic Networks; 15. ITG Symposium*, May 2014, pp. 1–5.
- [160] J. Segarra, V. Sales, V. Polo, and J. Prat, “Practical Design of a Coherent Ultra-Dense WDM-PON with Paired DFB Lasers,” in *2020 22nd International Conference on Transparent Optical Networks (ICTON)*, 2020, pp. 1–5. DOI: 10.1109/ICTON51198.2020.9203320.
- [161] J. Segarra, V. Sales, V. Polo, J. Tabares, and J. Prat, “Flexible coherent UDWDM-PON with dynamic user allocation based on limited-tunability lasers,” *J. Opt. Commun. Netw.*, vol. 12, no. 9, pp. D27–D35, Sep. 2020. DOI: 10.1364/JOCN.391023.

- [162] D. Coelho, P. Marciano, T. Coelho, M. Segatto, and M. Pontes, "Frequency Domain Interleaving for Dense WDM Passive Optical Network," *Journal of Microwaves, Optoelectronics and Electromagnetic Applications*, vol. 18, pp. 196–207, Jun. 2019. DOI: 10.1590/2179-10742019v18i21643.
- [163] M. Ferchichi, M. Najjar, and H. Rezig, "Design of Temperature-Strain Tunable UDWDM, DWDM, WDM FBG filter for Passive Optical Network Access," in *2008 2nd ICTON Mediterranean Winter*, Dec. 2008, pp. 1–5. DOI: 10.1109/ICTONMW.2008.4773074.
- [164] M. Sung, S. Cho, K. S. Kim, *et al.*, "Demonstration of IFoF based 5G mobile fronthaul in 28 GHz millimeter wave testbed supporting giga-bit mobile services," in *2017 Optical Fiber Communications Conference and Exhibition (OFC)*, Mar. 2017, pp. 1–3.
- [165] X. Guan, W. Shi, and L. A. Rusch, "Ultra-dense wavelength-division multiplexing with microring modulator," *Journal of Lightwave Technology*, vol. 39, no. 13, pp. 4300–4306, 2021. DOI: 10.1109/JLT.2021.3070515.
- [166] *Recommendation ITU-T G.694.1: Spectral grids for WDM applications: DWDM frequency grid*. International Telecommunication Union, 2020.
- [167] R. Huelsermann, K. Grobe, and D. Breuer, "Cost and performance evaluation of WDM-based access networks," in *2013 Optical Fiber Communication Conference and Exposition and the National Fiber Optic Engineers Conference (OFC/NFOEC)*, Mar. 2013, pp. 1–3. DOI: 10.1364/NFOEC.2013.NTh3F.4.
- [168] K. Grobe, M. Roppelt, M. Eiselt, and J. Elbers, "Combined reach, client-count, power-consumption, and cost analysis of wdm-based next-generation pon," in *2011 37th European Conference and Exhibition on Optical Communication*, Sep. 2011, pp. 1–3. DOI: 10.1364/ECOC.2011.We.10.P1.113.
- [169] M. Forzati, A. Bianchi, J. Chen, *et al.*, "Next-generation optical access seamless evolution: concluding results of the European FP7 Project OASE," *IEEE/OSA Journal of Optical Communications and Networking*, vol. 7, no. 2, pp. 109–123, Feb. 2015. DOI: 10.1364/JOCN.7.000109.
- [170] J. Segarra, V. Sales, V. Polo, and J. Prat, "Versatile Metro-Access Network Integrating FTTH, Enterprises, IoT and 5G Services," in *2019 21st International Conference on Transparent Optical Networks (ICTON)*, 2019, pp. 1–6. DOI: 10.1109/ICTON.2019.8840263.
- [171] R. Alaa, D. Forsyth, and K. Tariq, "Review of Comparative Booster Performances of Semiconductor Optical Amplifier and Erbium-doped-fiber Amplifier for use in Future Long-haul Optical Networks," *Research Journal of Applied Sciences, Engineering and Technology*, vol. 13, pp. 606–610, Oct. 2016. DOI: 10.19026/rjaset.13.3020.
- [172] S. Singh, A. Singh, and R. Kaler, "Performance evaluation of EDFA, RAMAN and SOA optical amplifier for WDM systems," *Optik*, vol. 124, no. 2, pp. 95–101, 2013. DOI: 10.1016/j.ijleo.2011.11.043.

- [173] X. Li, M. Luo, T. Zeng, *et al.*, “Coherent Bidirectional UDWDM-PON for 1000 ONUs with Real-Time Digital Signal Processing,” in *2018 European Conference on Optical Communication (ECOC)*, 2018, pp. 1–3. DOI: 10.1109/ECOC.2018.8535135.
- [174] J. Segarra, V. Sales, V. Polo, and J. Prat, “Flexible Mobile Fronthaul with Coherent UDWDM-PON,” in *2018 20th International Conference on Transparent Optical Networks (ICTON)*, 2018, pp. 1–6. DOI: 10.1109/ICTON.2018.8473897.
- [175] D. J. Richardson, J. Fini, and L. Nelson, “Space division multiplexing in optical fibres,” *Nature Photonics*, vol. 7, pp. 354–362, May 2013. DOI: 10.1038/nphoton.2013.94.
- [176] W. Klaus, B. J. Puttnam, R. S. Luis, *et al.*, “Advanced space division multiplexing technologies for optical networks [invited],” *IEEE/OSA Journal of Optical Communications and Networking*, vol. 9, no. 4, pp. C1–C11, 2017. DOI: 10.1364/JOCN.9.0000C1.
- [177] S. Rommel, J. M. Delgado Mendinueta, W. Klaus, *et al.*, “Characterization of a fiber-coupled 36-core 3-mode photonic lantern spatial multiplexer,” *Optical Society of America*, 2017, NeW3B.2. DOI: 10.1364/NETWORKS.2017.NeW3B.2.
- [178] T. Morishima, J. Ito, T. Shimazu, *et al.*, “MCF-enabled ultra-high-density 256-core MT connector and 96-core physical-contact MPO connector,” in *2017 Optical Fiber Communications Conference and Exhibition (OFC)*, 2017, pp. 1–3. DOI: 10.1364/OFC.2017.Th5D.4.
- [179] G. J. Foschini, “Layered space-time architecture for wireless communication in a fading environment when using multi-element antennas,” *Bell Labs Technical Journal*, vol. 1, no. 2, pp. 41–59, 1996. DOI: 10.1002/bltj.2015.
- [180] P. J. Winzer, “Spatial Multiplexing in Fiber Optics: The 10X Scaling of Metro/-Core Capacities,” *Bell Labs Technical Journal*, vol. 19, pp. 22–30, 2014. DOI: 10.15325/BLTJ.2014.2347431.
- [181] Y. Jung, J. R. Hayes, S. U. Alam, and D. J. Richardson, “Multicore Fibre Fan-In/Fan-Out Device using Fibre Optic Collimators,” in *2017 European Conference on Optical Communication (ECOC)*, 2017, pp. 1–3. DOI: 10.1109/ECOC.2017.8345892.
- [182] Y. Tottori, T. Kobayashi, and M. Watanabe, “Compact Fan-in/fan-out optical devices for multi-core fiber transmission,” in *2013 18th OptoElectronics and Communications Conference held jointly with 2013 International Conference on Photonics in Switching (OECC/PS)*, 2013, pp. 1–2. DOI: 10.1364/OECC_PS.2013.ThT1_1.
- [183] Z. Zakrzewski and J. Majewski, “Aspects of connecting the single-core and multi-core optical fibers,” in *Optical Fibers and Their Applications 2017*, J. Dorosz and R. S. Romaniuk, Eds., International Society for Optics and Photonics, vol. 10325, SPIE, 2017, pp. 114–126. DOI: 10.1117/12.2271081.
- [184] H. Yuan, A. Saljoghei, A. Peters, and G. Zervas, “Comparison of SDM-WDM based Data Center Networks with equal/unequal core pitch Multi-Core Fibers,” in *2018 Optical Fiber Communications Conference and Exposition (OFC)*, 2018, pp. 1–3. DOI: 10.1364/OFC.2018.M3J.4.

- [185] A. Morales, I. Tafur Monroy, F. Nordwall, and T. Sørensen, “50 GHz optical true time delay beamforming in hybrid optical/mm-wave access networks with multi-core optical fiber distribution,” *Chinese Optics Letters*, vol. 16, no. 4, p. 040603, Apr. 2018.
- [186] J. Brenes, T. D. Lagkas, D. Klonidis, *et al.*, “Network slicing architecture for SDM and analog-radio-over-fiber-based 5G fronthaul networks,” *IEEE/OSA Journal of Optical Communications and Networking*, vol. 12, no. 4, B33–B43, 2020. DOI: 10.1364/JOCN.381912.
- [187] J. H. Yan, Y. W. Chen, K. H. Shen, and K. M. Feng, “An experimental demonstration for carrier reused bidirectional PON system with adaptive modulation DDO-OFDM downstream and QPSK upstream signals,” *Opt. Express*, vol. 21, no. 23, pp. 28 154–28 166, Nov. 2013. DOI: 10.1364/OE.21.028154.
- [188] C. Beckman and B. Lindmark, “The Evolution of Base Station Antennas for Mobile Communications,” in *2007 International Conference on Electromagnetics in Advanced Applications*, Sep. 2007, pp. 85–92. DOI: 10.1109/ICEAA.2007.4387244.
- [189] Y. S. Cho, J. Kim, W. Y. Yang, and C. G. Kang, *MIMO-OFDM Wireless Communications with MATLAB*. Wiley Publishing, 2010.
- [190] C. Jeong, J. Park, and H. Yu, “Random access in millimeter-wave beamforming cellular networks: issues and approaches,” *IEEE Communications Magazine*, vol. 53, no. 1, pp. 180–185, Jan. 2015. DOI: 10.1109/MCOM.2015.7010532.
- [191] R. Karimian and H. Tadayon, “Multiband MIMO antenna system with parasitic element for WLAN and WiMAX application,” *International Journal of Antennas and Propagation*, vol. 2013, p. 7, Nov. 2013. DOI: 10.1155/2013/365719.
- [192] S. Parkvall, E. Dahlman, A. Furuskar, and M. Frenne, “NR: The New 5G Radio Access Technology,” *IEEE Communications Standards Magazine*, vol. 1, no. 4, pp. 24–30, Dec. 2017. DOI: 10.1109/MCOMSTD.2017.1700042.
- [193] R. Dilli, “Performance analysis of multi user massive MIMO hybrid beamforming systems at millimeter wave frequency bands,” *Wireless Networks*, vol. 27, Apr. 2021. DOI: 10.1007/s11276-021-02546-w.
- [194] B. Mondal, A. Sengupta, G. Ermolaev, V. Sergeev, A. Davydov, and E. Kwon, “Impact of Analog Beamforming on 5G-NR mmWave System Performance,” in *2018 IEEE 88th Vehicular Technology Conference (VTC-Fall)*, 2018, pp. 1–5. DOI: 10.1109/VTCFall.2018.8690942.
- [195] W. Roh, J. Y. Seol, J. Park, *et al.*, “Millimeter-wave beamforming as an enabling technology for 5G cellular communications: theoretical feasibility and prototype results,” *IEEE Communications Magazine*, vol. 52, no. 2, pp. 106–113, 2014. DOI: 10.1109/MCOM.2014.6736750.
- [196] N. H. M. Adnan, I. M. Rafiqul, and A. H. M. Z. Alam, “Massive MIMO for Fifth Generation (5G): Opportunities and Challenges,” in *2016 International Conference on Computer and Communication Engineering (ICCCE)*, Jul. 2016, pp. 47–52. DOI: 10.1109/ICCCE.2016.23.

- [197] A. B. Smolders, R. M. C. Mestrom, A. C. F. Reniers, and M. Geurts, “A Shared Aperture Dual-Frequency Circularly Polarized Microstrip Array Antenna,” *IEEE Antennas and Wireless Propagation Letters*, vol. 12, pp. 120–123, 2013. DOI: 10.1109/LAWP.2013.2242427.
- [198] A. Dubok, A. Al-Rawi, N. Tessema, *et al.*, “Double-Reflector Configuration for Optimal Exposure of Wideband Focal-Plane Arrays With Optical Beamforming,” *IEEE Transactions on Antennas and Propagation*, vol. 65, no. 8, pp. 4316–4321, Aug. 2017. DOI: 10.1109/TAP.2017.2709620.
- [199] M. V. Ivashina, O. Iupikov, R. Maaskant, W. A. van Cappellen, and T. Oosterloo, “An Optimal Beamforming Strategy for Wide-Field Surveys With Phased-Array-Fed Reflector Antennas,” *IEEE Transactions on Antennas and Propagation*, vol. 59, no. 6, pp. 1864–1875, Jun. 2011. DOI: 10.1109/TAP.2011.2123865.
- [200] A. B. Smolders, A. Dubok, N. M. Tessema, *et al.*, “Building 5G millimeter-wave wireless infrastructure: wide-scan focal plane arrays with broadband optical beamforming,” English, *IEEE Antennas and Propagation Magazine*, 2018. DOI: 10.1109/MAP.2019.2895662.
- [201] A. Elsakka, T. A. H. Bressner, A. J. van den Biggelaar, *et al.*, “On the use of focal-plane arrays in mm-wave 5G base stations,” English, in *12th European Conference on Antennas and Propagation (EuCAP 2018)*, United Kingdom: Institution of Engineering and Technology (IET), Dec. 2018, pp. 1–4. DOI: 10.1049/cp.2018.1207.
- [202] T. A. H. Bressner, U. Johannsen, and A. B. Smolders, “Single shot DoA estimation for large-array base station systems in multi-user environments,” in *Loughborough Antennas Propagation Conference (LAPC 2017)*, Nov. 2017, pp. 1–4. DOI: 10.1049/cp.2017.0288.
- [203] A. Morales, S. Rodríguez, O. Gallardo, J. J. Vegas Olmos, and I. Tafur Monroy, “Beam Steering Application for W-Band Data Links with Moving Targets in 5G Wireless Networks,” *Journal of Communications and Information Networks*, vol. 2, no. 2, pp. 91–100, 2017. DOI: 10.1007/s41650-017-0023-9.
- [204] S. Rommel, S. Rodríguez, L. Chorchos, *et al.*, “Outdoor W-Band Hybrid Photonic Wireless Link Based on an Optical SFP+ Module,” *IEEE Photonics Technology Letters*, vol. 28, no. 21, pp. 2303–2306, 2016. DOI: 10.1109/LPT.2016.2592326.
- [205] S. Rommel, S. Rodríguez, L. Chorchos, *et al.*, “225m Outdoor W-band radio-over-fiber link using an optical SFP+ module,” in *2016 Optical Fiber Communications Conference and Exhibition (OFC)*, 2016, pp. 1–3.
- [206] S. Alavi, R. Soltanian, I. Sadegh Amiri, M. Khalily, A. Supa’at, and H. Ahmad, “Towards 5G: A Photonic Based Millimeter Wave Signal Generation for Applying in 5G Access Fronthaul,” *Scientific Reports*, vol. 6, 2016.
- [207] L. Chorchos, S. Rommel, J. P. Turkiewicz, I. Tafur Monroy, and J. J. Vegas Olmos, “Reconfigurable Radio Access Unit for DWDM to W-Band Wireless Conversion,” *IEEE Photonics Technology Letters*, vol. 29, no. 6, pp. 489–492, 2017. DOI: 10.1109/LPT.2017.2656894.

- [208] L. C. P. Cavalcante, S. Rommel, R. Dinis, J. L. G. Q. Silveira, L. F. Q. Silveira, and I. Tafur Monroy, "Performance Evaluation of Wavelet-Coded OFDM on a 4.9 Gb/s W-Band Radio-Over-Fiber Link," *Journal of Lightwave Technology*, vol. 35, no. 14, pp. 2803–2809, 2017. DOI: 10.1109/JLT.2017.2701358.
- [209] S. Rommel, D. Dodane, E. Grivas, *et al.*, "Towards a Scaleable 5G Fronthaul: Analog Radio-over-Fiber and Space Division Multiplexing," *Journal of Lightwave Technology*, vol. 38, no. 19, pp. 5412–5422, 2020. DOI: 10.1109/JLT.2020.3004416.
- [210] SILIKA. "Silicon-based Ka-band massive MIMO antenna systems for new telecommunication services (SILIKA), This project has received funding from the European Union's Horizon 2020 research and innovation programme under the Marie Skłodowska Curie grant agreement No: 721732." (2016), [Online]. Available: <http://silika-project.eu/>.
- [211] blueSPACE. "Building on the Use of Spatial Multiplexing 5G Networks Infrastructures and Showcasing Advanced Technologies and Networking Capabilities (blueSPACE), This project has received funding from the European Union's Horizon 2020 research and innovation programme under grant agreement No: 762055." (2017), [Online]. Available: <https://www.bluespace-5gpp.eu/>.
- [212] M. SalarRahimi, E. Vilela Pinto dos Anjos, P. Taghikhani, *et al.*, "A Cost-Efficient 28 GHz Integrated Antenna Array With Full Impedance Matrix Characterization for 5G NR," *IEEE Antennas and Wireless Propagation Letters*, vol. 19, no. 4, pp. 666–670, 2020. DOI: 10.1109/LAWP.2020.2976188.
- [213] W. Shockley, "The theory of p-n junctions in semiconductors and p-n junction transistors," *The Bell System Technical Journal*, vol. 28, no. 3, pp. 435–489, 1949. DOI: 10.1002/j.1538-7305.1949.tb03645.x.
- [214] D. Benedikovic, L. Virost, G. Aubin, *et al.*, "Silicon-germanium receivers for short-wave-infrared optoelectronics and communications," *Nanophotonics*, vol. 10, no. 3, pp. 1059–1079, 2021. DOI: doi:10.1515/nanoph-2020-0547.
- [215] S. Kasap and P. Capper, *Springer Handbook of Electronic and Photonic Materials* (Springer Handbooks), Second Edition. Springer International Publishing, 2017.
- [216] M. Nada, F. Nakajima, T. Yoshimatsu, *et al.*, "High-speed III-V based avalanche photodiodes for optical communications—the forefront and expanding applications," *Applied Physics Letters*, vol. 116, no. 14, p. 140502, 2020. DOI: 10.1063/5.0003573. eprint: <https://doi.org/10.1063/5.0003573>.
- [217] L. Shen, "Ultrafast photodetector on the InP-membrane-on-silicon platform," Ph.D. dissertation, Department of Electrical Engineering, Nov. 2016.
- [218] H. Rongqing, *Introduction to Fiber-Optic Communications*. Academic Press, 2020.
- [219] J. Kniepert and N. Dieter, "Effect of the RC time on photocurrent transients and determination of charge carrier mobilities," *Journal of Applied Physics*, vol. 122, no. 19, p. 195501, 2017. DOI: 10.1063/1.4999278.
- [220] N. Shimizu, Y. Miyamoto, A. Hirano, K. Sato, and T. Ishibashi, "RF saturation mechanism of InP/InGaAs uni-travelling-carrier photodiode," *Electronics Letters*, vol. 36, pp. 750–751, 2000. DOI: 10.1049/el:20000555.

- [221] Z. Zhao, J. Liu, Y. Liu, and N. Zhu, "High-speed photodetectors in optical communication system," *Journal of Semiconductors*, vol. 38, p. 121 001, Dec. 2017. DOI: 10.1088/1674-4926/38/12/121001.
- [222] P. Safa O. Kasap, *Principles of Electronic Materials and Devices*. McGraw-Hill Education, 2005.
- [223] H. Ito, "Photonic terahertz-wave generation using uni-traveling-carrier photodiodes," in *Terahertz Physics, Devices, and Systems*, M. Anwar, A. J. DeMaria, and M. S. Shur, Eds., International Society for Optics and Photonics, vol. 6373, SPIE, 2006, pp. 1–12. DOI: 10.1117/12.684362.
- [224] T. Ishibashi, N. Shimizu, S. Kodama, H. Ito, T. Nagatsuma, and T. Furuta, "Uni-Traveling-Carrier Photodiodes," in *Ultrafast Electronics and Optoelectronics*, Optical Society of America, 1997, UC3. DOI: 10.1364/UEO.1997.UC3.
- [225] H. Ito, T. Nagatsuma, and T. Ishibashi, "Uni-traveling-carrier photodiodes for high-speed detection and broadband sensing - art. no. 64790x," *Proceedings of SPIE - The International Society for Optical Engineering*, vol. 6479, Mar. 2007. DOI: 10.1117/12.698221.
- [226] Q. Zhou, A. S. Cross, A. Beling, Y. Fu, Z. Lu, and J. C. Campbell, "High-Power V-Band InGaAs/InP Photodiodes," *IEEE Photonics Technology Letters*, vol. 25, no. 10, pp. 907–909, 2013. DOI: 10.1109/LPT.2013.2253766.
- [227] S. Preu, G. Dohler, S. Malzer, L. Wang, and A. Gossard, "Tunable, continuous-wave Terahertz photomixer sources and applications," *Journal of Applied Physics*, vol. 109, pp. 061 301–061 301, Mar. 2011. DOI: 10.1063/1.3552291.
- [228] J. Thobel, L. Baudry, A. Cappy, P. Bourel, and R. Fauquembergue, "Electron transport properties of strained In_xGa_{1-x}As," *Applied Physics Letters*, vol. 56, pp. 346–348, Feb. 1990. DOI: 10.1063/1.102780.
- [229] T. Ishibashi, T. Furuta, H. Fushimi, and H. Ito, "Photoresponse characteristics of uni-traveling-carrier photodiodes," in *Physics and Simulation of Optoelectronic Devices IX*, Y. Arakawa, P. Blood, and M. Osinski, Eds., International Society for Optics and Photonics, vol. 4283, SPIE, 2001, pp. 469–479. DOI: 10.1117/12.432597.
- [230] P. Razavi, S. Schulz, B. Roycroft, B. Corbett, and E. O'Reilly, "Design guidelines for edge-coupled waveguide unitraveling carrier photodiodes with improved bandwidth," *IET Optoelectronics*, vol. 13, May 2019. DOI: 10.1049/iet-opt.2018.5171.
- [231] H. Ito, S. Kodama, Y. Muramoto, T. Furuta, T. Nagatsuma, and T. Ishibashi, "High-speed and high-output InP-InGaAs unitraveling-carrier photodiodes," *IEEE Journal of Selected Topics in Quantum Electronics*, vol. 10, no. 4, pp. 709–727, Jul. 2004. DOI: 10.1109/JSTQE.2004.833883.
- [232] K. J. Williams and R. D. Esman, "Design considerations for high-current photodetectors," *Journal of Lightwave Technology*, vol. 17, no. 8, pp. 1443–1454, Aug. 1999.
- [233] K. Sun and A. Beling, "High-speed photodetectors for microwave photonics," *Applied Sciences*, vol. 9, no. 4, 2019. DOI: 10.3390/app9040623.

- [234] R. P. Riesz, "High speed semiconductor photodiodes," *Review of Scientific Instruments*, vol. 33, no. 9, pp. 994–998, 1962. DOI: 10.1063/1.1718049.
- [235] Q. Li, K. Sun, K. Li, *et al.*, "High-Power Evanescently Coupled Waveguide MUTC Photodiode With > 105-GHz Bandwidth," *Journal of Lightwave Technology*, vol. 35, no. 21, pp. 4752–4757, 2017. DOI: 10.1109/JLT.2017.2759210.
- [236] B. Zhang, Y. Xiong, L. Wang, S. Hu, and J. L. Li, "On the De-Embedding Issue of Millimeter-Wave and Sub-Millimeter-Wave Measurement and Circuit Design," *IEEE Transactions on Components, Packaging and Manufacturing Technology*, vol. 2, no. 8, pp. 1361–1369, 2012.
- [237] M. Achouche, V. Magnin, J. Harari, *et al.*, "High performance evanescent edge coupled waveguide untraveling-carrier photodiodes for >40-gb/s optical receivers," *IEEE Photon. Technol. Lett.*, vol. 16, no. 2, pp. 584–586, 2004.
- [238] A. Rumiantsev and N. Ridler, "Vna calibration," *IEEE Microwave Magazine*, vol. 9, no. 3, pp. 86–99, 2008. DOI: 10.1109/MMM.2008.919925.
- [239] J. Martens, D. Judge, and J. Bigelow, "Multiport vector network analyzer measurements," *IEEE Microwave Magazine*, vol. 6, no. 4, pp. 72–81, 2005. DOI: 10.1109/MMW.2005.1580339.
- [240] V. Teppati and A. Ferrero, "A Comparison of Uncertainty Evaluation Methods for On-Wafer *S*-Parameter Measurements," *IEEE Transactions on Instrumentation and Measurement*, vol. 63, no. 4, pp. 935–942, 2014. DOI: 10.1109/TIM.2013.2287796.
- [241] B. Elamran, R. D. Pollard, and S. Iezekiel, "Implementation and calibration of a two-port electrooptic network analyzer," *IEEE Microwave and Guided Wave Letters*, vol. 9, no. 9, pp. 369–371, 1999. DOI: 10.1109/75.790477.
- [242] S. Zhang, C. Zhang, H. Wang, Y. Liu, J. D. Peters, and J. E. Bowers, "On-wafer probing-kit for RF characterization of silicon photonic integrated transceivers," *Opt. Express*, vol. 25, no. 12, pp. 13 340–13 350, Jun. 2017. DOI: 10.1364/OE.25.013340.
- [243] Z. Chen, Y. L. Wang, Y. Liu, and N. H. Zhu, "Two-port calibration of test fixtures with OSL method," in *2002 3rd International Conference on Microwave and Millimeter Wave Technology, 2002. Proceedings. ICMMT 2002.*, 2002, pp. 138–141. DOI: 10.1109/ICMMT.2002.1187654.
- [244] C. Souria, T. Parra, G. Montoriol, and C. Landez, "Accurate package model extraction up to 110 GHz using one-port measurements. Application to a 77 GHz radar transceiver," in *2016 IEEE Radio and Wireless Symposium (RWS)*, 2016, pp. 91–94. DOI: 10.1109/RWS.2016.7444374.
- [245] G. J. Scalzi, A. J. Slobodnik, and G. A. Roberts, "Network analyzer calibration using offset shorts," *IEEE Transactions on Microwave Theory and Techniques*, vol. 36, no. 6, pp. 1097–1100, 1988. DOI: 10.1109/22.3638.
- [246] C. Cho, J.-S. Kang, J.-G. Lee, and H. Koo, "Characterization of a 1 mm (DC to 110 GHz) Calibration Kit for VNA," *J. Electromagn. Eng. Sci.*, vol. 19, no. 4, pp. 272–278, 2019. DOI: 10.26866/jees.2019.19.4.272. eprint: <http://jees.kr/journal/view.php?number=3362>.

- [247] *EURAMET Calibration Guide No. 12: Guidelines on the Evaluation of Vector Network Analysers (VNA)*. EURAMET e.V., Technical Committee for Electricity and Magnetism, 2018.
- [248] J. P. Hoffmann, P. Leuchtmann, and R. Vahldieck, "Over-determined offset short calibration of a VNA," in *2008 71st ARFTG Microwave Measurement Conference*, 2008, pp. 1–4. DOI: 10.1109/ARFTG.2008.4633318.
- [249] D. Rytting, "Appendix to an analysis of vector measurement accuracy enhancement techniques," *Hewlett Packard*, pp. 1–42, 1982.
- [250] G. N. Phung, F. J. Schmückle, and W. Heinrich, "Parasitic effects and measurement uncertainties in multi-layer thin-film structures," in *2013 European Microwave Conference*, 2013, pp. 318–321. DOI: 10.23919/EuMC.2013.6686655.
- [251] F. J. Schmückle, R. Doerner, G. N. Phung, W. Heinrich, D. Williams, and U. Arz, "Radiation, multimode propagation, and substrate modes in W-band CPW calibrations," in *2011 41st European Microwave Conference*, 2011, pp. 297–300. DOI: 10.23919/EuMC.2011.6101804.
- [252] M. Spirito, G. Gentile, and A. Akhnoukh, "Multimode analysis of transmission lines and substrates for (sub)mm-wave calibration," in *82nd ARFTG Microwave Measurement Conference*, 2013, pp. 1–6. DOI: 10.1109/ARFTG-2.2013.6737356.
- [253] R. Torres-Torres, G. Hernandez-Sosa, G. Romo, and A. Sanchez, "Characterization of Electrical Transitions Using Transmission Line Measurements," *IEEE Transactions on Advanced Packaging*, vol. 32, no. 1, pp. 45–52, 2009. DOI: 10.1109/TADVP.2008.2004631.
- [254] H. Votsi, I. Roch-Jeune, K. Haddadi, *et al.*, "Development of a reference wafer for on-wafer testing of extreme impedance devices," in *2016 88th ARFTG Microwave Measurement Conference (ARFTG)*, 2016, pp. 1–4. DOI: 10.1109/ARFTG.2016.7839719.
- [255] M. A. Yeganeh, S. Rahmatallahpur, A. Nozad, and R. K. Mamedov, "Effect of diode size and series resistance on barrier height and ideality factor in nearly ideal au/n type-GaAs micro schottky contact diodes," *Chinese Physics B*, vol. 19, no. 10, p. 107 207, Oct. 2010. DOI: 10.1088/1674-1056/19/10/107207.
- [256] J. Lee, S. Kim, J. Hong, and S. Lee, "Erratum: STI edge effect on the series resistance of CMOS Schottky barrier diodes," *Microwave and Optical Technology Letters*, vol. 56, no. 8, pp. 1970–1970, 2014. DOI: <https://doi.org/10.1002/mop.28494>. eprint: <https://onlinelibrary.wiley.com/doi/pdf/10.1002/mop.28494>.
- [257] Y. Tang, J. Liu, D. Wang, and Y. Wang, "RF characterization and modeling of CMOS Schottky diodes," in *2015 IEEE MTT-S International Microwave Symposium*, 2015, pp. 1–4. DOI: 10.1109/MWSYM.2015.7166913.
- [258] Y. Wang, Z. Pan, Y. Tang, and J. Liu, "Modeling of Si Schottky diodes and its application in THz imaging," in *2015 Asia-Pacific Microwave Conference (APMC)*, vol. 1, 2015, pp. 1–3. DOI: 10.1109/APMC.2015.7411759.

- [259] O. Doussin, D. Bajon, S. Wane, P. Magnan, and T. Parra, "Integrated Schottky Diodes for sub-millimeter and THz passive imaging: Influence of detector arrays topology," in *2013 IEEE Radio and Wireless Symposium*, 2013, pp. 52–54. DOI: 10.1109/RWS.2013.6486638.
- [260] T. Kiuru, K. Dahlberg, J. Mallat, A. V. Räisänen, and T. Närhi, "Comparison of low-frequency and microwave frequency capacitance determination techniques for mm-wave schottky diodes," in *2011 6th European Microwave Integrated Circuit Conference*, 2011, pp. 53–56.
- [261] E. C. Marques da Costa, S. Kurokawa, A. J. do Prado, and J. Pissolato, "Proposal of an alternative transmission line model for symmetrical and asymmetrical configurations," *International Journal of Electrical Power & Energy Systems*, vol. 33, 2011.
- [262] C. Fritsche and V. Krozer, "Large-signal PIN diode model for ultra-fast photode-tectors," in *2005 EuMC*, vol. 2, 2005, 4 pp.–1218.
- [263] Gang Wang, T. Tokumitsu, I. Hanawa, Y. Yoneda, K. Sato, and M. Kobayashi, "A time-delay equivalent-circuit model of ultrafast p-i-n photodiodes," *IEEE Trans. Microw. Theory Tech.*, vol. 51, no. 4, pp. 1227–1233, Apr. 2003. DOI: 10.1109/TMTT.2003.809642.
- [264] P. Angelini, F. Blache, C. Caillaud, *et al.*, "Record -22.5-dBm Sensitivity SOA-PIN-TIA Photoreceiver Module for 40-Gb/s Applications," *IEEE Photonics Technology Letters*, vol. 27, no. 19, pp. 2027–2030, 2015. DOI: 10.1109/LPT.2015.2449356.
- [265] V. Velayudhan, E. Pistono, and J. Arnould, "Half-Thru de-embedding method for millimeter-wave and sub-millimeter-wave integrated circuits," in *2014 10th Conference on Ph.D. Research in Microelectronics and Electronics (PRIME)*, 2014, pp. 1–4. DOI: 10.1109/PRIME.2014.6872692.
- [266] M. K. Matters-Kammerer, L. Tripodi, R. van Langevelde, J. Cumana, and R. H. Jansen, "RF Characterization of Schottky Diodes in 65-nm CMOS," *IEEE Transactions on Electron Devices*, vol. 57, no. 5, pp. 1063–1068, 2010. DOI: 10.1109/TED.2010.2043402.
- [267] M. Anagnosti, C. Caillaud, J. Paret, *et al.*, "Record Gain x Bandwidth (6.1 THz) Monolithically Integrated SOA-UTC Photoreceiver for 100-Gbit/s Applications," *Journal of Lightwave Technology*, vol. 33, no. 6, pp. 1186–1190, 2015. DOI: 10.1109/JLT.2014.2372816.
- [268] M. C. A. M. Koolen, "On-wafer high-frequency device characterization," in *ESS-DERC '92*, Sep. 1992, pp. 679–686. DOI: 10.1016/0167-9317(92)90521-R.
- [269] L. F. Tiemeijer, R. M. T. Pijper, and E. van der Heijden, "Two Multiport De-Embedding Methods for Accurate On-Wafer Characterization of 60-GHz Differential Amplifiers," *IEEE Transactions on Microwave Theory and Techniques*, vol. 59, no. 3, pp. 763–771, 2011. DOI: 10.1109/TMTT.2010.2095879.
- [270] G. Lucovsky, M. E. Lasser, and R. B. Emmons, "Coherent light detection in solid-state photodiodes," *Proceedings of the IEEE*, vol. 51, no. 1, pp. 166–172, 1963.

- [271] D. M. Cortés-Hernández, R. J. Sánchez-Mesa, S. C. Sejas-García, and R. Torres-Torres, "Extraction of Frequency-Dependent Characteristic Impedance and Complex Permittivity in Single-Ended and Edge-Coupled Transmission Lines Using the Calculated Series Parasitic Effects," *IEEE Trans. Microw. Theory Techn.*, vol. 65, no. 9, pp. 3116–3122, Sep. 2017. DOI: 10.1109/TMTT.2017.2730842.
- [272] D. Pozar, *Microwave Engineering, 4th Edition*. Wiley, 2011.
- [273] A. R. M. Alamoud, B. A. Al-Mashary, and H. F. Ragaie, "Static and Dynamic Characterization of P-N Junction Solar Cells," *Journal of King Saud University - Engineering Sciences*, vol. 10, no. 2, pp. 183–199, 1998. DOI: 10.1016/S1018-3639(18)30695-0.
- [274] A. H. Steinbach, I. Penn, N. Chokshi, *et al.*, "Equivalent circuit modelling of p-i-n photodiodes for 40 Gb/s receivers," in *The 15th Annual Meeting of the IEEE Lasers and Electro-Optics Society*, vol. 2, 2002, 486–487 vol.2. DOI: 10.1109/LEOS.2002.1159393.
- [275] J. Semple, D. G. Georgiadou, G. Wyatt-Moon, G. Gelinck, and T. D. Anthopoulos, "Flexible diodes for radio frequency (RF) electronics: A materials perspective," *Semiconductor Science and Technology*, vol. 32, no. 12, p. 123 002, Oct. 2017. DOI: 10.1088/1361-6641/aa89ce.
- [276] M. Natrella, C. Liu, C. Graham, *et al.*, "Accurate equivalent circuit model for millimetre-wave UTC photodiodes," *Opt. Express*, vol. 24, no. 5, pp. 4698–4713, Mar. 2016. DOI: 10.1364/OE.24.004698.
- [277] Z. Xu and J. Gao, "Semi-analytical small signal parameter extraction method for PIN photodiode," *IET Optoelectronics*, vol. 11, no. 3, pp. 103–107, 2017. DOI: 10.1049/iet-opt.2016.0051.
- [278] D. A. Frickey, "Conversions between S, Z, Y, H, ABCD, and T parameters which are valid for complex source and load impedances," *IEEE Trans. Microw. Theory Techn.*, vol. 42, no. 2, pp. 205–211, Feb. 1994. DOI: 10.1109/22.275248.
- [279] W.-C. Chuang, C.-W. Wang, W.-C. Chu, P.-Z. Chang, and Y.-C. Hu, "The fringe capacitance formula of microstructures," *Journal of Micromechanics and Micro-engineering*, vol. 22, no. 2, p. 025 015, Jan. 2012. DOI: 10.1088/0960-1317/22/2/025015.
- [280] K. Srinivasa Rao, B. V. Sailaja, G. Sravani, *et al.*, "A Generalized Capacitance Model of RF MEMS Switch by considering the Fringing Effect," *IEEE Access*, pp. 1–1, Mar. 2019. DOI: 10.1109/ACCESS.2018.2889724.
- [281] F. Yu, K. Sun, Q. Yu, and A. Beling, "High-speed evanescently-coupled waveguide type-II mutc photodiodes for zero-bias operation," *Journal of Lightwave Technology*, pp. 1–1, 2020. DOI: 10.1109/JLT.2020.3014056.
- [282] W. Khelifi, T. Reveyrand, J. Lintignat, *et al.*, "Pad-open-short de-embedding method extended for 3-port devices and non-ideal standards," in *2017 89th ARFTG Microwave Measurement Conference (ARFTG)*, 2017, pp. 1–4.
- [283] P. Angelini, F. Blache, F. Jorge, *et al.*, "64-Gb/s Optical Transmission Using DFB-EAM Transmitter and SOA-PIN-TIA Receiver with -23.5-dBm Record Sensitivity," in *ECOC 2016; 42nd European Conference on Optical Communication*, 2016, pp. 1–3.

- [284] H. Li, C. M. Hsu, J. Sharma, J. Jaussi, and G. Balamurugan, "A 100-Gb/s PAM-4 Optical Receiver With 2-Tap FFE and 2-Tap Direct-Feedback DFE in 28-nm CMOS," *IEEE Journal of Solid-State Circuits*, pp. 1–1, 2021. DOI: 10.1109/JSSC.2021.3110088.
- [285] L. Zhihao, M. Berroth, V. Hurm, *et al.*, "25 Gb/s AGC amplifier, 22 GHz transimpedance amplifier and 27.7 GHz limiting amplifier ICs using AlGaAs/GaAs-HEMTs," in *1997 IEEE International Solids-State Circuits Conference. Digest of Technical Papers*, 1997, pp. 356–357. DOI: 10.1109/ISSCC.1997.585418.
- [286] D. Streit, R. Lai, A. Gutierrez-Aitken, *et al.*, "InP and GaAs components for 40 Gbps applications," in *GaAs IC Symposium. IEEE Gallium Arsenide Integrated Circuit Symposium. 23rd Annual Technical Digest 2001 (Cat. No.01CH37191)*, 2001, pp. 247–250. DOI: 10.1109/GAAS.2001.964387.
- [287] D. Y. Jung, S. H. Park, K. H. Lee, *et al.*, "An InGaP/GaAs HBT transimpedance amplifier for 10 Gbps optical communication," in *2002 3rd International Conference on Microwave and Millimeter Wave Technology, 2002. Proceedings. ICMMT 2002.*, 2002, pp. 974–977. DOI: 10.1109/ICMMT.2002.1187866.
- [288] T. Shivan, E. Kaule, M. Hossain, *et al.*, "Design and modeling of an ultra-wideband low-noise distributed amplifier in InP DHBT technology," *International Journal of Microwave and Wireless Technologies*, vol. 11, no. 7, pp. 635–644, 2019. DOI: 10.1017/S1759078719000515.
- [289] F. Schwierz and J. Liou, "Semiconductor devices for rf applications: Evolution and current status," *Microelectronics Reliability*, vol. 41, no. 2, pp. 145–168, 2001. DOI: 10.1016/S0026-2714(00)00076-7.
- [290] P. Ashburn, *Basic Bipolar Transistor Theory*. John Wiley & Sons, Ltd, 2003.
- [291] W. Liu, *Handbook of III-V Heterojunction Bipolar Transistors*. Wiley, 1998.
- [292] H. Kroemer, "Theory of a wide-gap emitter for transistors," *Proceedings of the IRE*, vol. 45, no. 11, pp. 1535–1537, 1957. DOI: 10.1109/JRPROC.1957.278348.
- [293] N. Kashio, T. Hoshi, K. Kurishima, M. Ida, and H. Matsuzaki, "Improvement of High-Frequency Characteristics of InGaAsSb-Base Double Heterojunction Bipolar Transistors by Inserting a Highly Doped GaAsSb Base Contact Layer," *IEEE Electron Device Letters*, vol. 36, no. 7, pp. 657–659, 2015. DOI: 10.1109/LED.2015.2429142.
- [294] T. K. Johansen, M. Hossain, R. Doerner, *et al.*, "Modeling of InP DHBTs in a Transferred-Substrate Technology with Diamond Heat Spreader," in *2020 15th European Microwave Integrated Circuits Conference (EuMIC)*, 2021, pp. 169–172. DOI: 10.1109/EuMIC48047.2021.00054.
- [295] T. Shivan, M. Hossain, R. Doerner, *et al.*, "A 175 GHz Bandwidth High Linearity Distributed Amplifier in 500 nm InP DHBT Technology," in *2019 IEEE MTT-S International Microwave Symposium (IMS)*, 2019, pp. 1253–1256. DOI: 10.1109/MWSYM.2019.8700895.
- [296] N. G. Weimann, T. K. Johansen, D. Stoppel, *et al.*, "Transferred-Substrate InP/GaAsSb Heterojunction Bipolar Transistor Technology With f_{\max} 0.53 THz," *IEEE Transactions on Electron Devices*, vol. 65, no. 9, pp. 3704–3710, 2018. DOI: 10.1109/TED.2018.2854546.

- [297] G. Bruun, "Common-Emitter Transistor Video Amplifiers," *Proceedings of the IRE*, vol. 44, no. 11, pp. 1561–1572, 1956. DOI: 10.1109/JRPROC.1956.274875.
- [298] C. Sahu and N. Agrawal, "Mixed-Mode Simulation of Common Emitter Amplifier Design Using Bipolar Charge Plasma Transistor," in *2016 IEEE International Symposium on Nanoelectronic and Information Systems (iNIS)*, 2016, pp. 149–154. DOI: 10.1109/iNIS.2016.043.
- [299] J. L. Hood, *The Art of Linear Electronics* (EDN Series). Butterworth-Heinemann, 1993.
- [300] A. S. Sedra and K. C. Smith, *Microelectronic Circuits* (Oxford series in electrical and computer engineering), Seventh Edition. Oxford University Press, 2015.
- [301] M. Hossain, N. Weimann, V. Krozer, and W. Heinrich, "A 100 GHz fundamental oscillator with 25% efficiency based on transferred-substrate InP-DHBT technology," in *2016 46th European Microwave Conference (EuMC)*, 2016, pp. 497–500. DOI: 10.1109/EuMC.2016.7824388.
- [302] T. K. Johansen, M. Rudolph, T. Jensen, *et al.*, "Small- and large-signal modeling of InP HBTs in transferred-substrate technology," *International Journal of Microwave and Wireless Technologies*, vol. 6, no. 3-4, pp. 243–251, 2014. DOI: 10.1017/S1759078714000051.
- [303] N. V. L. Narasimha Murty and M. Hemalata Rao, "Analytical study of substrate parasitic effects in common-base and common-emitter SiGe BHT amplifiers," *Journal of Microwaves, Optoelectronics and Electromagnetic Applications*, vol. 12, pp. 217–228, Jun. 2013. DOI: 10.1590/S2179-10742013000100017.
- [304] T. Shivan, M. Hossain, R. Doerner, *et al.*, "A Highly Linear Dual-Stage Amplifier With Beyond 1.75-THz Gain-Bandwidth Product," *IEEE Microwave and Wireless Components Letters*, vol. 31, no. 6, pp. 717–720, 2021. DOI: 10.1109/LMWC.2021.3067145.
- [305] G. Coviello, F. Cannone, and G. Avitabile, "Robust behavioral non uniform look-up table spacing in adaptive digital baseband predistortion technique for rf power amplifier," in *2013 Africon*, 2013, pp. 1–5. DOI: 10.1109/AFRCON.2013.6757706.
- [306] J. Rollett, "Stability and Power-Gain Invariants of Linear Twoports," *IRE Transactions on Circuit Theory*, vol. 9, no. 1, pp. 29–32, 1962. DOI: 10.1109/TCT.1962.1086854.
- [307] G. Gonzalez, *Microwave Transistor Amplifiers: Analysis and Design*. Prentice Hall, 1997.
- [308] J. Mullrich, H. Thurner, E. Mullner, *et al.*, "High-gain transimpedance amplifier in InP-based HBT technology for the receiver in 40-Gb/s optical-fiber TDM links," *IEEE Journal of Solid-State Circuits*, vol. 35, no. 9, pp. 1260–1265, 2000. DOI: 10.1109/4.868033.
- [309] H. Escid, N. Gachi, A. Sebti, and A. Slimane, "High bandwidth 0.18 μ m CMOS transimpedance amplifier for photoreceiver circuit," in *2012 24th International Conference on Microelectronics (ICM)*, 2012, pp. 1–4. DOI: 10.1109/ICM.2012.6471431.

- [310] J. E. Goell, "An optical repeater with high-impedance input amplifier," *The Bell System Technical Journal*, vol. 53, no. 4, pp. 629–643, 1974. DOI: 10.1002/j.1538-7305.1974.tb02761.x.
- [311] S. D. Personick, N. L. Rhodes, D. C. Hanson, and K. H. Chan, "Contrasting fiber-optic-component-design requirements in telecommunications, analog, and local data communications applications," *Proceedings of the IEEE*, vol. 68, no. 10, pp. 1254–1262, 1980. DOI: 10.1109/PROC.1980.11841.
- [312] M. Reinhold, C. Dorschky, E. Rose, *et al.*, "A fully integrated 40-Gb/s clock and data recovery IC with 1:4 DEMUX in SiGe technology," *IEEE Journal of Solid-State Circuits*, vol. 36, no. 12, pp. 1937–1945, 2001. DOI: 10.1109/4.972144.
- [313] A. Kowalski and A. Zakrzewski, "The Calculation Of Optical Receiver Sensitivity," in *Optical Fibres and Their Applications IV*, R. S. Romaniuk and M. Szustakowski, Eds., International Society for Optics and Photonics, vol. 0670, SPIE, 1986, pp. 85–87. DOI: 10.1117/12.938970.
- [314] J. Leibrich, M. Serbay, S. Baumgart, W. Rosenkranz, and M. Schimmmler, "Receiver Sensitivity of Advanced Modulation Formats for 40 Gb/s DWDM Transmission with and without FEC," in *2006 European Conference on Optical Communications*, 2006, pp. 1–2. DOI: 10.1109/ECOC.2006.4801301.
- [315] B. Sklar, "The Sixteen Faces of Feedback: A Catalogue of the Basic Negative Feedback Amplifier Configurations," *IEEE Transactions on Education*, vol. 10, no. 3, pp. 161–166, 1967. DOI: 10.1109/TE.1967.4320268.
- [316] W. K. Chen, *Active Network Analysis* (Advanced series in electrical and computer engineering). World Scientific, 1991.
- [317] J. H. Mulligan, "Transient response and the stabilization of feedback amplifiers," *Transactions of the American Institute of Electrical Engineers, Part II: Applications and Industry*, vol. 78, no. 6, pp. 495–503, 1960. DOI: 10.1109/TAI.1960.6371619.
- [318] J. G. Graeme, *Photodiode Amplifiers: OP AMP Solutions* (Gain technology). McGraw-Hill Education, 1996.
- [319] M. Demirtas, Erismis, and S. Gunes, "Analysis and design of a transimpedance amplifier based front-end circuit for capacitance measurements," *SN Applied Sciences*, vol. 2, pp. 2523–3971, 2019. DOI: 10.1007/s42452-020-2104-x.
- [320] B. Razavi, *Design of Integrated Circuits for Optical Communications*. Wiley, 2012.
- [321] A. Romanova and V. Barzdenas, "A Review of Modern CMOS Transimpedance Amplifiers for OTDR Applications," *Electronics*, vol. 8, no. 10, 2019. DOI: 10.3390/electronics8101073.
- [322] P. Muller and Y. Leblebici, "Transimpedance Amplifier Design," in *CMOS Multichannel Single-Chip Receivers for Multi-Gigabit Optical Data Communications*. Dordrecht: Springer Netherlands, 2007, pp. 73–93. DOI: 10.1007/978-1-4020-5912-4_6.
- [323] C. Hermans and M. Steyaert, "Transimpedance Amplifier Design," in *Broadband Opto-Electrical Receivers in Standard CMOS*. Dordrecht: Springer Netherlands, 2007, pp. 61–105. DOI: 10.1007/978-1-4020-6222-3_4.

- [324] A. Awmy, R. Nagulapalli, M. Kroh, *et al.*, “A Linear Differential Transimpedance Amplifier for 100-Gb/s Integrated Coherent Optical Fiber Receivers,” *IEEE Transactions on Microwave Theory and Techniques*, vol. 66, no. 2, pp. 973–986, 2018. DOI: 10.1109/TMTT.2017.2752170.
- [325] D. Li, M. Liu, S. Gao, *et al.*, “Low-Noise Broadband CMOS TIA Based on Multi-Stage Stagger-Tuned Amplifier for High-Speed High-Sensitivity Optical Communication,” *IEEE Transactions on Circuits and Systems I: Regular Papers*, vol. 66, no. 10, pp. 3676–3689, 2019. DOI: 10.1109/TCSI.2019.2916150.
- [326] “Thermal noise,” in SPIE PRESS. DOI: 10.1117/3.2186106.ch27.
- [327] D. Li, G. Minoia, M. Repossi, *et al.*, “A Low-Noise Design Technique for High-Speed CMOS Optical Receivers,” *IEEE Journal of Solid-State Circuits*, vol. 49, no. 6, pp. 1437–1447, 2014. DOI: 10.1109/JSSC.2014.2322868.
- [328] E. Hammoudi and A. Mokhtar, “2.75 GHz low noise 0.35 μm CMOS transimpedance amplifier,” in *18th Mediterranean Conference on Control and Automation, MED’10*, 2010, pp. 928–932. DOI: 10.1109/MED.2010.5547749.
- [329] M. R. B. Samadi, A. I. Karsilayan, and J. Silva-Martinez, “Design of transimpedance and limiting amplifiers for 10 Gb/s optical communication systems,” in *The 2002 45th Midwest Symposium on Circuits and Systems, 2002. MWSCAS-2002.*, vol. 3, 2002, pp. III–III. DOI: 10.1109/MWSCAS.2002.1186996.
- [330] B. Razavi, *Fundamentals of Microelectronics, 2nd Edition*. Wiley Global Education, 2013.
- [331] V. N. Kuleshov and T. I. Boldyreva, “1/f AM and PM noise in bipolar transistor amplifiers: sources, ways of influence, techniques of reduction,” in *Proceedings of International Frequency Control Symposium, 1997*, pp. 446–455. DOI: 10.1109/FREQ.1997.638642.
- [332] J. Kim and J. F. Buckwalter, “A 40-Gb/s Optical Transceiver Front-End in 45 nm SOI CMOS,” *IEEE Journal of Solid-State Circuits*, vol. 47, no. 3, pp. 615–626, 2012. DOI: 10.1109/JSSC.2011.2178723.
- [333] J. J. Morikuni, A. Dharchoudhury, Y. Leblebici, and S. M. Kang, “Improvements to the standard theory for photoreceiver noise,” *Journal of Lightwave Technology*, vol. 12, no. 7, pp. 1174–1184, 1994. DOI: 10.1109/50.301810.
- [334] T. J. Karras, *Equivalent Noise Bandwidth Analysis from Transfer Functions* (NASA technical note). National Aeronautics and Space Administration, 1965.
- [335] D. R. White, “The noise bandwidth of sampled data systems,” *IEEE Transactions on Instrumentation and Measurement*, vol. 38, no. 6, pp. 1036–1043, 1989. DOI: 10.1109/19.46397.
- [336] H. S. Dutta and N. R. Das, “Calculating the noise equivalent bandwidth of a ge-based schottky photodetector at 1.55 μm wavelength,” in *2009 International Conference on Emerging Trends in Electronic and Photonic Devices Systems*, 2009, pp. 479–482. DOI: 10.1109/ELECTRO.2009.5441063.
- [337] Y. H. Chien, K. L. Fu, and S. I. Liu, “A 3–25 Gb/s Four-Channel Receiver With Noise-Canceling TIA and Power-Scalable LA,” *IEEE Transactions on Circuits and Systems II: Express Briefs*, vol. 61, no. 11, pp. 845–849, 2014. DOI: 10.1109/TCSII.2014.2350372.

- [338] E. Säckinger, *Analysis and Design of Transimpedance Amplifiers for Optical Receivers*. Wiley, 2017.
- [339] F. Tavernier and M. S. J. Steyaert, “High-Speed Optical Receivers With Integrated Photodiode in 130 nm CMOS,” *IEEE Journal of Solid-State Circuits*, vol. 44, no. 10, pp. 2856–2867, 2009. DOI: 10.1109/JSSC.2009.2028755.
- [340] S. Giannakopoulos, Z. S. He, I. Darwazeh, and H. Zirath, “Transimpedance amplifiers with 133 GHz bandwidth on 130 nm indium phosphide double heterojunction bipolar transistors,” *Electronics Letters*, vol. 55, Jan. 2019. DOI: 10.1049/el.2018.8135.
- [341] S. P. Voinigescu, T. O. Dickson, T. Chalvatzis, *et al.*, “Algorithmic design methodologies and design porting of wireline transceiver IC building blocks between technology nodes,” in *Proceedings of the IEEE 2005 Custom Integrated Circuits Conference, 2005.*, 2005, pp. 111–118. DOI: 10.1109/CICC.2005.1568621.
- [342] K. Vasilakopoulos, S. P. Voinigescu, P. Schvan, P. Chevalier, and A. Cathelin, “A 92GHz bandwidth SiGe BiCMOS HBT TIA with less than 6dB noise figure,” in *2015 IEEE Bipolar/BiCMOS Circuits and Technology Meeting - BCTM*, 2015, pp. 168–171. DOI: 10.1109/BCTM.2015.7340554.
- [343] E. Säckinger, “The Transimpedance Limit,” *IEEE Transactions on Circuits and Systems I: Regular Papers*, vol. 57, no. 8, pp. 1848–1856, 2010. DOI: 10.1109/TCSI.2009.2037847.
- [344] G. S. Jeong, W. Bae, and D. K. Jeong, “Review of CMOS Integrated Circuit Technologies for High-Speed Photo-Detection,” *Sensors*, vol. 17, no. 9, 2017. DOI: 10.3390/s17091962.
- [345] J. W. Park, S. Mohammadi, D. Pavlidis, C. Dua, J. L. Guyaux, and J. G. Garcia, “GaInP/GaAs HBT broadband monolithic transimpedance amplifiers and their high frequency small and large signal characteristics,” in *1998 IEEE MTT-S International Microwave Symposium Digest (Cat. No.98CH36192)*, vol. 1, 1998, 39–42 vol.1. DOI: 10.1109/MWSYM.1998.689319.
- [346] M. Neuhauser, H. M. Rein, and H. Wernz, “Design and realization of low-noise, high-gain Si-bipolar transimpedance preamplifiers for 10 Gb/s optical-fiber links,” in *Proceedings of IEEE Bipolar/BiCMOS Circuits and Technology Meeting*, 1994, pp. 163–166. DOI: 10.1109/BIPOL.1994.587885.
- [347] M. S. Mikhemar, K. W. Sharaf, and H. F. Ragaie, “On the performance of transimpedance amplifier,” in *2003 46th Midwest Symposium on Circuits and Systems*, vol. 1, 2003, 25–28 Vol. 1. DOI: 10.1109/MWSCAS.2003.1562210.
- [348] S. V. Pawan, T. K. Johansen, K. Erkelenz, *et al.*, “An Improved EM-Simulation Procedure to Extract Extrinsic Elements of Terahertz InP DHBTs,” in *2020 German Microwave Conference (GeMiC)*, 2020, pp. 240–243.
- [349] G. Valdecasa Silva, J. Jensen Bevensee, M. Didriksen, and T. K. Johansen, “A 2-38 GHz Linear GaAs pHEMT TIA for a Quasi-Coherent Optical Receiver,” in *2019 14th European Microwave Integrated Circuits Conference (EuMIC)*, 2019, pp. 160–163. DOI: 10.23919/EuMIC.2019.8909685.

- [350] B. Analui and A. Hajimiri, "Bandwidth enhancement for transimpedance amplifiers," *IEEE Journal of Solid-State Circuits*, vol. 39, no. 8, pp. 1263–1270, 2004. DOI: 10.1109/JSSC.2004.831783.
- [351] S. S. Mohan, M. D. M. Hershenson, S. P. Boyd, and T. H. Lee, "Bandwidth extension in CMOS with optimized on-chip inductors," *IEEE Journal of Solid-State Circuits*, vol. 35, no. 3, pp. 346–355, 2000. DOI: 10.1109/4.826816.
- [352] J. Sangirov, I. A. Ukaegbu, T. W. Lee, M. H. Cho, and H. H. Park, "10 Gbps Transimpedance Amplifier-Receiver for Optical Interconnects," *J. Opt. Soc. Korea*, vol. 17, no. 1, pp. 44–49, Feb. 2013. DOI: 10.3807/JOSK.2013.17.1.044.
- [353] S. Daneshgar, H. Li, T. Kim, and G. Balamurugan, "A 128 Gb/s PAM4 Linear TIA with 12.6 pA/ $\sqrt{\text{Hz}}$ Noise Density in 22nm FinFET CMOS," in *2021 IEEE Radio Frequency Integrated Circuits Symposium (RFIC)*, 2021, pp. 135–138. DOI: 10.1109/RFIC51843.2021.9490496.
- [354] Y. Shi, D. Li, S. Gao, Y. Zhang, and L. Geng, "A 112Gb/s Low-Noise PAM-4 Linear Optical Receiver in 28nm CMOS," in *2019 IEEE International Conference on Electron Devices and Solid-State Circuits (EDSSC)*, 2019, pp. 1–3. DOI: 10.1109/EDSSC.2019.8753978.
- [355] L. Aschei, N. Cordioli, P. Rossi, D. Montanari, R. Castello, and D. Manstretta, "A 42-GHz TIA in 28-nm CMOS With Less Than 1.8% THD for Optical Coherent Receivers," *IEEE Solid-State Circuits Letters*, vol. 3, pp. 238–241, 2020. DOI: 10.1109/LSSC.2020.3012691.
- [356] K. S. Yngvesson, T. L. Korzeniowski, Y. S. Kim, E. L. Kollberg, and J. F. Johansson, "The tapered slot antenna-a new integrated element for millimeter-wave applications," *IEEE Trans. Microw. Theory Techn.*, vol. 37, no. 2, pp. 365–374, 1989. DOI: 10.1109/22.20062.
- [357] T. Djerafi, A. Doghri, and K. Wu, "Substrate Integrated Waveguide Antennas," in *Handbook of Antenna Technologies*, Z. N. Chen, Ed. Singapore: Springer Singapore, 2014, pp. 1–60. DOI: 10.1007/978-981-4560-75-7_57-1.
- [358] D. S. Woo, Y. G. Kim, K. W. Kim, and Y. K. Cho, "Ultra-wideband millimeter-wave tapered slot antennas," in *2007 IEEE Antennas and Propagation Society International Symposium*, 2007, pp. 1969–1972. DOI: 10.1109/APS.2007.4395908.
- [359] D. Schaubert, E. Kollberg, T. Korzeniowski, T. Thungren, J. Johansson, and K. Yngvesson, "Endfire tapered slot antennas on dielectric substrates," *IEEE Trans. Antennas Propag.*, vol. 33, no. 12, pp. 1392–1400, 1985. DOI: 10.1109/TAP.1985.1143542.
- [360] P. J. Gibson, "The vivaldi aerial," in *1979 9th European Microwave Conference*, 1979, pp. 101–105. DOI: 10.1109/EUMA.1979.332681.
- [361] *RO4000 Series: High Frequency Circuit Materials*, Rogers Corporation, 2018.
- [362] *RO5870/RO5880 Series: High Frequency Laminates*, Rogers Corporation, 2017.
- [363] *RO6006/RO6010 Series: High Frequency Laminates*, Rogers Corporation, 2017.
- [364] A. R. Djordjevic, R. M. Biljie, V. D. Likar-Smiljanic, and T. K. Sarkar, "Wide-band frequency-domain characterization of fr-4 and time-domain causality," *IEEE Transactions on Electromagnetic Compatibility*, vol. 43, no. 4, pp. 662–667, 2001. DOI: 10.1109/15.974647.

- [365] U. Kotthaus and B. Vowinkel, "Investigation of planar antennas for submillimeter receivers," *IEEE Trans. Microw. Theory Techn.*, vol. 37, no. 2, pp. 375–380, 1989. DOI: 10.1109/22.20063.
- [366] M. El-Gibari and H. Li, "A Comparative Study between Via-Hole and Via-Free Grounded Coplanar Waveguide to Microstrip Transitions on Thin Polymer Substrate," *Int. J. Antennas and Propag.*, vol. 2015, Dec. 2015. DOI: 10.1155/2015/481768.
- [367] W. H. Haydl, "On the use of vias in conductor-backed coplanar circuits," *IEEE Transactions on Microwave Theory and Techniques*, vol. 50, no. 6, pp. 1571–1577, 2002. DOI: 10.1109/TMTT.2002.1006419.
- [368] K. Rao, V. Meshram, and H. Suresh, "Optimization Assisted Antipodal Vivaldi Antenna for UWB Communication: Optimal Parameter Tuning by Improved Grey Wolf Algorithm," *Wirel. Pers. Commun.*, vol. 118, Jun. 2021. DOI: 10.1007/s11277-021-08165-0.
- [369] L. Chitturi Prasanna, M. B. Bhagya, and N. Narasimha Sastry, "A Parametric Analysis & Design of All Metal Vivaldi Antenna Covering 3.0-18 GHz for DF and Phased Array Applications," *Progress In Electromagnetics Research C*, vol. 92, pp. 57–69, 2019. DOI: doi:10.2528/PIERC19020601.
- [370] Z. Tahar, X. Dérobert, and M. Benslama, "An Ultra-Wideband Modified Vivaldi Antenna Applied to Ground and Through the Wall Imaging," *Progress In Electromagnetics Research C*, vol. 86, pp. 111–122, Jan. 2018. DOI: 10.2528/PIERC18051502.
- [371] M. D. Elsheakh and E. A. Abdallah, "Novel shapes of Vivaldi antenna for ground penetrating radar (GPR)," in *2013 7th European Conference on Antennas and Propagation (EuCAP)*, 2013, pp. 2886–2889.
- [372] K. P. Ma and T. Itoh, "A new broadband coplanar waveguide to slotline transition," in *1997 IEEE MTT-S International Microwave Symposium Digest*, vol. 3, 1997, 1627–1630 vol.3. DOI: 10.1109/MWSYM.1997.596685.
- [373] K. P. Ma, Y. Qian, and T. Itoh, "Analysis and applications of a new CPW-slotline transition," *IEEE Trans. Microw. Theory Techn.*, vol. 47, no. 4, pp. 426–432, 1999. DOI: 10.1109/22.754876.
- [374] A. Zandieh, N. Ranjkesh, S. Safavi-Naeini, and M. Basha, "A low-loss CPW to dielectric waveguide transition for millimeter-wave hybrid integration," in *ISAP 2012 - Int. Symp. Antennas Propag.*, 2012, pp. 1–2. DOI: 10.1109/APS.2012.6348787.
- [375] M. Chiappe and G. L. Gragnani, "Vivaldi antennas for microwave imaging: Theoretical analysis and design considerations," *IEEE Trans. Instrum. Meas.*, vol. 55, no. 6, pp. 1885–1891, 2006. DOI: 10.1109/TIM.2006.884289.
- [376] A. Bhattacharjee, A. Bhawal, A. Karmakar, A. Saha, and D. Bhattacharya, "Vivaldi antennas: A historical review and current state of art," *International Journal of Microwave and Wireless Technologies*, pp. 1–18, 2020. DOI: 10.1017/S1759078720001415.

- [377] J. Shin and D. H. Schaubert, "A parameter study of stripline-fed vivaldi notch-antenna arrays," *IEEE Trans. Antennas Propag.*, vol. 47, no. 5, pp. 879–886, 1999. DOI: 10.1109/8.774151.
- [378] M. Moosazadeh, S. Kharkovsky, Z. Esmati, and B. Samali, "UWB elliptically-tapered antipodal Vivaldi antenna for microwave imaging applications," in *2016 IEEE-APS Topical Conference on Antennas and Propagation in Wireless Communications (APWC)*, 2016, pp. 102–105. DOI: 10.1109/APWC.2016.7738131.
- [379] M. T. Islam, M. Z. Mahmud, M. Tarikul Islam, S. Kibria, and M. Samsuzzaman, "A Low Cost and Portable Microwave Imaging System for Breast Tumor Detection Using UWB Directional Antenna array," *Scientific Reports*, vol. 9, Oct. 2019. DOI: 10.1038/s41598-019-51620-z.
- [380] C. Li, H. Zhang, M. Yu, and G. Q. Lo, "CMOS-compatible high efficiency double-etched apodized waveguide grating coupler," *Opt. Express*, vol. 21, no. 7, pp. 7868–7874, Apr. 2013. DOI: 10.1364/OE.21.007868.
- [381] P. Cheben, J. H. Schmid, S. Wang, *et al.*, "Broadband polarization independent nanophotonic coupler for silicon waveguides with ultra-high efficiency," *Opt. Express*, vol. 23, no. 17, pp. 22 553–22 563, Aug. 2015. DOI: 10.1364/OE.23.022553.
- [382] Y. Xu, F. Wang, Y. Gao, *et al.*, "Efficient polymer waveguide grating coupler with directionality enhancement," *Opt. Commun.*, vol. 463, p. 125 418, 2020. DOI: 10.1016/j.optcom.2020.125418.
- [383] I. Flammia, B. Khani, S. Arafat, and A. Stöhr, "60 GHz grounded-coplanar-waveguide-to-substrate-integrated-waveguide transition for RoF transmitters," *Electronics Letters*, vol. 50, no. 1, pp. 34–35, 2014. DOI: <https://doi.org/10.1049/el.2013.3533>.
- [384] I. Flammia, T. Kleinfeld, M. Frei, A. Utreras-Rivera, and A. Stöhr, "71–76GHz grounded-coplanar-waveguide-to-rectangular-waveguide transition with integrated planar bias tee for quasi-hermetic radio-over-fiber wireless transmitter," in *2012 7th European Microwave Integrated Circuit Conference*, 2012, pp. 512–515.
- [385] I. Flammia, B. Khani, and A. Stohr, "A novel transition from grounded coplanar waveguide to substrate inte grated waveguide for 60 GHz Radio-over-Fiber photonic transmitters," in *2013 Conference on Microwave Techniques (COMITE)*, 2013, pp. 73–76. DOI: 10.1109/COMITE.2013.6545046.
- [386] S. K. Prasad, *Advanced Wirebond Interconnection Technology*. Springer US, 2004.
- [387] G. Harman, *Wire Bonding in Microelectronics*. McGraw-Hill Education, 2009.
- [388] L. Young, *Advances in microwaves, vol. 8*. Academic Press, 1974.
- [389] G. Roelkens, J. Brouckaert, D. van Thourhout, R. Baets, R. Nötzel, and M. Smit, "Adhesive Bonding of InP InGaAsP Dies to Processed Silicon-On-Insulator Wafers using DVS-bis-Benzocyclobutene," vol. 153, no. 12, G1015, 2006. DOI: 10.1149/1.2352045.
- [390] J. Salvia, P. Lajevardi, M. Hekmat, and B. Murmann, "A 56M Ω CMOS TIA for MEMS applications," in *2009 IEEE Custom Integrated Circuits Conference*, 2009, pp. 199–202. DOI: 10.1109/CICC.2009.5280878.

- [391] I. Brandon, S. Pinna, Y. Liu, and J. Klamkin, "Efficiency of Waveguide Uni-Traveling-Carrier Photodiodes for Microwave Signal Generation," Optical Society of America, 2019, Th3B.6. DOI: 10.1364/OFC.2019.Th3B.6.
- [392] J. Perez Santacruz, S. Rommel, U. Johannsen, A. Jurado-Navas, and I. Tafur Monroy, "Analysis and Compensation of Phase Noise in Mm-Wave OFDM ARoF Systems for Beyond 5G," *Journal of Lightwave Technology*, vol. 39, no. 6, pp. 1602–1610, 2021. DOI: 10.1109/JLT.2020.3041041.
- [393] I. Yildirim, A. Uyrus, and E. Basar, "Modeling and Analysis of Reconfigurable Intelligent Surfaces for Indoor and Outdoor Applications in Future Wireless Networks," *IEEE Transactions on Communications*, vol. 69, no. 2, pp. 1290–1301, 2021. DOI: 10.1109/TCOMM.2020.3035391.
- [394] L. Chorchos, J. P. Turkiewicz, S. Rommel, I. Tafur Monroy, J. J. Vegas Olmos, and S. Spolitis, "W-band real-time transmission utilizing a reconfigurable RAU for NG-PON networks," in *2016 Advances in Wireless and Optical Communications (RTUWO)*, 2016, pp. 66–69. DOI: 10.1109/RTUWO.2016.7821857.
- [395] K. Q. Huang and M. Swaminathan, "Antennas in Glass Interposer For sub-THz Applications," in *2021 IEEE 71st Electronic Components and Technology Conference (ECTC)*, 2021, pp. 1150–1155. DOI: 10.1109/ECTC32696.2021.00188.
- [396] L. Wang, C. Liu, S. Shen, M. Xu, and X. Liu, "Low dielectric constant polymers for high speed communication network," *Advanced Industrial and Engineering Polymer Research*, vol. 3, no. 4, pp. 138–148, 2020. DOI: 10.1016/j.aiepr.2020.10.001.
- [397] M. Palandoken, V. Rymanov, A. Stohr, and T. Tekin, "Compact Metamaterial-based Bias Tee Design for 1.55 μ m Waveguide-photodiode Based 71-76GHz Wireless Transmitter," in *2012 Progress In Electromagnetics Research Symposium (PIERS)*, 2012.
- [398] B. Khani, V. Rymanov, M. Steeg, A. Buck, S. Dulme, and A. Stohr, "Compact E-Band (71-86 GHz) bias-tee module for external biasing of millimeter wave photodiodes," in *2015 International Topical Meeting on Microwave Photonics (MWP)*, 2015, pp. 1–4. DOI: 10.1109/MWP.2015.7356673.
- [399] Y. Jiao, J. van der Tol, V. Pogoretskii, *et al.*, "Indium Phosphide Membrane Nanophotonic Integrated Circuits on Silicon," *physica status solidi (a)*, vol. 217, no. 3, p. 1900606, 2020. DOI: 10.1002/pssa.201900606.
- [400] A. M. de Oliveira, H. D. A. Orrillo, W. A. M. van Noije, S. T. Kofuji, and L. C. Moreira, "A CMOS UWB pulse beamforming transmitter with Vivaldi array antenna for vital signals monitoring applications," in *2012 IEEE 3rd Latin American Symposium on Circuits and Systems (LASCAS)*, 2012, pp. 1–4. DOI: 10.1109/LASCAS.2012.6180337.
- [401] A. Morales, S. Rommel, and I. Tafur Monroy, "Centralized optical true time delay beamforming at 60 GHz with multicore fiber distribution," in *Latin America Optics and Photonics Conference*, Optical Society of America, 2018, Tu2B.3. DOI: 10.1364/LAOP.2018.Tu2B.3.

- [402] A. Morales and I. Tafur Monroy, “Silicon Nitride Integrated Optical Beamforming Network for Millimeter Wave Photonics Systems,” in *2018 48th European Microwave Conference (EuMC)*, 2018, pp. 785–788. DOI: 10.23919/EuMC.2018.8541583.
- [403] R. Muñoz, S. Rommel, P. van Dijk, *et al.*, “Experimental Demonstration of Dynamic Optical Beamforming for Beyond 5G Spatially Multiplexed Fronthaul Networks,” *IEEE Journal of Selected Topics in Quantum Electronics*, vol. 27, no. 6, pp. 1–16, 2021. DOI: 10.1109/JSTQE.2021.3079726.
- [404] H. Schröder, L. Brusberg, N. Arndt-Staufenbiel, J. Hofmann, and S. Marx, “Glass panel processing for electrical and optical packaging,” in *2011 IEEE 61st Electronic Components and Technology Conference (ECTC)*, 2011, pp. 625–633. DOI: 10.1109/ECTC.2011.5898578.
- [405] *ECC Report 218: Point-to-Point Radio Links in the Frequency Ranges 92-114.25 GHz and 130-174.8 GHz*. Electronic Communications Committee, 2018.

List of Acronyms

5G	Fifth generation
5G NR	Fifth generation new radio
ABF	Analogue beamforming
ADC	Analogue to digital converter
APD	Avalanche photodiode
ARoF	Analogue radio-over-fiber
ASE	Amplified spontaneous emission
ATT	Attenuator
AWG	Arrayed waveguide grating
BBU	Baseband unit
BER	Bit error rate
BERT	Bit error rate tester
BPF	Band pass filter
CAGR	Compound annual growth rate
CB-CPW	Conductor backed coplanar-waveguide
CD	Chromatic dispersion
CDR	Clock data recovery
CE	Common emitter
CLC	Clock
CMOS	Complementary metal–oxide–semiconductor
CO	Central office
CP	Cyclic prefix
CPRI	Common public radio interface
CPW	Coplanar-waveguide
C-RAN	Centralised radio access network
CW	Continuous wave
CWSA	Constant width slot antenna
DAC	Digital to analogue converter

DBF	Digital beamforming
DC	Direct current
DeMUX	De-multiplexer
DHBT	Double heterojunction bipolar transistor
DML	Directly modulated laser
D-RAN	Distributed radio access networks
DRoF	Digital radio-over-fibre
DSO	Digital storage oscilloscope
DSP	Digital signal processing
DUT	Device under test
E/E	Electrical-electrical
E/O	Electro-optical
EAM	Electro-absorption modulator
EB	Exabyte
ECL	External cavity laser
ED	Envelope detector
EDFA	Erbium doped fiber amplifier
EF-TIA	Emitter-follower transimpedance amplifier
EMC	Electromagnetic compatibility
ESA	Electrical spectrum analyzer
ETSA	Exponential tapered slot antenna
FB	Forward bias
FBG	Fibre Bragg grating
FBH	Ferdinand Braun Institute
FEC	Forward error correction
FFT	Fast-Fourier transform
FPGA	Field programmable gate array
FSPL	Free space path loss
FTTH	Fibre to the home
FTTx	Fibre to the x
FWA	Fibre-wireless access
GCPW	Grouded coplanar-waveguide
GH	Gain horn
GSG	Ground-signal-ground
GSM	Global system mobile
HBF	Hybrid beamforming
HBT	Heterojunction bipolar transistor
HEMT	High electron mobility transistor
IC	Integrated circuit
IEEE	Institute of Electrical and Electronics Engineers

IF	Intermediate frequency
IFoF	Intermediate frequency over fibre
IMOS	InP membrane on silicon
IoT	Internet of things
IP	Internet protocol
IP3	Third-order intercept point
ISI	Inter-symbol interference
ITU	International telecommunication union
KPI	Key performance indicator
LCA	Lightwave component analyser
LNA	Low noise amplifier
LO	Local oscillator
LoS	Line-of-sight
LTE	Long-term evolution
LTE-A	Long-term evolution advanced
LTSA	Linear tapered slot antenna
M2M	Machine-to-machine
MAG	Maximum available power gain
MC	Multi-carrier
MCF	Multicore fibre
MIMO	Multiple-input and multiple-output
mm-wave	Millimetre wave
M-OFDM	Multi-band orthogonal frequency division multiplexing
MPA	Medium power amplifier
MS-TIA	Multi-stage transimpedance amplifier
MUX	Multiplexer
MZM	Mach-Zehnder modulator
NF	Noise figure
NFV	Network function virtualisation
NLoS	Non-line-of-sight
NLSE	Nonlinear Schrödinger equation
NRZ	Non-return to zero
O/E	Optical-electrical
OADM	Optical add drop multiplexer
OCS	Optical carrier supression
OFDM	Orthogonal frequency division multiplexing
OH	Overhead
OLT	Optical line terminal
ONU	Optical network unit
OOK	On-off keying

ORR	Optical ring resonator
OSL	Open, short and load calibration
OSLT	Open, short, load and thru calibration
OTTD	Optical true time delay
PA	Power amplifier
PAF	Phased array fed
PAM	Pulse-amplitude modulation
PC	Polarization controller
PCB	Printed circuit board
PD	Photodiode
PhA	Phased array
PIC	Photonic integrated circuit
PIN-PD	PIN photodiode
PMD	Polarization mode dispersion
PNA	Performance network analyser
PON	Passive optical network
PPG	Pulse pattern generator
PRBS	Pseudo random bit sequence
PS	Phase shifter
PSD	Power spectral density
PSK	Phase-shift keying
QAM	Quadrature amplitude modulation
QoS	Quality of service
QPSK	Quadrature phase-shift keying
RAN	Radio access network
RB	Reverse bias
RF	Radio frequency
RIS	Reconfigurable intelligent surfaces
RoF	Radio-over-fiber
RU	Remote unit
SBS	Stimulated Brillouin scattering
SC	Single-carrier
SDM	Space division multiplexing
SDN	Software defined networking
SFP	Small form-factor pluggable
SMF	Single-mode fiber
SNR	Signal to noise ratio
SPM	Self-phase modulation
SSS	Three-offset shorts calibration
S-TIA	Single-stage transimpedance amplifier

SW	Switch
SWP	Smart wireless pluggable
TDD	Time-division duplexing
TIA	Transimpedance amplifier
TML	Transmission line
TSA	Tapered slot antenna
UDWDM	Ultra dense wavelength division multiplexing
UE	End-user
UTC-PD	Uni-travelling carrier photodiode
V2V	Vehicle to vehicle
V2X	Vehicle to everything
VNA	Vector network analyser
VOA	Variable optical attenuator
VSG	Vector signal generator
WDM	Wavelength division multiplexing
WG	Waveform generator
WG HPF	Waveguide high pass filter
WiFi	Wireless fidelity
WSS	Wavelength selective switch
XPM	Cross-phase modulation

List of Publications

Journal articles

- [J1] **D. Konstantinou**, T. A. H. Bressner, S. Rommel, *et al.*, “5G RAN architecture based on analog radio-over-fiber fronthaul over UDWDM-PON and phased array fed reflector antennas,” *Optics Communications*, vol. 454, p. 124 464, 2020. DOI: 10.1016/j.optcom.2019.124464.
- [J2] J. de Graaf, X. Zhao, **D. Konstantinou**, *et al.*, “Beyond 110 GHz uni-traveling carrier photodiodes on an InP-membrane-on-silicon platform,” *IEEE Journal of Selected Topics in Quantum Electronics*, vol. 28, no. 2, pp. 1–10, 2021. DOI: 10.1109/JSTQE.2021.3110411.
- [J3] **D. Konstantinou**, C. Caillaud, S. Rommel, U. Johannsen, and I. Tafur Monroy, “Investigation of de-embedding techniques applied on uni-traveling carrier photodiodes,” *International Journal of Microwave and Wireless Technologies*, pp. 1–13, 2021. DOI: 10.1017/S1759078721000210.

Conference contributions

- [C1] **D. Konstantinou**, T. A. H. Bressner, S. Rommel, U. Johannsen, A. B. Smolders, and I. Tafur Monroy, “High Capacity Real-Time Hybrid Optical-Wireless 5G Fronthaul with Dynamic Beam Steering,” in *2021 Opto-Electronics and Communications Conference (OECC)*, 2021, W2B.3. DOI: 10.1364/OECC.2021.W2B.3.
- [C2] **D. Konstantinou**, A. Morales, S. Rommel, T. R. Raddo, U. Johannsen, and I. Tafur Monroy, “Analog Radio Over Fiber Fronthaul for High Bandwidth 5G Millimeter-Wave Carrier Aggregated OFDM,” in *21st International Conference on Transparent Optical Networks (ICTON)*, Angers, France: IEEE, Jul. 2019, pp. 1–4. DOI: 10.1109/ICTON.2019.8840525.
- [C3] **D. Konstantinou**, A. Morales, I. Aghmari, *et al.*, “High-speed wireless access in forested rural areas using analog radio-over-fiber technology,” in *Latin America Optics and Photonics Conference*, Lima, Peru: Optical Society of America (OSA), Nov. 2018, Tu2B.4. DOI: 10.1364/LAOP.2018.Tu2B.4.

- [C4] **D. Konstantinou**, C. Caillaud, S. Rommel, U. Johannsen, and I. Tafur Monroy, "Investigation of De-embedding Techniques Applied on Uni-Traveling Carrier Photodiodes," in *2020 50th European Microwave Conference (EuMC)*, 2021, pp. 320–323. DOI: 10.23919/EuMC48046.2021.9338063.
- [C5] **D. Konstantinou**, C. Caillaud, T. Shivan, *et al.*, "Simulation of an Integrated UTC-Photodiode with a High-Speed TIA for 5G mm-Wave Generation," in *2020 International Conference on Numerical Simulation of Optoelectronic Devices (NUSOD)*, 2020, pp. 1–2. DOI: 10.1109/NUSOD49422.2020.9217642.
- [C6] **D. Konstantinou**, J. de Graaf, S. Rommel, U. Johannsen, Y. Jiao, and I. Tafur Monroy, "V-Band Vivaldi Antenna for Beyond-5G Integrated Photonic-Wireless Millimetre Wave Transmitter," in *Accepted - 2022 European Conference on Antennas and Propagation (EuCAP)*, 2022.
- [C7] **D. Konstantinou**, A. Morales, S. Rommel, T. R. Raddo, U. Johannsen, and I. Tafur Monroy, "An eHealth-Care Driven Perspective on 5G Networks and Infrastructure," English, in *Internet of Things, Infrastructures and Mobile Applications - Proceedings of the 13th IMCL Conference, IMCL 2019*, ser. Advances in Intelligent Systems and Computing, Springer, 2021, pp. 1076–1088. DOI: 10.1007/978-3-030-49932-7_101.
- [C8] A. Morales, **D. Konstantinou**, S. Rommel, *et al.*, "Bidirectional K-band Photonic/Wireless Link for 5G Communications," in *44th International Conference on Infrared, Millimeter, and Terahertz Waves (IRMMW-THz)*, Paris, France: IEEE, 2019, pp. 1–2. DOI: 10.1109/IRMMW-THz.2019.8874031.
- [C9] A. B. Granja, **D. Konstantinou**, S. Rommel, *et al.*, "High data rate W-band balanced Schottky diode envelope detector for broadband communications," English, in *2019 49th European Microwave Conference, EuMC 2019*, United States: Institute of Electrical and Electronics Engineers, 2019, pp. 864–867. DOI: 10.23919/EuMC.2019.8910949.
- [C10] A. Morales, **D. Konstantinou**, S. Rommel, U. Johannsen, C. Okonkwo, and I. Tafur Monroy, "Physical-Layer Confidentiality by Chaotic Encoding in Radio-Over-Fiber Systems," in *Optical Fiber Communications Conference and Exhibition (OFC)*, San Diego, CA, USA: Optical Society of America (OSA), 2019, W1I.1. DOI: 10.1364/OFC.2019.W1I.1.
- [C11] R. Schulpen, **D. Konstantinou**, S. Rommel, U. Johannsen, I. Tafur Monroy, and A. B. Smolders, "Extended Range Ultra-Wideband Millimeter-Wave Channel Sounder with Over-The-Air Calibration," in *2019 13th European Conference on Antennas and Propagation (EuCAP)*, 2019, pp. 1–5.
- [C12] S. Rommel, A. Morales, **D. Konstantinou**, T. Salgals, and I. Tafur Monroy, "Millimeter Wave Hybrid Photonic Wireless Links - Also for Broadcast?" In *IEEE International Symposium on Broadband Multimedia Systems and Broadcasting (BMSB)*, Valencia, Spain: IEEE, 2018, pp. 1–5. DOI: 10.1109/BMSB.2018.8436888.

- [C13] S. Rommel, A. Morales, **D. Konstantinou**, T. R. Raddo, and I. Tafur Monroy, “mm-Wave and THz Analog Radio-over-Fiber for 5G, Wireless Communications and Sensing,” in *Latin America Optics and Photonics Conference*, Lima, Peru: Optical Society of America (OSA), 2018, W3D.1. DOI: 10.1364/LAOP.2018.W3D.1.

Other scientific publications

- [O1] U. Johannsen, S. Rommel, A. Al-Rawi, *et al.*, “ARoF-Fed antenna architectures for 5G networks,” English, in *2019 Optical Fiber Communications Conference and Exhibition, OFC 2019 - Proceedings*, United States: Optical Society of America (OSA), 2019. DOI: 10.1364/OFC.2019.W1I.3.
- [O2] **D. Konstantinou**, L. Xue, T. Shivan, *et al.*, “Integrated Optical-Wireless Interface and Detection,” in *Enabling 6G Mobile Network*, J. Rodriguez, C. Verikoukis, J. S. Vardakas, and N. Passas, Eds. Springer International Publishing, 2021. DOI: 10.1007/978-3-030-74648-3_7.
- [O3] A. Fernandez Olvera, A. Morales, Y. Dong, *et al.*, “W-Band Heterodyne Wireless System with 2.3 GHz Intermediate Frequency Driven Entirely by ErAs:In(Al)GaAs Photoconductors,” in *21st International Conference on Transparent Optical Networks (ICTON)*, Angers, France: IEEE, 2019, pp. 1–3. DOI: 10.1109/ICTON.2019.8840209.

Acknowledgements

Four years ago, I started a journey pursuing my PhD degree at the Eindhoven University of Technology (TU/e) under the ITN EU project 5G STEP FWD. I went through some difficult moments during this period but primarily happy and exciting times. I broadened my scientific horizons and grew as a researcher. In addition, I learned many aspects about myself and evolved as a person. My scientific and personal growth is also due to the people who supported me and stood by me over these years, and it is with great pleasure of mine to dedicate this section to them.

First of all, I would like to express my gratitude to my promotor Prof. Idelfonso Tafur Monroy, for providing me with the opportunity to work on my PhD at TU/e. I appreciate your supervision, support, guidance and encouragement during my studies. Your positivity and trust allowed my work to flourish. With your effort, you built an excellent team I am proud to be a member of during this time. You always care about us and prioritise our well-being and health while you helped me whenever there was an emergency. I am very grateful for teaching me the importance of scientific collaboration that helped me immensely during my PhD and its a trait that will always follow me for the rest of my life.

I also want to thank my co-promotor, Dr. Simon Rommel, for your support. You were the first to teach me the fundamental aspects of hybrid photonic-wireless systems when I was a master student at the Technical University of Denmark (DTU) in 2016. This made me highly motivated to continue this work in the latter stages of my academic life. You substantially helped me in my theoretical and experimental work all these years, making sure that I grasped all the fundamental requirements for each assignment I had to work with. Our everyday morning coffees where we discussed about the tasks of the day as well as different topics about life were always a motivating daily start for me.

Furthermore, I would like to thank my co-promotor, Dr. Ulf Johannsen. You agreed to become my supervisor when I came to Eindhoven and set the milestones of my supervision while playing an essential role in coordinating and structuring my external stays in France and Germany. I appreciate your time and effort to provide me with all the necessary tools in order to simulate and synthesise the

Vivaldi antenna. Finally, to both my co-promotors, I would like to thank them for planning one hour per week for supervision meetings despite their busy schedule to monitor my progress, exchange ideas and discuss future tasks.

Moreover, I am very grateful to all the terahertz photonic systems (THs) team members for the joint work and for being my friends. The bond that we all built, I believe it is unique and special. Even at difficult times during my PhD, I knew that I would go for lunch with you all and would start smiling and laughing. This fantastic atmosphere always filled me with positivity, inspiration and happy thoughts. A very special thanks to my former colleague and good friend, Álvaro. Thank you for all the personal, professional support and the eagerness to help in my difficult moments. Building experimental setups and performing measurements in the lab with you was seamless and excellent. I also want to thank my PhD colleague Javier. It was a pleasure to work with you on the same project, and I appreciate your positive attitude and your input during our brainstorming sessions and technical presentations. I would like to thank the former visiting colleague Angel for the experimental work we did in W-band communications. I would also like to thank Thiago for our scientific conversations, your eagerness to help and provide feedback in various of my publications. Also, to Bruno, thank you very much for your feedback on the fundamentals of advanced electronic simulations. It was a pleasure sharing the same office with you and Gleb. I also want to thank the rest of the THs members (former and present): Imane, Gleb, Juliana, Shihab, Mariëlle, Catalina, Carlos, Mehmet, Hui, Afra, Oumayma, Maira, Marijn, Doruk and Diana. Finally, it is also fair to express my sincere and deep gratitude to Femke. You are always there, being so eager to support. I really enjoyed all the team activities that you planned for all of us. I will always remember our amazing first activity with tandem bikes around Eindhoven.

I would like to thank all the electro-optical communications (ECO) group members, Ketema, Ailee, John, Sjoerd, Xuebing, Bin, Menno... You were always willing to help us by sharing equipment, and you were very open to discussions and collaborations. I am very thankful to the colleagues from the electromagnetics (EM) group Thomas and Robbert. We investigated various aspects of mm-wave wireless communications and channel sounding for 5G leading to great experimental work that has been published. Furthermore, I would like to express my gratitude to Jasper from the photonic integration (PHI) group on our work on integrated photodiodes and antenna characterisation experiments. I want to thank all the people involved in the 5G STEP FWD consortium for their excellent planning and support. To the fellow ESRs, we had many shared moments, schools, conferences, and deliverables. During these meetings, I had the opportunity to get to know you all, discuss many inspiring ideas and enjoy many happy moments with you.

I am deeply grateful to Dr. Christophe Caillaud for giving me the opportunity to work for six months at III-V Lab. Within this period, I substantially enhanced my experimental and scientific knowledge in photonic integrated photodiodes. I also want to thank my friend and colleague, Kebede. You assisted me a lot on my moving to Paris, and I always enjoyed our discussions and the ideas we shared dur-

ing our lunch and coffee times. I also want to thank all my former colleagues Joan, Alessandro, Sylvain, Theo, Hajar, Giancarlo... for making a very friendly and very productive atmosphere at work. In addition, I would like to express my gratitude to Prof. Viktor Krozer for providing me with an eight-month internship position at Ferdinand Braun Institute (FBH). You encouraged to decisively enhance my knowledge in high-speed electronic integration. Thank you for always being eager to answer all my questions despite your busy schedule. I would also like to thank Tanjil and Maruf for their support during my stay and their feedback on the final design and functionality of the EF-TIA before being sent to fabrication. It was a pleasure that I shared the office with both of you. I also want to thank Prof. Tom Johansen for his intuitive tutorials on electronic amplifiers and Hady for our fruitful discussions on on-wafer co-integration between photonics and electronics.

I am grateful to all collaborators and co-authors who have been directly or indirectly involved in the experiments and publications of this work. I would also like to thank the members of my PhD committee for taking the time to review and approve this work. Finally, I am thankful to my former supervisors both in Denmark and Greece. I still apply your teachings and knowledge I acquired under your supervision.

I want to dedicate this paragraph to my family and friends. Søren, Galal, Josko, Nikos, Alba, Nikos, Susan, Alexandros, Eleni, Peter Jan, Giuseppe, Benjamin and Ilias, thank you all for being in my life and being there for me in my difficult and happy times. You are all wonderful people giving me strength and support. I would also like to thank my beloved brother in law Spyros, my niece Evangelia and nephew Nikolaos. A special thanks to my sister Andriana. You explained the importance of science in our lives and made me fall in love with mathematics and physics. Finally, to my mother Eva, I want to thank you for your moral support and for being there for me all the time. You inspired me to make my choices in life with ethos, love and respect for the people around me and our society.

Ευχαριστώ, thank you, tusind tak, dank je wel, merci beacoup, dankeschön.

Eindhoven, January 2022

Dimitrios Konstantinou

Curriculum Vitae



Dimitrios Konstantinou was born on 17-11-1989 in Athens, Greece. He received his Diploma in electrical and computer engineering from the National Technical University of Athens (NTUA) in 2015. He obtained an MSc degree in Telecommunications with focus on optical communications from the Technical University of Denmark (DTU) in 2017.

The same year, he started a PhD project within the Electrical Engineering Department at the Eindhoven University of Technology (TU/e). His research has been carried out under the framework of the EU H2020 project 5G STEP FWD. The results obtained in the PhD project are presented in this dissertation and have led to several scientific publications and conference contributions. One of these publications was awarded with the Best Student Paper Award of the 26th Optoelectronics Communications Conference in Hong Kong.

His expertise focuses on millimetre wave communications, radio-over-fiber systems, and interfacing photonic and electronic integrated circuits on InP.